Brain rhythm fluctuations: Envelope-Phase modeling and Phase synchronization

by

Arthur Sadrack Powanwe

Thesis submitted to the University of Ottawa
in partial fulfillment of the requirements for
the degree of Ph.D. in Physics

Ottawa-Carleton Institute for Physics
Department of Physics
Faculty of Science
University of Ottawa
May 2021

© Arthur Sadrack Powanwe, Ottawa, Canada, 2021

Abstract

Fast neural oscillations known as beta (12-30Hz) and gamma (30-100Hz) rhythms are recorded across several brain areas of various species. They have been linked to diverse functions like perception, attention, cognition, or interareal brain communication. The majority of the tasks performed by the brain involves communication between brain areas. To efficiently perform communication, mathematical models of brain activity require representing neural oscillations as sustained and coherent rhythms. However, some recordings show that fast oscillations are not sustained or coherent. Rather they are noisy and appear as short and random epochs of sustained activity called bursts. Therefore, modeling such noisy oscillations and investigating their ability to show interareal coherence and phase synchronization are important questions that need to be addressed.

In this thesis, we propose theoretical models of noisy oscillations in the gamma and beta bands with the same properties as those observed in in *vivo*. Such models should exhibit dynamic and statistical features of the data and support dynamic phase synchronization. We consider networks composed of excitatory and inhibitory populations. Noise is the result of the finite size effect of the system or the synaptic inputs. The associated dynamics of the Local Field Potentials (LFPs) are modeled as linear equations, sustained by additive and/or multiplicative noises. Such oscillatory LFPs are also known as noise-induced or quasi-cycles oscillations. The LFPs are better described using the envelope-phase representation. In this framework, a burst is defined as an epoch during which the envelope magnitude exceeds a given threshold. Fortunately, to the lowest order, the envelope dynamics are uncoupled from the phase dynamics for both additive and multiplicative noises. For additive noise, we derive the mean burst duration via a mean first passage time approach and uncover an optimal range of parameters for healthy rhythms. Multiplicative noise is shown theoretically to further synchronize neural activities and better explain pathologies with an excess

of neural synchronization. We used the stochastic averaging method (SAM) as a theoretical tool to derive the envelope-phase equations. The SAM is extended to extract the envelope-phase equations of two coupled brain areas. The goal is to tackle the question of phase synchronization of noise-induced oscillations with application to interareal brain communication. The results show that noise and propagation delay are essential ingredients for dynamic phase synchronization of quasi-cycles. This suggests that the noisy oscillations recorded in *vivo* and modeled here as quasi-cycles are good candidates for such neural communication. We further extend the use of the SAM to describe several coupled networks subject to white and colored noises across the Hopf bifurcation ie in both quasi-cycle and limit cycle regimes. This allows the description of multiple brain areas in the envelope-phase framework. The SAM constitutes an appropriate and flexible theoretical tool to describe a large class of stochastic oscillatory phenomena through the envelope-phase framework.

Sommaire

Des oscillations neuronales rapides appelées rythmes beta (12-30Hz) et gamma (30-100Hz) sont observées dans plusieurs zones cérébrales de diverses espèces. Elles ont été liées à diverses fonctions comme la perception, l'attention, la cognition ou la communication cérébrale. La majorité des tâches effectuées par le cerveau impliquent la communication entre regions cérébrales. Pour effectuer une communication efficace, les modèles mathématiques de l'activité cérébrale nécessitent de représenter les oscillations neuronales comme des rythmes soutenus et cohérents. Cependant, les observations experimentales montrent que les oscillations rapides ne sont ni soutenues ni cohérentes. Au contraire, elles sont stochastiques et apparaissent sous forme de périodes brèves et aléatoires d'activité soutenue appelées "décharges" ou "bursts". Par conséquent, la modélisation de ces oscillations stochastiques et l'étude de leur capacité à montrer la cohérence entre les régions du cerveau et la synchronisation de phase sont des questions importantes qui doivent être abordées.

Dans cette thèse, nous proposons des modèles théoriques d'oscillations stochastiques dans les bandes gamma et beta avec les mêmes propriétés que celles observées *in vivo*. Ces modèles devraient présenter des caractéristiques dynamiques et statistiques des données experimentales et rendre compte de la synchronisation de phase dynamique. Nous considérons des réseaux composés de populations excitatrices et inhibitrices. Le bruit est le résultat de l'effet de taille finie du système ou des signaux synaptiques. La dynamique associée des potentiels de champ locaux (LFP) est modélisée à l'aide des équations linéaires, soutenues respectivement par des bruits additifs et multiplicatifs. Ces LFP oscillatoires sont également appelées oscillations induites par le bruit ou quasi-cycles. Les LFP sont mieux décrits en utilisant la représentation enveloppe-phase. Dans ce cadre, un "burst" est défini comme une époque pendant laquelle l'amplitude de l'enveloppe dépasse un seuil donné. Heureusement, à l'ordre le plus bas, la dynamique d'enveloppe est découplée de celle de la phase

pour les bruits additifs et multiplicatifs. Pour le bruit additif, nous calculons la durée moyenne des "bursts" via une approche du temps moyen de premier passage et découvrons une région optimale de paramètres pour des rythmes sains. Le bruit multiplicatif synchronise davantage les activités neuronales et explique mieux les pathologies causées par un excès de synchronisation neuronale. Nous avons utilisé la méthode du moyennage stochastique (SAM) comme outil théorique pour déduire les équations de type enveloppe-phase. Le SAM est étendu pour extraire les équations de type enveloppe-phase de deux zones cérébrales couplées. L'objectif est d'aborder la question de la synchronisation de phase des oscillations induites par le bruit avec pour application la communication entre régions cérébrales. Les résultats montrent que le bruit et le délai de propagation sont des ingrédients essentiels pour la synchronisation dynamique de phase des quasi-cycles. Cela suggère que les oscillations stochastiques enregistrées *in vivo* et modélisées ici comme des quasi-cycles sont de bons candidats pour une telle communication neuronale. Nous étendons encore l'utilisation du SAM pour décrire plusieurs réseaux couplés sujets à des bruits blancs et colorés à travers la bifurcation de Hopf, c'est-à-dire dans des régimes de quasi-cycle et de cycle limite. Cela permet la description de plusieurs zones cérébrales dans le cadre de la répresentation enveloppe-phase. Le SAM constitue un outil théorique approprié et flexible pour décrire une grande classe de phénomènes oscillatoires stochastiques dans la répresentation enveloppe-phase.

Acknowledgments

During my thesis, I receive support from many people. Without these persons I wouldn't have been able to complete this Thesis.

I would like first to give many thanks to my supervisor André Longtin. He believed in my potential and accepted me in his group. That wasn't an easy choice, especially because it was his first time to have a student from Africa. Still from the beginning of my thesis, he has been patient, understanding, generous and caring. More importantly, he gave me the freedom and independence to explore and/or work on my own ideas. Such independence and freedom have strongly shaped my discipline, creativity and ability to navigate among several disciplines.

I would also like to thank past members of the Longtin's Lab, Belen, Gregory, Nicola, Alexandre. I had my first beer in Canada with you. Special thank to Alexandre Payeur, who provided me valuable advices and read my first paper.

To my family, specially my father Jean-Roger and my mother Denise. Thank you for your comprehension and your support.

To you, Winnie, my love. Thank you to be there. To understand and accept who I am. To finish, as a believer, I want to thank GOD for the grace he gave me during all these years.

Statement of Originality

I have Included in Chapter 1 the essential materials necessary for the understanding of the rest of the Thesis. Chapters 2, 3, 4 and 5 are submitted, accepted or published articles. All the articles were made under the supervision of Prof. André Longtin. Below, I outline my own contributions.

- **Chapter 2 :** A.S. Powanwe and A. Longtin. Determinants of Brain Rhythm Burst Statistics, Sci. Rep.9 1(2019).

  At the beginning of my PhD thesis, André had a strong interest in the dynamics and statistics of the stochastic oscillation envelopes. I then used the Stochastic Averaging Method (SAM) to obtain such envelope dynamics. The use of the SAM which is the main analytical technique applied from chapter 2 to 5 of my PhD thesis was my idea. I performed all the numerical simulations and derived all the analytical results under the supervision and advice of André. André edited and corrected it and I made additional corrections to obtain the final version of the paper. I am the corresponding author.

- **Chapter 3:** A.S. Powanwe and A. Longtin. Brain rhythm bursts are enhanced by multiplicative noise. Accepted in *Chaos*.

  The main idea of the paper which is the enhancement of beta rhythm synchronization by the multiplicative noise was mine. I performed all the numerical simulations and derived all the analytical results under the guidance and advices of Andre. I wrote a first version of the manuscript. André edited and corrected it and I made additional corrections to obtain the final version of the paper. I am the corresponding author.

- **Chapter 4:** A.S. Powanwe and A. Longtin. Phase dynamics of delay-coupled quasi-cycles with application to brain rhythms, Phys. Rev. Research, 2:043067, 2020.

The main idea of the paper which is the mechanism by which noise and coupling delay induce out-of-phase locking of coupled quasi-cycle oscillators was mine. I performed all the numerical simulations and derived all the analytical results under the guidance and advices of André. I wrote a first version of the manuscript. André edited and corrected it and I made additional corrections to obtain the final version of the paper. I am the corresponding author.

- **Chapter 5:** A.S. Powanwe and A. Longtin. Amplitude-phase description of the stochastic neural oscillators across the Hopf bifurcation, *Under review in Physical Review Research.*

  The main idea of the paper which is the extension of the SAM to describe to describe limit cycles and take into account several coupled networks and different type of stochastic inputs was mine. I performed all the numerical simulations and derived all the analytical results under the guidance and advices of André. I wrote a first version of the manuscript. André edited and corrected it and I made additional corrections to obtain the final version of the paper.

Contents

List of Tables

List of Figures

Introduction

Oscillations are ubiquitous and pervasive. The motion of a pendulum, the rotation of the earth around the sun, circadian rhythm, menstrual cycle in women, or a firefly that emits a pulse are common examples of rhythmic behaviors that everybody can observe. Oscillations are also seen in more complex phenomena like chemical and biochemical reactions. The number of predators and prey, or susceptible, infectious, and recovered subjects in given ecosystems are examples of ecological and epidemiological oscillations respectively. However, oscillations are even more present and important in biological systems. The cardiac beats, the regulation of human genes are important rhythmic processes for human life. Other interesting and critical biological rhythms for life are neural rhythms. They are observed in the brain of several species. They represent the electrical spiking activity of a single neuron or the collective dynamic of a large number of cells in a given region of the brain. In this work, we are particularly interested in the dynamics and the function of neural oscillations generated by large groups of neurons.

Neural oscillations are observed in the brains of several species, ranging from mice, monkeys to humans[41]. They usually represent the rhythmic or repetitive excitability of the activities of large groups of neurons recorded from specific brain regions like the cortex and subcortical structures. They are grouped into several bands depending on their mean frequency, which represents the rate at which the excitability of the activity is repeated. The functional role attributed to such oscillations is linked to the precise frequency band where they belong. The slower delta oscillations (frequency less than 5Hz) are believed to be related to memory consolidation while the theta rhythms (4-10 Hz) are linked to navigation, memory in the hippocampus, and working memory [41]. Fast rhythms like beta (12-30 Hz) and gamma oscillations (30-100 Hz) are also seen. Beta oscillations are usually related to motor functions. They are observed preferentially during muscle contraction and holding

and disappear during the execution of movements [80]. They are linked to information storage and working memory [80, 154]. The dysfunctions of beta oscillations are correlated with neurological disorders such as Parkinson's disease [147]. Gamma oscillations are among the most prevalent in the brain. They appear in most cases as a response to a stimulus and have been associated with attention, perception, cognition, working memory and interareal brain communication [42, 83, 85]. Their dysfunctions are manifested in patients suffering from Alzheimer's disease, epilepsy, or attention-deficit hyperactivity disorder (ADHD) [113]. Faster rhythms than gamma (greater than 100Hz) have also been recorded in the brain; these fast-gamma or "sharp wave-ripples" are mostly linked to memory. All these rhythms operate together and in a complementary way to allow efficient brain functioning [41].

In this thesis, we are particularly interested in modeling fast beta and gamma oscillations. They are believed to be important because their communication function is thought to be the basis of large-scale integration i.e. the mechanism that coordinates the activities of distinct brain areas to enable the emergence of coherent behavior and cognition [219]. To perform communication, neural oscillations are believed to show sustained synchrony and to exhibit coherence with analog rhythms, known as communication through coherence (CTC) [85]. However, several neural rhythms recorded in *vivo* are not sustained but exhibit short and transient epochs of synchrony called bursts. The appearance and duration of such bursts are random variables. The envelope, the frequency, and the phase of the overall rhythms show strong fluctuations. These oscillations are closer to a filtered noise than to coherent oscillations.

Given the strong stochasticity of neural oscillations *in vivo*, it may be hard to believe that they can actually play a role in cognitive processes like previously claimed [41, 80, 85, 154]. In fact, some authors believe that neural oscillations do not have any role in brain functioning. They are only a reflection of excitation-inhibition interactions. One of their powerful arguments is the fact that the phase of a stochastic gamma oscillation is not consistent to support a communication function as formulated by CTC [185]. To reconcile the stochastic behavior of neural oscillations with their hypothetic function like communication, we proceed theoretically and with numerical simulations. More precisely, we ask two fundamental questions. 1) How can we mathematically model noisy oscillations? 2) Are these models of noisy oscillations good candidates for interareal

brain communication? The answers to these two questions are the focus of this thesis.

Previous studies have addressed the two main questions of this thesis. In recent studies, authors have examined Local Field Potentials (LFPs) recorded in the primary visual cortex of awake and anesthetized monkeys [228]. The results showed that oscillatory neural activities are compatible with a filtered noise origin. Time-frequency analysis of the LFPs shows transient episodes of sustained power with fluctuating frequency. To characterize such noisy oscillations, attention is paid to the episodes of high power also known as bursts [228]. The mean duration and the variability of the mean frequency of the bursts are computed and considered as essential markers of gamma oscillations. The values of these markers are similar for both awake and anesthetized monkeys, suggesting that the dynamics and statistics of gamma oscillations do not depend on brain states. Such behavior is also observed in other species like cats and humans. The precise values of the gamma oscillation markers vary depending on the subject. However, an acceptable range for the mean gamma burst duration is 65-150 ms [228, 80]. Deviations from this range are related to neurological disorders like epilepsy, ADHD, and Alzheimer's disease.

Modeling of noisy oscillations in the gamma band is done using a network of coupled excitatory and inhibitory populations. The effective dynamics of such populations for an isolated network is a two-dimensional system of differential equations driven by noises [228]. In the dynamic point of view, these oscillations are known as quasi-cycles[220]. Studies further reported the lack of auto-coherence in such oscillations[39]. The majority of works done to address the high variability of gamma oscillations *in vivo* have been performed using computational techniques of signal processing like time-frequency analysis [228, 39, 38, 175, 154]. Theoretical frameworks such as the envelope-phase description allowing the computation of burst duration are lacking. A recent study [102] has however attempted to formulate such a description but is only partially satisfactory because it misses the biological ingredients of the former two-dimensional equations.

The ability of noisy oscillations (similar *in vivo* recordings) to show flexible communication has also been investigated recently [175]. The study was done computationally with two connected networks, each representing a part of the brain. The results showed that despite the stochasticity of gamma oscillations, flexible communication was possible during matching episodes of the burst

within each network. However, the theoretical basis of such flexible communication was not addressed. More precisely, the work did not provide a theoretical basis of the consistent phase relation between the two connected networks. Here, we aim to shed more light on the theoretical modeling of stochastic gamma oscillations by performing the amplitude-phase decomposition of a stochastic oscillatory network dynamics. We also want to provide a theory that shows how noise-induced gamma oscillations can exhibit robust and consistent phase locking, an essential ingredient for interareal brain communication.

We proceed by using theoretical techniques of nonlinear and stochastic dynamics, numerical simulations and techniques of signal processing. We model noisy oscillations with the bursting structure using coupled stochastic differential equations (SDE) which are known as generalized Langevin equations. Each equation mimics the dynamic of an excitatory (E) or inhibitory (I) population subject to noise. Noise is the result of the finite size-effect of the system and/or the random synaptic bombardment from other neurons. The effective dynamics of the Local Field potentials (LFPs) are linear equations sustained by additive and multiplicative noise. Without noise, oscillations vanish to a fixed point; noise is therefore critical for the maintenance of oscillations. This class of oscillations is known in the literature as noise-induced or quasi-cycle oscillations respectively. Within our models of linear equations sustained by noise, we define the bursts as the epoch where the envelope of the LFP is sustained above a particular threshold. The time spent by the envelope above the threshold is the duration of the burst.

To fully capture the bursting dynamics of the oscillatory LFPs we perform an envelope-phase decomposition of the process. For that, we adapted the Stochastic Averaging Method (SAM) [187, 6] previously used in another context to extract the envelope and the phase of the stochastic processes represented by the E-I LFPs. The resulting envelope-phase dynamics shows an envelope that is not coupled to the phase and allows us to compute the mean burst duration using first passage time analysis. Multiplicative noise was found to cause even stronger oscillations and longer bursts than additive noise.

We then extend to two brain areas these envelope-phase dynamics and investigate the possibility of the areas to phase synchronize. This allows addressing the question of the ability for noise-induced

oscillations to communicate since interareal brain communication is strongly linked to phase synchronization or phase-locking. This is done through numerical simulations as well as our theoretical models of envelope-phase dynamics obtained from the Stochastic Averaging Method (SAM). We further extend the SAM theory to describe nonlinear oscillations known as noisy limit cycle oscillations, and look at the dynamics of coupled brain areas in this context. The result is a set of envelope-phase equations describing the slow envelope and phase components of the rhythms in each of the coupled areas.

We note that the SAM method is not limited to neural oscillations and can be generalized to other disciplines. It allows an envelope-phase description with a reduced number of parameters than the former dynamics and is thus more appropriate for data-driven analysis. The SAM represents from our point of view an appropriate and flexible method to extract the envelope and phase dynamics of a large class of oscillatory phenomena present in nature.

The thesis is organized as follows. In chapter 1, we present the essential notions and concepts necessary to understand the rest of the thesis. We review the notion of oscillation from a nonlinear dynamics point of view using a general approach. We also extend the notion of oscillations in the presence of noise and explain the meaning of its components. The notions of quasi-cycle and limit cycle are then detailed. This establishes the importance of the envelope-phase description of the oscillations. Since oscillations investigated in the rest of the thesis are noisy, we then indicate the essential requirements for a theoretical treatment of stochastic phenomena. Among those important notions, we focus on the concept of first passage time and stochastic averaging. We end this chapter by introducing the particular case of neural oscillations. Chapter 2 presents the dynamics of Local Field potential (LFPs) within an envelope-phase description starting from two linear coupled equations sustained by additive noise. We define the notion of a burst from the envelope dynamics alone and compute the mean burst duration from a first passage time analysis. This chapter closes by discussing the dynamics of the envelope in the parameter space and its ability to describe real brain oscillations in healthy and diseased individuals as found in other studies.

In Chapter 3 we use different modeling of the noise which is assumed to have a synaptic origin rather than a finite size-effect origin as in the previous Chapter. This leads to more realistic modeling where Local Field potential is now described by linear equations sustained by multiplicative

noise. An envelope-phase decomposition is performed and the resulting envelope dynamics is again uncoupled from the phase dynamics. The first passage time analysis can also be done, but we do not perform it here since it does not add anything new and unexpected. We discuss the additional synchronization behavior with multiplicative noise compared to additive noise and its consequence for disease dynamics. Chapter 4 is dedicated to the second question of the thesis related to the ability of coupled oscillatory brain areas to communicate. This question is answered by investigating the phase-locking dynamics of two coupled networks each described by quasi-cycle oscillations. We then extended the SAM from a single brain area as in chapters 2 and 3 to two coupled areas. We obtained the envelope-phase dynamics for the coupled brain areas. This allows us to study the phase-locking mechanisms of coupled quasi-cycles and to highlight the critical parameters, as the propagation delay that enables such phase-locking. The SAM is studied more deeply in chapter 5. There, we include nonlinear terms to account for both quasi and noisy limit cycles in the same dynamical equations instead of having separate dynamics for each regime. We also extended the method to include more than 2 networks as in chapter 4. The new envelope-phase equations provide a set of coupled SDE which can describe a large class of oscillatory phenomena in biology and other disciplines across the deterministic threshold for oscillation onset.

Chapter 1

Background

1.1 Stochastic Processes

1.1.1 Definitions and concepts

Many physical and biological systems do not evolve deterministically in time. Instead, their dynamics are inherently random or stochastic. The times at which neurons in the brain emit action potentials [92], the brain electrical activity of several species [215], the internal open and closed states on an ion channel[29], and many chemical reactions are examples of stochastic processes [217]. In fact, since the ambient environment is constantly fluctuating, many physical processes can be modeled as stochastic processes [115]. This shows the importance of studying such processes. A stochastic process can be defined as a process that evolves probabilistically in time. A system describing a stochastic process possesses a time-dependent random variable. The outcomes of such a process are not specified by its initial conditions as it is the case for deterministic one (except chaotic one). To properly describe a stochastic system, we have to measure the values of its outcomes at each small time increment.

In probability theory, we define a stochastic process as a family of random variables indexed by the parameter time t. More precisely, a stochastic process is an indexed set $X(t), t \in T$ of random variables $X(t)$ defined on the sample space Ω that includes all the possible outcomes of $X(t)$. T is the index set. T can be discrete or continuous. In this thesis, we focus on the case where T is continuous. An element of Ω is called a random sample. A subset B of the sample space is called a random event. The likelihood of the random event B is measured by the quantity $P(B)$ known

as the probability. We denote by x a particular outcome of $X(t)$ at time t [115]. Similarly, the set $(x_1, x_2, x_3, ..., x_n)$ are possible outcomes $X(t_1), X(t_2), ..., X(t_n)$ of the stochastic process at times $(t_1, t_2, t_3, ..., t_n)$ respectively.

A random variable is characterized by its distribution functions and a pair of random variables by their joint distribution function. The behavior of the stochastic process can be completely described by the joint distribution function [207]

$$F_X(x_1, t_1; x_2, t_2; ...; x_n, t_n) = P_X(X_1 \leq x_1; X_2 \leq x_2; ...; X_n \leq x_n). \tag{1.1}$$

The joint probability density is obtained as

$$p_X(x_1, t_1; x_2, t_2; ...; x_n, t_n) = \frac{\partial^n F_X(x_1, t_1; x_2, t_2; ...; x_n, t_n)}{\partial x_1 \partial x_2, ..., \partial x_n}. \tag{1.2}$$

The mean value function $\mu_X(t)$ of the stochastic process $X(t)$ is given as

$$\mu_X(t) = E[X(t)] = \int_{-\infty}^{\infty} x p_X(x, t) dx. \tag{1.3}$$

The autocorrelation function at two different time t_1 and t_2 is given by

$$R_{XX}(t_1, t_2) = E[X(t_1)X(t_2)] = \int_{-\infty}^{\infty} \int_{-\infty}^{\infty} x_{t_1} x_{t_2} p_X(x_1, t_1; x_2, t_2) dx_1 dx_2. \tag{1.4}$$

The autocovariance function is similarly defined as

$$\begin{aligned} C_{XX}(t_1, t_2) =& E[(X(t_1) - \mu_X(t_1))(X(t_2) - \mu_X(t_2))] \\ =& \int_{-\infty}^{\infty} \int_{-\infty}^{\infty} (x_{t_1} - \mu_X(t_1))(x_{t_2} - \mu_X(t_2)) p_X(x_1, t_1; x_2, t_2) dx_1 dx_2. \end{aligned} \tag{1.5}$$

If we consider the symmetry of the expectation integral we have the following relations

$$R_{XX}(t_1, t_2) = R_{XX}(t_2, t_1), \quad C_{XX}(t_1, t_2) = C_{XX}(t_2, t_1). \tag{1.6}$$

The variance function is obtained from the autocovariance function when $t_1 = t_2 = t$:

$$\sigma_X^2(t) = C_{XX}(t,t) = E[(X(t) - \mu_X(t))^2]. \tag{1.7}$$

The stochastic process $X(t)$ is said to be strictly stationary if all its finite-dimensional probability densities are invariant against a linear time-translation. This is expressed as:

$$p_X(x_1,t_1;x_2,t_2;...;x_n,t_n) = p_X(x_1,t_1+s;x_2,t_2+s;...;x_n,t_n+s). \tag{1.8}$$

For the one-dimensional probability density, this becomes

$$p_X(x,t) = p_X(x,t+s).$$

If we choose the particular value $s = -t$, the one-dimensional probability density is reduced to

$$p_X(x,t) = p_X(x,0) = p_X(x).$$

The probability density becomes time-independent. It follows that the corresponding mean value function (if it exists) of the one-dimensional stochastic process is constant:

$$\mu_X(t) = E[X(t)] = \int_{-\infty}^{\infty} x p_X(x,t)dx = \int_{-\infty}^{\infty} x p_X(x)dx = \mu.$$

Moreover, the two-dimensional probability density becomes

$$p_X(x_1,t_1;x_2,t_2) = p_X(x_1,t_1+s;x_2,t_2+s).$$

Similarly, for the particular choice $s = -t_1$, we have

$$p_X(x_1,t_1+s;x_2,t_2+s) = p_X(x_1,0;x_2,t_2-t_1) = p_X(x_1,x_2,t_2-t_1).$$

Then the two-dimensional probability density depends only on the difference $t_2 - t_1$:

$$p_X(x_1,t_1;x_2,t_2) = p_X(x_1,x_2,t_2-t_1).$$

The autocovariance takes the form

$$\begin{aligned} C_{XX}(t_1,t_2) =& E[(X(t_1)-\mu)(X(t_2)-\mu)] \\ =& \int_{-\infty}^{\infty}\int_{-\infty}^{\infty}(x_{t_1}-\mu)(x_{t_2}-\mu)P_X(x_1,x_2,t_2-t_1) \qquad (1.9) \\ =& C_{XX}(|t_2-t_1|) \qquad (1.10) \\ =& C_{XX}(\tau) \end{aligned}$$

and also depends only on $t_2 - t_1$. Similarly, the autocorrelation of a stationary stochastic process also depends only on the difference $t_2 - t_1$ and can be written as $R_{XX}(t_1, t_2) = R_{XX}(\tau)$, where $\tau = |t_2 - t_1|$.

If one is interested in the frequency content of a stationary stochastic process $X(t)$, the useful quantity to investigate is the power spectral density function. We define it as the Fourier transform of the stationary autocorrelation function

$$S_{XX}(\omega) = \frac{1}{2\pi}\int_{-\infty}^{\infty} R_{XX}(\tau)e^{-i\omega\tau}d\tau. \qquad (1.11)$$

The power spectral density function $S_{XX}(\omega)$ exists when the autocorrelation function $R_{XX}(\tau)$ is absolutely integrable. The inverse fourier transform of $S_{XX}(\omega)$ returns the autocorrelation function

$$R_{XX}(\tau) = \int_{-\infty}^{\infty} S_{XX}(\omega)e^{i\omega\tau}d\omega. \qquad (1.12)$$

The integral relations between the power spectral density and the autocorrelation functions are called the *Wiener-Khintchine* relations. Some stochastic processes can be characterized by their autocorrelation or their power spectral density functions. A stochastic process with a pronounced concentration of its power spectral density function near a particular frequency is called a *narrowband process*. If there is no single significantly dominating frequency and the power spectrum is distributed over a wide band of frequencies, then the process is said to be a *broadband process*.

1.1.2 Markov Processes

In nature, many physical and biological systems have a short memory of their past behavior. The outcome in a near future is conditioned only by the most recent history behavior. The stochastic processes of such systems are called *Markov processes* [207]. In other words, a stochastic process $X(t)$ is said to be Markovian if the knowledge of its present state is sufficient to predict its future behavior without referring to any additional information on its history [115, 91]. Mathematically, let t_k be a sequence of times such that $t_1 < t_2 < ... < t_n$ and $x_n = X(t_n)$. If the conditional probability density satisfies the relation

$$p_X(x_n, t_n|x_{n-1}, t_{n-1}; ...; x_1, t_1) = p_X(x_n, t_n|x_{n-1}, t_{n-1}), \tag{1.13}$$

then $X(t)$ is said to be a *Markov process*. The probability of the event (x_n, t_n) conditional on the past history $(x_{n-1}, t_{n-1}; ...; x_1, t_1)$ depends only on the most recent past event (x_{n-1}, t_{n-1}). The conditional probability $p(x_n, t_n|x_{n-1}, t_{n-1})$ is also known as the *Transition probability*. It completely determines the evolution of the stochastic process $X(t)$ provided some initial conditions. If the process is stationary, the conditional probability density function only depends on the time difference ,

$$p_X(x_n, t_n|x_{n-1}, t_{n-1}) = p_X(x_n, t_n - t_{n-1}|x_{n-1}, 0). \tag{1.14}$$

The joint probability of a Markov process can be expressed as

$$\begin{aligned} p_X(x_n, t_n; x_{n-1}, t_{n-1}; ...; x_1, t_1) = & \\ =& p_X(x_n, t_n|x_{n-1}, t_{n-1}) p_X(x_{n-1}, t_{n-1}|x_{n-2}, t_{n-2}) ... \\ & p_X(x_2, t_2|x_1, t_1) P_X(x_1, t_1). \end{aligned} \tag{1.15}$$

The joint probability also depends on the conditional or transition probabilities $p_X(x_i, t_i|x_j, t_j)$. Looking for analytical methods to compute the transition probability becomes more critical and will be the focus of the next subsection.

1.1.3 Diffusion Process: The Fokker Planck Equation

Let consider the three first events $(x_1, t_1; x_2, t_2; x_3, t_3)$ of the stochastic process $X(t)$. We define

$$\begin{aligned} p_X(x_3, t_3|x_1, t_1) &= \int_{-\infty}^{\infty} p_X(x_3, t_3; x_2, t_2|x_1, t_1)dx_2 \\ &= \int_{-\infty}^{\infty} p_X(x_3, t_3|x_2, t_2; x_1, t_1)p_X(x_2, t_2|x_1, t_1)dx_2. \end{aligned}$$

We introduce the Markov hypothesis,

$$p_X(x_3, t_3|x_2, t_2; x_1, t_1) = P_X(x_3, t_3|x_2, t_2).$$

The conditional probability $p_X(x_3, t_3|x_1, t_1)$ is reduced to

$$p_X(x_3, t_3|x_1, t_1) = \int_{-\infty}^{\infty} p_X(x_3, t_3|x_2, t_2)p_X(x_2, t_2|x_1, t_1)dx_2. \tag{1.16}$$

This relation is known as the *Chapman-Kolmogorov* equation. It relates all conditional probabilities $p_X(x_i, t_i|x_j, t_j)$ to each other.

Let consider an arbitrary function $Q(z)$. We assume that Q is also infinitely differentiable such that,

$$\lim_{z\to\pm\infty} \frac{d^n Q(z)}{dz^n} = 0 \quad for \quad any \quad n > 0.$$

We consider the following integral

$$\begin{aligned} J &= \int_{-\infty}^{\infty} Q(z)\frac{\partial}{\partial t}p_X(z, t|x_0, t_0)dz \\ &= \int_{-\infty}^{\infty} Q(z) \lim_{dt\to 0} \frac{1}{dt}\Big(p_X(z, t + dt|x_0, t_0) - p_X(z, t|x_0, t_0)\Big)dz. \end{aligned}$$

Here, $t > t_0$. Following the Chapman-Kolmogorov equation we have the relation

$$p_X(z, t + dt|x_0, t_0) = \int_{-\infty}^{\infty} p_X(z, t + dt|x, t)p_X(x, t|x_0, t_0)dx.$$

We perform the Taylor expansion of $Q(z)$ around the point x and get the following relation

$$Q(z) = Q(x) + (z-x)Q^{'}(x) + \frac{(z-x)^2}{2}Q^{''}(x) + \dots .$$

We define the following quantities

$$A(x,t) = \lim_{dt\to 0}\frac{1}{dt}\int_{-\infty}^{\infty}(z-x)P_X(z,t+dt|x,t)dz$$

and

$$B(x,t) = \lim_{dt\to 0}\frac{1}{dt}\int_{-\infty}^{\infty}(z-x)^2P_X(z,t+dt|x,t)dz.$$

Setting $dx = z - x$, the above quantities $A(x,t)$ and $B(x,t)$ may be rewritten as

$$A(x,t) = \lim_{dt\to 0}\frac{1}{dt}E\big[dX|X=x\big]$$

and

$$B(x,t) = \lim_{dt\to 0}\frac{1}{dt}E\big[dX^2|X=x\big].$$

Using all these relations and performing an integration by part, we obtain the following expression

$$0 = \int_{-\infty}^{\infty}\left(\frac{\partial}{\partial t}p_X + \frac{\partial}{\partial x}\big[A(x,t)p_X\big] - \frac{1}{2}\frac{\partial^2}{\partial x^2}\Big[B(x,t)p_X\Big] + ...\right)Q(x)dx.$$

Recall that $Q(x)$ is an arbitrary function, therefore the partial differential equation governing the dynamic of the conditional probability function is given as [207]

$$\frac{\partial p_X(x,t|x_0,t_0)}{\partial t} = -\frac{\partial}{\partial x}\big[A(x,t)p_X\big] + \frac{1}{2}\frac{\partial^2}{\partial x^2}\Big[B(x,t)p_X\Big] - ... \tag{1.17}$$

The *Pawula* theorem provides an answer to when to stop the series expansion in Eq.1.17.

It is stated that, in order for the probability density function $p_X(x,t|x_0,t_0)$ to be positive, the series in Eq. 1.17 must stop after the first or second term. If it does not stop at the second term, it must contain an infinite number of terms.

For the case where the stochastic process $X(t)$ is a diffusion process, ie a process with continuous

sample paths, it can be described by an *Itô* differential equation driven by Brownian motion. Then the series expansion can be truncated at the second order. We then obtain the Fokker-Planck Equation

$$\frac{\partial p_X(x,t|x_0,t_0)}{\partial t} = -\frac{\partial}{\partial x}\big[A(x,t)p_X\big] + \frac{1}{2}\frac{\partial^2}{\partial x^2}\Big[B(x,t)p_X\Big]. \tag{1.18}$$

The function $A(x,t)$ is known as the *drift term* and describes the deterministic behavior of the system at hand, while the function $B(x,t)$ which is due to the stochasticity of the system is called the *diffusion term*. For the case of an n-dimensional vector stochastic process $\mathbf{X(t)}$, the Fokker-Planck equation can be obtained following the same steps as for the case of a one-dimensional stochastic process. It is formulated as follows

$$\frac{\partial p_{\mathbf{X}}(\mathbf{x},t|\mathbf{x}_0,\mathbf{t}_0)}{\partial t} = -\sum_{k=1}^{n}\frac{\partial}{\partial x_k}\big[A_k(\mathbf{X},t)p_{\mathbf{X}}\big] + \frac{1}{2}\sum_{j=1}^{n}\sum_{k=1}^{n}\frac{\partial^2}{\partial x_j \partial x_k}\Big[B_{j,k}(\mathbf{X},t)p_{\mathbf{X}}\Big]. \tag{1.19}$$

In contrast with the case of a one-dimensional stochastic process, the drift coefficients $A_k(\mathbf{X},t)$ are now elements of an n-dimensional drift vector $A(\mathbf{X},t)$. The diffusion coefficients $B_{jk}(\mathbf{X},t)$ are coefficients of an $n \times n$-symmetric diffusion matrix $B(\mathbf{X},t)$. The complete determination of the probability density function $p_{\mathbf{X}}(\mathbf{X},t_0|\mathbf{X}_0,t_0)$ needs the specification of initial and boundary conditions in the n-dimensional space spanned by the variables $\mathbf{X}$. We note that the derivation of the Fokker-Planck equations for one and n-dimensional stochastic vector process assumes that the stochastic processes are Markov processes.

The corresponding *Itô* stochastic differential equation of the Fokker Planck equation (Eq.1.18) can be written as

$$\begin{aligned} dX(t) =& A(x,t)dt + \sqrt{B(x,t)}dW(t) \\ X(t_0) =& x_0. \end{aligned} \tag{1.20}$$

The term $W(t)$ is known as the *Wiener process* which is a mathematical formulation of the *Brownian motion* which describe the rapid, perpetual, highly irregular motion of small particles

suspended in a fluid [115]. It was named after the botanist Robert Brown who was the first to observe the phenomenon and was theoretically formalized by Einstein [78]. The *Wiener process* is a special stochastic process with the following properties:

- its mean is zero: E[W(t)]=0 ;
- its autocorrelation function is : $E[W(t)W(s)] = min(t, s)$.

It can be shown that $W(t)$ has independent increments over non-overlapping time intervals. The increments of a *Wiener process* have zero mean:

$$E[W(t) - W(s)] = E[W(t)] - E[W(s)] = 0.$$

Let the differential increment of the *Wiener process* W(t) at time t be $dW(t) = W(t + dt) - W(t)$. We then have the following relation

$$E[dW(t)dW(s)] = \begin{cases} dt, & t = s \\ 0, & otherwise\,. \end{cases}$$

The derivative of the *Wiener process* $\frac{dW(t)}{dt} = \xi(t)$ is known as Gaussian white noise. It is a stationary broadband process with zero mean and a delta distributed autocorrelation function. We can define it by

- its mean, $E[\xi(t)] = 0$
- its autocorrelation, $E[\xi(t)\xi(s)] = \delta(t - s)$,

where the Dirac delta function is $\delta(t - s) = \infty$ if $t = s$ and $\delta(t - s) = 0$ if $t \neq s$. From the autocorrelation function, we can anticipate a constant power spectral density function for the white noise for frequencies extending from zero to infinity. When the drift term of Eq.1.20 is a linear function of the stochastic process with negative slope $A(\eta, t) = -\frac{1}{\tau}\eta$ and the diffusion constant a $B(\eta, t) = D^2$, the stochastic differential equation Eq.1.20 is known as the Ornstein Uhlenbeck (OU) process with the following properties [115]

- its mean is zero: $E[\eta(t)] = 0$.

- its autocorrelation function is: $E[\eta(t)\eta(s)] = \frac{\tau D^2}{2} exp\big(-\frac{1}{\tau}\big|t-s\big|\big)$.

In contrast with the white noise which is delta correlated and therefore does not have any memory, the OU process is exponentially correlated with a correlation time τ. The power spectrum of the OU process can be easily obtained by taking the Fourier transform of its autocorrelation function. The intensity Q of the OU process is obtained by integrating the autocorrelation function: the result is $Q = (\tau D)^2$. It can be shown that the white noise limit can be obtained if we keep Q constant while decreasing the correlation time to zero. Explicitly the white noise is obtained when $\tau \to 0$, $D \to \infty$ such that $Q = const$ [115].

So far, we have introduced the name Itô without explaining its meaning. We will give a brief explanation. To solve the stochastic differential equation (Eq.1.20), one can try to perform a simple integration with the usual rules of Riemann integration. However, the stochastic part of the SDE is hard to interpret using the usual rules. In other words, the integral $\int \sqrt{B(x,t)}dW(t)$ is not uniquely defined. Itô and Stratonovitch used different integration paths. Itô calculus approximates the integral as the summation over small intervals of times $[t_{i-1}, t_i]$ where the function $B(x,t)$ is evaluated at the left boundary of the time steps t_{i-1} whereas the *Stratonovitch* calculus evaluates the same function at the center $\frac{t_{i-1}+t_i}{2}$ of the interval [207, 91, 115]. The two approximations are correct in the mathematical sense but lead to different results and different calculus rules. However, one can shift from one to the other type of SDE (from Itô to Stratonovitch and vice versa) using a correction known as *Wong-Zakai correction*. In this thesis, we will mainly use the Itô interpretation of the SDE.

For an n-dimensional vector stochastic process, the Itô stochastic differential equation corresponding to the Fokker-Planck equation 1.19 is given by

$$\begin{aligned} d\mathbf{X}(t) =& A(\mathbf{X},t)dt + \sqrt{B(\mathbf{X},t)}d\mathbf{W}(t) \\ \mathbf{X}(t_0) =& \mathbf{X}_0 \end{aligned} \tag{1.21}$$

where $\mathbf{W(t)}$ is an n-dimensional vector *Wiener process*.

1.1.4 First passage Time analysis

An important problem in stochastic dynamics is to know how long a homogeneous process described by the Fokker-Planck equation returns outcomes in a certain range of the possible outcomes. In other words, let suppose that the stochastic process $X(t)$ describes the random position x of a particle. The question will be to know how long the particle remains in a certain interval $[a, b]$. Put in other words, we may ask how long it takes for the particle to leave for the first time the interval $[a, b]$. This is called the *first passage time*. The mean of this time is known as the *mean first passage time*. Such a mean first passage time has a significant meaning in many physical and biological systems. For example, the mean interspike interval of neurons in the brain can be interpreted as the mean first passage time of the electrical voltage from a resting voltage to a threshold value.

Theoretically, the derivation of the formula to compute the mean first passage time involves similar reasoning starting from the *Chapman-Kolmogorov equation* to obtain another version of the Fokker-Planck equation known as the *Backward Fokker-Planck equation*. We will not review all the steps of the derivation of this *Backward equation*. Instead, we simply state that it leads to the following dynamics for the mean first passage time $T(x)$ of a Markov stochastic process described by the SDE Eq.1.20 [91]:

$$A(x)\frac{dT(x)}{dx} + \frac{1}{2}B(x)\frac{d^2T(x)}{dx^2} = -1, \tag{1.22}$$

where $T(x)$ is the mean first passage time. The exact calculation of $T(x)$ depends on the boundary conditions which themselves specify exactly the mean first passage time problem. The boundary conditions are usually specified as absorbing or reflecting. An absorbing boundary condition means that when the particle reaches such a boundary, it is absorbed and removed from the considered interval where it was. If for example b is an absorbing boundary condition then $T(b) = 0$. In the case where the boundary condition is reflecting, the particle is re-injected in the interval where it was after hitting the boundary. At a reflecting boundary we then have $\frac{dT(x)}{dx}\big|_{x=a} = 0$. The mean first passage time is considered to be the moment of order 1 of $T(x)$. Similarly, the moment of order n can be obtained by solving the following second-order differential equation [91]

$$A(x)\frac{dT_n(x)}{dx} + \frac{1}{2}B(x)\frac{d^2T_n(x)}{dx^2} = -T_{n-1}(x) \quad n > 1. \tag{1.23}$$

Then, for a homogeneous Markov process described by an *Itô* differential equation, the mean first passage time can be computed by solving the second-order differential equation Eq.1.22 with the appropriate boundary conditions. However, the vast majority of physical and biological systems cannot be described by Markov processes of the form Eq.1.20. Markov processes are the exception and non-Markovian processes are what we are usually faced with in real situations. The concept of first passage time as defined here no longer apply and needs to be redefined [216]. An important path may be to first approximate such a Non-Markovian process to Markov process and then solve the corresponding first passage time problem. Then, approximation methods to transform non-Markovian to Markovian stochastic processes [187] are of great interest. In the following, we will present one powerful method to approximate non-Markovian stochastic processes by Markovian ones.

1.1.5 Stochastic Averaging Method

We consider the process $\mathbf{X}$ the dynamics of which can be separated in two parts: a deterministic $\epsilon^2\mathbf{F}$ and a stochastic $\epsilon\mathbf{G}$ dynamics. The process $\mathbf{X}$ is therefore a stochastic process which can be described by a stochastic differential equation in the following form:

$$\frac{d\mathbf{X}}{dt} = \epsilon^2\mathbf{F}(\mathbf{X}, t) + \epsilon\mathbf{G}(\mathbf{X}, t, \mathbf{Y}(t)). \tag{1.24}$$

In this stochastic differential equation, $\mathbf{X}$ is an n-dimensional vector stochastic process and $\mathbf{Y(t)}$ a p-dimensional vector stochastic process that drives the system. Let us assume that the elements of $\mathbf{Y(t)}$ are broadband processes with zero means. Further, the vectors $\mathbf{F}$ and $\mathbf{G}$ verify certain conditions [133] related to the measurability of the stochastic process and the boundedness of their partial derivatives. Then $\mathbf{X}$ may be uniformly approximated over a time interval of order $O(\epsilon^{-1})$ by an n-dimensional Markov process [6, 187]:

$$d\mathbf{X(t)} = \epsilon^2\mathbf{m}(\mathbf{X})dt + \epsilon h(\mathbf{X})d\mathbf{W(t)}. \tag{1.25}$$

Here $\mathbf{m(X)}$ is the new drift vector, while $h(\mathbf{X})$ is the new diffusion matrix. This equation must be interpreted in the *Itô* sense. $\mathbf{W(t)}$ is an n-dimensional vector of independent Brownian motions. The limit theorem in [133] specifies that $\mathbf{X}$ converges weakly to a Markov process as $\epsilon \to 0$. The quantities $\mathbf{m}$ and h are defined as [187]:

$$\mathbf{m} = T^{av}\Big(E\big\{\mathbf{F}\big\} + \int_{-\infty}^{0} E\Big\{\Big(\frac{\partial \mathbf{G}}{\partial \mathbf{X}}\Big)_t (\mathbf{G})_{t+\tau}\Big\}d\tau\Big) \tag{1.26}$$

$$hh^{'} = T^{av}\Big(\int_{-\infty}^{\infty} E\big\{(\mathbf{G})_t(\mathbf{G}^{'})_{t+\tau}\big\}d\tau\Big), \tag{1.27}$$

where (') denotes transposition. In the explicit form [6] this leads to

$$m_i(\mathbf{X}) = T^{av}\Big(E\big\{F_i\big\} + \sum_j \int_{-\infty}^{0} E\Big\{\Big(\frac{\partial G_i}{\partial X_j}\Big)_t (G_j)_{t+\tau}\Big\}d\tau\Big) \tag{1.28}$$

$$[hh^{'}]_{ij} = T^{av}\Big(\int_{-\infty}^{\infty} E\big\{(G_i)_t(G_j)_{t+\tau}\big\}d\tau\Big), \quad i,j = 1,n. \tag{1.29}$$

For illustration, let us consider the 2-dimensional case $n = 2$, we have the following vectors $\mathbf{X} = \begin{pmatrix} X_1 \\ X_2 \end{pmatrix}, \mathbf{F} = \begin{pmatrix} F_1 \\ F_2 \end{pmatrix}$ and $\mathbf{G} = \begin{pmatrix} G_1 \\ G_2 \end{pmatrix}$. Then Eq.1.28 leads to

$$m_1(\mathbf{X}) = T^{av}\Big(E\big\{F_1(\mathbf{X},t)\big\} + \int_{-\infty}^{0} E\Big\{\frac{\partial G_1(t)}{\partial X_1} G_1(t+\tau)\Big\}d\tau + \int_{-\infty}^{0} E\Big\{\frac{\partial G_1(t)}{\partial X_2} G_2(t+\tau)\Big\}d\tau\Big),$$
$$m_2(\mathbf{X}) = T^{av}\Big(E\big\{F_2(\mathbf{X},t)\big\} + \int_{-\infty}^{0} E\Big\{\frac{\partial G_2(t)}{\partial X_1} G_1(t+\tau)\Big\}d\tau + \int_{-\infty}^{0} E\Big\{\frac{\partial G_2(t)}{\partial X_2} G_2(t+\tau)\Big\}d\tau\Big).$$

The coefficients h_{ij} of the diffusion matrix h are obtained from Eq.1.29 as

$$
\begin{aligned}
[hh']_{11} &= h_{11}^2 + h_{12}^2 = T^{av}\Big(\int_{-\infty}^{\infty} E\big\{G_1(t)G_1(t+\tau)\big\}d\tau\Big) \\
[hh']_{12} &= h_{11}h_{21} + h_{12}h_{22} = T^{av}\Big(\int_{-\infty}^{\infty} E\big\{G_1(t)G_2(t+\tau)\big\}d\tau\Big) \\
[hh']_{21} &= h_{11}h_{21} + h_{12}h_{22} = T^{av}\Big(\int_{-\infty}^{\infty} E\big\{G_2(t)G_1(t+\tau)\big\}d\tau\Big) \\
[hh']_{22} &= h_{21}^2 + h_{22}^2 = T^{av}\Big(\int_{-\infty}^{\infty} E\big\{G_2(t)G_2(t+\tau)\big\}d\tau\Big).
\end{aligned}
$$

The coefficients h_{ij} can be obtained by solving the above 4-dimensional nonlinear system of equations. In the case where [hh'] is a diagonal matrix, an easy solution is obtained as

$$
\begin{aligned}
h_{12} &= h_{21} = 0 \\
h_{11}^2 &= T^{av}\Big(\int_{-\infty}^{\infty} E\big\{G_1(t)G_1(t+\tau)\big\}d\tau\Big) \\
h_{22}^2 &= T^{av}\Big(\int_{-\infty}^{\infty} E\big\{G_2(t)G_2(t+\tau)\big\}d\tau\Big).
\end{aligned}
$$

In all the equations Eqs.1.26,1.27,1.28,1.29 above, E(.) denotes the expectation over the stochastic processes and T^{av} is a time-averaging operator:

$$
T^{av}(.) = \lim_{T\to 0}\frac{1}{T}\int_{t0}^{t0+T}(.)dt
$$

in which the integration is performed over t. When evaluating the expectations in equations 1.27 and 1.26 or 1.29 and 1.28 , the elements of $\mathbf{X}$ are considered as constants. When the expected quantities in equations 1.27 and 1.26, or 1.29 and 1.28 are periodic of period T_0, T^{av} becomes an averaging over one period:

$$
T^{av}(.) = \frac{1}{T_0}\int_{t0}^{t0+T_0}(.)dt\,,
$$

and the result will be independent of t_0.

The step-by-step mathematical reasoning and details about the stochastic averaging method can be found in [203] and [133]. In this thesis, we will be mostly interested in its direct application. The

stochastic averaging method will be used in all the chapters and will be our main analytical tool. For simplicity, we will omit the small parameter ϵ in the formulation but we will implicitly consider that the deterministic and stochastic functions $\mathbf{F}$ and $\mathbf{G}$ are of orders $O(\epsilon^2)$ and $O(\epsilon)$ respectively. Similarly, the function $\mathbf{m}$ and the coefficients of the matrix h will be of orders $O(\epsilon^2)$ and $O(\epsilon)$ respectively.

1.2 Stochastic oscillations or rhythms

Despite the fact that many physical, biological, and physiological processes can be considered as stochastic processes, they still bear a strong regular behavior. Among such stochastic processes with dominant regular behavior, we have *stochastic oscillations* or *rhythms*. An oscillation in a deterministic sense describes the repetitive and regular variation in time of a given quantity about some mean value. The time after which the quantity timeseries repeats itself is constant and known as the period. The amplitude of the oscillation is a constant value usually measured as the maximum variation of the quantitative measure. This definition of an oscillation is an idealization. In a real situations, oscillations are never perfectly regular: they bear stochasticity. The amplitude and the period are no longer constant but vary from cycle to cycle. The regular behavior of an oscillation defined previously disappears. We then have stochastic oscillations which are now considered stochastic processes. The electrical activity of the brain which reflects the rhythmic collective and coordinated spiking of several neurons, the almost 24-hour cycle shown by physiological processes known as circadian rhythm or cardiac rhythm are examples of common stochastic oscillations inside every human being. Other stochastic oscillations observed in nature include earthquake vibrations and the variation in time of the number of prey and predators in an eco-system just to mention a few. In Figs. 1.1, we have shown two different types of stochastic oscillations. The one in Fig. 1.1-**A** is recorded from the brain of an anesthetized rat. The others Fig. 1.1-**B** are circadian oscillations exhibited by two cells.

1.2.1 Stochastic description

Stochastic oscillations like many other stochastic processes can be described by a general non-Markov stochastic differential equation of the form Eq. 1.24 (for simplicity we have dropped ϵ),

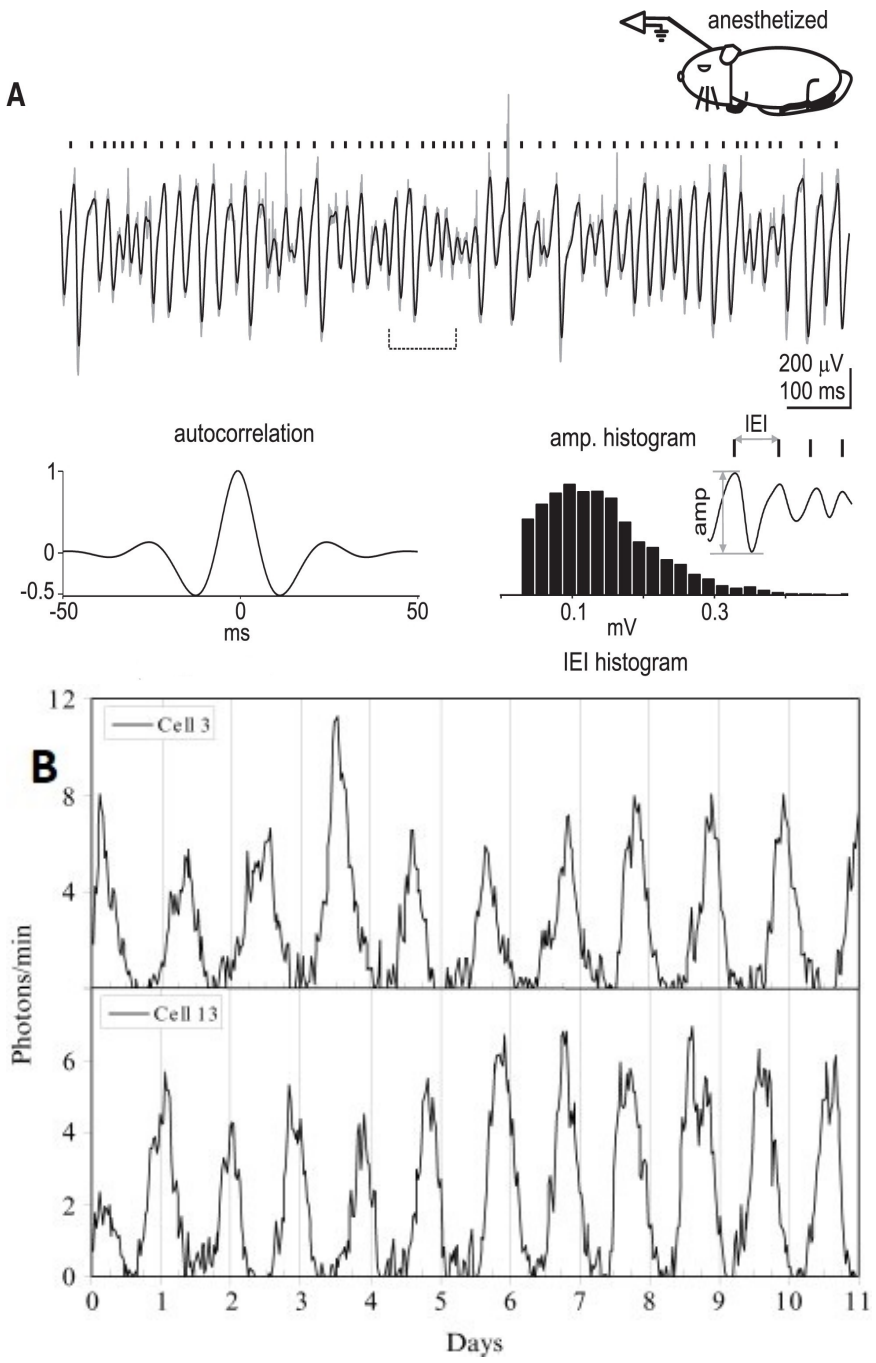

Figure 1.1: **Two types of "real" stochastic oscillations**. (**A,Top**) Stochastic oscillations recorded from the brain of an anesthetized rat, taken from [9]. **(Bottom, Left)** Autocorrelation function decreases quickly. **(Right)** Cycle-to-cycle amplitude and period with their corresponding histogram. (**B**). Stochastic circadian rhythm. The figure was taken from [222].

$$\frac{d\mathbf{X}}{dt} = \mathbf{F}(\mathbf{X}, t) + \mathbf{G}(\mathbf{X}, t, \mathbf{Y}(t)) \tag{1.30}$$

where $\mathbf{X}$ describes the stochastic n-dimensional oscillatory vector process and $\mathbf{Y(t)}$ is a broadband input process. In Figs. 1.1, we can observe that, despite the fact that the two oscillations (Figs. 1.1-(**A, B**)) are stochastic, some look more regular than others. In fact, stochastic oscillations in Fig. 1.1-**A** seem less regular or more stochastic than those in Fig. 1.1-**B**. What are the origins of such apparent differences? And how can we understand the dynamics of such oscillations from a theoretical point of view? To answer those questions it is of interest to investigate the deterministic behavior of Eq. 1.30 to better appreciate the effect of the noise on these dynamics.

1.2.2 Deterministic dynamic

The corresponding deterministic dynamic of Eq. 1.30 is obtained by setting $G = 0$,

$$\frac{d\mathbf{X}}{dt} = \mathbf{F}(\mathbf{X}, t). \tag{1.31}$$

The behavior of the former oscillatory stochastic process described by Eq. 1.30 and reflected in Fig. 1.1 depends strongly on the dynamics of the corresponding deterministic dynamic Eq. 1.31. The study of this dynamic relies on the use of techniques of nonlinear dynamics [205]. We start with the stability analysis.

Linear stability analysis

The first step towards understanding the behavior is to study the stability of its fixed points. They are defined as specific points where the system is static ie where it does not evolve with time. Such points are solutions of the time-independent Eq. 1.31 given as

$$\mathbf{F}(\mathbf{X}_0) = 0, \tag{1.32}$$

where $\mathbf{X}_0$ is the specific value (or values) of $\mathbf{X}$ where the condition Eq. 1.32 is met. The behavior of the time-dependent Eq. 1.31 depends on the stability of the fixed point $\mathbf{X}_0$. To study the stability of the fixed point, it suffices to examine how an infinitesimal perturbation $\delta\mathbf{X}$ around the fixed point

behaves. For that, we seek for solution of Eq. 1.31 in the form $\mathbf{X}^* = \mathbf{X}_0 + \delta\mathbf{X}$. After a Taylor expansion truncated at the first order we get:

$$\begin{aligned}\frac{d(\mathbf{X}_0 + \delta\mathbf{X})}{dt} &= \mathbf{F}(\mathbf{X}_0 + \delta\mathbf{X}) \\ \frac{d\mathbf{X}_0}{dt} + \frac{d\delta\mathbf{X}}{dt} &= \mathbf{F}(\mathbf{X}_0) + \left(\frac{\partial\mathbf{F}}{\partial\mathbf{X}}\right)_{\mathbf{X}_0}\delta\mathbf{X} + O(\delta\mathbf{X})^2.\end{aligned}$$

Taking in account the fixed point condition Eq. 1.32, we get the following dynamical system for the perturbation:

$$\frac{d\delta\mathbf{X}}{dt} = \left(\frac{\partial\mathbf{F}}{\partial\mathbf{X}}\right)_{\mathbf{X}_0}\delta\mathbf{X}. \tag{1.33}$$

Here, $\left(\frac{\partial\mathbf{F}}{\partial\mathbf{X}}\right)_{\mathbf{X}_0}$ is the so-called Jacobian matrix evaluated at the fixed point $\mathbf{X}_0$. More precisely, let writes $\mathbf{X}_0$, $\mathbf{X}$, $\delta\mathbf{X}$ and $\mathbf{F}$ in the following matrix form:

$$\mathbf{X}_0 = \begin{bmatrix} X_{01} \\ X_{02} \\ \vdots \\ X_{0n} \end{bmatrix}, \quad \mathbf{X} = \begin{bmatrix} X_1 \\ X_2 \\ \vdots \\ X_n \end{bmatrix}, \quad \delta\mathbf{X} = \begin{bmatrix} \delta X_1 \\ \delta X_2 \\ \vdots \\ \delta X_n \end{bmatrix} \quad and \quad \mathbf{F} = \begin{bmatrix} F_1 \\ F_2 \\ \vdots \\ F_n \end{bmatrix}.$$

The Jacobian matrix then reads:

$$\left(\frac{\partial\mathbf{F}}{\partial\mathbf{X}}\right)_{\mathbf{X}_0} = \begin{bmatrix} \frac{\partial F_1}{\partial X_1}\big|_{\mathbf{X}=\mathbf{X}_0} & \frac{\partial F_1}{\partial X_2}\big|_{\mathbf{X}=\mathbf{X}_0} & \cdots & \frac{\partial F_1}{\partial X_n}\big|_{\mathbf{X}=\mathbf{X}_0} \\ \frac{\partial F_2}{\partial X_1}\big|_{\mathbf{X}=\mathbf{X}_0} & \frac{\partial F_2}{\partial X_2}\big|_{\mathbf{X}=\mathbf{X}_0} & \cdots & \frac{\partial F_2}{\partial X_n}\big|_{\mathbf{X}=\mathbf{X}_0} \\ \vdots & \vdots & \ddots & \vdots \\ \frac{\partial F_n}{\partial X_1}\big|_{\mathbf{X}=\mathbf{X}_0} & \frac{\partial F_n}{\partial X_2}\big|_{\mathbf{X}=\mathbf{X}_0} & \cdots & \frac{\partial F_n}{\partial X_n}\big|_{\mathbf{X}=\mathbf{X}_0} \end{bmatrix}.$$

If the perturbation $\delta\mathbf{X}$ vanishes with time, then the fixed point $\mathbf{X}_0$ is asymptotically stable. If instead, the perturbation grows infinitely with time, the fixed point $\mathbf{X}_0$ is said to be unstable. An appropriate way to solve Eq. 1.33 is to look for a solutions in the exponential form,

$$\delta\mathbf{X}(t) = \tilde{\mathbf{B}}e^{\lambda t}. \tag{1.34}$$

The parameter λ shows the rate of growth or decay of the perturbation $\delta\mathbf{X}$ and $\tilde{\mathbf{B}}$ represents the complex amplitude of the perturbation. To find appropriate conditions on λ and $\tilde{\mathbf{B}}$, we substitute

the trial solution Eq. 1.34 inside Eq. 1.33 and obtain:

$$\left(\frac{\partial \mathbf{F}}{\partial \mathbf{X}}\right)_{\mathbf{X}_0} \tilde{\mathbf{B}} = \lambda \tilde{\mathbf{B}}. \tag{1.35}$$

In the language of linear algebra, if $\tilde{\mathbf{B}}$ is an eigenvector and λ an eigenvalue of Eq. 1.35, then Eq. 1.34 is an eigen-solution. This leads to the following condition to obtain a non-trivial solution to Eq. 1.35 :

$$\left|\left(\frac{\partial \mathbf{F}}{\partial \mathbf{X}}\right)_{\mathbf{X}_0} - \lambda \mathbf{I}_n\right| = 0. \tag{1.36}$$

The symbol || means *determinant*, Eq. 1.36 is known as the *characteristic equation* and $\mathbf{I}_n$ is an $n \times n$ identity matrix. Put in a matrix form the characteristic equation becomes

$$\begin{vmatrix} \frac{\partial F_1}{\partial X_1}\big|_{\mathbf{X}=\mathbf{X}_0} - \lambda & \frac{\partial F_1}{\partial X_2}\big|_{\mathbf{X}=\mathbf{X}_0} & \cdots & \frac{\partial F_1}{\partial X_n}\big|_{\mathbf{X}=\mathbf{X}_0} \\ \frac{\partial F_2}{\partial X_1}\big|_{\mathbf{X}=\mathbf{X}_0} & \frac{\partial F_2}{\partial X_2}\big|_{\mathbf{X}=\mathbf{X}_0} - \lambda & \cdots & \frac{\partial F_2}{\partial X_n}\big|_{\mathbf{X}=\mathbf{X}_0} \\ \vdots & \vdots & \ddots & \vdots \\ \frac{\partial F_n}{\partial X_1}\big|_{\mathbf{X}=\mathbf{X}_0} & \frac{\partial F_n}{\partial X_2}\big|_{\mathbf{X}=\mathbf{X}_0} & \cdots & \frac{\partial F_n}{\partial X_n}\big|_{\mathbf{X}=\mathbf{X}_0} - \lambda \end{vmatrix} = 0. \tag{1.37}$$

This *determinant* leads to a polynomial of order n in λ. The n solutions of the characteristic equation Eq. 1.37 are the eigenvalues of the system Eq.1.31. In general, the eigenvalues can be real or complex. For an oscillatory behavior, the dimension of the system should be greater than 1 ($n \geq 2$), oscillations do not exist for a one-dimensional system. Moreover, the spectrum of eigenvalues should show complex conjugates eigenvalues since the characteristic equation has real coefficients. The behavior of the oscillatory stochastic system is related to those eigenvalues as we will show below.

Limit cycle

Let consider the case where the dimension of the system is even, $n = 2 \times k$. Moreover, the n-dimensional system is made of k 2-dimensional subsystems. This may be the case where several 2-dimensional subsystems are connected through coupling coefficients. In such a case, the eigenvalues occur in complex conjugate pairs. The stability of the perturbation Eq. 1.34 depends on the

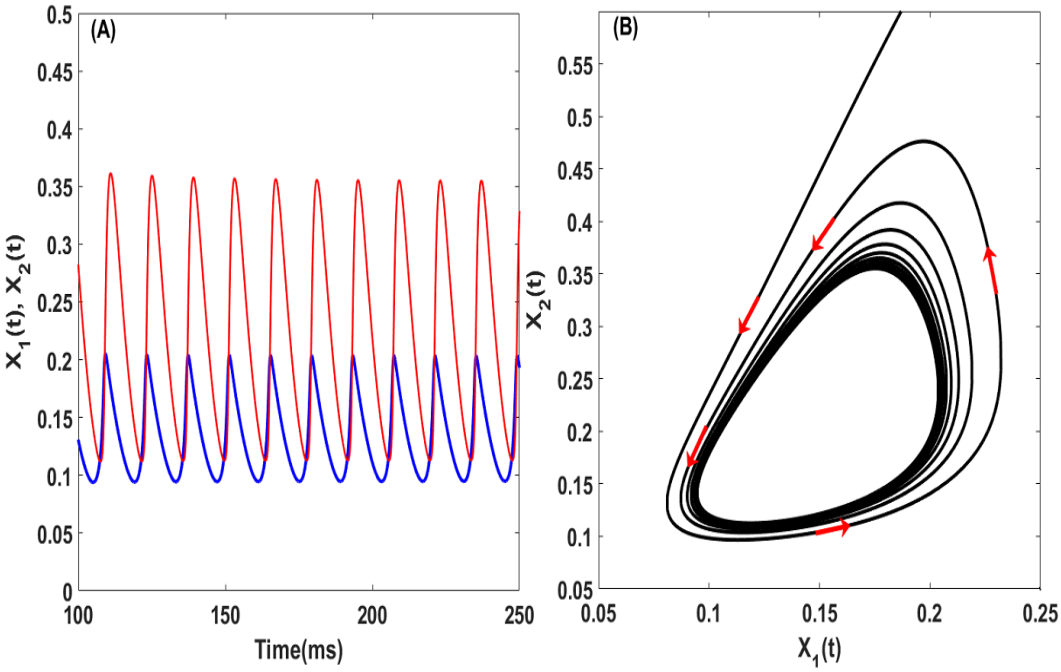

Figure 1.2: **Example of oscillations generated by a limit cycle**. **(A)** Deterministic oscillations generated by a two-dimensional model with the coefficient $a = 31.4$ and $f(x) = 1/(1 + e^{-x})$. The color blue corresponds to the variable X_1 and the color red with X_2. (**(B)**) The corresponding limit cycle attractor. We observe how the trajectory spirals towards a closed orbit. For this example, the system exhibits a single pair of complex conjugate eigenvalues with real positive part $Re(\lambda) = 0.011$. Results are obtained using numerical simulations of Eq. 1.31 with the specific two-dimensional function $\mathbf{F} = [F_1, F_2]^T$ specified in Eqs. 1.38. A simple Euler integration scheme was used with time step dt=0.025 ms.

eigenvalue with the largest real part. If the largest real part is positive, then the perturbation $\delta\mathbf{X}$ grows infinitely in an oscillatory way. However, if we take into account the full nonlinear system Eq. 1.31, we can see regular oscillations with bounded amplitudes. Then, the perturbation saturates on an attractor called a *limit cycle*. This is the case of interest in Chapter 5 of this Thesis. The notion of the limit cycle is more accessible in two dimensions. It represents an isolated closed trajectory. The word *isolated* here refers to the fact that neighboring trajectories spiral towards or away from the limit cycle. We will focus on the former "stable" case where nearby trajectory spiral towards a single limit cycle and will avoid other complex situations which involve for example co-existing stable and unstable limit cycles. Limit cycles are important in many areas of science. They represent self-sustained oscillations, ie oscillations that are not induced by any external periodic force. For

illustrative purposes, we consider a two-dimensional system which exhibits a limit cycle attractor. The deterministic function $\mathbf{F}$ is specified as follows:

$$\mathbf{F}(X_1, X_2) = \begin{bmatrix} F_1(X_1, X_2) \\ F_2(X_1, X_2) \end{bmatrix} = \begin{bmatrix} -0.1X_1 + (1 - X_1)f(aX_1 - 26.3X_2 - 3.8) \\ -0.2X_2 + 2(1 - X_2)f(32X_1 - 1.3X_2 - 8) \end{bmatrix}, \tag{1.38}$$

where the function $f(x) = 1/(1+e^{-x})$. The factor $(1-\mathbf{X})f(\mathbf{X})$ in these equations is inspired from the Wilson-Cowan neural system that we study throughout this thesis. Numerical simulations show that the variables X_1 and X_2 oscillate Fig. 1.2-(**A**). The corresponding attractor is a close orbit for the specific value $a = 31.4$ as shown in Fig. 1.2-(**B**). The corresponding complex conjugate eigenvalues have a positive real part $Re(\lambda) = 0.011$. However, if for example the value of the coefficient a is lowered to $a = 25.4$, the two-dimensional model no longer exhibit self-sustained oscillations. In fact, oscillations are short-lived and disappear after a short transient Fig. 1.3-(**A**). The corresponding attractor is no longer a limit cycle but a stable fixed point Fig. 1.3-(**B**). The transition from the fixed point to the limit cycle happens when the parameter a is increased and crosses a critical value a^*. At the same time, the real part of the complex conjugate eigenvalue changes its sign from negative to positive. The change of the behavior of a system when a critical parameter is crossed is called a *Bifurcation*. For an oscillatory process, the emergence of a long-lived oscillation when a parameter is crossed is known as a *Hopf bifurcation*. There exist two principal types of Hopf bifurcation: subcritical and supercritical. Here, we will focus on the simpler *supercritical Hopf bifurcation* which happens when a stable focus loses its stability and gives birth to a small-size limit-cycle, the amplitude of which increases with the bifurcation parameter approximately as $\sqrt{a - a^*}$, where a^* is the value of the parameter at which the bifurcation occurs.

Deterministic systems with delay have infinite dimension. They can therefore exhibit a stable fixed point and a transition towards a limit cycle via a Hopf bifurcation. The analysis done for the case of two-dimensional system is valid for the dynamics with delay. However, the stability of the delayed dynamics is investigated by looking at the sign of the eigenvalue with the maximal real part.

Deterministic oscillations in the absence of any time-dependent external signal are the consequence of the presence of a limit cycle generated by the system. Now, let's suppose that the deterministic system is coupled to its random environment. Taking into account the external stochastic

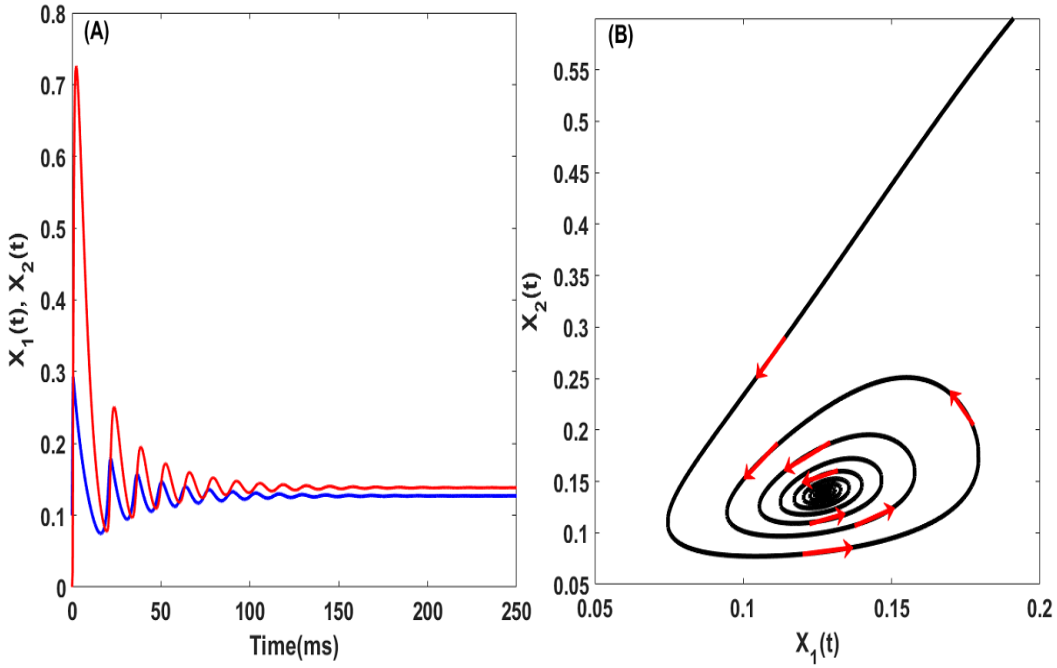

Figure 1.3: **Damped oscillations when the system has complex conjugate eigenvalues with negative real part**. **(A)** Deterministic damped oscillations generated by a two-dimensional model with the coefficient $a = 25.4$ and $f(x) = 1/(1 + e^{-x})$. The color blue corresponds to the variable X_1 while the color red matches with X_2. **(B)** The corresponding stable focus attractor. We observe how the trajectory spirals towards a fixed point. For this example, the system exhibits a single pair of complex conjugate eigenvalues with real negative part $Re(\lambda) = -0.0321$. Results are obtained using numerical simulations of Eq. 1.31 with the specific two-dimensional function $\mathbf{F} = [F_1, F_2]^T$ specified in Eqs. 1.38.

effects results in a system described by the stochastic differential equation Eq. 1.30. The behaviors of the corresponding stochastic processes X_1 and X_2 depend on the associated deterministic system Eq. 1.31. In other words, the fact that the stochastic processes look like Fig. 1.1 -(**A**) and Fig. 1.1-(**B**) depends on the fact that the attractor of the associated deterministic system is a stable fixed point or a stable limit cycle.

1.2.3 Types of stochastic oscillations

Having described the deterministic behavior of an oscillatory system. We now assume that it is coupled to random forces from the environment. As in the previous section, we consider a reduced two-dimensional system. The expression of the stochastic function $\mathbf{G}(\mathbf{X}, \mathbf{Y}(t))$ in Eq. 1.30 is given

as

$$\begin{aligned}\mathbf{G}(X_1, X_2, Y_1(t), Y_2(t)) &= \begin{bmatrix} G_1(X_1, X_2, Y_1(t), Y_2(t)) \\ G_2(X_1, X_2, Y_1(t), Y_2(t)) \end{bmatrix} \\ &= \varepsilon \begin{bmatrix} \frac{1}{2} Y_1(t) \sqrt{0.1X_1 + (1 - X_1) f(aX_1 - 26.3X_2 - 3.8)} \\ Y_2(t) \sqrt{0.2X_2 + 2(1 - X_2) f(32X_1 - 1.3X_2 - 8)} \end{bmatrix} . \end{aligned} \tag{1.39}$$

This is an example where the strength of the noise is dependent on the state of the system. Here, the stochastic processes $Y_1(t)$ and $Y_2(t)$ are two independent Gaussian white noises with zero mean previously defined in section **STOCHASTIC PROCESSES** (**section 1.1**), and the parameter ε measures the strength of the stochastic function G. We will choose the value of $\varepsilon = 10^{-2}$ throughout this chapter. We now investigate the behavior of the stochastic process Eq. 1.39 depending on the fact that its corresponding deterministic system admits a stable limit cycle or a stable fixed point (stable focus). In other words, what becomes the regular dynamic of the oscillations observed when a stable limit cycle is present? What happens to the regular oscillating dynamics in the presence of noise?

Stochastic limit-cycle oscillations

We first consider the case where the deterministic dynamics exhibit a stable limit cycle attractor. Oscillations of the two variables are regular as shown in Fig. 1.2. We now coupled such deterministic dynamics to the stochastic function $\mathbf{G}$. This could mimic the case of a population of neurons coupled to their noisy-environment, or the finite-size fluctuations in the activity of the population. The state variables $X_1(t)$ and $X_2(t)$ are now stochastic processes and may be described by the properties of stochastic processes mentioned in the previous section. For the sake of illustration, we will proceed by numerical simulations to observe the behavior of the stochastic processes $X_1(t)$ and $X_2(t)$. The results of such simulations are shown in Figs. 1.4.

We observe in Fig. 1.4-(**A**) that the effect of the stochastic part is to create slightly fluctuating oscillations compared to the former deterministic ones in Fig. 1.2-(**B**). However, the corresponding attractor is a stochastic limit cycle where the trajectory spirals randomly towards a closed orbit. We call these oscillations *stochastic limit cycle oscillations*. A visual inspection leads to the assertion

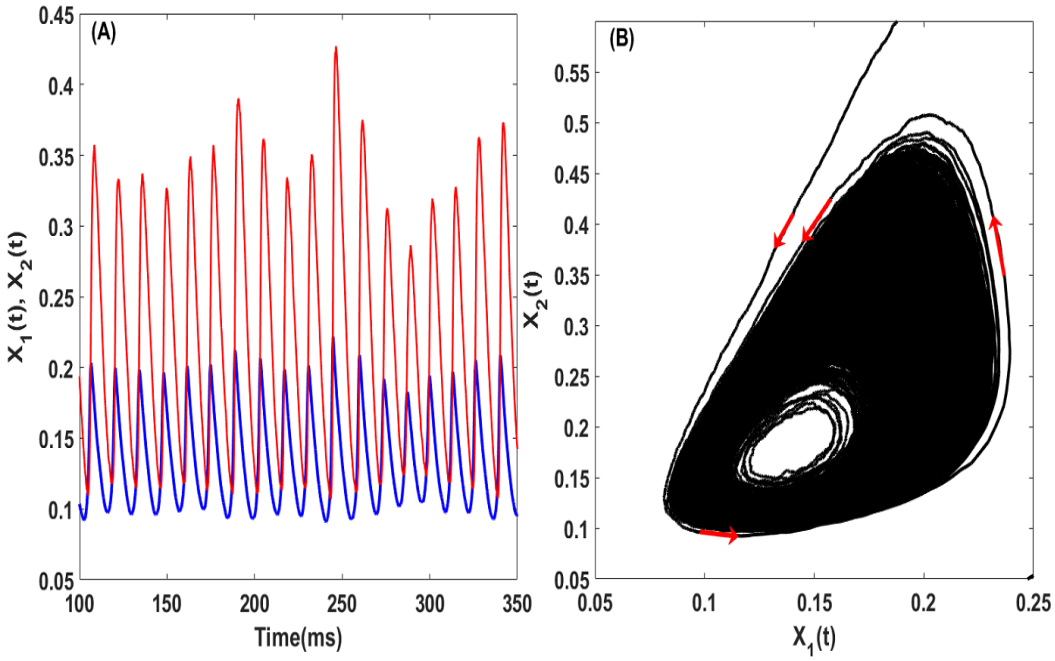

Figure 1.4: **Stochastic behavior of oscillations when the underlying deterministic system exhibits a stable limit cycle**. **(A)** Stochastic oscillations generated by a two-dimensional model with the coefficient $a = 31.4$ and $f(x) = 1/(1 + e^{-x})$. The color blue corresponds to the variable X_1 and the color red with X_2. **(B)** The corresponding stochastic limit-cycle attractor. We observe how the trajectory spirals stochastically towards a closed orbit. Results are obtained using numerical simulations of Eq. 1.30 with the deterministic function $\mathbf{F} = [F_1, F_2]^T$ specified in Eqs. 1.38 and the stochastic function $\mathbf{G} = [G_1, G_2]^T$ in Eqs. 1.39. The equations were integrated numerically using the Euler-Maruyama technique with time-step dt=0.025 ms.

that *stochastic limit cycle oscillations* generated by our stochastic differential equations may be of similar nature to stochastic oscillations observed *in vivo* and reported in Fig. 1.1-(**B**). This suggests that *stochastic limit cycle oscillations* modeled mathematically here could be observed in real data from living cells.

Quasi-cycle or noise-induced oscillations

Now let us investigate what happens if the deterministic dynamics spiral towards a stable fixed point as reported in Fig. 1.3. For this case the parameter a is shifted to a lower value $a = 25.4$. We performed numerical simulations including the stochastic part $\mathbf{G}$ described in Eqs. 1.39 and the full dynamics of the two processes X_1 and X_2 are described by Eqs. 1.30. The results of the

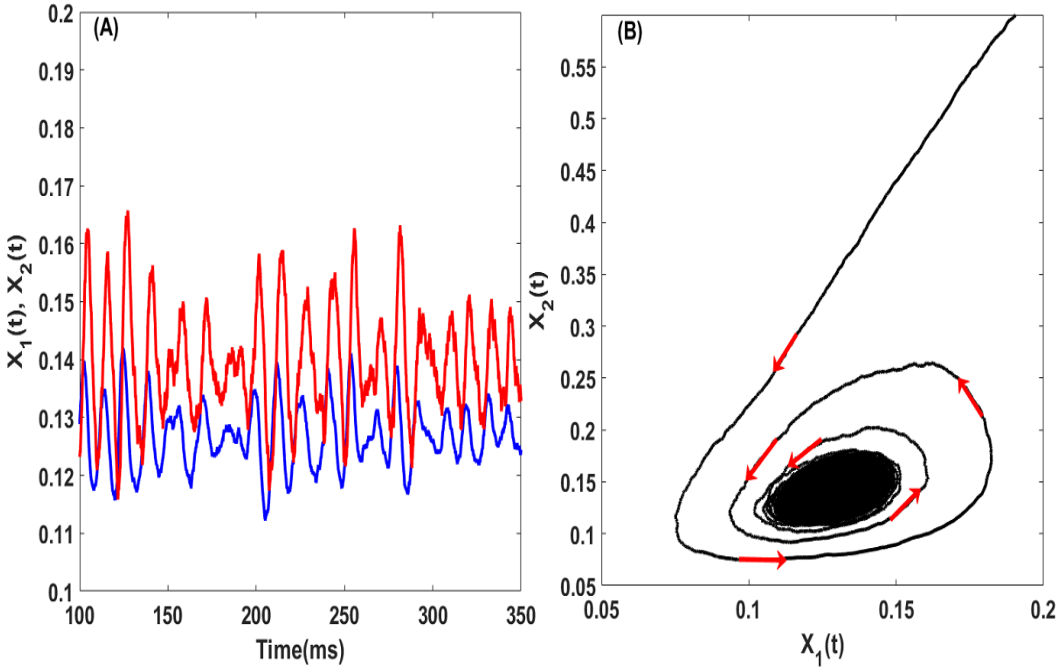

Figure 1.5: **Stochastic behavior of oscillations when the deterministic system exhibit a stable limit cycle.(A)**: Stochastic oscillations generated by a two-dimensional model with the coefficient $a = 31.4$ and $f(x) = 1/(1 + e^{-x})$. The color blue corresponds to the variable X_1 while the color red matches with X_2. **(B)**: The corresponding stochastic limit-cycle attractor. We observe how the trajectory spirals stochastically towards a closed orbit. Results are obtained using numerical simulations of Eq. 1.30 with the specific two-dimensional deterministic function $\mathbf{F} = [F_1, F_2]^T$ specified in Eqs. 1.38 and the stochastic function $\mathbf{G} = [G_1, G_2]^T$ in Eqs. 1.39.

simulations show that oscillations are now sustained. The dampened oscillations observed when the dynamics were deterministic Fig. 1.3-(**A**) now persist Fig. 1.5-(**A**). This suggests that oscillations are noise-induced since they do not survive in the deterministic case. The corresponding attractor Fig. 1.5-(**B**) is called a *quasi-cycle*.

The resulting oscillations are known as *quasi-cycle oscillations* or *noise-induced oscillations*. The irregular behavior of such oscillations is more pronounced than what is seen for *stochastic limit-cycle oscillations*. Such irregular or stochastic behavior is observed in many recorded data. For example, oscillations recorded from the brain of a rat and presented in Fig. 1.1-**(A)** exhibit a similar irregular behavior seen in the *noise-induced oscillations* generated by the stochastic differential equations in Fig. 1.5-**(A)**. Thus *quasi-cycle oscillations* may also be observed in living systems.

Differences between *noise-induced oscillations* and *stochastic limit cycle oscillations* may be made by characterizing their apparent **"irregular behavior"** ie the variation of their amplitude, their cycle to cycle period (or frequency), and the time instances at which peaks appear, and the phase. Those characteristics may be crucial to discriminate the two types of stochastic oscillations which may have different roles and functions. However, one should mention that such discrimination is only possible when the stochastic function **G** is a weak function such that it represents the weak coupling of the deterministic dynamics to its random environment. In the situations where the stochastic function **G** is strong ie of similar size to the deterministic dynamics, it may be difficult to discriminate between the two oscillation types at least by characterizing their components like the amplitude, the frequency, and the phase. The situations with strong stochastic function **G** need specialized techniques and we will not focus on those cases in this thesis. However, we will pay special attention to the components of a stochastic oscillation like its amplitude, phase, and frequency. In chapter 2, we use the term **Transient synchrony regime** to refer to the Quasi-cycle regime.

1.2.4 Components of a stochastic oscillation

A better way to characterize a stochastic oscillation and maybe to discriminate whether it belongs to the class of *quasi-cycle* or *stochastic limit cycle oscillations* is to extract its cycle-to-cycle amplitude, phase and frequency processes which may themselves be stochastic processes .

The envelope

For the stochastic dynamics considered in Fig. 1.4-(**A**) and Fig. 1.5-(**A**) the cycle-to-cycle amplitude as defined in Fig.1.1-(**A**) is not regular. We observe a tremendous variation for the case of *noise-induced oscillations* Fig. 1.5-(**A**) while the variation is less pronounced for the case of *stochastic limit cycle oscillations* in Fig. 1.4-(**A**). The process connecting the peaks of the cycle-to-cycle amplitude is called the *envelope process*. The study of the dynamics of the envelope process may give meaningful information about the dynamics of the oscillatory process itself. The appropriate quantities to fully capture the envelope dynamics are the stochastic deviations from the fixed point $\delta X_1 = X_1 - X_{01}$ and $\delta X_2 = X_2 - X_{02}$. We consider the dynamics of such deviations beyond the

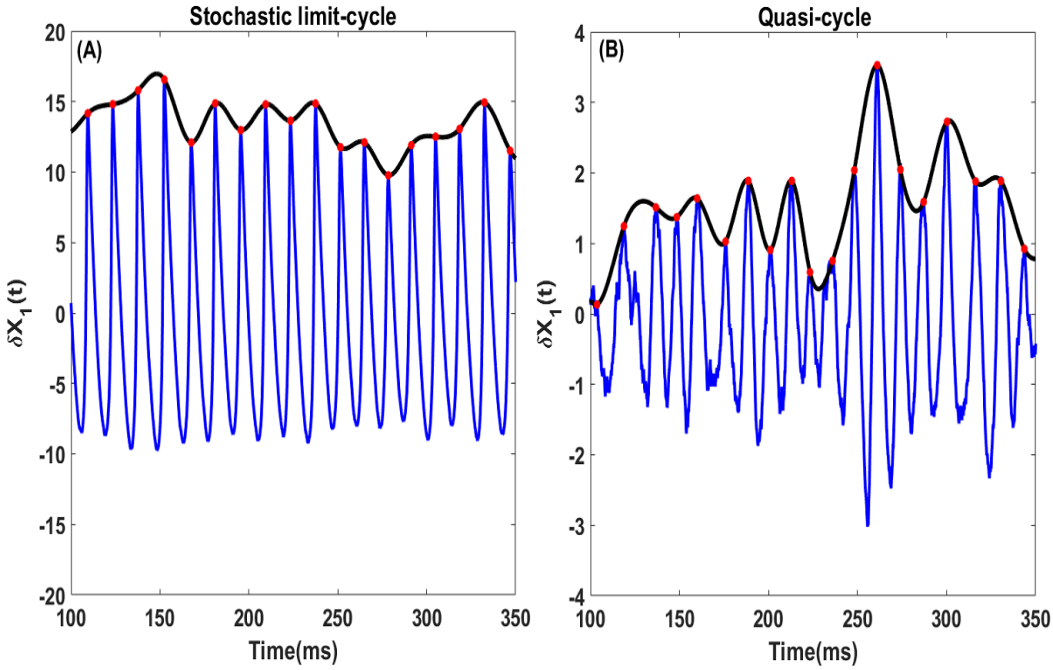

Figure 1.6: **Envelope description of the stochastic oscillatory processes for both quasi and stochastic limit cycles regimes**. **(A)** The corresponding deterministic dynamic lies in the limit cycle regime $a = 31.4$. The blue curve is the deviation process $\delta X_1(t)$ from the fixed point X_{10} and is also a stochastic process. The red dots represent the peaks of the cycle-to-cycle amplitude fluctuations of $\delta X_1(t)$. The black curve connecting the red dots is defined as the envelope of the stochastic limit cycle oscillations. **(B)** Quasi-cycle regime for $a = 25.4$. The deterministic dynamics exhibit a damped oscillation towards the stable fixed point. The black curves connecting the red dots is defined as the envelope process of the quasi-cycle oscillations. The red dots were obtained by using the *findpeak* Matlab function and the envelope black curves are obtained by a third-order polynomial interpolation through these red dots.

deterministic and linear analysis performed so far. We can compute them numerically and extract their envelope processes by connecting the cycle-to-cycle peak amplitudes. For illustrative purposes, we only consider the deviation from the process X_1, however similar behavior also happens for the process X_2.

The envelope dynamic is also a stochastic process but no longer oscillatory. Its dynamics differ depending on whether the oscillatory stochastic process is a stochastic limit cycle oscillation or a quasi-cycle oscillation. For the stochastic limit cycle oscillation Fig. 1.6-(**A**) the deviation dynamic is not symmetric about zero. The peaks of the cycle-to-cycle oscillation (red dots) have high values and the corresponding envelope process (Black curve) does not exhibit strong variation. In contrast,

for the quasi-cycle oscillation Fig. 1.6-(**B**) the deviation process is more symmetric about zero. The peaks (red dots) have weaker values and the associated envelope process (black curve) exhibits strong variations from one peak to the next. The dynamics of the envelope process is therefore an important marker that can be used to characterize stochastic oscillations. This method results in smooth curves that only connect peaks. Even if such curves already give the essential meaning of the envelope processes, other definitions can be used. A common definition of the envelope process is based on the *Hilbert transform*. In mathematics, the *Hilbert transform* is a linear operation which takes a function $x(t)$ and returns its corresponding analytic representation $x(t) + jH[x](t)$. The imaginary part $H[x](t)$ of the analytic representation is defined as the convolution of the real function $x(t)$ with the function $\frac{1}{\pi t}$ known as the *Cauchy kernel*. The convolution integral defining $H[x](t)$ is an improper integral. It does not always converge due to the presence of the term $\frac{1}{t}$ which is not integrable across $t = 0$. For this reason, the Hilbert transform is interpreted in the *Cauchy principal value* sense. More precisely we have the following:

$$H[x] = \frac{1}{\pi} P \int_{-\infty}^{\infty} \frac{x(\tau)}{t - \tau} d\tau \tag{1.40}$$

where P signifies the Cauchy principal value. The envelope process of the function $x(t)$ is then defined as

$$Env(x)(t) = \sqrt{x(t)^2 + H^2[x](t)}. \tag{1.41}$$

The envelope defined in Eq.1.41 is the magnitude of the analytic signal. As in Fig. 1.6, it captures the slowly varying features of the signal $x(t)$. In this thesis, we will mostly apply the **Hilbert transform** to numerically extract the envelope of the stochastic processes of interest. The envelopes extracted from the *Hilbert transform* are not smoothed curves (as in Fig.1.6) but show strong stochasticity as we will see in the main chapters of this thesis.

The Phase

As we have illustrated in Figs. 1.6, the envelope processes describe the slowly varying features of the stochastic oscillatory processes both in the limit cycle and quasi-cycle regimes. However, this is not

enough to describe the processes. Another important quantity of an oscillatory process is its phase. Imagine a point on the limit cycle orbit, and a coordinate frame with origin at the center of the orbit. This point can be identified in polar coordinates by its amplitude r and its angle θ. In this illustration, the point is considered as the oscillatory process and the angle represents its phase. For a limit cycle, with constant amplitude r, the phase alone defines the state of the oscillatory system. This description assumes that the phase is a deterministic concept. For stochastic oscillatory systems, the phase is not well defined, as the notion of a unique closed orbit is ambiguous. However, recent studies have attempted to give alternative definitions of the phase in terms of Kolmogorov Backward operator [209] and mean first passage times [197]. Another practical way to extract the phase of a stochastic oscillatory system involves numerically computing the *Hilbert transform*. The phase is usually defined through the *Hilbert transform* as the argument of the corresponding analytical signal

$$Arg(x)(t) = \arctan\left[\frac{H[x](t)}{x(t)}\right]. \tag{1.42}$$

In contrast to the slow features described by the envelope process, the phase contains the high-frequency information about the oscillatory process of interest. The physical meaning of the phase is a measure of the number of periods spanned by the process. Its actual value is usually scaled in radians by multiplication by 2π. For example, a phase of 2π radian signifies that the process has completed a full period of an oscillation and a phase of π radian is attained when the process has accomplished only half of the period oscillation. This illustration of course considers a phase of 0 radian as the beginning of an oscillation period and the phase of 2π radian as its end. However, another illustration may consider $-\pi$ as the start of the oscillation period and π as its end. For our oscillatory stochastic process of interest δX_1, we have illustrated the notion of phase by numerical extraction from the *Hilbert transform*. The phase time series are the black curves in Figs. 1.7 **(A-B)** denoted $\theta(t)$. The analytic signal returns a phase defined from $-\pi$ to π radians, the value $-\pi$ radian corresponds to the beginning of an oscillation period which matches with a trough of $\delta X_1(t)$, and the value π corresponds to the end of the oscillation period which coincides with the next trough of $\delta X_1(t)$. The phase of the stochastic limit cycle oscillation Fig.1.7 **(A)** is regular and does not depend on the cycle-to-cycle amplitude values (red dots). However, for the quasi-cycle oscillations,

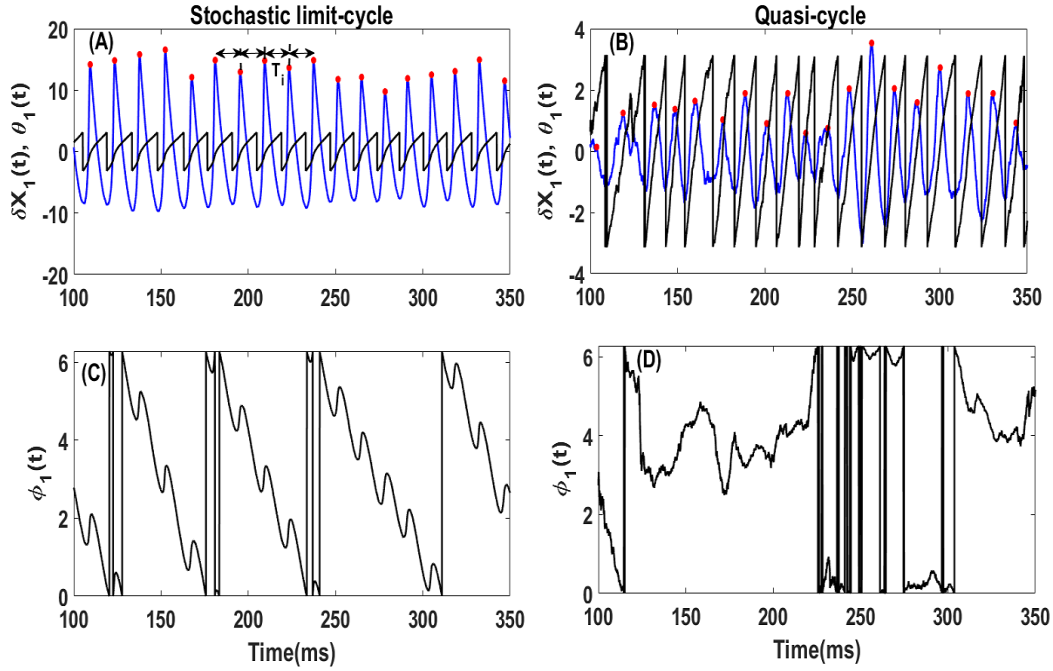

Figure 1.7: **Phase description of the stochastic oscillatory processes for the quasi- and stochastic limit cycle regimes.(A)** The corresponding deterministic dynamic lies in the limit cycle regime $a = 31.4$. The blue curve is the deviation process $\delta X_1(t)$ from the fixed point X_{10}. The black curve represents the phase θ of the stochastic process $\delta X_1(t)$. Red dots are the peak values of the cycle-to-cycle amplitude of the oscillation. We define by T_i the time interval between the peaks at time t_i and t_{i+1}. **(B)** The corresponding deterministic dynamics is a damped oscillation towards the stable fixed point $a = 25.4$, in this quasi-cycle regime. The black curve is the phase of the deviation process $\delta X_1(t)$. **(C)** Slow phase obtained from the fast phase $\theta_1(t)$ in **(A)**. **(D)** Slow phase corresponding to the quasi-cycle oscillations in **(B)**. All the curves in black were obtained by using the Hilbert transform in Matlab.

Fig. 1.7 (**B**), the phase is a stochastic signal which seems to be more irregular when the cycle-to-cycle amplitudes (red dots) have weak values. This suggests that the phase could be modulated by the envelope process when oscillations are quasi-cycles; this property will be demonstrated in this thesis.

An alternative definition of the phase involves two components: a fast component that linearly increases at a constant rate, and a slow component which represents the deviation from this fast and regular component. In this latter definition, the term phase then refers to the slow component, since the fast part is regular and is known from the constant rate of its variation. We mathematically define this latter phase using the relation

$$\theta(t) = \omega_0 t + \phi(t), \tag{1.43}$$

where $\theta(t)$ is the fast phase extracted through the Hilbert transform and $\phi(t)$ the corresponding slow phase. The parameter ω_0 is called the angular frequency and can be computed from the stochastic process of interest. It will be subject to deeper analysis in the next section. We represent this latter slow phase for our stochastic process $\delta X_1(t)$ for both the stochastic limit-cycle oscillation in Fig. 1.7-(**C**) and the quasi-cycle oscillation in Fig. 1.7-(**D**). For the first regime, the variation of phase $\phi_1(t)$ is almost regular. However, for the second regime, the phase $\phi_1(t)$ shows strong fluctuations mostly corresponding with weak values of the cycle-to-cycle amplitudes (red dots) and therefore of the envelope process. For these slow phases, we choose to change the references and consider the phase now between 0 and 2π radian. Of course, this is just a choice for illustrative purpose and one can bring back the range from $-\pi$ to π as for the fast Hilbert phases. The two definitions of the phase can be used equally since we can easily shift from one to the other. In many, studies the Hilbert phase is used since it directly relates to the oscillation.

For limit cycle and weakly stochastic limit cycle oscillations, the Hilbert phase can be used alone to represent the dynamic of the process, avoiding in this way the slow envelope. This makes sense because the envelope is then almost constant and does not give any additional information about the process than its constant value. The phase alone can then accurately describe this class of oscillations. An illustration is seen in Fig. 1.7-(**A**) where the Hilbert phase is regular and describes pretty well the start and the end of an oscillation and can be used alone to describe the process $\delta X_1(t)$ if we can assume an almost constant value for its envelope. However, the slow phase $\phi_1(t)$ of the stochastic process can also be necessary in many situations. For quasi-cycle oscillations, this slow phase seems to bear meaningful information since its variation is connected to the envelope process. Also, the Hilbert phase cannot be used alone to describe the process as in the limit cycle regime. The slow feature of the envelope is tied to the slow feature of the phase $\phi_1(t)$. Another advantage of the slow phase $\phi_1(t)$ is the fact that it is more suitable for some analytical operations such as the averaging procedure which usually requires a slow envelope and phase. We will mostly use this second definition of the phase in Eq. 1.43 and take advantage of its suitability for averaging methods.

The frequency

We have defined the phase as an essential variable describing the state of a periodic system during an oscillation period. To measure "the velocity" of the phase e.g how fast the phase variable evolves, e.g. another quantity known as the *instantaneous frequency* is used [20]. It measures the variation of the phase at each instant of time t and is mathematically defined as the temporal derivative of the phase. The instantaneous frequency of the stochastic process $\delta X_1(t)$ is then expressed as

$$f(t) = \frac{1}{2\pi}\frac{d\theta_1(t)}{dt}. \tag{1.44}$$

The corresponding signal $f(t)$ computed through $\theta_1(t)$ is a stochastic process or not, depending on whether the corresponding phase is stochastic or not. The instantaneous frequency may be characterized by its mean value called the *frequency* defined as:

$$f_0 = E[f(t)]. \tag{1.45}$$

The *mean frequency* or *frequency* is an essential marker of an oscillatory process and measures the mean number of oscillation cycles per unit time. For deterministic processes, the *instantaneous frequency* coincides with its mean. The main concern for stochastic processes is to extract their *frequency*. The frequency of a stochastic oscillation can be computed in several ways. Let us define by T_i the time interval between the peaks at time instances t_i and t_{i+1} as described in Fig. 1.7-(**A**). The values of T_i described a stochastic process depending on whether the corresponding oscillatory process is stochastic. The mean of this latter stochastic process is the mean period T_0 of the oscillatory process, and the inverse of this mean is the *frequency*.

$$T_0 = E[T_i] \quad and \quad f_0 = \frac{1}{E[T_i]}. \tag{1.46}$$

The angular frequency ω_0 used in Eq. 1.43 is expressed using the frequency as $\omega_0 = 2\pi f_0$. The frequency can also be computed using the spectral properties of the stochastic process of interest. In fact the frequency can be extracted from the autocorrelation function and the power spectral density of the stochastic process.

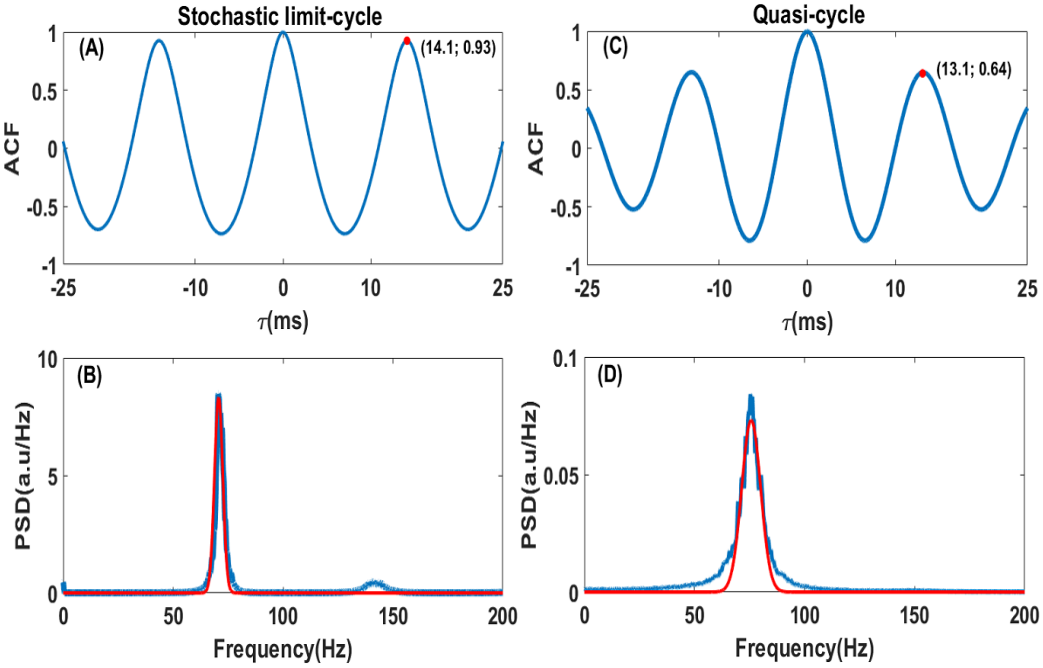

Figure 1.8: **Frequency extraction from the stochastic oscillatory processes for both quasi and stochastic limit cycle regimes.(A,B)** The corresponding deterministic dynamic lies in the limit cycle regime $a = 31.4$. The blue curve in **(A)** is the autocorrelation function of the process $\delta X_1(t)$. The red dot corresponds to the first maximum after the peak at zero lag. The location of this peak is the period of the oscillation ($T_0 = 14.1ms$) and its inverse is the frequency. In **(B)** the power spectral density is represented in blue curve with its corresponding Gaussian fit in red. The mean of the Gaussian fit is the frequency of the oscillation. **(C,D)** The deterministic dynamics is a damped oscillation towards the stable fixed point with $a = 25.4$. The autocorrelation function is represented in **(C)**, while the power spectral density is showed in **(D)** with the same interpretation for the red dot and the red curve as for the stochastic limit cycle.

Consider the normalized version of the autocorrelation function of the stochastic process $\delta X_1(t)$:

$$R_{\delta X_1}(\tau) = \frac{E[(\delta X_1(t) - \mu_{\delta X_1})(\delta X_1(t+\tau) - \mu_{\delta X_1})]}{\sigma^2_{\delta X_1}}. \tag{1.47}$$

It measures the similarity between the stochastic process $\delta X_1(t)$ and time-shifted copies of itself as a function of the lag τ. For a lag $\tau = 0$ the autocorrelation measures the similarity with an identical copy of itself. Then we expect to have a maximum value of the autocorrelation which is 1, as seen in Figs. 1.8-(**A,C**). The next maximum of the autocorrelation function corresponds to the period of the stochastic oscillatory process $\delta X_1(t)$. To compute the frequency it suffices to take the

inverse of the location of the next maximum of the autocorrelation function after the maximum at zero lag. We have illustrated such maxima in Figs. 1.8-(**A,C**) as red dots. Their locations are the periods of $\delta X_1(t)$ with value $T_0 = 14.1ms$ and $T_0 = 13.1ms$ for the stochastic limit cycle and quasi-cycle oscillations, respectively. The corresponding frequencies are $f_0 = 71Hz$ and $f_0 = 76.33Hz$ for the stochastic limit-cycle and the quasi-cycle oscillations, respectively. The autocorrelation, therefore, provides a useful tool to compute the frequency of an oscillatory process. Moreover, it is an important potential marker of the process and differs depending on whether the process describes a stochastic limit cycle or a quasi-cycle oscillation. For instance the autocorrelation function vanishes more quickly for the quasi-cycle (see,Figs. 1.8-(**A,C**)). This may be a tool to identify the regime of *in vivo* oscillations. The power spectral density may also be a suitable quantity to compute the frequency. Since it describes how the power of a signal is distributed over frequencies, we expect to observe a maximum at the frequency of an oscillatory process. For our stochastic process $\delta X_1(t)$ the power spectral density can be computed as follows:

- We define the process $\delta X_{1T}(t)$ as the restriction of $\delta X_1(t)$ to the interval $[0, T]$, ie

$$\delta X_{1T}(t) = \begin{cases} \delta X_1(t), & if \quad 0 \leq t \leq T \\ 0, & otherwise\,. \end{cases} \tag{1.48}$$

- We further define by $\delta \hat{X}_{1T}(\omega)$ the Fourier transform of $\delta X_{1T}(t)$.

- The power spectral density PSD of $\delta X_{1T}(t)$ is given by

$$S_{\delta X_{1T}}(\omega) = \lim_{T\to\infty} \frac{\left\langle |\delta \hat{X}_{1T}(\omega)|^2 \right\rangle}{T}. \tag{1.49}$$

We therefore, use this latter expression Eq. 1.49 to compute the power spectral densities in Fig. 1.8- (**B,D**). We observe that the power spectral densities show maxima for both stochastic limit cycle and quasi-cycle oscillations. The locations of the maxima correspond to the values of the frequency of the process $\delta X_1(t)$. However, the behavior of the PSD differs depending on the regime considered. For the stochastic limit cycle oscillations in Fig. 1.8- (**B**) the PSD exhibits several (at least two) peaks with one stronger than the others. The strongest peak is the peak

at the oscillation frequency f_0, and the frequencies at the secondary peaks are multiple integer of the frequency ($f_{i-1} = if_0; i = 1, 2, ...$). They are called higher-order harmonics. In the quasi-cycle regime, the PSD has a single peak (see, Fig. 1.8- (**D**)); this peak has a smaller value than the principal peak in the stochastic limit cycle regime. To extract the value of the locations of the peaks of the PSD, we performed a Gaussian fitting of each of them (see red curves, Figs. 1.8- (**B,D**)). The means of the corresponding fitted Gaussian functions are the frequencies of interest. Several studies however represent the PSD on logarithmic scales. Such scaling allows extracting further information, such as power-law features which appear at lower and higher frequencies. However, the choice of scaling does not change the location of the frequency.

We have shown that the frequency can be extracted by several means. We can directly use the stochastic process itself, its phase component, or other related quantities like the autocorrelation function and the power spectral density PSD.

1.2.5 Envelope-Phase description

We have shown in the preceding sections that the stochastic oscillations $\delta X_1(t)$ can be decomposed principally in their envelope and phase components (since the frequency can be deduced from the phase). The envelope returns the slow features of the stochastic oscillations, and the phase describes information about the fast dynamics of the rhythms. It is therefore of great interest to extract these two important components. The envelope-phase description takes large importance in the quasi-cycle regime since the phase is significantly modulated by the envelope, and the two are coupled. The dynamics of the envelope is also an important marker to characterize quasi-cycle oscillations. For the stochastic limit cycle regime, the phase alone may be enough to describe the oscillatory dynamics if the envelope remains almost constant during the evolution of the process [2, 188, 225, 139]. This assumption holds if the strength **G** of the stochastic part of Eq. 1.30 is weak or if the system is deterministic.

However, for strong values of the stochastic function **G**, even the envelopes of limit cycles vary strongly, and the phase alone is no longer sufficient to fully describe the dynamics of the processes. In this strong noise limit, the envelope-phase decomposition is the appropriate framework. The envelope-phase framework is also appropriate to address the case of several coupled oscillatory

stochastic processes.

The dynamics of coupled stochastic oscillatory processes have been studied mostly using simple models of interacting phases [2]. Such models neglect the envelope dynamics when they do consider the envelope it is in the limit cycle regime, and typically for strong noise. A description that fully takes into account the stochastic envelope and phase may be a useful generalization of these simple phase models. However, such envelope-phase models have not received much attention because of the lack of theoretical methods for their treatment. Also, a general method for the extraction of envelope-phase representation for any specific oscillatory process is lacking. In this thesis, we are mainly interested in the envelope-phase decomposition of stochastic oscillations with application to neural rhythms. One of our goals is to extract the envelope-phase dynamics of stochastic neural rhythms in quasi- and limit cycle regimes and the coupling of such rhythms across different brain areas. For publication purpose, in chapter 5, we use the expression amplitude-phase to refer to the envelope-phase description.

1.3 Neural rhythms

Neural rhythms are a type of stochastic oscillations recorded from several parts of the brains of diverse species. They are seen in the brains of monkeys, cats, mice and even humans. Their origins and precise functions are still debated.

1.3.1 Origin and description of neural rhythms

The basic elements of mammalian brains are neurons. A neuron is an electrically excitable cell that consists of a body or soma, dendrites, and a single axon. Neurons like all cell are made of an intracellular medium separated by an insulator membrane from the extracellular medium. In contrast to other cell membranes, the neuron membrane is composed of a special combination of ion channels that permits electrically charged particles (ions) to flow across it [202]. The membrane also has ion pumps that chemically transport ions from one side of the membrane to the other. The majority of ion channels are permeable only to specific types of ions. Some channels can be switched between open and closed states by altering the voltage difference across the membrane. Others can be switched between open and closed states by interactions with chemicals that diffuse through the

extracellular fluid. The first type of ion channel is said to be voltage-gated, while the second is chemically gated [202, 92].

A neuron has a net potential difference due to the intracellular and the extracellular media called the resting membrane potential which lies at around -70 mV (the interior being more). When an electrical stimulus of sufficient strength reaches the neuron, it can drastically change the value of the resting membrane potential and creates an electrical signal which then propagates through the axon. This electrical signal caused by the stimulus is called an action potential and is the basic unit of information used by a neuron to communicate with other neurons. An action potential is created when a stimulus raises the membrane potential past the threshold potential which lies usually around -50 to -55 mV. If the stimulus is too small i.e subthreshold, no action potential is created. However, when the stimulus is just enough (threshold) or suprathreshold, an action potential is created. The shape of the action potential is the same for all threshold or suprathreshold stimuli. But a continuous applied suprathreshold stimulus creates action potentials at a rate proportional to the stimulus intensity. The action potential is generated at the soma and then propagates through the axon to the synapses where it is then transmitted to other neurons that are connected to it. During its propagation through the axon, the shape, the velocity, and the intensity of an action potential remain constants.

Consider two connected neurons, one sending an action potential through its synapses to the other one. The neuron that sends an action potential is called the presynaptic neuron, and the one which receives it is called the postsynaptic neuron. The postsynaptic neuron receives the action potential through one of its dendrites. The action potential causes the presynaptic neuron to release neurotransmitter molecules from its synapse onto such a dendrites. A neuron is called an excitatory neuron if its neurotransmitters raises the membrane potential of target cells closer to or beyond the threshold for an action potential generation. On the other hand, if its neurotransmitters inhibit the target cells, the neuron is inhibitory. All brains are then made of excitatory and inhibitory neurons.

A neuron is not isolated in the brain but is connected to several other neurons through its synapses and several neurons are connected to it through its dendrites. A group of interconnected neurons is called a neural circuit or a neural network. The net sum of action potentials received by a neuron from its presynaptic neurons in the network is integrated at the soma. If the voltage at the

soma is above the threshold, the neuron emits an action potential or a spike. Neural activity can be defined as the sum of all the electrical action potentials emitted by all the neurons in a specific brain area. Such activity is usually measured using electrodes implanted inside the brain, and exhibits a diverse range of behaviors. The names usually assigned to those recordings depend on the size of the implanted electrodes and therefore the extent of the recorded region. For example, to record from a single cell, an electrode with a diameter at the order of $1\mu m$ is needed. For the activity of a small area known as a Local field potential (LFP), the diameter of the electrode should be on the order of $1mm$. And an electrode diameter on the order of $1cm$ correspond to recording from a larger area known as Electroencephalogram (EEG) [219].

Neural oscillations are a specific behavior of neural activity recorded from the brain which increases and decreases almost periodically. They can be seen in LFPs or EEG, however, the frequency of LFPs and EEGs are different. While LFPs are usually fast rhythms such as beta (30-100Hz) or gamma (30-100 Hz) oscillations, EEGs on the contrary are generally dominated by slower rhythms such as alpha and delta [41]. However, even if the activity recorded from a particular brain area is almost periodic, the emission of action potentials by a single neuron i.e. its spiking behavior, is not always periodic. Single neuron spiking behavior can be highly irregular, similar to a Poisson process when at the same time the activity of several similar neurons is periodic. Also, we can have a situation where the oscillatory behavior comes from the oscillatory spiking of a single neuron. To reconcile the spiking behavior of a single cell with the oscillatory activity of several neurons, many mathematical models have been proposed .

1.3.2 Gamma oscillations

Understanding the behavior of a large group of neurons ie of neural networks is often achieved by studying their corresponding mathematical models. The idea is to first write the dynamic of a single neuron which reproduces the stochastic firing behavior observed *in vivo*. From a single neuron model, one can therefore construct the corresponding network by adding coupling with other neurons. Such models are usually known as spiking neural networks since the stochastic spiking activity of every single neuron in the network can be mimicked and visualized. The activity of such networks is usually defined as the sum of all action potentials (or time-course of the voltages) of all the neurons

in the network divided by the total number of neurons. However, if someone is interested in the activity dynamics only, the detailed modeling of every single neuron provided by spiking neural networks may not be useful. All that matters is the dynamics of the activity of the populations of neurons. In this spirit, mean-field models which only take into account population averaged quantities have been developed. These models are sometimes stochastic since they represent the average of stochastic quantities plus their fluctuations. They have a lower dimension than spiking neural networks, which facilitates their mathematical analysis. In the case where their dynamics are also oscillatory, they are governed by mathematical laws of stochastic oscillatory dynamics presented in the previous sections. However, what is the real mechanism behind neural oscillations? In other words, what causes the activity to oscillate? To answer these questions we consider a particular type of oscillation known as fast neural rhythms of gamma oscillations (30-100 Hz). They have been recorded in several brain areas and are believed to be involved in several cognitive processes [41, 42]. Two principal types of mechanisms have been invoked to explain their genesis.

PING Mechanism or E-I model

The first mechanism used to explain the generation of gamma oscillations is the Pyramidal-Interneuron Network Gamma (PING) or the E-I model. This model is based on the reciprocal connections between populations of Pyramidal (excitatory or E) and Interneuron (inhibitory or I) neurons. Fast excitation and delayed inhibition alternate in a rhythmic way. Excitatory neurons fire first due to some excitation which can be an input from neurons external to the network. Then, they excite inhibitory neurons, in return which fire and inhibit excitatory neurons. This eventually leads to a decrease in the inhibition and the cycle starts again. In this model, a single neuron can fire stochastically or periodically. Excitatory neurons fire early since they are the ones that excite inhibitory neurons. The frequency of the underline rhythm depends on the propagation delay between excitatory and inhibitory neurons. Several mathematical models have been proposed to describe such a PING mechanism, among which the Wilson-Cowan model [224]. In this thesis, we will mostly use the Wilson-Cowan model to describe Gamma as well as Beta oscillations. We will use a modified version of this model that includes stochastic inputs of finite-size and synaptic origins [220].

ING Mechanism or I-I model

Gamma oscillations can also occur in networks of only inhibitory neurons known as Interneuron Network Gamma (ING). In this mechanism, an external excitatory input excites inhibitory neurons, which then fire rhythmically. The external excitatory input provides the excitation to generate the spiking behavior observed during the peak of the oscillation, whereas the firings of inhibitory neurons provide inhibition to silence the network as seen in the through of the oscillation. No matter the mechanism of gamma oscillations, inhibitory neurons are required; They are critical to producing gamma oscillations. Mathematically, mean-field models of gamma oscillations with only inhibitory neurons may require to explicitly include a propagation delay [73]. The firing behavior of a single neuron can also be periodic or stochastic in the ING mechanism.

1.4 Numerical Methods

Stochastic processes are not analytically solvable. We therefore referred to numerical methods to obtain several results in this Thesis. Especially, numerical methods are required to obtain approximate solutions of the Stochastic Differential Equations (SDE). The autocorrelation functions and the power spectral densities are obtained from numerical methods.

- **Euler-Maruyama method**.

  The majority of the SDE in this Thesis was simulated using the *Euler-Maruyama scheme*. Let us consider the one-dimensional SDE in Eq.1.20. We suppose that the time axis is divided in time-steps of equal size, Δt. Practically, we assume that the process evolves during a total time T sufficiently long ($T \to \infty$). The number of time-step of size dt is $N = T/dt$. The time can be defined by the relation $t_{n+1} = t_n + \Delta t$, with $n = 0, ..., N-1$ and $t_0 = 0$. Morever, X_n is the value of the stochastic process $X(t)$ at t_n and X_0 is the initial condition. The value of the stochastic process at time t_{n+1} can be obtained using the following

$$X_{n+1} = X_n + A(X_n, t_n)\Delta t + \sqrt{B(X_n, t_n)}\Delta W_n. \tag{1.50}$$

In addition we have the relation:

$$\Delta W_n = \sqrt{\Delta t} N(0,1),$$

where $N(0,1)$ is a Gaussian process with zero mean an unit standard deviation. The *Euler-Maruyama scheme* is therefore expressed as

$$X_{n+1} = X_n + A(X_n, t_n)\Delta t + \sqrt{B(X_n, t_n)\Delta t} N(0,1). \tag{1.51}$$

The *Euler-Maruyama scheme* can be extended to the case of an N-dimensional stochastic differential equation as in Eq.1.21. However, in chapter 5, we also used for some simulations the fourth order runge-kutta numerical scheme and its stochastic version [131].

- **Power spectral densities and Autocorrelation functions**

  The power spectral densities were obtained using the Welch's method as implemented in MATLAB R2019b. We use a window size of 10 seconds with 50 percent overlap. The autocorrelation functions were computed using the xcov method as implemented in MATLAB R2019. The maximum lag was set to 50 ms.

Chapter 2

Determinants of Brain Rhythm Burst Statistics

Abstract

Brain rhythms recorded *in vivo*, such as gamma oscillations, are notoriously variable both in amplitude and frequency. They are characterized by transient epochs of higher amplitude known as bursts. It has been suggested that, despite their short-life and random occurrence, bursts in gamma and other rhythms can efficiently contribute to working memory or communication tasks. Abnormalities in bursts have also been associated with e.g. motor and psychiatric disorders. It is thus crucial to understand how single cell and connectivity parameters influence burst statistics and the corresponding brain states. To address this problem, we consider a generic stochastic spiking recurrent network of Pyramidal Interneuron Network Gamma (PING) type. Using the stochastic averaging method, we derive dynamics for the phase and envelope of the amplitude process, and find that they depend on only two meta-parameters that combine all the model parameters. This allows us to identify an optimal parameter regime of healthy variability with similar statistics to that seen *in vivo*; in this regime, oscillations and bursts are supported by synaptic noise. The probability density for the rhythm's envelope as well as the mean burst duration are then derived using first passage time analysis. Our analysis enables us to link burst attributes, such as duration and frequency content, to system parameters. Our general approach can be extended to different frequency bands, network topologies and extra populations. It provides the much needed insight into the biophysical determinants of rhythm burst statistics, and into what needs to be changed to correct rhythms with pathological statistics.

2.1 Introduction

Fast oscillations in brain activity in the 30-100 Hz range, known as gamma rhythms, are observed across many brain regions and species, both *in vitro* and *in vivo* [53, 51, 208, 212]. They occur either autonomously or are induced by external stimulation [50, 36, 56, 81, 3]. They have received much attention because of their proposed roles in several major neuronal processes like perception, cognition, binding, working memory or inter-areal communication [112, 24, 84, 86, 116, 104]. To perform such tasks, it is generally believed that the gamma rhythm should be a coherent oscillation with relatively constant amplitude and frequency, in particular in theories where the oscillation acts as a clock signal [43, 11] with regular neuronal firing [124, 87].

However, several studies, focussing especially on gamma-range oscillations in monkey primary visual cortex, have reported that the rhythms are broadband rather than coherent, and exhibit transient epochs of elevated synchrony aptly termed "gamma bursts". The underlying neuronal spiking activity is also quite irregular. These bursts of large oscillation amplitude alternate with epochs of almost no synchrony where the oscillation amplitude is low. The frequency shows a lot of variability, a consequence of the significant noisiness of the phase of the rhythm. Moreover, the occurrence times and durations of gamma bursts are random, making such rhythms closer to a broadband filtered noise than to a well-structured, almost periodic signal [229, 37, 40].

Despite their stochasticity, such bursty rhythms have been shown to correlate better with the performance of certain tasks than more regular oscillations. Indeed, a recent study examined local field potentials (LFP) and spiking activity from the prefrontal cortex of monkeys performing a working memory task, and reported that working memory manifests itself through gamma bursts rather than sustained activity [155]. Another study measured neuronal activity in the entorhinal-hippocampal circuit while mice performed a reward-based spatial working memory task, and showed that gamma bursts contribute to the successful execution of the task [230]. A plausible role for such gamma bursts has recently been formulated computationally in the context of inter-areal synchronization and communication [152, 175].

There is currently no theory that links the properties of a network to those of the bursty rhythm. Here we provide such a general theory for a recurrent excitatory-inhibitory network. We show how the burst statistics relate to single cell and network parameters, and consequently to different

regimes of oscillation. Apart from shedding light on how the bursts arise and can be used for neural computations, this theory provides the much-needed insight into how a system can be modified to rectify undesirable burst statistics associated with pathology. A useful framework to address the dynamics of such broadband oscillations is the amplitude-phase decomposition. The amplitude in this framework reflects the level of network synchronization, where weak values of the amplitude reflect little or no synchronization, whereas strong values reflect higher network synchronization. The phase, which depends on the amplitude to a good approximation, contains all the information about the temporal structure of the oscillation.

Amplitude-phase decompositions have been used in a number of computational studies to address phase synchronization [219], inter-areal phase communication (generally known as communication through coherence or CTC) [134, 175] and more generally different types of cross-frequency-coupling (CFC) between brain circuits [121]. At the theoretical level, the search for such decompositions has been pursued over the last decades, particularly for oscillations of varying degree of coherence both at the single neuron and population levels [21, 30, 194, 193, 58]. Such studies belong to the broader effort to describe stochastic oscillations, sometimes called "quasi-cycles" in many areas of science including nonlinear chemical oscillators and population biology (see e.g. [158, 159]). For the case of broadband gamma oscillations, recent studies [17, 102, 103] have extracted from firing-rate-level descriptions of the network the generic dynamics for the slowly-evolving envelope of the rapidly-varying amplitude of the rhythm. This envelope can be seen as approximately connecting the peaks of the fast rhythm. They also extracted dynamics for the rapidly-varying phase of the rhythm. A burst is then seen as an epoch during which the envelope exceeds some threshold. This provided insight into properties of the fluctuations of the gamma rhythm, although it did not allow the role of the noise strength to be investigated.

Here, we first directly relate the dynamics of the envelope and phase of the rhythm to all the biophysical parameters, including synaptic noise strength. From there, we develop a first passage time analysis of the envelope to quantify the mean duration of bursts as a function of the parameters. This enables us to uncover an "optimal" dynamical regime of healthy amplitude and frequency variability with similar statistics to those seen in certain *in vivo* data. Below, we use the term "amplitude" to signify the magnitude of the fast variables, as distinguished from its slowly evolving

"envelope".

For concreteness, we focus on a known simple excitatory-inhibitory recurrent network of spiking neurons with self-couplings exhibiting gamma oscillations, and investigate its ability to produce bursting behavior. We find two master parameters that govern burst statistics, giving much needed insight into burst generation and the correction of "faulty" burst statistics. Our simple model can also explain bursts observed in other frequency bands (such as beta), and thus constitutes a general framework for studying bursty brain rhythms.

We first motivate the choice of microscopic model and its associated formulation in terms of a noisy population firing rate model. We then derive (with details in the Methods) the noisy dynamics of the amplitude and phase of the rhythm, identify dynamical regimes of interest for gamma bursts, and perform first passage time (Fokker-Planck) analysis to characterize burst statistics. Comparisons of envelope-phase dynamics to full network simulations validate our approach. We then discuss how different combinations of biophysical parameters can underlie healthy and pathological rhythm variability.

2.2 Methods

The Model

We begin by summarizing a recent model of noisy gamma activity that is based on a network of nonlinear neurons that spike probabilistically [220]. This more biophysically realistic model is used here to illustrate gamma bursts. We then review the relation of this model to the stochastic Wilson-Cowan firing rate model and show its ability to also generate gamma bursts in terms of firing rate rather than spike events. Our envelope-phase reduction will be derived from this rate model.

The network is composed of fully connected N_E excitatory neurons and N_I inhibitory neurons. Each neuron can exist in one of the two following states: an active state (a) representing the firing of an action potential and its accompanying refractory period, and a quiescent state (q) associated with a neuron at rest. Each neuron follows a two-state Markov process. The dynamics of a neuron are specified by the transition rates between the two states. The transition probability for the i^{th}

neuron to decay from the active to the quiescent state is

$$P_i(active \rightarrow quiescent, in\ time\ dt) = \alpha_i dt$$

where α_i, $i = E, I$ is a constant; thus this transition probability does not depend on the input to the neuron. It is typically high to mimic the largely deterministic nature of voltage reset after a spike. In contrast, the transition probability from quiescent to active is:

$$P_i(quiescent \rightarrow active, in\ time\ dt) = \beta_i f(s_i(t))dt$$

with input

$$s_i(t) = \sum_j W_{ij} a_j(t) + h_i \ .$$

Here f is the neuron input-output response function, typically a sigmoid, W_{ij} is the strength of the positive or negative synaptic weight from a j-type cell onto an i-type cell, h_i the external input, $\sum_j W_{ij} a_j(t)$ the network input and $s_i(t)$ the total input to neuron i. We set $a_i(t) = 0$ if neuron i is quiescent and $a_i(t) = 1$ if it is active.

At the network level, we assume that the total synaptic weight from the excitatory population to itself is W_{ee}; the mean synaptic weight from an excitatory cell to another excitatory cell in the excitatory population is just W_{ee}/N_E. Similar assumptions hold for the other connection strengths, namely $-W_{ii}/N_I$ between inhibitory neurons, W_{ie}/N_e from excitatory to inhibitory neurons, and $-W_{ei}/N_I$ from inhibitory to excitatory neurons. Also, each excitatory neuron receives the same external input h_E; likewise, all inhibitory neurons receive the external input h_I. The total input current s_E to excitatory neurons and s_I to inhibitory neurons are then given by

$$s_E(t) = \frac{W_{ee}}{N_E} k(t) - \frac{W_{ei}}{N_I} l(t) + h_E \tag{2.1}$$

$$s_I(t) = \frac{W_{ie}}{N_E} k(t) - \frac{W_{ii}}{N_I} l(t) + h_I \tag{2.2}$$

where $k(t)$ is the number of active excitatory neurons and $l(t)$ the number of active inhibitory neurons. This network is simulated in discrete time using the Gillespie algorithm as in [220]. A

typical simulation result is shown in Fig 2.3 where, in spite of the presence of a noisy rhythm, the firing behavior of individual neurons (excitatory and inhibitory) is close to a Poisson process. Short-lived gamma oscillations are produced at the network level especially in the transient synchrony regime [220].

In this formalism, it is possible to approximate the Poisson statistics by Gaussian statistics for firings in any time interval. This leads to the following activity of the excitatory population defined as $E(t) = k(t)/N_E$ [220]:

$$\frac{dE(t)}{dt} = -\alpha_E E(t) + \big(1 - E(t)\big)\beta_E f(s_E(t)) + I_E(t) \tag{2.3}$$

Similarly for inhibitory neurons, we have:

$$\frac{dI(t)}{dt} = -\alpha_I I(t) + \big(1 - I(t)\big)\beta_I f(s_I(t)) + I_I(t) \tag{2.4}$$

with noise sources with time-dependent variances given by

$$I_E(t) = \sqrt{\frac{\big(1 - E(t)\big)\beta_E f(s_E(t)) + \alpha_E E(t)}{N_E}}\eta_E(t) \quad \text{and}$$
$$I_I(t) = \sqrt{\frac{\big(1 - I(t)\big)\beta_I f(s_I(t)) + \alpha_I I(t)}{N_I}}\eta_I(t) \ .$$

Here $\eta_{E,I}(t)$ are Gaussian white noises satisfying:

$$\langle \eta_i(t) \rangle = 0, \quad \langle \eta_i(t)\eta_j(t') \rangle = \delta_{ij}\delta(t - t') \quad i, j = \{E, I\} \, .$$

From the Linear Noise Approximation (LNA), if N_E and N_I are large but stochasticity is still important, Gaussian approximation may be further apply. The activities (k, l) can then be represented as the sum of a deterministic component $\big(E_0, I_0\big)$ scaled by the population sizes and stochastic perturbations $\big(\tilde{V_E}(t), \tilde{V_I}(t)\big)$ scaled by square root of the population sizes [220]. We then have

$$E(t) = E_0(t) + \frac{1}{\sqrt{N_E}}\tilde{V_E}, \quad I(t) = I_0(t) + \frac{1}{\sqrt{N_I}}\tilde{V_I}(t) \tag{2.5}$$

where $E_0(t)$ and $I_0(t)$ are solutions of the deterministic version of Eqs 2.3,2.4 above:

$$\frac{dE_0(t)}{dt} = -\alpha_E E_0(t) + \big(1 - E_0(t)\big)\beta_E f(s_{E_0}(t)) \tag{2.6}$$

$$\frac{dI_0(t)}{dt} = -\alpha_I I_0(t) + \big(1 - I_0(t)\big)\beta_I f(s_{I_0}(t)) \tag{2.7}$$

with

$$s_{E_0} = W_{ee}E_0 - W_{ei}I_0 + h_E, \quad s_{I_0} = W_{ie}E_0 - W_{ii}I_0 + h_I\,.$$

We focus on oscillations induced by noise, for which Eqs 2.6,2.7 must admit a stable equilibrium or "fixed" point (i.e. its complex eigenvalues have negative real part). This fixed point is the solution of

$$\begin{aligned} 0 &= -\alpha_E E_0^* + \big(1 - E_0^*\big)\beta_E f(s_{E_0^*}) \\ 0 &= -\alpha_I I_0^* + \big(1 - I_0^*\big)\beta_I f(s_{I_0^*})\,. \end{aligned} \tag{2.8}$$

After a transient, the deterministic solution $\big(E_0(t), I_0(t)\big)$ converges to the fixed point $\big(E_0^*, I_0^*\big)$ and the LNA becomes:

$$E(t) = E_0^* + \frac{1}{\sqrt{N_E}}\tilde{V_E}(t), \quad I(t) = I_0^* + \frac{1}{\sqrt{N_I}}\tilde{V_I}(t)\,. \tag{2.9}$$

Replacing Eq 2.9 into Eqs 2.3,2.4 and keeping the terms of order $\mathcal{O}(\sqrt{N_E})$ and $\mathcal{O}(\sqrt{N_I})$, the dynamics of fluctuations around the equilibrium point are obtained:

$$\frac{d\tilde{V_E}(t)}{dt} = A_{11}\tilde{V_E}(t) + A_{12}\tilde{V_I}(t) + \sigma_E\eta_E(t) \tag{2.10}$$

$$\frac{d\tilde{V_I}(t)}{dt} = A_{21}\tilde{V_E}(t) + A_{22}\tilde{V_I}(t) + \sigma_I\eta_I(t)\,. \tag{2.11}$$

In terms of all the biophysical parameters of the original nonlinear stochastic spiking E-I network,the seven parameters governing these fluctuations around the equilibrium are given by:

$$A_{11} = -\alpha_E - \beta_E f\left(s_{E_0^*}\right) + \left(1 - E_0^*\right) W_{ee} \beta_E f^{'}\left(s_{E_0^*}\right) = -\frac{\alpha_E}{1 - E_0^*} + \alpha_E E_0^* \left[1 - \frac{\alpha_E E_0^*}{(1 - E_0^*)\beta_E}\right] W_{ee}$$

$$A_{12} = -\left(1 - E_0^*\right) W_{ei} \beta_E f^{'}\left(s_{E_0^*}\right) c_{EI} = -c_{EI} \alpha_E E_0^* \left[1 - \frac{\alpha_E E_0^*}{(1 - E_0^*)\beta_E}\right] W_{ei}$$

$$A_{21} = \left(1 - I_0^*\right) W_{ie} \beta_I f^{'}\left(s_{I_0^*}\right) c_{EI}^{-1} = c_{EI}^{-1} \alpha_I I_0^* \left[1 - \frac{\alpha_I I_0^*}{(1 - I_0^*)\beta_I}\right] W_{ie}$$

$$A_{22} = -\alpha_I - \beta_I f\left(s_{I_0^*}\right) - \left(1 - I_0^*\right) W_{ii} \beta_I f^{'}\left(s_{I_0^*}\right) = -\frac{\alpha_I}{1 - I_0^*} - \alpha_I I_0^* \left[1 - \frac{\alpha_I I_0^*}{(1 - I_0^*)\beta_I}\right] W_{ii}$$

$$\sigma_E = \sqrt{\alpha_E E_0^* + \left(1 - E_0^*\right) \beta_E f\left(s_{E_0^*}\right)}; \quad \sigma_I = \sqrt{\alpha_I I_0^* + \left(1 - I_0^*\right) \beta_I f\left(s_{I_0^*}\right)}; \quad c_{EI} = \sqrt{\frac{N_E}{N_I}}\,.$$

Using the fixed point equations, the noise intensities can be rewritten as $\sigma_E = \sqrt{2\alpha_E E_0^*}$ and $\sigma_I = \sqrt{2\alpha_I I_0^*}$. Therefore we obtain linear equations driven by noise which represent the LFP dynamics $\tilde{V_E}$ and $\tilde{V_I}$. Changing one parameter, such as the strength of connectivity of I cells onto E cells W_{ei}, will change a number of these parameters as well as the fixed points. In turn we will see below that these changes impact only two "master parameters" that govern the envelope dynamics.

2.2.1 Linear Analysis

We consider the linear stochastic Eqs 2.10,2.11 and first consider the deterministic case $\sigma_E = \sigma_I = 0$. The associated noise-free linear system is written in the following matrix form:

$$\frac{dV^0(t)}{dt} = AV^0(t)$$

where

$$V^0(t) = \begin{bmatrix} V_E^0(t) \\ V_I^0(t) \end{bmatrix} \quad and \quad A = \begin{bmatrix} A_{11} & A_{12} \\ A_{21} & A_{22} \end{bmatrix}\,.$$

We look for a trial solution in the form:

$$\begin{bmatrix} V_E^0(t) \\ V_I^0(t) \end{bmatrix} = \begin{bmatrix} \tilde{B_E} \\ \tilde{B_I} \end{bmatrix} e^{\lambda t}$$

where $\tilde{B_E} = B_E e^{j\theta_E}$ and $\tilde{B_I} = B_I e^{j\theta_I}$. The eigenvalue λ of the associated matrix A is found by substituting the trial solution into the linear system, yielding

$$\frac{\tilde{B_E}}{\tilde{B_I}} = \frac{-A_{12}}{A_{11}-\lambda} = -\frac{A_{22}-\lambda}{A_{21}} \ .$$

The second equality leads to

$$\lambda = \frac{1}{2}(A_{11}+A_{22}) \pm \frac{j}{2}\sqrt{-(A_{11}-A_{22})^2 - 4A_{12}A_{21}} \ .$$

We rewrite the eigenvalue in the compact form

$$\lambda = -\nu \pm j\omega_0 \tag{2.12}$$

with

$$\nu = -\frac{A_{11}+A_{22}}{2}, \quad \omega_0 = \frac{1}{2}\sqrt{-(A_{11}-A_{22})^2 - 4A_{12}A_{21}} \quad and \quad j = \sqrt{-1}\,.$$

This leads to the exact expression of the real amplitude ratio between the excitatory and inhibitory LFPs:

$$\frac{B_E}{B_I} = \sqrt{\frac{-A_{12}}{A_{21}}} = \sqrt{\frac{c_{EI}\alpha_E E_0^* \left[1 - \dfrac{\alpha_E E_0^*}{(1-E_0^*)\beta_E}\right] W_{ei}}{c_{EI}^{-1}\alpha_I I_0^* \left[1 - \dfrac{\alpha_I I_0^*}{(1-I_0^*)\beta_I}\right] W_{ie}}} \approx \sqrt{\frac{N_I W_{ei}}{N_E W_{ie}}}$$

Note that the expression above is the modulus of the complex number $\frac{\tilde{B}_E}{\tilde{B}_I}$. Likewise, the corresponding phase difference is obtained by taking the argument Arg of the complex number $\frac{\tilde{B}_E}{\tilde{B}_I}$

$$\delta = \theta_E - \theta_I = Arg\left(\frac{\tilde{B}_E}{\tilde{B}_I}\right).$$

For the parameters used here we have the following expression for δ

$$\delta = \theta_E - \theta_I = \arctan\left(\frac{2\omega_0}{A_{11}-A_{22}}\right).$$

Note that in the absence of noise, the time-dependent amplitudes both go to zero exponentially with characteristic time ν^{-1}. One can nevertheless compute the ratio of amplitudes as above. However, in the presence of noise, one can compute the ratio from simulated time series using the analytic

signal technique. The amplitudes ratio and the phase difference are obtained by the following approximations:

$$\alpha = \frac{B_I}{B_E} \approx \left\langle \frac{Env\big[\tilde{V_I}(t)\big]}{Env\big[\tilde{V_E}(t)\big]} \right\rangle \quad and \quad \delta = \theta_E - \theta_I \approx \left\langle Arg\big[\tilde{V_E}(t)\big] - Arg\big[\tilde{V_I}(t)\big] \right\rangle . \tag{2.13}$$

Here $\langle . \rangle$ can be considered a time average of the stochastic process in Eq 2.10. Env is defined as the envelope of the analytic signal associated with the LFP. For example, the analytic signal corresponding to $V_E(t)$ is $V_E(t) + jH\big[V_E(t)\big]$, with the Hilbert transform H defined as

$$H[x] = \frac{1}{\pi} P \int_{-\infty}^{\infty} \frac{x(\tau)}{t-\tau} d\tau \tag{2.14}$$

where P signifies the Cauchy principal value. The envelope of the stochastic signal is then $Env[V_E] = \sqrt{V_E^2 + H^2[V_E]}$. Likewise, the phase angle of the analytic signal is defined as $Arg[\tilde{V_E}] = \arctan\big[H[V_E]/V_E\big]$.

The transition between the transient and high synchrony regimes happens when the real part of the eigenvalue is zero. This condition is expressed as

$$-\frac{\alpha_E}{1-E_0^*} + \alpha_E E_0^* \left[1 - \frac{\alpha_E E_0^*}{(1-E_0^*)\beta_E}\right] W_{ee} - \frac{\alpha_I}{1-I_0^*} - \alpha_I I_0^* \left[1 - \frac{\alpha_I I_0^*}{(1-I_0^*)\beta_I}\right] W_{ii} = 0 \,. \tag{2.15}$$

We use this expression to plot Fig 2.6 (Left panel). For Fig 2.6 (Right panel), we first use Eq 2.1 to shift from the self-connectivity parameters to the $\big(W_{ei}, W_{ie}\big)$ plane. We next derive an expression for the dynamics governing the time evolution of the envelopes of the excitatory and inhibitory stochastic processes themselves.

2.2.2 Stochastic Averaging Method (SAM)

Taking into account the constant ratio of envelopes and constant phase difference, the expression of the excitatory and inhibitory LFPs are given by

$$V_E(t) = Z_E(t)\cos(\omega_0 t + \phi_E(t)) \quad and \quad V_I(t) = \alpha Z_E(t)\cos(\omega_0 t + \phi_E(t) - \delta) \,. \tag{2.16}$$

We plug these expressions into the linear stochastic equations Eqs 2.10 and rewrite the resulting equations in terms of variables Z_E and ϕ_E as follows:

$$\dot{Z_E}(t) = f_1\left(Z_E, \phi_E\right) + g_1\left(Z_E, \phi_E, \eta_E, \eta_I\right) \tag{2.17}$$

$$\dot{\phi_E}(t) = f_2\left(Z_E, \phi_E\right) + g_2\left(Z_E, \phi_E, \eta_E, \eta_I\right) \tag{2.18}$$

with

$$f_1\left(Z_E, \phi_E\right) = \frac{Z_E}{\alpha \sin\delta}\Big[\alpha\big(-\omega_0 \sin(\omega_0 t + \phi_E) + A_{11}\cos(\omega_0 t + \phi_E) + \alpha A_{12}\cos(\omega_0 t + \phi_E - \delta)\big)\sin(\omega_0 t + \phi_E - \delta)\big) - \big(\alpha\omega_0 \sin(\omega_0 t + \phi_E - \delta) + A_{21}\cos(\omega_0 t + \phi_E) + \alpha A_{22}\cos(\omega_0 t + \phi_E - \delta)\big)\sin(\omega_0 t + \phi_E)\Big] \tag{2.19}$$

$$f_2\left(Z_E, \phi_E\right) = \frac{1}{\alpha \sin\delta}\Big[\alpha\big(-\omega_0 \sin(\omega_0 t + \phi_E) + A_{11}\cos(\omega_0 t + \phi_E) + \alpha A_{12}\cos(\omega_0 t + \phi_E - \delta)\big)\cos(\omega_0 t + \phi_E - \delta) - \big(\alpha\omega_0 \sin(\omega_0 t + \phi_E - \delta) + A_{21}\cos(\omega_0 t + \phi_E) + \alpha A_{22}\cos(\omega_0 t + \phi_E - \delta)\big)\cos(\omega_0 t + \phi_E)\Big] \tag{2.20}$$

and

$$g_1\left(Z_E, \phi_E, \eta_E, \eta_I\right) = \frac{1}{\alpha \sin\delta}\Big[-\sigma_E \alpha \sin(\omega_0 t + \phi_E - \delta)\eta_E + \sigma_I \sin(\omega_0 t + \phi_E)\eta_I\Big] \tag{2.21}$$

$$g_2\left(Z_E, \phi_E, \eta_E, \eta_I\right) = \frac{1}{\alpha Z_E \sin\delta}\Big[\sigma_I \cos(\omega_0 t + \phi_E)\eta_I - \sigma_E \alpha \cos(\omega_0 t + \phi_E - \delta)\eta_E\Big]. \tag{2.22}$$

The equations above can be written in a more compact form as

$$\dot{X}(t) = f^{(}X) + g(X, \eta)\,, \tag{2.23}$$

with the following 2x1 matrix definitions: $X = \begin{bmatrix} Z_E \\ \phi_E \end{bmatrix}$, $f = \begin{bmatrix} f_1 \\ f_2 \end{bmatrix}$, $g = \begin{bmatrix} g_1 \\ g_2 \end{bmatrix}$ and $\eta = \begin{bmatrix} \eta_E \\ \eta_I \end{bmatrix}$. The stochastic averaging method (see **section (1.1.5)**) says that, under certain conditions (usually met for regular functions like f and g), the above system of two stochastic differential equations can be

approximated by the following 2-dimensional Markov process [187, 6]:

$$dX(t) = m(X)dt + h(X)dW(t)\,, \tag{2.24}$$

where m is a 2x1 matrix, h is a 2x2 matrix and $W(t)$ denotes a 2-dimensional vector of independent Wiener processes with unit variance. Also, m and h are respectively $O(\epsilon^2)$ and $O(\epsilon)$ functions defined as:

$$m = T^{av}\Big(E\{f\} + \int_{-\infty}^{0} E\Big\{\Big(\frac{\partial g}{\partial X}\Big)_t (g)_{t+\tau}\Big\}d\tau\Big) \tag{2.25}$$

$$h(h^{'}) = T^{av}\Big(\int_{-\infty}^{\infty} E\big\{(g)_t((g)^{'})_{t+\tau}\big\}d\tau\Big) \tag{2.26}$$

Here $(')$ denotes transposition, and $\Big(\frac{\partial g}{\partial X}\Big)_t$ is a 2x2 Jacobian matrix. Moreover, $E.$ denotes the expectation operator and T^{av} is the time averaging operator defined by

$$T^{av}(.) = \frac{1}{T_0}\int_{t0}^{t0+T0} (.)dt \tag{2.27}$$

where $T_0 = \frac{2\pi}{\omega_0}$ is the period of a gamma oscillation cycle. When evaluating the expectations in the stochastic averages formula, the elements of X are treated as constants in time. A somewhat lengthy calculation leads to the resulting Markov processes for the LFP envelope and phase:

$$dZ_E(t) = \Big(-\nu Z_E(t) + \frac{D}{2Z_E(t)}\Big)dt + \sqrt{D}dW_1(t) \tag{2.28}$$

$$d\phi_E(t) = \frac{\sqrt{D}}{Z_E(t)}dW_2(t) \tag{2.29}$$

Note that the coefficient D is zero when both the excitatory and/or inhibitory noise intensities σ_E and σ_I are zero. One can call it a noise-induced coefficient in the drift part of the stochastic differential equation for the envelope.

For computational purposes, the envelope and phase equations above can be rewritten using two

independent Ornstein-Uhlenbeck (OU) processes as:

$$dE_1(t) = -\nu E_1(t)dt + \sqrt{D}dW_1(t) \tag{2.30}$$

$$dE_2(t) = -\nu E_2(t)dt + \sqrt{D}dW_2(t) \tag{2.31}$$

from which we can extract the envelope and phase:

$$Z_E(t) = \sqrt{E_1^2(t) + E_2^2(t)} \quad \phi_E(t) = \arctan\left(\frac{E_2(t)}{E_1(t)}\right). \tag{2.32}$$

These quantities satisfy the differential equations for Z_E and ϕ_E above. The envelope and phase processes are then the envelope and phase of two independent Ornstein-Uhlenbeck processes with the same parameters. Our simulations actually use these two OU processes, rather than the $Z_E - \phi_E$ equations above, in order to avoid the occurrence of negative values of Z_E. The corresponding equations for the inhibitory population are obtained from these ones by using the ratio and phase difference factors in Eq 2.13. This ratio and phase difference are to be interpreted as constant averaged quantities; they will fluctuate around these quantities in any finite realization.

Probability distributions in Figs 2.1 show that the dynamics obtained from SAM are statistically equivalent to those of the LNA. This suggests that our SAM is an appropriate framework for envelope and phase dynamics of bursty gamma oscillations

2.2.3 Probability density and Mean First Passage Times (MFPT)

For simplicity, we consider the envelope of the excitatory population and denote it $z(t)$. The envelope process with its initial condition is given by (see Eqs 2.28):

$$\begin{aligned} dz(t) &= \left(-\nu z(t) + \frac{D}{2z(t)}\right)dt + \sqrt{D}dW(t) \\ z(0) &= z_0\,. \end{aligned} \tag{2.33}$$

The associated Fokker-Planck equation for the probability density of $z(t)$, conditioned on the initial condition, is given by

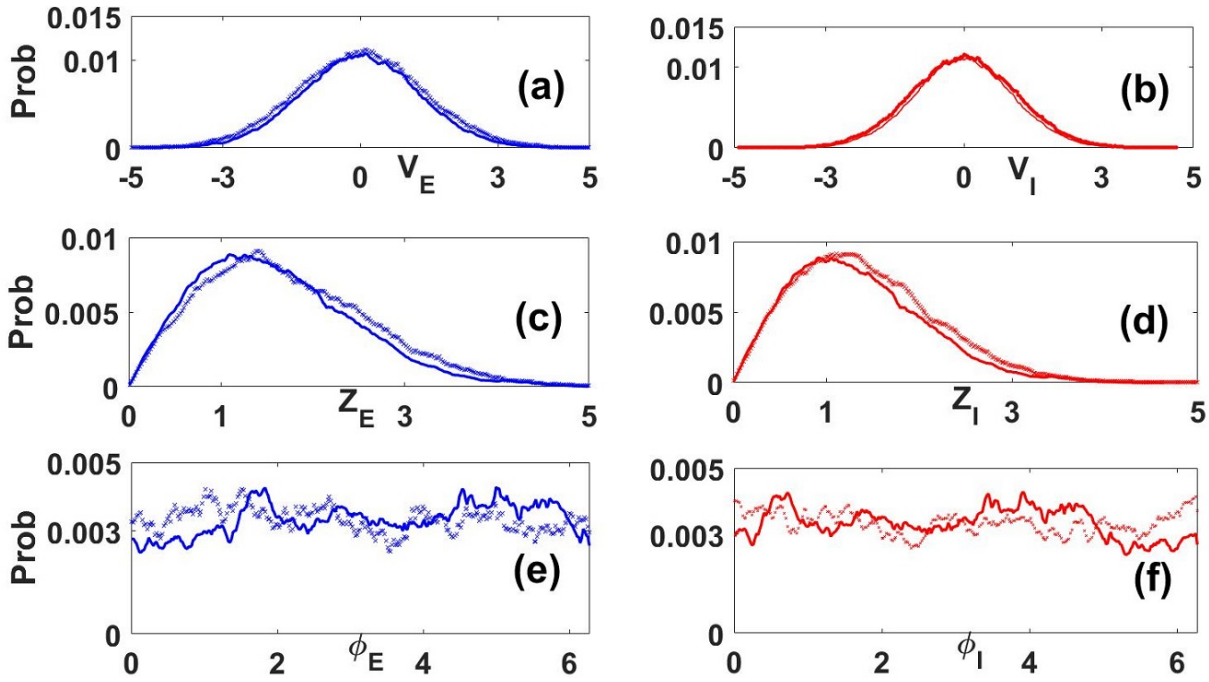

Figure 2.1: **Probability distributions of LFPs ((a) and (b)), envelopes ((c) and (d)) and phases ((e) and (f)) computed from LNA versus SAM.** Solid lines are distributions computed from LNA Eqs 2.10,2.11, while crossed lines are those computed from SAM Eqs 2.28,2.29 and Eq 2.16. Blues (a), (c) and (e) corresponds to excitatory components and reds (b), (d) and (f) to Inhibitory ones. We can observe good matching between LNA and SAM dynamics, this shows that the dynamics obtained from SAM are statistical equivalent to those in the LNA. The parameters are taken from Table 2.1.

$$\frac{\partial P(z,t|z_0,0)}{\partial t} = -\frac{\partial}{\partial z}\left[-\nu z + \frac{D}{2z}\right] P(z,t|z_0,0) + \frac{D}{2}\frac{\partial^2 P(z,t|z_0,0)}{\partial z^2}\,. \tag{2.34}$$

In the stationary limit, this reduces to the differential equation

$$-\frac{d}{dz}\left[-\nu z + \frac{D}{2z}\right] P(z) + \frac{D}{2}\frac{d^2 P(z)}{dz^2} = 0\,.$$

The stationary probability function then reads

$$P(z) = \left(\frac{2\nu}{D}\right) z \exp\left(-\frac{\nu}{D} z^2\right). \tag{2.35}$$

The peak value is obtained by imposing

$$\left.\frac{dP(z)}{dz}\right|_{z=z^*} = 0 \tag{2.36}$$

which leads to

$$z^* = \sqrt{\frac{D}{2\nu}}\,. \tag{2.37}$$

Note that $z^* \equiv R$ in the main text. Properties such as the mean and standard deviation of $z(t)$ can be easily computed from the stationary probability density function, and are known for decades as properties of the Rayleigh distribution [207]. The mean and the standard deviation are given by:

$$E[z] = \sqrt{\frac{\pi}{2}}z^* \quad \text{and} \quad std[z] = \sqrt{E[z^2] - E[z]^2} = z^*\left(\sqrt{\frac{4-\pi}{2}}\right)\,.$$

A burst is defined as an epoch during which the envelope process stays above a particular threshold (see Fig 2.2). A full theoretical treatment leading to the density of such epochs - known as residence times - is mathematically very involved and beyond the scope of this paper. Rather, here we resort to an approximate derivation of the properties of these epochs that yields some analytical insight into their parameter dependence. The burst duration can be seen to correspond roughly to the time the amplitude process spends reaching its maximum value after crossing the threshold from below, plus the time it spends from this maximum value until it crosses the threshold again but from above (see Fig 2.2). These two durations can be expressed distinctly by their associated Mean First Passage Times (MFPT). Generally, the MFPT from an initial condition z_0 to a specific border of an interval A where the amplitude process is confined is given by [91]:

$$T(z_0) = -\int_0^\infty t\frac{\partial}{\partial t}\int_A dz P(z,t|z_0,0)dt\,. \tag{2.38}$$

The MFPT also satisfies the following first-order differential equation [91]:

$$\left(-\nu z_0 + \frac{D}{2z_0}\right)\frac{dT(z_0)}{dz_0} + \frac{D}{2}\frac{d^2T(z_0)}{d^2z_0} = -1\,. \tag{2.39}$$

In our case, we define the interval where the process lies to be $A = [b, c]$ where b is the threshold defining the start and the end of a burst, while c is a "typical" maximum value that the envelope

process can attain during that burst. During the period when the envelope increases towards its maximum, an absorbing boundary condition is imposed at c leading to $T_1(c) = 0$, and a reflecting boundary condition is imposed at b, given by $\left.\frac{dT_1(z_0)}{dz_0}\right|_{z_0=b} = 0$. This results in the following expression for the "first" MFPT on the way up:

$$T_1(z_0) = \frac{e^{\left(-\frac{\nu}{D}b^2\right)}}{2\nu}\left[Ei\left(\frac{\nu}{D}c^2\right) - Ei\left(\frac{\nu}{D}z_0^2\right)\right] - \frac{1}{\nu}\log\left(\frac{c}{z_0}\right) \tag{2.40}$$

where Ei is the integral exponential function defined as [101] :

$$Ei(x) = -\int \frac{e^x}{x}dx\,.$$

Further, assigning the threshold value b to the initial condition of an above-threshold epoch, then the first MFPT is given by

$$T_1(b) = \frac{e^{\left(-\frac{\nu}{D}b^2\right)}}{2\nu}\left[Ei\left(\frac{\nu}{D}c^2\right) - Ei\left(\frac{\nu}{D}b^2\right)\right] - \frac{1}{\nu}\log\left(\frac{c}{b}\right)\,. \tag{2.41}$$

To compute the time interval for the process to leave its maximum value and cross the threshold from above, a reflecting boundary condition is now set at c, which translates into $\left.\frac{dT_2(z_0)}{dz_0}\right|_{z_0=c} = 0$, and an absorbing condition at b, $T_2(b) = 0$. The associated "second" MFPT is then given by

$$T_2(z_0) = \frac{e^{\left(-\frac{\nu}{D}c^2\right)}}{2\nu}\left[Ei\left(\frac{\nu}{D}b^2\right) - Ei\left(\frac{\nu}{D}z_0^2\right)\right] + \frac{1}{\nu}\log\left(\frac{z_0}{b}\right)\,. \tag{2.42}$$

We now assign $z_0 = c$ and the second mean duration is

$$T_2(c) = \frac{e^{\left(-\frac{\nu}{D}c^2\right)}}{2\nu}\left[Ei\left(\frac{\nu}{D}b^2\right) - Ei\left(\frac{\nu}{D}c^2\right)\right] + \frac{1}{\nu}\log\left(\frac{c}{b}\right)\,. \tag{2.43}$$

Therefore, the approximated burst duration is given by $T = T_1(b) + T_2(c)$, which simplifies to

$$T = \left(\frac{1}{2\nu}\right)\left[\exp\left(-\frac{1}{2}\left(\frac{b}{R}\right)^2\right) - \exp\left(-\frac{1}{2}\left(\frac{c}{R}\right)^2\right)\right]\left[Ei\left(-\frac{1}{2}\left(\frac{c}{R}\right)^2\right) - Ei\left(-\frac{1}{2}\left(\frac{b}{R}\right)^2\right)\right], \tag{2.44}$$

Were we have used the relation $R = \sqrt{\frac{D}{2\nu}}$

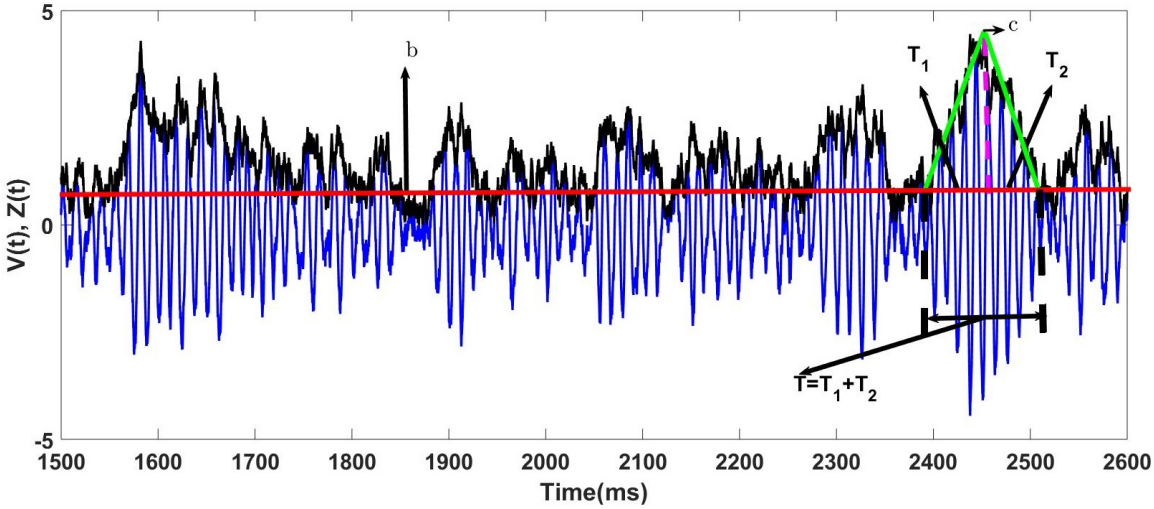

Figure 2.2: **Typical burst duration following our approach.** Computation of the mean burst duration. The green bars show the increase and decrease of the envelope process in black. The vertical dashed magenta line shows the separation between the two mean first passage times. The red bar sets the value of the threshold b. A typical burst is the epoch during which the envelope stays above the threshold and the burst duration is the corresponding time.

While the choice of b and c are arbitrary, we found that satisfactory estimates of mean burst durations followed from choices that made intuitive sense. Specifically, we chose the threshold to be equal to half the median of the envelope density $P(z)$; this corresponds to setting $b = R\sqrt{\ln(2)/2} \approx 0.59R$. We choose the value of c as the mean of $P(z)$, i.e. $R\sqrt{\pi/2}$ plus one standard deviation $R\sqrt{(4-\pi)/2}$:

$$c = R\left(\sqrt{\frac{\pi}{2}} + \sqrt{\frac{4-\pi}{2}}\right).$$

This approximate analysis provides an estimate of the mean burst duration as a function of the synchronization parameter R. One could also choose a threshold that does not depend on R or any other parameter, but that would yield no bursts for smaller R values, even though close inspection of the smaller envelope reveals burstiness at the smaller scale.

Table

Parameters values used throughout this chapter, unless specified in the caption of certain figures.

Table 2.1: Model parameters, definition and value.

Parameter	Desription	value
α_E	decay rate of an excitatory cell	0.1 ms^{-1}
α_I	decay rate of an inhibitory cell	0.2 ms^{-1}
β_E	maximal firing rate of an excitatory cell	1
β_I	maximal firing rate of an inhibitory cell	2
h_E	External input to the excitatory population	-3.8
h_I	External input to the inhibitory population	-8
W_{ee}	Recurrent excitatory synaptic coefficient	27.4
W_{ii}	Recurrent inhibitory synaptic coefficient	1.3
W_{ei}	Synaptic connection from inhibitory to excitatory cells	26.3
W_{ie}	Synaptic connection from excitatory to inhibitory cells	32
N_E	Number of excitatory cells	800
N_I	Number of inhibitory cells	200

2.3 Results

Our starting point is the work of Xing et al. (2012)[229]. They showed that for the specific case of bursty gamma rhythms, LFP's from macaque visual cortex are well modeled by a simplified version of the classic Wilson-Cowan (WC) rate model for reciprocally connected excitatory (E) and inhibitory (I) populations. The classic WC model (1972)[224], which accounts for oscillations in such EI networks, includes neurons with a graded response beyond threshold. Our goal is to characterize, both theoretically and numerically, the effect of system parameters including noise on bursting. However, the noise incorporated into the WC model in Xing et al [229] is not properly scaled with system size (i.e. with the number of neurons) as in recent theoretical work. Furthermore, the firing rate-versus-input characteristic for their neurons was a step function. This strong nonlinearity amounts to a less realistic two-state (active-inactive) description of single neuron function, and impedes analytical work. We therefore wish to use an improved version of their WC model, closer to the classic one and that allows us to formulate a theory in the first place. This requires a smooth nonlinearity with properly scaled noise. Applications of our approach to other LFP data including from humans are currently being pursued and will appear elsewhere. We therefore begin here by discussing why we focus on quasi-cycles, then show network simulations with two-state neurons to set the stage for the WC model we will use. This is because the network with two-state neurons has been shown to be well approximated by the WC model with smooth nonlinearities and system-size dependent noise (Wallace et al. 2011 [220]). Then we proceed with analyzing the bursty rhythm

properties of that model.

2.3.1 Network Model for stochastic gamma-band activity

Two principal types of computational models have been proposed to explain the variability, and in particular the bursts responsible for the fast temporal decorrelation of gamma rhythms seen *in vivo*. The first proposes that broadband gamma rhythms result from synchronous chaos, a form of randomness that does not rely on noise but rather on the nonlinear properties of the network and the external stimulus. This requires multiple PING or ING (Interneuron Network Gamma) circuits in the presence of strong long-range excitatory connections [13, 15]. The second type involves a single PING or ING circuit with a stable equilibrium, i.e. without noise all firing rates are constant; the operating regime must therefore be near the onset of oscillatory synchrony. The variability then results from the noise in the circuit [33, 229, 175]. We consider a simple model of this latter type, namely the network of stochastic spiking neurons in [220], where noise is due to the probabilistic transitions between quiescent and active states of single neurons. This noise vanishes when the network has an infinite number of cells. Intrinsic to the network, this noise reflects the probabilistic nature of spiking, with probability proportional to neural input, which mimics the biophysical reality of spontaneous and input-driven neural activity.

This simple network reproduces features such as bursts of population synchrony and irregular single neuron firing as seen *in vivo* and in more realistic networks. In addition, mean-field analysis [217] shows that such a network is a stochastic version of the well-known Wilson-Cowan firing rate model [224]. Average quantities like activities or LFPs can be described by analytical equations (see **Methods**), which is not generally possible for complex network models. This stochastic Wilson-Cowan model, like more complex biophysical network models [175], exhibits two oscillatory regimes. The ***Transient synchrony*** regime is one where noise is required to see oscillations, i.e. the noise induces them. In this regime, oscillations appear during transient epochs of network synchronization called "bursts" with varying lifetimes (Fig 2.3). In contrast, the ***High synchrony*** regime does not exhibit bursts for small noise; highly coherent oscillations occur in the absence of noise. The level of network synchronization is always high, and epochs of desynchronization are very rare. Moreover, the model can generate oscillations in several frequency bands (beta, gamma, and high gamma)

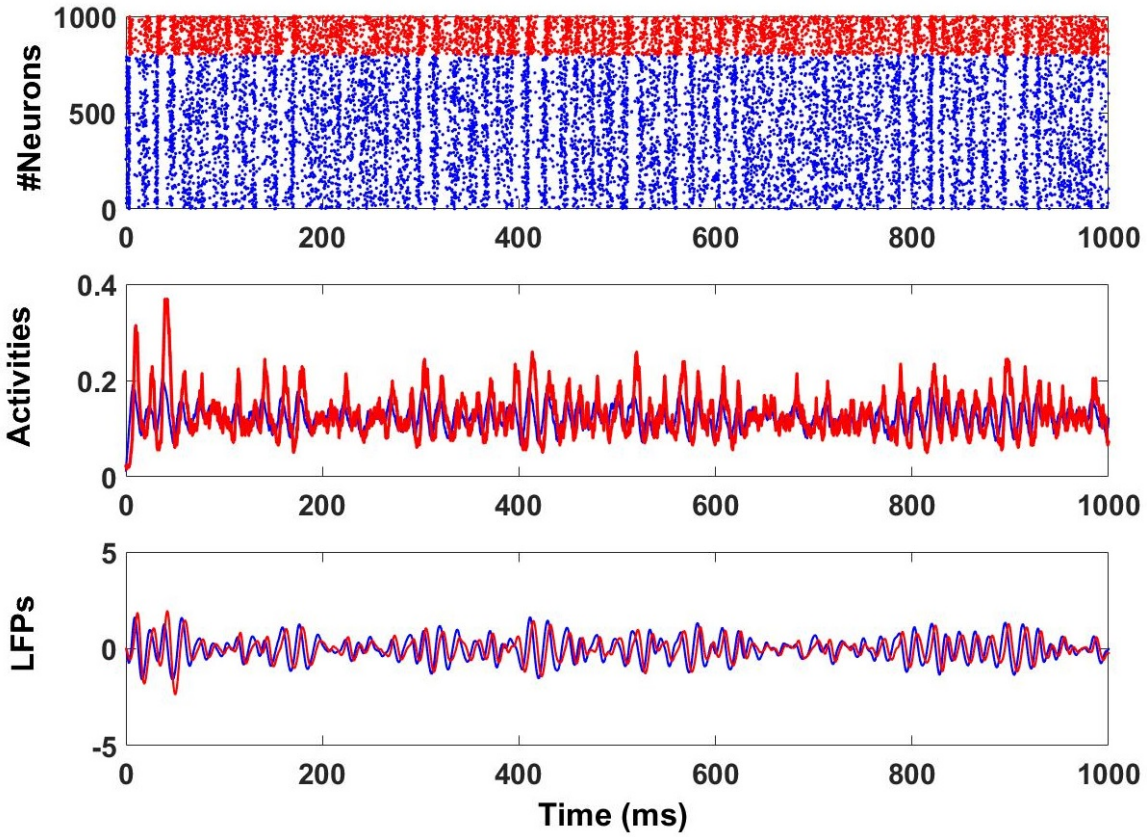

Figure 2.3: **Stochastic oscillatory rhythm generated by a recurrent stochastic Wilson-Cowan (E-I) network (see Methods) working in the transient synchrony regime. Top:** Raster plot. **Middle:** Excitatory $E(t)$ (blue) and inhibitory $I(t)$ (red) activities. **Bottom:** Excitatory (blue) and inhibitory (red) LFPs. They show epochs of high amplitude corresponding to synchronized activity followed by epochs of low amplitude corresponding to desynchronized or less synchronized activity. Excitatory and inhibitory activities and their corresponding LFPs display a slight phase difference. The raster plot and activities were simulated using the exact Gillespie algorithm [94, 220]). The LFPs were obtained by first removing the signal means from the respective excitatory and inhibitory activities, followed by filtering using a Butterworth second-order filter with a lower cutoff frequency of 20 Hz and upper cutoff frequency of 100 Hz. The parameters are taken in Table 2.1 excepted $W_{ee} = 25.3$.

and exhibits other non-oscillatory dynamics like the asynchronous regime . Direct simulations of the model use the exact Gillespie algorithm [93]. With parameters in the ***transient synchrony*** regime, it is possible to extract the activities of the excitatory and inhibitory populations and their corresponding LFPs (see Fig 2.3, lower panel).

2.3.2 Local Field Potentials (LFPs) can be described by stochastic linear equations

Recorded activities *in vivo* are usually filtered according to the frequency band of interest before analysis. Filtered activities are then considered as a measure of LFPs [41, 52]. A similar method can be applied to network activities extracted directly from numerical simulations Fig 2.3(**lower panel**). The filtering used here first removes the mean from any time-varying activity to keep the part induced by noise; broadband gamma activity *in vivo* has in fact been likened to filtered noise [40, 37, 229]. The zero-mean activity is then filtered using a bandpass filter with lower and higher cutoff frequencies in the gamma band limits Fig 2.3 (**Bottom**).

A similar result can be achieved analytically by deriving the dynamics of the stochastic parts of the activities. From mean field analysis [220, 26, 74], the dynamics of excitatory and inhibitory activities can be obtained in terms of the stochastic Wilson-Cowan equations, in which there is one (nonlinear) equation for each of the excitatory (E) and inhibitory (I) populations (**Methods**). The behavior of the E population is coupled to that of the I population and vice-versa. The linear stability analysis of the noise-free analogs of these equations (i.e. of the Wilson-Cowan equations) shows that many parameters lead to a stable fixed equilibrium (as we will see below). Oscillatory regimes correspond to the parameter ranges where the corresponding eigenvalues of the system are complex conjugates. If the real part of the eigenvalues is negative, the deterministic equations have damped oscillations; the corresponding stochastic Wilson-Cowan network operates then in the ***Transient synchrony*** regime (also know as the quasi-cycle regime) where oscillations, albeit irregular ones, are sustained by noise. This regime is very popular and has already been used to underlie frequency-specific, hierarchical corticocortical [162, 127] and thalamocortical [123] interactions, although with a reduced level of complexity. The analytical treatment in the present study might very well serve as a starting point to understand these large-scale interactions at a more fundamental level. If instead the real part of the eigenvalue is positive, the nonlinear deterministic equations exhibit coherent oscillations with almost constant amplitude and frequency; the stochastic network is then in the ***High synchrony*** regime where the noise has a relatively smaller effect. Mathematically, the transition from the transient to the high synchrony regime upon changing parameters corresponds to a Hopf bifurcation.

A Linear Noise Approximation (LNA) further yields a linear approximation to the stochastic

nonlinear dynamics for the LFPs [217, 220, 26, 74] :

$$\frac{d\tilde{V_E}(t)}{dt} = A_{11}\tilde{V_E}(t) + A_{12}\tilde{V_I}(t) + \sigma_E\eta_E(t) \quad (2.45)$$

$$\frac{d\tilde{V_I}(t)}{dt} = A_{21}\tilde{V_E}(t) + A_{22}\tilde{V_I}(t) + \sigma_I\eta_I(t) \quad (2.46)$$

The quantities $\tilde{V_E}$ and $\tilde{V_I}$ represent the excitatory and inhibitory LFPs respectively, and their time evolutions again depend on one another. The coefficients $A_{i,j}$ (i,j=1,2) and the noise strengths σ_E and σ_I all depend on the single cell and connectivity parameters of the original nonlinear system (**Methods**). The inputs η_E and η_I are two independent zero-mean Gaussian white noises. The LFPs, which are filtered, zero-mean versions of the activities, can also be seen here as filtered versions of two white noises driving the recurrent E-I network [229], where the filter parameters are the $A_{i,j}$'s.

The amplitudes of the LFPs directly simulated from the two coupled linear stochastic equations fluctuate stochastically [102]. The same is true for the frequency which also exhibits variability in the gamma band; not surprisingly, the E and I phases are stochastic. A closer inspection reveals that the epochs of nearly constant phase correspond to epochs of high LFP amplitudes (gamma bursts) [102]. Such noisy filtered signals exhibit the stochasticity and the bursting structure of recorded LFPs *in vivo* [40, 37, 229]. Moreover, analytical studies of these signals (**Methods**) reveal properties such as the approximately constant ratio of LFPs from E and I cells, and approximately constant phase differences [102].

The same properties are present in LFPs extracted directly from simulations of the full microscopic nonlinear network. Figure 2.4 presents properties of the envelopes and phases of the LFPs for this full nonlinear network, for its linear approximation using only two equations (Eqs.2.45,2.46), and corresponding theoretical predictions. This serves as a guide for the modeling hypotheses we make below to derive envelope-phase dynamics. It is clear that the envelope and phase properties for the full nonlinear network are in good agreement with those obtained from simulations of the linear stochastic dynamics (Fig 2.4 (a-b)). Frequencies present in the LFP have a mean in the gamma band (Fig 2.4 (c-d)); their distribution agrees well with that of the rhythms extracted from simulations of the full nonlinear network. LFP envelope distributions from the linear and nonlinear

systems are also in good agreement (Fig 2.4(e-f)). Thus LFPs generated using the simple linear stochastic equations are statistically similar to those extracted from the full nonlinear excitatory-inhibitory network, which themselves are similar to recorded LFPs *in vivo* [229]. Note that instead of considering a single LFP measure, namely the sum of the excitatory and inhibitory LFPs as is often done, here for completeness the two quantities are analyzed separately; they are linked by their ratio and phase difference as shown in Fig 2.4(a-b).

2.3.3 Envelope and Phase equations

We consider the coupled stochastic equations for the LFP dynamics in the transient synchrony regime. The goal is to derive equations governing the time evolution of the envelopes and phases of excitatory and inhibitory LFPs described in Eqs 2.45,2.46. We make three hypotheses about the LFP properties (Fig 2.4):

1. The distribution of the ratio between excitatory and inhibitory LFP envelopes is approximately Gaussian [102], as shown in Fig 2.4 **(a)**. Instead, a constant ratio is assumed, whose value equals the mean of the associated Gaussian distribution. This choice is made because in the PING model the numbers of E and I cells which fired during an oscillation cycle are almost proportional. This has been observed in a computational study of a more complex network [99] and *in vivo* as well [9].

2. The phase difference between excitatory and inhibitory oscillations is also approximately Gaussian [102] as observed in Fig 2.4 **(b)**. A constant phase difference is assumed, and made equal to the mean of the corresponding Gaussian distribution. This choice is based on the fact that the inhibitory neurons fire a small delay time after excitatory neurons during each oscillation cycle (this delay is smaller than the period of the oscillation), a known property of the PING model (Fig 2.3 bottom) [42, 220].

3. The frequencies of the excitatory and inhibitory LFPs have moderate variability but are also approximately Gaussian (Fig 2.4**(c-d)**); we choose the mean of those distributions as the mean LFP frequencies.

Without loss of generality, we seek an expression for the excitatory LFP in a sinusoidal form,

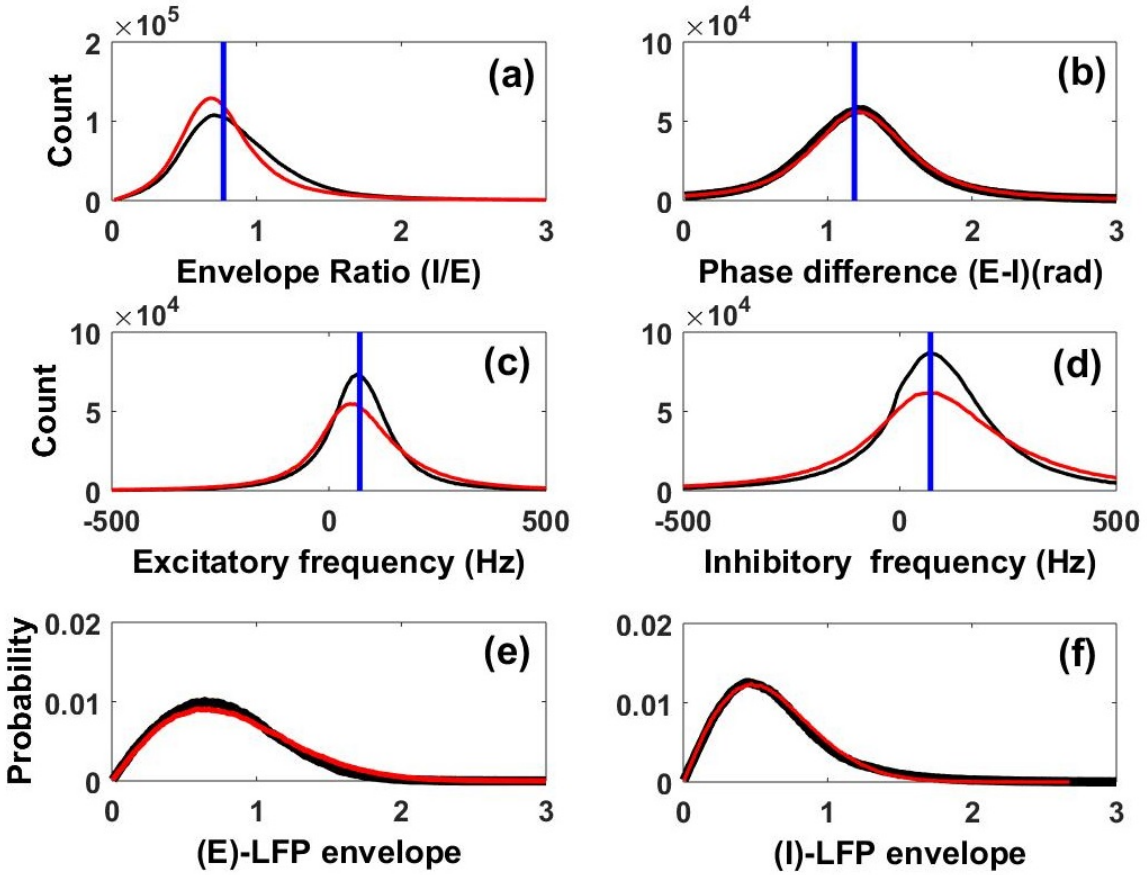

Figure 2.4: **Properties of analytic versus filtered LFPs.** Properties of the envelope and phase of the excitatory and inhibitory LFPs in Eqs2.45,2.46 obtained via the analytic signal technique (see Methods). Shown are the distributions of **(a)** the ratio of the envelopes of the inhibitory and excitatory LFPs (I/E), **(b)** the phase difference between E and I LFPs **(c)**, the instantaneous frequency of the excitatory LFP, **(d)** the instantaneous frequency of the inhibitory LFP, **(e)** the envelope of the excitatory LFP and **(f)** the envelope of the inhibitory LFP. For all panels, distributions in black come from exact numerical simulations of the full nonlinear stochastic Wilson-Cowan neural network with 2-state neurons (Fig 2.3 bottom panel), while those in red come from the approximate linear stochastic model, Eqs 2.45,2.46. In panels (a-d), the vertical blue lines represent analytical predictions of the means of those distributions (**Methods**). For panels (a-b), the means were computed using Eq 2.13, while for panels (c-d) we use the expression of ω_0 right after Eq 2.50. The instantaneous frequencies (Panels (e-f)) are obtained as in [102].

with an envelope $Z_E(t)$ and phase $\phi_E(t)$ and a constant mean frequency ω_0 to be defined below. The dynamics of the inhibitory LFP can be directly derived from this expression using the three assumptions above. The envelope ratio and phase difference between the excitatory and inhibitory LFPs are computed from the linear stochastic Eqs 2.45,2.46 as

$$\alpha \equiv \left\langle \frac{Env\big[\tilde{V_I}(t)\big]}{Env\big[\tilde{V_E}(t)\big]} \right\rangle \quad and \quad \delta \equiv \left\langle Arg\big[\tilde{V_E}(t)\big] - Arg\big[\tilde{V_I}(t)\big] \right\rangle \tag{2.47}$$

Here $\langle . \rangle$ can be considered a time average of the stochastic process in Eqs 2.45,2.46. The envelope Env is defined as the magnitude of the analytic signal associated with the LFP (see **Methods**). Likewise, $Arg[\tilde{V_E}]$ is the phase angle of the analytic signal. We choose to work with the excitatory LFP in the form

$$V_E(t) = Z_E(t)\cos\big(\omega_0 t + \phi_E(t)\big)\,. \tag{2.48}$$

We seek the functions $Z_E(t)$ and $\phi_E(t)$ by substituting Eq 2.48 into Eq 2.47 to first obtain their inhibitory counterparts, then inserting both into Eqs 2.45,2.46 and finally applying the *Stochastic Averaging Method* (SAM) (see **Methods**). This yields the following dynamics of the envelope and phase (see Eq 2.49-2.50):

$$dZ_E(t) = \left(-\nu Z_E(t) + \frac{D}{2Z_E(t)} \right) dt + \sqrt{D} dW_1(t) \tag{2.49}$$

$$d\phi_E(t) = \frac{\sqrt{D}}{Z_E(t)} dW_2(t) \tag{2.50}$$

where

$$\nu = -\frac{A_{11}+A_{22}}{2}, \quad \omega_0 = \frac{1}{2}\sqrt{-(A_{11}-A_{22})^2 - 4A_{12}A_{21}} \quad \text{and} \quad D = -\frac{A_{12}}{2\omega_0^2}\left(-A_{12}\sigma_I^2 + A_{21}\sigma_E^2 \right).$$

Here, $W_1(t)$ and $W_2(t)$ are independent Brownian motions (their time derivatives are Gaussian white noises), ν is the absolute value of the real part of the eigenvalues of the Eqs 2.45,2.46 with zero noise, and ω_0 is the peak frequency. The effective noise strength D in the envelope equation depends on the network coefficients governing the linear stochastic dynamics of the E and I populations, in particular on the two noise intensities. In the transient synchrony regime, D is either positive (A_{12}

is always negative, and A_{21} is always positive), or zero if both those intensities are zero.

Inspection of these dynamics reveals that the time evolutions of the envelope and the phase are both driven by noises. With $D = 0$, the envelope decays to zero, and the phase remains constant. This is again in agreement with the idea that gamma-band LFPs are close to filtered noise in this description. In particular, the envelope equation highlights the importance of noise for the appearance of bursts in the LFP dynamics.

Interestingly the dynamics of the envelope of the LFP is not coupled to that of the phase in this approximation; the reverse is not true, as the phase evolution depends on the envelope. The phase undergoes a Brownian motion with envelope-dependent intensity. In contrast with [102], our envelope-phase decomposition refers directly to all network parameters through ν and D and shows clearly the importance of the noise for the LFP dynamics. Consequently, it is easier with our description to investigate how different network parameters effectively shape the bursting structure of LFPs. In addition, our approach does not theoretically require the limitation $\nu/\omega_0 << 1$ as in [102]. In fact, we tested our approach for values of ν/ω_0 even close to one and found good agreement with the corresponding Eqs 2.45,2.46 (not shown).

Equation 2.49 is well-known in the statistics literature and is associated with the Rayleigh Process which describes the envelope of a periodic Gaussian process with uniformly distributed phase [91, 207]. It also finds applications in the theory of stochastic mechanical and seismic vibrations where it models the envelope of a damped harmonic oscillator sustained by noise [200]. Eqs 2.49,2.50 both represent the envelope and the phase of a 2-dimensional independent Ornstein-Uhlenbeck process with parameters ν and D see [91]. The uncoupling of the envelope and phase equations allows a derivation of certain statistical properties such as the joint probability of envelope and phase [200]. The dynamics of the inhibitory LFP can be easily recovered from Eqs 2.47-2.48 (see Eq 2.16 in Methods). Numerical simulations of LFPs derived from these envelope-phase equations show similar statistical properties as the simulated LFPs from the linear model driven by additive noise in Eqs 2.45,2.46 (see Figs. 2.5 and Methods).

From an experimental standpoint, it is of interest to know the proportion of time that the process spends near different envelopes. This can be obtained by computing the probability density for the process, either theoretically (if possible), or in an approximate form using numerical simulations of

the process. The density for the envelope can in fact be computed analytically as the stationary density of the Fokker-Planck equation Eq 2.34 obtained from Eq 2.49, namely Eq 2.35 in the **Methods** section:

$$P(Z_E) = \left(\frac{2\nu}{D}\right) Z_E \exp\left(-\frac{\nu}{D} Z_E^2\right). \tag{2.51}$$

The peak R of the stationary density of this noisy envelope process lies at

$$R \equiv \sqrt{\frac{D}{2\nu}}. \tag{2.52}$$

The peak value R, which is the most probable envelope amplitude value, will be used below as a measure of the degree of network synchronization. A low value of R reflects the fact that the network is poorly synchronized, and can't build up a strong oscillation; conversely, a high value of R implies a strong degree of network synchrony leading to strong oscillations in the recurrent circuit. One could use a more standard measure of the network oscillatory strength, such as a spectral coherence measure; generally we expect such measures to be proportional to R in this transient synchrony regime. But we have focused instead on a measure that is directly relevant to the envelope bursts.

We have thus provided a derivation for the envelope-phase dynamics for gamma oscillations in the transient synchrony regime that explicitly includes dependencies on all the parameters of the original full nonlinear model. The envelope-phase model is able to exhibit transient oscillations - and hence bursts - in other frequency bands by changing synaptic coefficients or synaptic time constants.

2.3.4 Envelope dynamics suggests distinct types of fluctuation amplification

Our envelope-phase equations depend on network parameters through ν and D which are functions of all the parameters of the original network model of the LFPs. We first investigate how these parameters lead to different network dynamics. We aim to understand this dependence in terms of connectivity parameters by varying two of them at a time while keeping constant the two others as well as all other parameters. In the plane of the parameters governing the strength of recurrent connections, (W_{ee},W_{ii}), we identify two easily separable regimes: transient synchrony and high synchrony (Fig 2.6 left panel). However, other dynamical regimes not reported here may also be present. The plane of the parameters governing feedforward connectivity, (W_{ei},W_{ie}), gives a more

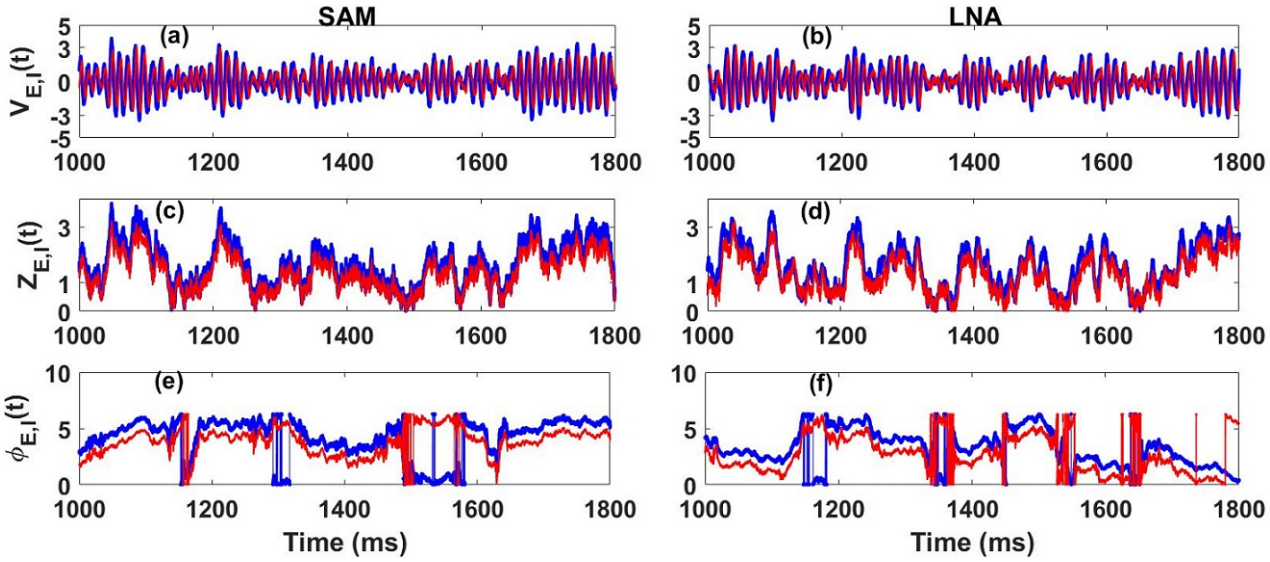

Figure 2.5: **Dynamics of the LFPs, their envelopes and their phases components from Eqs 2.45,2.46, Eqs 2.49,2.50 and Eq 2.48 (also Eq 2.16 in Methods). (a), (c) and (e):** LFPs, envelopes and phases from the Stochastic Averaging Method (SAM) Eqs 2.49,2.50 and Eq 2.48 (also Eq 2.16 in Methods). **(b), (d) and (f)**: LFPs, envelopes and phases from LNA Eqs 2.45,2.46. As in the previous figures, blue corresponds to excitatory components and red to inhibitory ones. In the SAM case, the envelopes and phases processes were simulated using two independent OU processes (see **Methods**, Eqs 2.30,Eq 2.34), integrated using the Euler-Maruyama method. The envelopes and phases dynamics in the LNA case were obtained by applying the Hilbert transform on the excitatory and inhibitory LFPs ($\tilde{V}_{E,I}(t)$).The parameters are taken in Table 2.1.

complex array of possible transitions, and involves a third regime: an asynchronous non-oscillatory state. Two types of transitions from transient synchrony can occur: one to a high synchrony regime via a Hopf bifurcation (an equilibrium gives way to a periodic activity pattern), and another to the asynchronous regime (Fig 2.6 right panel).

The value of R controls the magnitude of the envelope fluctuations, which in turn reflect different degrees of amplification of the white noise fluctuations that drive the E-I system. It also reflects the competition between the internal network noise and the deterministic oscillation. We can increase R by either decreasing the value of ν (which depends on A_{11} and A_{22}) at constant effective noise strength D, or increase the value of D at constant ν, or increase D while decreasing ν.

In the first scenario, decreasing ν increases the damping time of oscillations, i.e. they are longer-lived. This scenario affects both the amplification of the fluctuations, i.e. the burst size, as well as

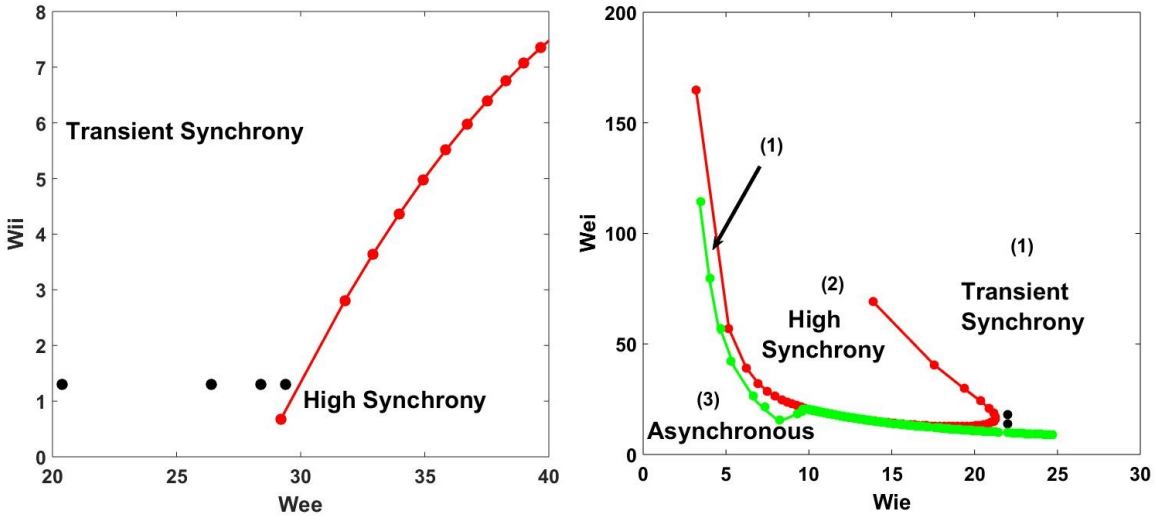

Figure 2.6: **Different dynamics of the stochastic spiking network in the parameter space. Left:** Recurrent plane (W_{ee}, W_{ii}). Black dots correspond to the four different values of the parameter R, obtained from left to right using the parameters (a) $W_{ee} = 20.4, \nu = 0.0648, D = 0.0512, R = 0.6288$. (b) $W_{ee} = 27.4, \nu = 0.0182, D = 0.0613, R = 1.2999$. (c) $W_{ee} = 28.4, \nu = 0.0110, D = 0.0613, R = 1.6900$. (d) $W_{ee} = 29.4, \nu = 0.0038, D = 0.0648, R = 2.9194$. **Right:** Feed-forward plane (W_{ie}, W_{ei}). Red and green curves with dots correspond respectively to the bifurcation lines between the transient and high synchrony regimes and the transient synchrony and asynchronous regimes. Left: The red bifurcation curve was plotted by setting $\nu = 0$ through linear stability analysis (see **Methods**, Eq 2.15). The transient synchrony regime then corresponds to the area $\nu < 0$ and the high synchrony regime to $\nu > 0$. Right: The red curve corresponds to the transition between the two oscillatory regimes as described in the Left case. The green curve corresponds to the case $\omega_0 = 0$ and the asynchronous regime corresponds to the case where $\nu < 0$. The two black dots in the right panel refer to two points at the same distance of the transition but at different frequencies (The diagram of frequencies is not displayed here). W_{ei} sets the strength of the feedback inhibition received by the excitatory population, and W_{ie} sets the strength of the feedback excitation received by the inhibitory population. And W_{ee} and W_{ii} are respectively recurrent excitation (excitation received by the excitatory population from itself) and recurrent inhibition (inhibition received by the inhibitory population from itself). For this right panel we have chosen $h_E = -7$ instead of $h_E = -8$ as in all other figures.

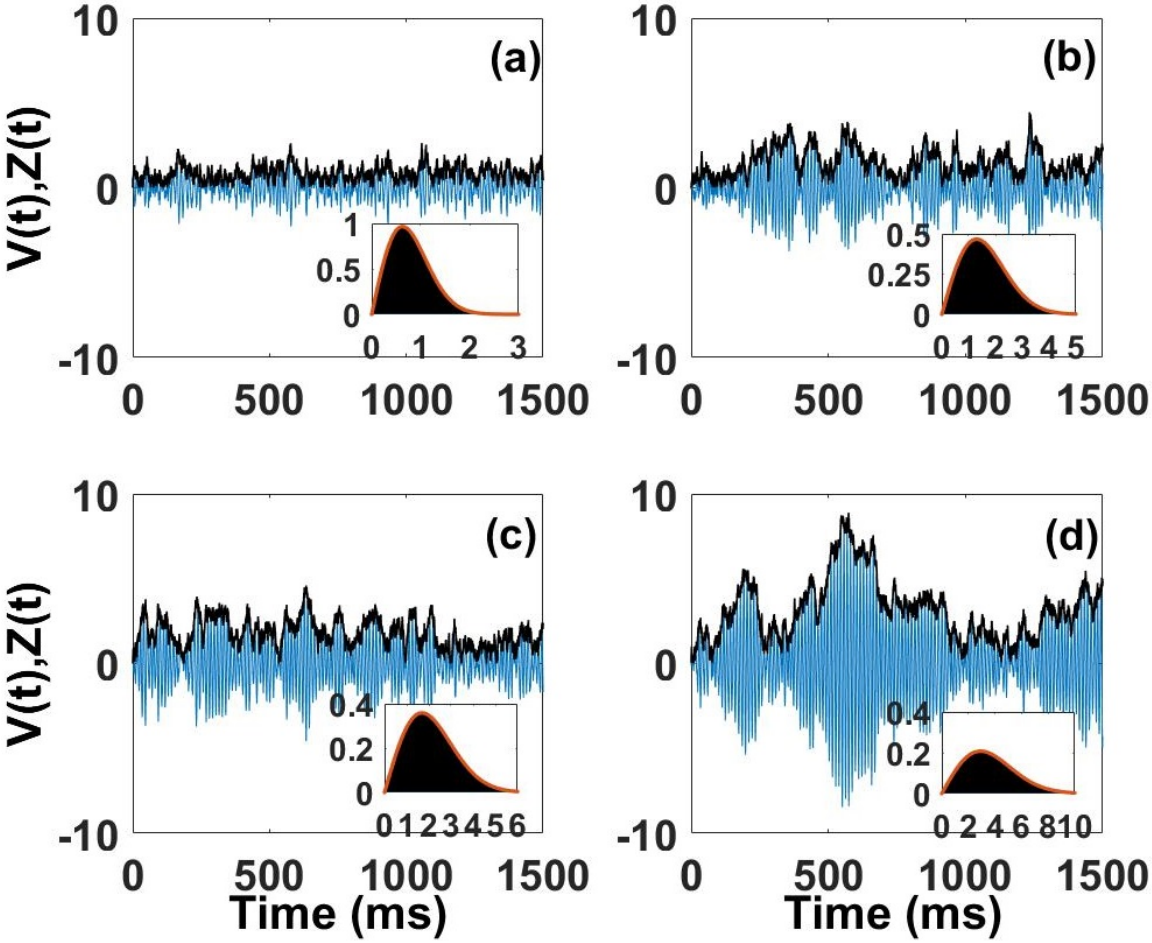

Figure 2.7: **Dynamics of the envelope fluctuations (black) and their associated LFPs (blue) for the same four parameter values used in Fig 2.6**:(a) R=0.6288, (b) R=1.2999, (c) R=1.6900, and (d) R=2.9194. Insets show the corresponding probability densities for these fluctuations, computed both numerically as well as analytically using Eq 2.35 (red curve). Note how the size of the fluctuations and their durations increase as R increases, i.e. as the network becomes more synchronized.

the duration of these amplifications, i.e. the burst duration; without fluctuations, the rhythm would just die out. Such envelope amplification has been observed both in computational studies and *in vivo* in another frequency band [181, 99]. A simple way to implement this scenario in our model is to increase the recurrent excitation. This reduces the value of ν without significantly changing D; this can be seen from the fact that ν clearly depends on W_{ee}, and D depends on W_{ee} through ω_0 (see expressions below Eq 2.50 and in **Methods**).

The second scenario corresponds to a different type of amplification since it does not change ν; it thus keeps the amplification duration constant. We do not detail this type of amplification; its complexity requires an elaborate treatment that goes beyond our study. We verified that feedback inhibition can cause the increase of D at constant ν (we do not detail it here; however the expression of D depends clearly on W_{ei} through A_{12}, see below Eq 2.50 and **Methods**). The third scenario is a mixture of the previous two.

The first scenario is appealing for our purposes since it yields rhythms similar to those seen in healthy and diseased states. We consider four points along a horizontal line in the recurrent plane of parameter space (Fig 2.6 left panel), lying increasingly closer to the transition between the transient and the high synchrony regimes. As R increases, so does the network synchronization (Fig 2.7), although the peak frequency of the rhythm stays around 85 Hz for our choice of parameters. Far from the transition, i.e. for a low value of R, there is a lack of synchronization (Fig 2.7(a)). The density of the envelope values has low variance (Fig 2.7(a) inset). But the mode of this density and the duration of bursts are likely too small to support reliable communication through coherent oscillations. The notion of burst itself is compromised as it is difficult to extract from the surrounding small fluctuations. In addition, a similar lack of synchronization is observed in patients suffering of schizophrenia (negative symptoms) [143, 142, 201]and constitutes one of the common markers of this pathology.

A working point too close to the transition, corresponding to a high value of R, leads to strong synchronization (Fig 2.7(d)). The broadness of the envelope distribution means high variability of the underlying amplitude value (Fig 2.7(inset)). Burst durations can last more than 1 second. However, it has been argued that such excessive synchronization could lead to the repetition of the same message and impede the transmission of other messages [80]. This could also destroy the

flexible routing of information observed when synchronization is more moderate [175]. Also, such long burst durations go counter to the fast temporal decorrelation of gamma band activity observed *in vivo* [136, 55]. They have been associated with dysfunctions resulting from an excess of excitation or lack of inhibition which lead to sustained high envelope amplitude as seen in epilepsy [82, 4, 223] or Attention Deficit Hyperactivity Disorder (ADHD)[232] .

Between these extremes, we show two working points with intermediate values of R (Fig 2.7 (b-c)). There we find moderate envelope values and burst durations (Fig 2.7(b-c)). This suggests an optimal brain state between excess and lack of synchronization. Here and below, we use the word "optimal" to describe a range of parameters, rather than a specific set of parameter values, for which the burst statistics resemble those seen in healthy recordings from the monkeys. We can in fact propose three regimes in the transient synchrony regime: a **noise-dominated** regime at low R, an **oscillation-dominated** regime at high R, and an **oscillation-noise** regime at intermediate values of R. We can then assign pathologies related to lack of synchronization to the **noise-dominated** regime, those related to excessive synchronization to the **oscillation-dominated** regime, and healthy states to the **oscillation-noise** regime. The fact that the **oscillation-noise** regime covers a range of parameters relates to the fact that different healthy subjects can exhibit different gamma amplitude modulations.

Along a vertical line in the (W_{ie},W_{ei}) parameter space (Fig 2.6 right), two points at a relative same distance to the transition line lead to rhythms that can differ significantly in their peak frequency (not shown). The amplitude modulations are however similar. Such points could correspond to separate brain states, such as awake or anesthetized, as reported in [229]. Our envelope-phase equations provide a simple explanation of how, in biophysical terms, different amplitude modulations of brain rhythms can relate to different brain states, assuming basic E-I connectivity.

2.3.5 Dynamics and statistics of Gamma bursts

Burst Extraction

We define gamma bursts formally as epochs where the envelope process is sustained above a specific threshold. The corresponding burst duration is, therefore, the time the process spends above that threshold. Burst durations recorded *in vivo* have short mean values (on the order 100 ms). Our

envelope process is not coupled with the phase process and allows in principle the derivation of the mean burst duration in terms of mean first passage times (MFPT) away from the threshold and back to it. Our derivation (see Eq 2.44 in **Methods**) gives the following approximate mean burst duration in terms of network parameters:

$$T = \left(\frac{1}{2\nu}\right)\left[\exp\left(-\frac{1}{2}\left(\frac{b}{R}\right)^2\right) - \exp\left(-\frac{1}{2}\left(\frac{c}{R}\right)^2\right)\right]\left[Ei\left(-\frac{1}{2}\left(\frac{c}{R}\right)^2\right) - Ei\left(-\frac{1}{2}\left(\frac{b}{R}\right)^2\right)\right],$$

with $b \approx 0.59R$ and

$$c = R\left(\sqrt{\frac{\pi}{2}} + \sqrt{\frac{4-\pi}{2}}\right) .$$

Here Ei is the exponential integral function, **b** is the threshold and **c** is an estimate of a typical maximal value that the process can reach during the burst.

Choosing the values of b and c to reveal burst characteristics regardless of the magnitude and durations scales of the fluctuations, as we did here, requires that these values be proportional to R. This enables the extraction of bursts and estimates of burst duration using a threshold and maximum value that scale with the mean size of the envelope fluctuations. Other choices are possible, but with this choice, the substantial variation of the burst duration is governed by the value of ν only (in the first scenario discussed at the end of the previous section). This choice would also work in the second scenario where D increases while ν is kept fixed, and the scenario where both covary.

Numerically, choosing a threshold for burst extraction is known as the $P_{episode}$ technique [49, 52, 166, 218]. This technique has the advantage that it easily detects bursts. However, it also has some limitations. The first limitation is the fact that the choice of the threshold quantitatively affects the results. The second limitation comes from the fact that, since the envelope process is a noisy signal, rapid fluctuations regularly occur that spend too little time above threshold to be considered as meaningful bursts. Such rapid fluctuations create false bursts and their consideration leads to biased exponential distributions for burst durations. To address the first point, we avoid choosing a value of threshold that is too small relative to the typical size of fluctuations, thereby averting most false bursts, or that is so high that several relevant bursts are excluded.

After choosing the threshold b, we deal with the second limitation by implementing a second

"threshold", or rather, second criterion: a fluctuation is considered a burst only if its envelope exceeds the mean of the envelope process for at least two oscillation cycles. This removes the artefactual short bursts, keeping only proper bursts. Further testing has revealed that changing the threshold value only modifies our results quantitatively rather than qualitatively. For example, increasing (decreasing) b slightly decreases (increases) the mode of the density of burst durations.

Gamma burst extraction in previous studies has been done using time-frequency analysis of the LFP. This involves thresholding the power of the smoothed version of the LFP. The advantage of those analyses is that they return both the burst duration and peak frequency content of the LFP. This usually allows one to compute marginal distributions of burst duration and burst peak frequency. From those distributions, one can calculate the mean burst duration and the mean burst peak frequency. Here, burst extraction using our criteria naturally returns a range of durations. Furthermore, to obtain the range of associated peak frequencies, we computed the corresponding peak frequency in each burst using the corresponding LFP epoch. With the set of burst durations and their corresponding peak frequencies, we can then compute the marginal distributions of the burst duration, their corresponding peak frequency, and their associated mean values.

Burst Duration and Peak Frequency: Mean and Variability

The mean burst duration observed *in vivo* is usually short (less than 100 ms on average) but its exact value varies depending on the brain state and animal subject, as well as the accuracy of the method used to extract bursts [37, 229]. A normal mean burst duration observed in data is in the range (60-150 ms) [37, 229]. The mean burst durations computed from marginal distributions and from Eq 2.44 vary across parameter space, and thus for the four R values of interest in our study (Fig 2.8). We observe an increase in the mean values as the transition between the transient and high synchrony regimes is approached (Fig 2.6 and insets). The precise values are respectively 35.00 ms (a), 74.50 ms (b), 112.25 ms (c) and 514.60 ms (d) for the four points in the phase parameters (see green and red vertical bars in Fig 2.8, computed from burst duration marginal distributions and from Eq 2.44, respectively). The durations computed in (b) and (c) fall inside the *in vivo* range. The duration of 35.00 ms calculated in (a) is too short and the corresponding envelope amplification too weak compared to *in vivo* recordings. Such short durations are not seen in healthy subjects, but

have been seen in psychiatric disorders such as schizophrenia. Further, the duration of 514.60 ms observed in (d) is too long, with a corresponding excessive envelope amplification uncharacteristic of healthy subjects.

Burst peak frequencies obtained in our analysis are characterized by their marginal distributions (not shown here). Unlike the burst duration distributions, the burst peak frequency distributions are approximately Gaussian. Also unlike the burst durations, the mean extracted from burst peak frequency distributions is roughly the same across the four cases (it is around 85 Hz). However, visual inspection suggests that burst peak frequency variability is reduced as the transition from transient to high synchrony is approached; this is confirmed by their distributions (Fig 2.8 insets). Indeed, burst peak frequency variability is an essential marker of gamma bursts in data. We define variability (peak-frequency deviation) as the difference between absolute peak frequency for the gamma burst and the mean peak gamma frequency, averaged across all of the gamma bursts [229]. We then numerically compute from long time series a distribution of peak-frequency deviation values, and quantify the spread of this distribution by a standard deviation. This latter deviation is thus a measure of the burst peak frequency variability. We computed the standard deviations for each of the four points in the space parameter. Their values decrease as we get closer to the transition between the two regimes. The exact values of these standard deviations are respectively SD1=19.1 Hz (a), SD2=8.1 Hz (b), SD3=5.4 Hz (c) and SD4=1.6 Hz (d). We compared these values for those observed in recorded data and found that the cases (b) and (c) gave relatively good agreement.

For illustration, mean burst duration and burst peak frequency variability measures computed from recording on an anesthetized monkey in [229] are respectively 65 ms and SD=8.8 Hz. These values are relatively close to our case in (b) where we have a mean burst duration and a burst peak frequency variability of 74.50 ms and SD=8.1 Hz respectively. Furthermore, data from awake and anesthetized monkeys suggests that variability decreases as mean burst duration increases. This is illustrated by a slight decrease in the burst peak frequency variability from SD=9 Hz to SD=8.8 Hz, following a small increase of the mean burst duration from 62 ms to 65 ms for an anesthetized and an awake monkey, respectively. This supports the relative weakness of our computed burst peak frequency variability (SD=5.4 ms) associated with a relatively high value of the mean burst duration (112.25 ms) in case (c) of our analysis. The burst peak frequency variability in cases (b)

and (c) are therefore more likely to be observed *in vivo*. For the case (a) the burst peak frequency variability SD=19.1 Hz is too high. In contrast, the case (d) shows a reduced variability SD=1.6 Hz, close to a highly coherent oscillation process. Such regularity disagrees with the stochastic nature of gamma-band oscillations observed *in vivo* [37].

Joint Distribution of Burst Duration and Peak Frequency

Next, we investigate the count of occurrences of a burst at a given oscillatory frequency with a specific duration. This is done using the joint distribution of burst duration and peak frequency [37, 229]. Such distributions are investigated over the same four values of R (Fig 2.9). The first case (Fig 2.9**(a)**) does not show any structure close to what is observed in the data, as the bursts are too short and frequencies quite high. In Fig 2.9**(d)** the joint distribution shows a mode corresponding to the mean burst duration of 514 ms and peak frequency around 85 Hz. However, the lack of variability of the burst peak frequency and the excessive burst durations associated with this process disqualifies it as a model of stochastic gamma oscillations observed *in vivo*.

The remaining cases (Fig 2.9**(b-c)**) are good approximations of observed gamma oscillations [37, 229]. They show modes corresponding respectively to mean burst duration and peak frequency similar to what has been done in previous computational and experimental studies [175, 37, 229]. We therefore conclude that there exists an optimal parameter range which reproduces the burst durations and their corresponding peak frequency variability observed *in vivo*. This region coincides with the **oscillation-noise** regime defined previously. This suggests that a mixture of intrinsic network noise and noise-free fixed point dynamics are needed to produce observed gamma oscillations. Indeed the two other regimes (noise-dominated and oscillation-dominated) both fail to reproduce *in vivo* data.

The theoretical expression of the mean burst duration Eq 2.44, through its direct dependence on R (note the prefactor $1/\nu$) can partially explain these normal, perhaps optimal brain states. In fact, we remark that choosing an optimal state in our model corresponds first to choosing ν such that its inverse falls inside or is near to the range (60-150 ms) of mean burst durations seen *in vivo*. Then, we need to make sure that the value of D is sufficient such that the value of the amplification strength R is high enough (and D needs to be not too small relative to ν, because values of D close to zero decrease R to zero). In our illustration, values of $(1/\nu)$ for the four increasing values of R

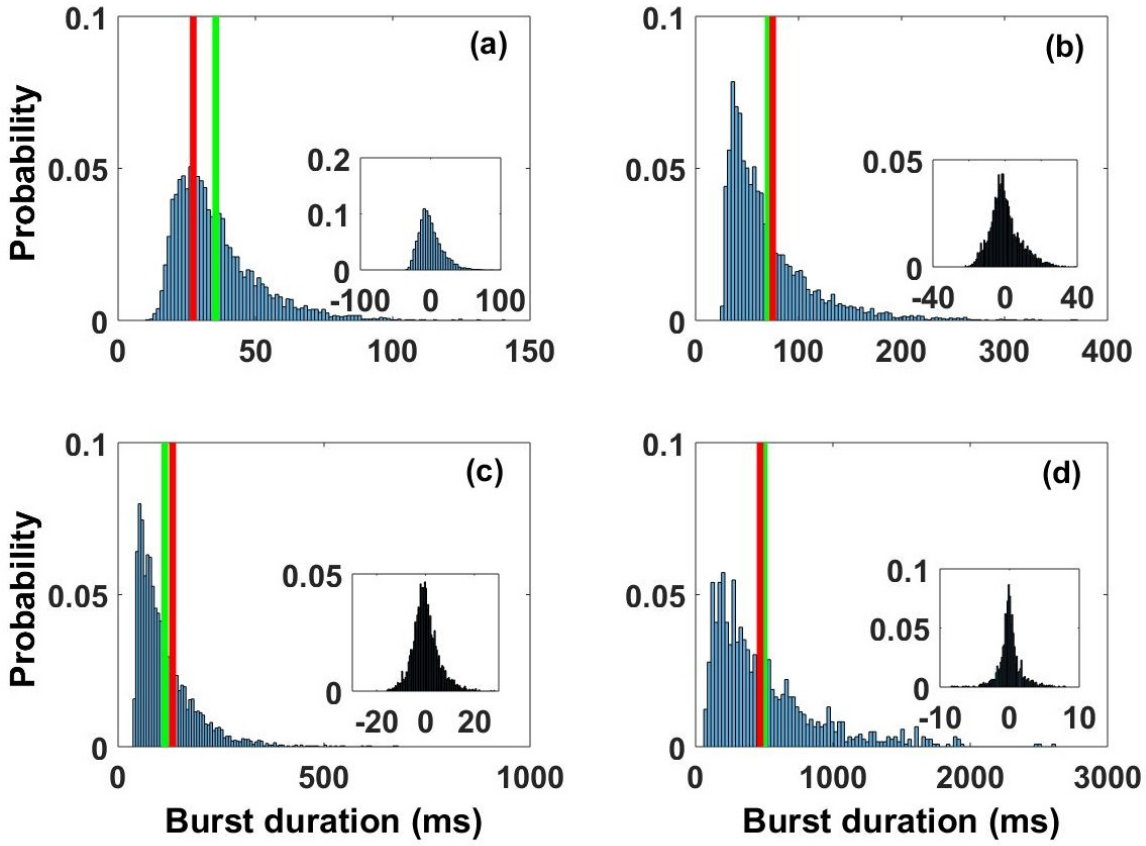

Figure 2.8: **Distributions of burst durations (histograms in blue), their corresponding means (vertical line in green) and theoretical mean values (vertical line red). Distributions in insets correspond to associated peak frequency variability in Hz**.Theoretical values were computed from Eq 2.44 and the value of c was chosen as the sum of the mean and the standard deviation of each envelope process (**Methods**). The four cases correspond respectively to different values of R in the previous figures, namely (a) R=0.6288, (b) R=1.2999, (c) R=1.6900, and (d) R=2.9194. The mean burst duration increases as we get closer to the transition between the high and transient synchrony regimes and the corresponding peak frequency variability decreases. The mean values computed from histograms (vertical green lines) are, respectively, 35.00 ms, 74.50 ms, 112.25 ms and 514.60 ms, and those from Eq 2.44 (vertical red lines) are 27 ms, 86.10 ms, 132.90 ms and 465.50 ms. The associated standard deviations of the peak frequency variability are respectively SD1=19.1 Hz, SD2=8.1 Hz, SD3=5.4 Hz and SD4=1.6 Hz. Furthermore, we observe mean burst durations with corresponding peak frequency variability in the range of the experimental observation for the two intermediate working points (b) and (c).

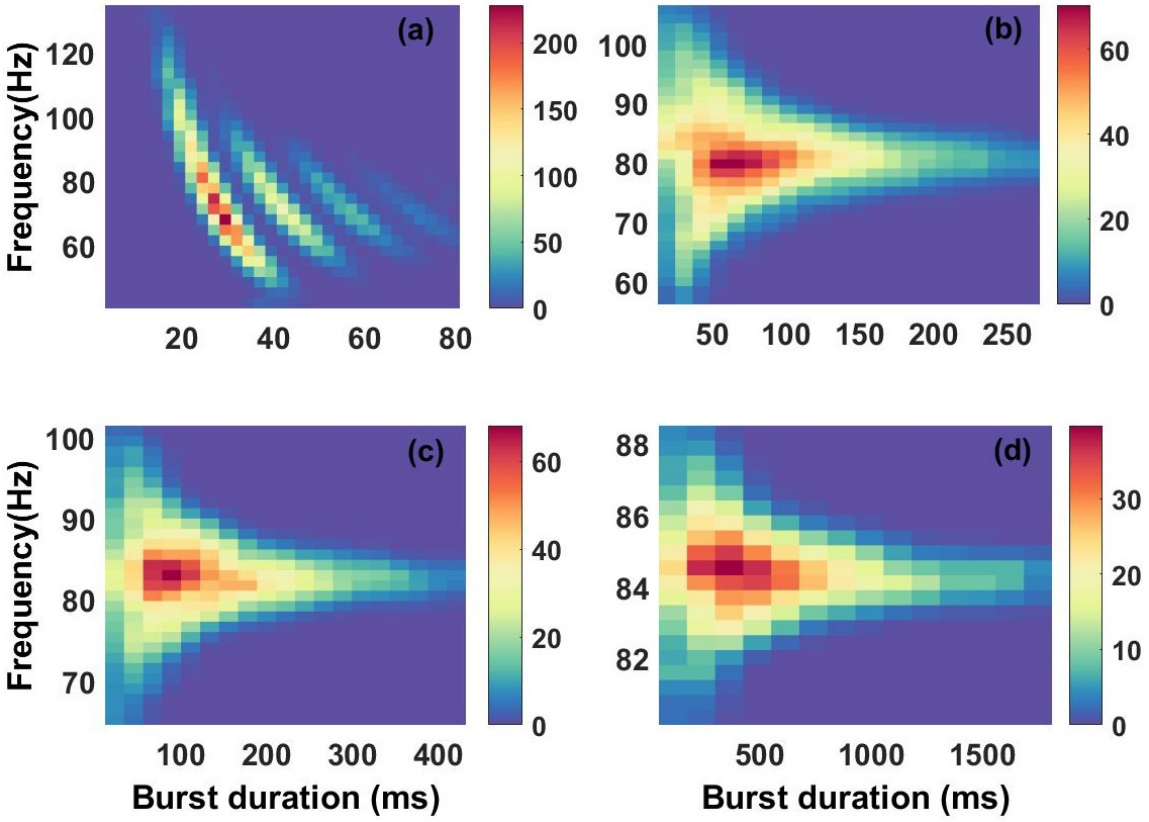

Figure 2.9: **Joint distribution of burst durations and burst peak frequencies.**The four cases correspond respectively to the four different values of R used in previous figures, namely (a) R=0.6288, (b) R=1.2999, (c) R=1.6900, and (d) R=2.9194. Panels **(b-c)** best represent the combinations of frequencies and burst durations seen experimentally.

are, respectively, 15.43 ms, 54.9 ms, 90.90 ms and 263.15 ms, and values of D are almost constant around 0.06, but not too small relative to values of ν. The values of $(1/\nu)$ in (a) and (d) are clearly away from the considered range. Also the value of $(1/\nu)$ of the paper of [229] is 66.67 ms and falls inside the normal range found here.

2.4 Discussion

We obtained an envelope-phase representation of broadband gamma oscillatory LFP's seen *in vivo*, and consequently of noisy rhythms in general, by considering a simple neural network in the PING

scenario with the essential properties of excitatory and inhibitory cell types. From numerical simulations of the excitatory and inhibitory LFP dynamics, we observed that their ratio of envelopes, their phase difference as well as their respective peak frequencies all follow approximately Gaussian distributions. This allowed us to link these LFPs together, and to consider just the excitatory LFP as the network LFP. We further applied the Stochastic Averaging Method (SAM) to extract evolution equations for the slow envelope of the LFP amplitude and the corresponding phase of the LFP in terms of the parameters of the original microscopic network. The distribution of frequencies in the LFP could also be derived from the phase dynamics. The envelope-phase equations depend on all single-neuron and network parameters, and are in agreement with these quantities extracted through the analytic signal technique based on the Hilbert transform of the LFP time series.

Under certain conditions, the envelope-phase equations produce dynamics that resemble recorded LFPs *in vivo*. The model therefore provides an appropriate theoretical framework for studying LFPs of rhythms and for our ultimate goal of characterizing burst dynamics in terms of all network parameters. We have followed our formulation for that latter purpose. While many parameters govern the E-I dynamics, surprisingly few combinations of those parameters actually determine the envelope and phase dynamics. We investigated how the envelope process evolves across the parameter subspace relating to connectivity. Specifically, we chose four points in that subspace below the bifurcation between the transient synchrony and high synchrony regimes, which appears most relevant to gamma bursts. We found that the amplification of noisy perturbations - seen in large excursions of the envelope, i.e. bursts - and the corresponding burst durations increase as the transition is approached.

In the close vicinity of the transition, envelope amplifications and their durations become excessive, with possible relevance to disorders such as epilepsy and ADHD [113]. Far away from the transition, the process appears more noise-like, with the envelope exhibiting weak amplifications with very short lifetimes. The lack of synchronization in this latter case is accompanied by a reduced spectral power at gamma frequencies, and is sometimes observed in patients with neurological disorders like schizophrenia [113]. Between these two points, the two other parameter sets yield moderate amplifications and durations. These provide a better match to modulations observed *in vivo*. This suggests that there is an optimal region in the parameter space where healthy dynamics lie.

2.4.1 Non-normal amplification as a mechanism for Gamma bursts?

We showed that burst generation can depend on ν by changing W_{ee}, and on D by changing W_{ei}. The notion of an optimal region for *in vivo* gamma bursts first requires that the inverse of ν falls inside or lies near the healthy range (60-150 ms). But this is not sufficient, since a value of D close to zero will lead to a value of R close to zero and therefore to very little amplification; decreasing ν further to recover some amplification then leads to burst durations outside the healthy range. Thus, the value of D also has a great importance for burst generation. The parameters ν and D appear to influence distinct types of amplification, but what types specifically?

While a full answer to this question exceeds the scope of our paper, we remark that amplification in the envelope process obtained by approaching the transition (through decreasing ν in our "first scenario") ressembles what is known as "normal amplification". Normal amplification results from the real part of the eigenvalues of the linear noise-free dynamics being small. Very close to the transition, the absolute value of the real part of the eigenvalues, i.e. ν, approaches zero. Consequently, the amplification scales as $\nu^{-1/2}$ (Eq 2.52), while the amplification duration is proportional to ν^{-1} (Eq 2.44). Therefore, bursts occur with explosive amplification and very long duration. Such amplification in a neural network is mostly induced by mutual excitation among neurons, resulting from strong recurrent excitation coefficients (Fig 2.6); recall that increasing W_{ee} makes ν tend toward zero, since A_{11}, which increases with W_{ee}, is positive and $A_{22} < 0$. In contrast, far from the transition, ν is not that small, and as a consequence, the corresponding normal amplification and its lifetime are smaller.

The two points in the middle correspond to sufficient normal amplification (not too weak and not too strong). This suggests that strong normal amplification does not agree with *in vivo* data. Furthermore, the value of D must be sufficient to avoid very weak amplification.

Interestingly, the amplification seen by increasing D at fixed ν (second scenario) may produce bursts that are compatible with those seen experimentally, as long as the values of ν are in the middle range mentioned above. Increasing D under these conditions has the advantage of increasing the burst magnitude without increasing burst duration. This corresponds better to the so-called non-normal amplification [213, 111, 110, 89]. Such amplification is believed to play an important role in selective amplification observed in cat primary visual cortex (V1) [174, 167]. It is also called

balanced amplification because it is associated with the stabilization of strong recurrent excitation by feedback inhibition [167]. This could be the dominant amplification used by a healthy brain to produce bursts in gamma and perhaps also beta rhythms, as long as ν is properly set to produce normal amplification. Therefore, the two types of amplifications may underlie healthy conditions.

2.4.2 Envelope-phase decomposition of more complex neural networks using SAM

Our study uses a network which does not model neurons with intrinsic voltage dynamics, and neglects the additional excitatory (AMPA and NMDA) and inhibitory (GABA-A) synaptic receptor dynamics [35]. Furthermore, noise is an intrinsic property in our network due to finite-size effects. But noise in real neural networks *in vivo* comes also from the constant bombardment of synaptic inputs, including those whose origin is outside the network [35]. Our approach could be applied to such detailed spiking networks given the approximate linear dynamics that have been extracted for those networks. For example, the Dynamic Mean Field (DMF) technique can be applied to more detailed realistic models [227, 65, 63]. DMF adequately approximates the temporal dynamics of the complex network by stochastic nonlinear equations close to our stochastic equations for the excitatory and Inhibitory activities (**Methods**) (Eqs 2.3,2.4). Such stochastic nonlinear equations can be further linearized around the stable fixed point; the resulting linear stochastic equations sustained by noise provide a fairly good approximation of the complex network dynamics [65, 63, 65]. Therefore for the purpose of studying gamma bursts in such realistic networks, it could suffice to tune parameters in the vicinity of the transient and high synchrony regimes, as in our study.The same can be said of neural field theoretic approaches with intrinsic noise to describe rhythms where linearization can be used to investigate spectra and the emergence of rhythms [119].

Rate dynamics can also be derived for conductance-based spiking networks [129]. Such dynamics can be linearized, and our envelope-phase decomposition can be fully applied. In fact, this is true for any spiking network which can be described by 2D rate equations or 2D activity dynamics. Our approach could further be extended to networks with complex topology, such as the 2D plane model of the primary visual cortex [130, 129], or to multiple coupled E-I networks [61, 63, 65]. The resulting dynamics can be used to study the effect of the feedback from extrastriate cortex on visual cortex [130, 129], phase-synchronization between brain rhythms [219, 152], inter-areal brain communication

[84, 86, 175], functional connectivity [45, 46, 61] or cross-frequency coupling more generally.

The extension of our model to beta rhythms may involve considering other mechanistic origins of the oscillations, such as thalamocortical loops. Likewise, bursty gamma rhythms may arise from inputs from extrastriate cortex [129]. Our method could be applied to the putative circuitry as long as the associated loop causes a damped oscillation.

It may be that bursts in one frequency range are the result of a cross-frequency interaction, i.e. between a fast rhythm and another slower rhythm both emerging from the feedback structure. Our modeling framework could still be used if the dynamics of the corresponding two networks are damped, i.e. with linearized dynamics having eigenvalues with negative real part and imaginary values corresponding to the two frequencies present.

Alternately, we could further develop our framework to describe the potential situation where a quasi-cycle in e.g. the gamma range is driven by a slower (e.g. beta) rhythm arising outside of the feedback loop. This would likely lead to stochastic amplitude-phase equations as we have described in our work, with the noise-induced rhythm being modulated by the time-dependent forcing. The mean frequency of the quasi-cycle would have to be significantly faster than the external forcing. Its mean amplitude would also have to be smaller than that of the quasi-cycle for the analysis to carry through to this driven case – otherwise, the external modulation could drag the fast rhythm in and out of the quasi-cycle regime. This analysis could be further developed to account for the transients that occur when this external input is switched on.

Preliminary simulations of a periodically forced gamma quasi-cycle reveal that the properties of the bursts change according to the frequency and the amplitude of the external input (not shown). The effect also depends on whether the forcing is applied to the excitatory population only, the inhibitory population only, or to both populations. The precise dependence of gamma burst properties on such external input parameters and network regimes is not a trivial problem, and our work in this direction promises to be a stand-alone hefty story.

2.4.3 Envelope-phase decomposition of an all-to-all delayed inhibitory network

We have also investigated broadband rhythms generated by a population of stochastic two-state neurons (as in Fig 2.3) but with all-to-all delayed inhibitory coupling. The delay and the proximity

of a Hopf bifurcation are necessary for the appearance of the quasi-cycles [34, 73], and differs from the ING mechanism. The same transition between transient synchrony and high synchrony occurs in that model as it does in our study based on the PING mechanism. We have verified numerically, using the Hilbert transform to extract the envelope of the rhythm, that a qualitatively similar behaviour of the burst magnitude and duration occurs in this inhibitory system as the transition is approached from the transient synchrony side (not shown). We also see an analogous optimal region in the subspace of parameter space spanned by the delay and the inhibitory coupling strength, where the variability in the burst duration and in the peak frequency during bursts resembles those seen *in vivo*. This further supports the generality of our result, in the sense that the essential determinants of the burst statistics are there again the presence of noise in the vicinity of a bifurcation to synchrony. Again, to understand rhythm bursts, our envelope approach could be applied to the linearizable formalisms that have been proposed for noise-induced rhythms and their spectra in this case such as [34, 73], and [120] in the spatio-temporal noise-driven neural field case.

Future work should also consider the statistics of bursts in the chaotic networks with long range excitatory connections that produce fast decorrelating gamma rhythms [13, 15], to see whether they exhibit qualitatively different features than those discussed here. And while our approach can easily be adapted to rhythms in other frequency bands, it does rely on linearization, and thus may not provide adequate descriptions of envelope and phase dynamics for all nonlinearities that underlie brain rhythms. One expects in those cases as well that our approach will provide a good first understanding of the parameter range underlying observed burst statistics, and what to do in case these statistics fall out of the healthy range.

Chapter 3

Brain Rhythm Are Enhanced by Multiplicative Noise

Abstract

Many healthy and pathological brain rhythms, including beta and gamma rhythms and essential tremor, are suspected to be induced by noise. This yields randomly occurring, brief epochs of higher amplitude oscillatory activity known as "bursts", the statistics of which are important for proper neural function. Here we consider a more realistic model with both multiplicative and additive noise instead of only additive noise, to understand how state-dependent fluctuations further affect rhythm induction. For illustrative purposes, we calibrate the model at the lower end of the beta band that relates to movement; parameter tuning can extend the relevance of our analysis to the higher frequency gamma band or to lower frequency essential tremors. A stochastic Wilson-Cowan model for reciprocally as well as self-coupled excitatory (E) and inhibitory (I) populations is analyzed in the parameter regime where the noise-free dynamics spiral in to a fixed point. Noisy oscillations known as quasi-cycles are then generated by stochastic synaptic inputs. The corresponding dynamics of E and I local field potentials can be studied using linear stochastic differential equations subject to both additive and multiplicative noises. As the prevalence of bursts is proportional to the slow envelope of the E and I firing activities, we perform an envelope-phase decomposition using the Stochastic Averaging Method (SAM). The resulting envelope dynamics are uni-directionally coupled to the phase dynamics as in the case of additive noise alone; but both dynamics involve new noise-dependent terms. We derive the stationary probability and compute power spectral densities of envelope fluctuations. We find that multiplicative noise can enhance network synchronization by

reducing the magnitude of the negative real part of the complex conjugate eigenvalues. Higher noise can lead to a "virtual limit cycle" where the deterministically stable eigenvalues around the fixed point acquire a positive real part, making the system act more like a noisy limit cycle rather than a quasi-cycle. Multiplicative noise can thus exacerbate synchronization, and possibly contribute to the onset of symptoms in certain motor diseases.

Neural signals recorded from the brain of patients suffering from motor dysfunctions can exhibit exaggerated oscillatory activity. Rhythms in healthy patients are not continually sustained, but rather appear in random epochs known as bursts. The duration, amplitude and frequency of such bursts are critical markers that increasingly help characterize the degree of dysfunction. Hence the study of bursts provides an additional tool towards understanding the origin and function of brain rhythms. At the microscopic level, the appearance of exaggerated bursts is believed to be the consequence of an increase in excitability of the cells as well as enhanced cellular connectivity. In this study, we model low-frequency brain rhythms in terms of fluctuations in the rhythm's slow envelope and phase. The increase in excitability of the cells is accounted for by including noise inside the response function of a single neuron. This analysis leads to two kinds of noise, called additive and multiplicative, which are shown to extend the epochs of network synchronization compared to previous, simpler analyses based solely on additive noise. More generally our study expands our understanding of how more realistic noise in neural circuits can generate and sustain brain oscillations in health and disease.

3.1 Introduction

Oscillations are recorded in brain of several species [41]. They are grouped depending on the values of their mean frequencies. Among the most prevalent are beta (13-30 Hz) and gamma (30-100 Hz) band oscillations. Certain important movement disorders like essential tremor actually occur around 5Hz. Gamma-band oscillations have been linked to inter-areal communication [83, 85, 175], neural computation and working memory [154, 153], and their dysfunction associated to epilepsy and Alzheimer's disease. Beta-band oscillations play an important role in motor function [80, 79, 146] and working memory [154, 153] and their dysfunction is most dramatically seen in Parkinson's disease (PD) that affects the sub-thalamic nuclei [47, 147, 60]. Other brain oscillations include the slower delta (0.5-3.5 Hz), theta (3.5-7 Hz) and alpha (7-13 Hz) rhythms [41]. Slightly below the beta range is that of essential tremor (ET) [71], which can occur at the same time as PD, yet originates in thalamic structures (with paths through the cortex) without self-inhibition. Based on that study of ET, self-inhibition is actually excluded below to simplify our analysis; self-connectivity of the inhibitory population can however be included with results qualitatively similar to those reported here.

In health, such rhythms often appear randomly as short epochs of synchrony called "bursts" (see Fig.1) [154, 80, 228]. Despite their variability, the rhythms can still be characterized by their distributions of burst duration and frequency content. The stochastic nature of such oscillations suggests an important role for noise in their generation and statistics. The goal of this paper is to develop our understanding of these bursts beyond linear models with additive noise.

Bursts are also used in another context in neuroscience, namely, single cell activity that consists of alternating phases of fast repetitive firing and quiescence. This differs from the bursts we focus on here, which occur at the population level and do not require such single cell dynamics. We further clarify the meaning of other terms that will recur below.

In this paper we are not simulating a network of cells, but rather only two population activity variables. These variables denote, respectively, the fraction of cell of a given type that are firing at any given time. The agreement between the dynamics of these variables and detailed network simulations has already been established [220]. That study also showed that higher network synchrony drives large amplitude oscillations. So while we consider only two population variables, we use "synchrony"

to denote strong collective firing which is reflected in large positive excursions in the two population activities.

Here an oscillation corresponds to the approximately periodically synchronized spiking of many cells. Several neurons fire together during a small interval of time, after which the network activity is low or "quiescent". Then the synchronized firing repeats. Together these active and quiescent intervals, or phases, constitute an oscillation. The period of this oscillation is the sum of the durations of these two phases. The amplitude of the oscillation refers to the difference between the maximum number of neurons that fired during the active phase and the minimum number during the quiescent phase. When noise is present, this cycle-to-cycle difference will be averaged across many cycles. In a spiking neural network, one could quantify the amplitude by counting the actual number of spikes fired by neurons of a given type in every cycle.

While the dynamical behavior is not strictly periodic when noise is present, here the network oscillation is closer to periodic the weaker the noise is and the closer the system is to the limit cycle regime. If the system lies in the quasi-cycle regime, the amplitude, and to a lesser extent the period of the oscillation, are irregular, as a consequence of the fluctuations in the synchronized firings of the neurons. But without noise, the dynamics decay to a fixed point. The rhythm is characterized by short and randomly occurring epochs of random duration - typically three or four oscillation cycles - during which stronger synchronized spiking is observed followed by quiescence. Such epochs of high amplitude and more regular period are called "bursts"; they are separated by epochs of low amplitude associated with poor synchronization between the neurons.

We also refer to synchronization as the coordinated spiking of many neurons, regardless of whether such spiking events repeat at periodic intervals. The level of synchronization then corresponds to the number of neurons that fire together in a synchronization event. If the network now evolves in the limit cycle regime, oscillations are regular, and bursts are rare. at least in the weak noise limit. The level of synchronization during the active phase of the oscillation is again a measure of the amplitude, and is higher compared to the quasi-cycle regime.

Current models of bursty network oscillations suggest that without noise, of synaptic and/or other origin, the burstiness would disappear, and any transient would exhibit an underdamped behaviour back to some stable equilibrium [220, 228, 182, 71]. Noise is thus assumed to be a stochastic input

critical to trigger the oscillations, leading even to the assertion that rhythms may only be linearly filtered noise [228]. The context of those papers as well as of the current paper is an underdamped regime close to a Hopf bifurcation.

However, the mechanisms by which noise triggers population oscillations is slowly being developed, and important questions remain. Does noise act at the population level, and just population-averaged quantities like local field potentials (LFPs) feel it? Or is it important to consider the effect of noise on every neuron arising from e.g. its synaptic input? Much modeling work considers the first scenario [102, 182, 228], leading to additive noise-driven population activity. Here, we consider the latter scenario where noise is added to the input of the firing (or "input-output response") function of the neuron, thereby mimicking more closely synaptic noise, albeit in a population model context. The dynamics of the corresponding macroscopic quantities like the LFPs are now subject to multiplicative noise, which turns into both additive and multiplicative noise when the model nonlinearities are expanded to lowest order. This is a novel modeling direction for rhythm bursts observed *in vivo*.

Bursts can also be seen as temporary increases in the slowly-evolving amplitude of the oscillation, i.e. in the rhythm's "envelope". Thus a better understanding of burst dynamics and statistics may rely on an envelope-phase decomposition as an appropriate framework. Within this framework, a burst can be defined as the epoch where the envelope of an oscillation is moderate to large by some criterion. Such an envelope-phase decomposition has been recently performed in the gamma frequency range and in the scenario where noise is only additive [102, 182]. It is important to note that envelopes are a nonlinear feature of a system, and can be calculated analytically or numerically (e.g. via the analytical signal technique) for both linear or nonlinear narrowband systems generating fluctuating rhythms. The work on rhythm bursts can thus be seen as complementary to other efforts to understand the origin and processing of envelopes in neural systems [163], and in communication systems more generally.

Here we consider the scenario where noise acts as both additive and multiplicative. We chose model parameters that lead to the lower beta range, and in fact they could easily be tuned to bring them a bit lower into that of essential tremor with the same qualitative results - or higher into the gamma range. As in our previous study with purely additive noise [182], we use an analytical

technique, the Stochastic Averaging Method (SAM) [187], to calculate the envelope-phase dynamics. We also exploit again the constant amplitude ratio and phase difference which exists between the inhibitory and excitatory components in the deterministic limit. As in previous models with only additive noise, we find that the envelope dynamics are uncoupled from the phase dynamics to lowest order of approximation; this is generally possible if we replace the sum of two Wiener processes by another Wiener process.

We study the dynamics of the envelope depending on its distance to the bifurcation as previously. But in addition, we investigate the effect of noise type and intensity. Our results show again that the oscillations have larger mean amplitude and hence higher envelope values when we are close to the transition to the Hopf bifurcation, but this effect is amplified by multiplicative noise. Paradoxically, this noise acts like a deterministic synchronizing effect, in the sense that it increases the real part of the complex conjugate eigenvalues around the fixed point, and therefore pushes the system closer to the Hopf bifurcation. From the point of view of the slow envelope of the rhythm, this noise decreases the decay rate of the envelope to zero, enabling the noise to kick the envelope to larger values, thereby producing larger bursts. This can be seen as the creation of a "virtual limit-cycle" by the multiplicative noise, even though the noiseless system has a simple stable focus. The analysis below shows that the damping rate, i.e. the real part of the eigenvalues around the fixed point, can become positive when the noise strength is sufficient large.

The virtual limit cycle created is highly synchronized, but nevertheless exhibits random bursts. However, these bursts are long epochs of aberrant synchronization, compared to the healthier range of 150-200 ms [80]. Such long epochs of aberrant synchronization is often observed in patients suffering from Parkinson's diseases (PD) [211, 148]. The mechanism by which the multiplicative noise induces a virtual limit cycle here adds to the list of possible mechanisms underlying pathological bursts in ET, or through simple modifications of model parameters, PD or other motor dysfunctions.

The outline of our paper is as follows. We first present the nonlinear Wilson-Cowan model with synaptic noise. Expansion of this model to quadratic order yields a simplified model in which we thereafter neglect the nonlinearities but keep the additive and novel multiplicative noise terms. We discuss the Itô and Stratonovich interpretations of the resulting stochastic differential equations (SDE), pursuing to show analysis and results with the Itô one, and eventually discussing how the

Stratonovich one just reinforces our results. The oscillatory properties of these "LFP" dynamics are then presented. An envelope-phase reduction using the Stochastic averaging method is applied to the linear SDE with additive and multiplicative noise, revealing the novel effect of the multiplicative noise on the envelope and phase dynamics: at low noise one sees a noise-induced oscillation, i.e. a quasi-cycle, around an otherwise stable fixed point, and a higher noise causes the effective damping rate to become smaller, even positive, creating a stronger noise-induced limit cycle. Using Fokker-Planck analysis, a closed form expression for the stationary probability density of envelope fluctuations and for the peak of this density are obtained. A Discussion follows, which also comments on the possible relevance of our work for understanding pathological brain rhythms.

3.2 The Model

3.2.1 Expanding the stochastic Wilson-Cowan model

We consider the classical Wilson-Cowan model (WC) for oscillation generation. The model involves a population (E) of excitatory cells and another (I) of inhibitory cells. Each population is coupled to itself, and reciprocally (although not symmetrically) coupled to the other. The mean synaptic coupling strengths between excitatory cells and from inhibitory to excitatory cells are given respectively by W_{EE} and W_{EI}. Similarly, the mean synaptic coupling among inhibitory cells and from excitatory to inhibitory cells are W_{II} and W_{IE}, respectively. In addition, an excitatory cell receives an external stimulus composed of a constant bias h_E and a stochastic part η_E; likewise, every inhibitory cell also receives an external stimulus h_I plus a stochastic component η_I.

We are interested in the parameter regime where the deterministic dynamics have complex conjugate eigenvalues. Moreover, our main focus is on beta-band oscillations (13-30 Hz). The WC model is a good candidate for such oscillations; one precise biophysical justification can be found in [71]. The corresponding equations for the activities of the E and I populations are given by:

$$\frac{dE(t)}{dt} = -\alpha_E E(t) + \big(1 - E(t)\big)\beta_E f(s_E(t)) \tag{3.1}$$

$$\frac{dI(t)}{dt} = -\alpha_I I(t) + \big(1 - I(t)\big)\beta_I f(s_I(t))\,. \tag{3.2}$$

where $f(x) = 1/(1 + exp(-x))$ is the single neuron firing (or "response") function of its combined

excitatory, inhibitory and external synaptic inputs:

$$s_E(t) = W_{EE}E(t) - W_{EI}I(t) + h_E + \eta_E(t) \tag{3.3}$$

$$s_I(t) = W_{IE}E(t) - W_{II}I(t) + h_I + \eta_I(t)\,. \tag{3.4}$$

Note that the coupling coefficients W are positive by definition. Here $\eta_E(t)$ and $\eta_I(t)$ are Gaussian, potentially broadband noises of the Ornstein-Uhlenbeck (OU) type:

$$< \eta_E(t) >=< \eta_I(t) >= 0, \quad < \eta_E(t)\eta_I(t) >= 0$$

$$P(\eta_E) = \frac{1}{\sqrt{\pi\tau_E\Sigma_E^2}} \exp\left[\frac{-\eta_E^2}{\tau_E\Sigma_E^2}\right], \quad P(\eta_I) = \frac{1}{\sqrt{\pi\tau_I\Sigma_I^2}} \exp\left[\frac{-\eta_I^2}{\tau_I\Sigma_I^2}\right]$$

$$< \eta_E(t)\eta_E(t^{'}) >= \frac{\tau_E\Sigma_E^2}{2} e^{\frac{-|t-t^{'}|}{\tau_E}}, \quad < \eta_I(t)\eta_I(t^{'}) >= \frac{\tau_I\Sigma_I^2}{2} e^{\frac{-|t-t^{'}|}{\tau_I}}\,.$$

These OU processes satisfy the following stochastic differential equations:

$$\frac{d\eta_E(t)}{dt} = -\eta_E(t)/\tau_E + \Sigma_E\xi_E(t) \tag{3.5}$$

$$\frac{d\eta_I(t)}{dt} = -\eta_I(t)/\tau_I + \Sigma_I\xi_I(t)\,. \tag{3.6}$$

where $\xi_{E,I}(t)$ are Gaussian white noises, with the following properties:

$$< \xi_E(t) >=< \xi_I(t) >= 0, \quad < \xi_E(t)\xi_I(t) >= 0$$

$$< \xi_E(t)\xi_E(t^{'}) >=< \xi_I(t)\xi_I(t^{'}) >= \delta(t - t^{'})\,.$$

The excitatory and inhibitory OU noises have correlation times τ_E and τ_I, respectively. The Gaussian white noise limit for the E or I noise can be taken by letting $\tau_{E,I} \to 0$, $\Sigma_{E,I} \to \infty$ while keeping constant the noise intensity (i.e. the integral of the E or I OU noise autocorrelation function), i.e. $(\tau_{E,I}\Sigma_{E,I})^2 = (\sigma_{E,I})^2 = const$ [115] . The noise appears on the input of the response function of every single cell. This suggests that every single cell receives stochastic inputs. This differs from the usual modeling approach where the stochastic inputs are added to the E and I

dynamical equations [220, 182, 71]. In these latter models, such noise has been added to simply account for stochastic effects, but has also been used to describe finite size effects (with state-dependent amplitude), vanishing in the limit of an infinite network. In that latter case, it is an emergent property which is felt by macroscopic quantities like the LFPs in each population.

Here, we wish to treat the case where noise acts directly at the microscopic level, accounting mainly for the stochastic synaptic input to each neuron. Such a description is also of interest in practical stimulation contexts such as non-invasive and deep brain stimulation [67], during which the synaptic bombardment of individual neurons is ongoing. In the WC model, individual neurons are not represented, but rather the activity of a population as a whole; yet the effect of synaptic noise can be approximated in the same way by including it in the response function.

We performed numerical simulations of the case described by Eqs.(3.1)-(3.2) with colored noises described above. The noise-free ($\Sigma_E = \Sigma_I = 0$) dynamics are assumed to have a stable focus fixed point (E_0, I_0). We are interested in the deviations from such a fixed point induced by noise. The simulations consist of the excitatory $(E(t) - E_0)$ and inhibitory $(I(t) - I_0)$ deviations time series Fig. 3.1-(a) and the spectrogram of the excitatory deviation Fig. 3.1-(b). The results of such simulations show stochastic oscillations appearing as short epochs of sustained activities (both excitatory and inhibitory). These transient epochs of sustained activities are clear representation of bursts as observed in Fig. 3.1-(a). The spectrogram Fig. 3.1-(b) is an efficient way to highlight the bursting structure of quasi-cycle oscillations. The spectrogram returns the transient nature of the envelope of the excitatory deviation $E(t) - E_0$. However, it does not give the dynamics of the envelope of the process and does not allow analytical treatment. An appropriate framework for theoretical purposes is the envelope-phase dynamics of the process $E(t) - E_0$.

To obtain such envelope dynamics of the deviation processes described in Fig. 3.1-(a), we look for solutions of Eqs.(3.1)-(3.2) in the form:

$$E(t) = E_0 + V_E(t)\,, \qquad I(t) = I_0 + V_I(t)\,. \tag{3.7}$$

The corresponding deviations $V_E(t)$ and $V_I(t)$, that we consider as measures of Local Field Potential (LFPs), are obtained here by Taylor expansion of the sigmoidal functions to first order as follows,

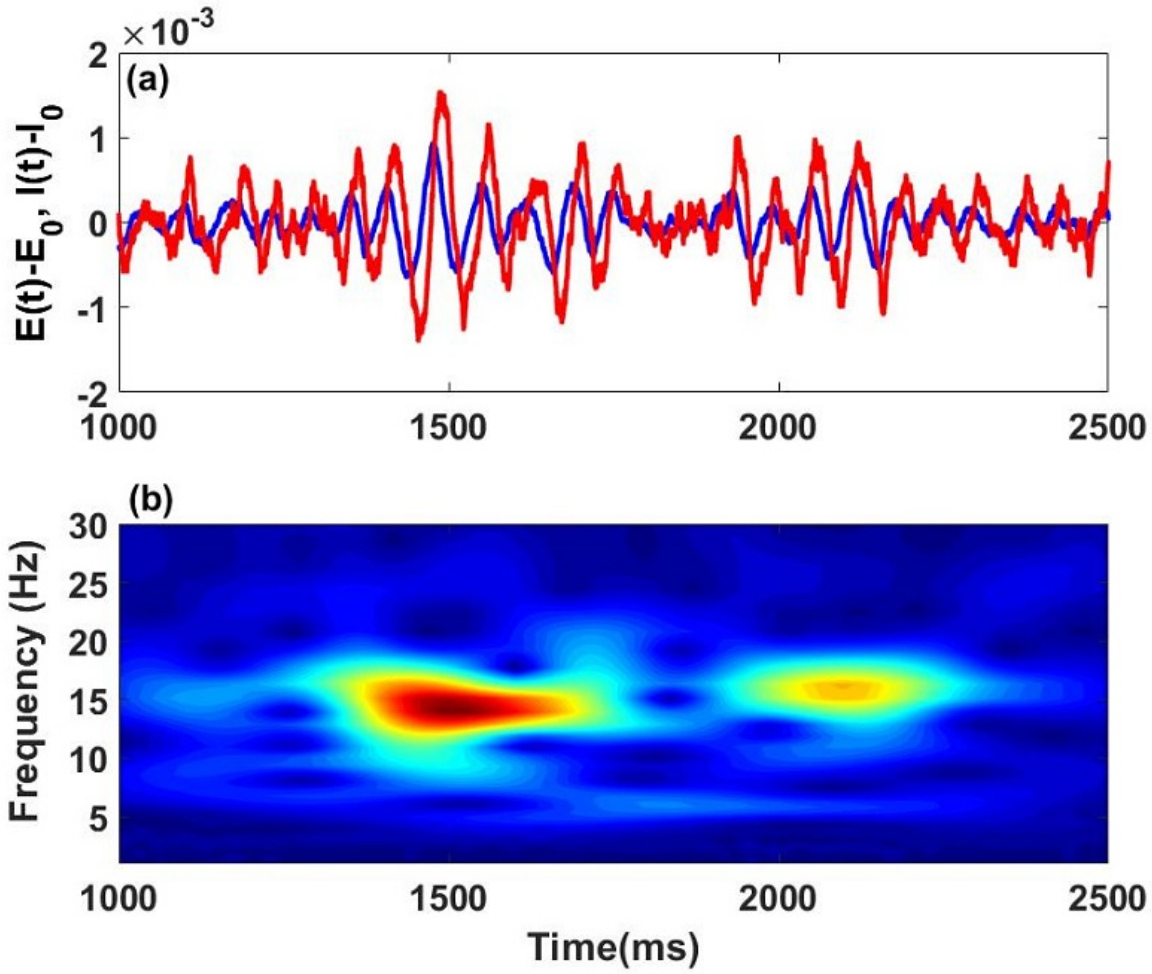

Figure 3.1: **Low frequency oscillations in the Stochastic Wilson-Cowan model Eqs.(3.1)-(3.2). (a)** Time series of the excitatory (blue) and inhibitory (red) deviations from equilibrium $E(t) - E_0$ and $I(t) - I_0$ respectively, computed from Eqs.(3.1) and (3.2). A smoothing second-order Butterworth filter was applied to the noisy oscillations beforehand. **(b)** Time-frequency description of the excitatory deviation $E(t) - E_0$. The transient nature of the oscillations is seen, especially in the form of two bursts around 1500 and 2000 ms. Bursts also stand out in the spectrogram as epochs when the power of the oscillation is large (warmer colors). Parameter values are: $W_{EE} = 27.4, W_{II} = 0, W_{EI} = 26.3, W_{IE} = 27, h_E = -3.8, h_I = -8, \alpha_E = 0.02ms^{-1}, \alpha_I = 0.04ms^{-1}, \beta_E = 1$, and $\beta_I = 2$. For this set of parameters, the system lies in the quasi-cycle regime. External OU processes are close to Gaussian white noises, with parameters $\tau_{E,I} = 0.1ms$, $\Sigma_{E,I} = 0.01ms^{-1/2}$. Numerical simulations were made using an Euler-Maruyama scheme with a time step of 0.025 ms. The same numerical scheme with the same time step was used for all other figures.

$$f(s_{E_0} + \delta s_{E(t)}) = f(s_{E_0}) + f^{'}(s_{E_0})(\delta s_{E(t)}) + O(\delta s_{E(t)})^2 \tag{3.8}$$

$$f(s_{I_0} + \delta s_{I(t)}) = f(s_{I_0}) + f^{'}(s_{I_0})(\delta s_{I(t)}) + O(\delta s_{I(t)})^2 \tag{3.9}$$

with

$$s_{E_0} = W_{EE}E_0 - W_{EI}I_0 + h_E, \quad s_{I_0} = W_{IE}E_0 - W_{II}I_0 + h_I$$

$$\delta s_{E(t)} = W_{EE}V_E(t) - W_{EI}V_I(t) + \eta_E(t), \quad \delta s_{I(t)} = W_{IE}V_E(t) - W_{II}V_I(t) + \eta_I(t)$$

The resulting dynamics are expressed as:

$$\frac{dV_E}{dt} = A_{EE}V_E + A_{EI}V_I + M_{EE}V_E^2 + M_{EI}V_EV_I + \big(a_E + b_EV_E\big)\eta_E(t) \tag{3.10}$$

$$\frac{dV_I}{dt} = A_{IE}V_E + A_{II}V_I + M_{II}V_I^2 + M_{IE}V_EV_I + \big(a_I + b_IV_I\big)\eta_I(t) \tag{3.11}$$

with the following definitions:

$$A_{EE} = -\big[\alpha_E + \beta_E f(s_{E_0}) - (1 - E_0)\beta_E f^{'}(s_{E_0})W_{EE}\big]$$

$$A_{II} = -\big[\alpha_I + \beta_I f(s_{I_0}) + (1 - I_0)\beta_I f^{'}(s_{I_0})W_{II}\big]$$

$$A_{EI} = -(1 - E_0)\beta_E f^{'}(s_{E_0})W_{EI}; \quad A_{IE} = (1 - I_0)\beta_I f^{'}(s_{I_0})W_{IE}$$

$$M_{EE} = -\beta_E f^{'}(s_{E_0})W_{EE}, \quad M_{IE} = -\beta_I f^{'}(s_{I_0})W_{IE}$$

$$M_{II} = \beta_I f^{'}(s_{I_0})W_{II}, \quad M_{EI} = \beta_E f^{'}(s_{E_0})W_{EI}$$

$$a_E = (1 - E_0)\beta_E f^{'}(s_{E_0}), \quad a_I = (1 - I_0)\beta_I f^{'}(s_{I_0})$$

$$b_E = -\beta_E f^{'}(s_{E_0}), \quad b_I = -\beta_I f^{'}(s_{I_0})$$

Note that Eqs.3.10, 3.11 do not contain all the nonlinear terms, but only those that arise by the Taylor expansion of the firing function in Eqs. 3.8, 3.9 which incorporate the noise inside f. Furthermore, we will be keeping only the linear terms for the rest of this chapter. The stochastic processes $\eta_{E,I}$ are correlated with correlation times $\tau_{E,I}$. The use of band-limited noise allowed us so far to avoid

the problem of taking a nonlinear function (namely, the response function f) of Gaussian white noise, and to use standard calculus.

Note that we could try to tackle the higher dimensional envelope-phase reduction and Fokker-Planck analysis required by the colored noise stochastic differential system Eqs.(3.10)-(3.11). We prefer to avoid this route and aim for a more tractable approach as a first pass to the effect of multiplicative and additive noise.

Thus we concentrate on weakly correlated or un-correlated noise. This limit is motivated by the fact that ET are relatively slow oscillations compared to $\tau_{E,I}$ which are typically less than 10 ms; past research has in fact shown that synaptic inputs can be modelled as Gaussian white noise [76, 186]. We restrict our study to the situation $\tau_{E,I} \to 0$, $\Sigma_{E,I} \to \infty$ while keeping constant the intensities $(\tau_{E,I}\Sigma_{E,I})^2 = (\sigma_{E,I})^2$. The correlated inputs $\eta_{E,I}$ are replaced by Gaussian white noises $\sigma_{E,I}\xi_{E,I}$.

The presence of multiplicative noise requires us however to choose an interpretation for the resulting stochastic integrals. We can choose the Itô interpretation of the resulting stochastic differential equation (SDE), which may arise in response to the question: what happens to quasi-cycles (oscillations below the Hopf bifurcation) when one includes stochastic effects inside the response function of a single neuron? The result is multiplicative and additive noise, and we can first look at the white noise case after the expansion has been performed. This is the approach followed below. Consequently, simulations are performed with the Euler-Maruyama method which is of Itô-type, and are compared to Fokker-Planck analysis carried out in the Itô picture.

An alternative approach, in answer to the same question, takes the white noise limit of Eqs.(3.10)-(3.11) by making the correlation times τ_E and τ_I tend to zero (keeping intensities constant). This question is the one associated with the Stratonovich interpretation of the stochastic integrals. A common approach is then to convert the Stratonovich SDE into its Itô counterpart, and integrate the latter numerically using the Euler-Maruyama method. This would lead to a different Itô dynamics than in the first approach due to the presence of multiplicative noise. Itô and Stratonovich interpretations are expected to yield similar results if the coefficients b_E and b_I are small to moderate. Below we pursue the approach with the Itô interpretation of Eqs.(3.10)-(3.11), and further show that the Stratonovich approach simply causes an increase in the A_{EE} and A_{II} coefficients in

an otherwise identical analysis of the stochastic WC model and envelope-phase equations. In fact, the Stratonovich interpretation amplifies the effects that we report.

The dynamics of excitatory and inhibitory LFPs Eqs.(3.10)-(3.11) can now be written in the Itô interpretation in the form:

$$\frac{dV_E}{dt} = A_{EE}V_E + A_{EI}V_I + M_{EE}V_E^2 + M_{EI}V_EV_I + \big(\sigma_E^1 + \sigma_E^2 V_E\big)\xi_E(t) \tag{3.12}$$

$$\frac{dV_I}{dt} = A_{IE}V_E + A_{II}V_I + M_{II}V_I^2 + M_{IE}V_EV_I + \big(\sigma_I^1 + \sigma_I^2 V_I\big)\xi_I(t) \tag{3.13}$$

with the following coefficients:

$$\sigma_E^1 = a_E\sigma_E, \quad \sigma_I^1 = a_I\sigma_I \tag{3.14}$$

$$\sigma_E^2 = b_E\sigma_E, \quad \sigma_I^2 = b_I\sigma_I\,. \tag{3.15}$$

Note in the last definitions that the "2"s are superscripts, not powers, and this notation will be used henceforth. In the rest of the paper we will use σ_I as our master noise parameter, which enslaves the computation of all other noise parameters since we will also set $\sigma_E^2 = \sigma_I^2$. We will refer to the Gaussian white noise-driven Eqs.(3.12)-(3.13) instead of Eqs.(3.1)-(3.2) as the stochastic WC model with quadratic nonlinearity. Oscillations are then seen to be driven by a combination of additive and multiplicative noise, in contrast to other models where only additive noise is present (see e.g. [102, 182, 71] for recent references), or where state-dependent finite size noise is used [220].

3.2.2 Stochastic oscillations

We investigate the generation of oscillations in our model. To understand the effect of noise on such behavior, we first simulate Eqs.(3.12)-(3.13) without external stochastic inputs ($\sigma_E = 0$ and $\sigma_I = 0$) to investigate its ability to generate long-lived oscillations. For that we compute the synchronization level as the mean of the amplitudes of oscillations after transients have passed (without noise, this can be done using one value). The results show that, for weak values of the feedback excitation W_{EI}, the model was able to produce oscillations. However, increasing the value of this coupling parameter decreases the oscillation amplitude until the oscillation disappears (black curve, Fig. 3.2-(a)). Oscillations emerge through a Hopf bifurcation (vertical dashed green line in Fig. 3.2(a)) at

$W^*_{IE} = 20.8$. Such a transition is characterized by a change in sign of the real part of the most unstable complex conjugate pair of eigenvalues.

We now take into account stochastic external inputs. Oscillations start to emerge even where they were not present in the deterministic case (see coloured curves Fig. 3.2-(a)). The stochastic inputs then induce oscillations in this regime. Also, high noise intensities induce on average higher amplitude oscillations in the stable-focus domain (below the Hopf) as expected; the situation is reversed in the limit-cycle domain. This is due to the fact the noise is multiplicative and its effect is non trivial when the system becomes highly nonlinear. We also compute the peak frequency of the oscillation in the deterministic and the noise-induced regions. The frequency values are in the low beta-band for our parameter choice (Fig. 3.2-(b)). The model without self-inhibition therefore generates oscillations in the beta range. These oscillations are known in the literature as quasi-cycles oscillations. In this domain, oscillations appear as short epochs of synchrony, i.e. as bursts. Such oscillations are observed in the brain of several species [228, 154, 80]. In the rest of this chapter, we will only focus on the noise-induced oscillations or quasi-cycle regime. All the results obtained have to be interpreted in that context.

3.2.3 Quasi-cycle regime

We now investigate the properties of noise-induced beta oscillations. The dynamics of slow oscillations have recently been modelled using linear equations sustained by additive noise, producing many features of the activity recorded *in vivo* fairly well [71]. In our case here, we face both additive and multiplicative noise components. We focus on modeling the LFPs by first linearizing Eqs.(3.12)-(3.13):

$$\frac{dV_E}{dt} = A_{EE}V_E + A_{EI}V_I + \big(\sigma^1_E + \sigma^2_E V_E\big)\xi_E(t) \tag{3.16}$$

$$\frac{dV_I}{dt} = A_{IE}V_E + A_{II}V_I + \big(\sigma^1_I + \sigma^2_I V_I\big)\xi_I(t)\,. \tag{3.17}$$

Hereafter, these two linear equations will be referred to as the stochastic Wilson-Cowan dynamics (SWC). This is the system used to analyze oscillatory properties and from which we derive - and to which we compare - envelope dynamics. As for the case of the LFP sustained by only additive

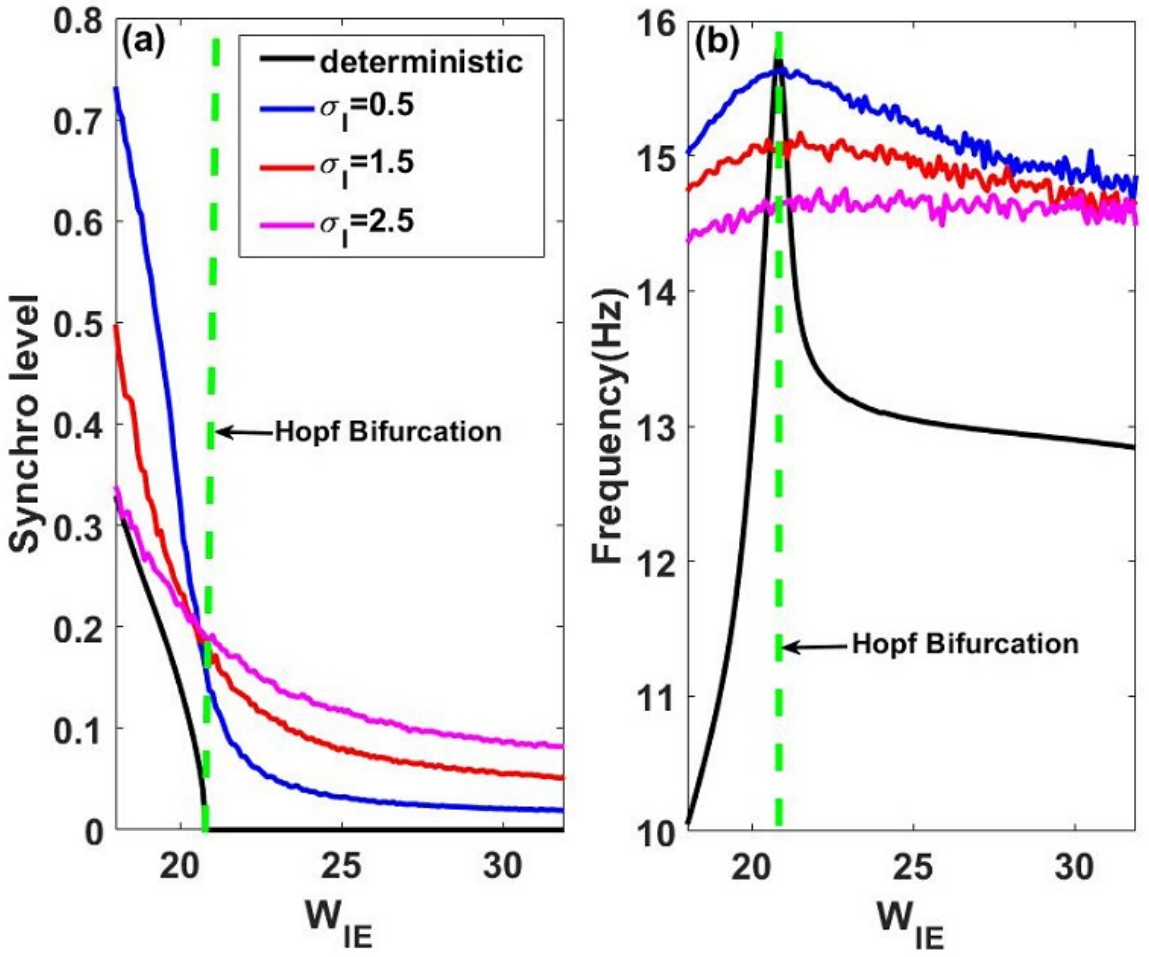

Figure 3.2: **Low frequency oscillations in the Stochastic Wilson-Cowan model with quadratic nonlinearity Eqs.(3.12)-(3.13). (a)** Synchronization level as a function of E to I connectivity, computed as cycle-to-cycle oscillation amplitudes (peak minus trough) averaged over a long simulation after transients. A smoothing convolution filter was applied to the noisy oscillation beforehand. For the deterministic case (black), oscillations appear only in the limit cycle region defined by $W_{IE} < W^*_{IE}$. When Gaussian white noise is added, oscillations are also induced in the complementary region $W_{IE} > W^*_{IE}$. The synchronization level of noise-induced oscillations increases with noise intensity, and the opposite holds in the limit cycle regime. The vertical dashed line (green) corresponds to the Hopf bifurcation at $W_{IE} = 20.8$. **(b)** Mean oscillation frequency for the deterministic (black, measured from transient response) and stochastic cases. This frequency increases with coupling strength in the limit-cycle region towards the Hopf bifurcation, and decreases thereafter until it stabilizes. Noise decreases the mean oscillation frequency. Parameter values are: $W_{EE} = 27.4, W_{II} = 0, W_{EI} = 26.3, h_E = -3.8, h_I = -8, \alpha_E = 0.02, \alpha_I = 0.04, \beta_E = 1$, and $\beta_I = 2$. In the next figures, only W_{IE} and σ_I will be changed, with $\sigma^2_E = \sigma^2_I$ (see Eqs.3.15).

noises, we found that in the quasi-cycle regime, the amplitude ratio and phase difference between inhibitory and excitatory populations converge to a fixed value. Also, the peak frequency of the excitatory and inhibitory LFPs converge to a fixed value. These fixed values can be computed in the deterministic limit of Eq.(3.16) and Eq.(3.17), as can the stability properties.

Linear Stability Analysis

We first consider the linear stochastic Eqs.(3.16)-(3.17) in the deterministic case $\sigma_E = \sigma_I = 0$. The associated noise-free linear system is written in matrix form:

$$\frac{dV^0(t)}{dt} = AV^0(t)$$

where

$$V^0(t) = \begin{bmatrix} V_E^0(t) \\ V_I^0(t) \end{bmatrix} \quad and \quad A = \begin{bmatrix} A_{EE} & A_{EI} \\ A_{IE} & A_{II} \end{bmatrix} .$$

We look for a trial solution in the form:

$$\begin{bmatrix} V_E^0(t) \\ V_I^0(t) \end{bmatrix} = \begin{bmatrix} \tilde{B_E} \\ \tilde{B_I} \end{bmatrix} e^{\lambda t}$$

where $\tilde{B_E} = B_E e^{j\theta_E}$ and $\tilde{B_I} = B_I e^{j\theta_I}$. The eigenvalues λ of the associated matrix A are found by substituting the trial solution into the linear system, yielding

$$\frac{\tilde{B_E}}{\tilde{B_I}} = \frac{-A_{EI}}{A_{EE} - \lambda} = -\frac{A_{II} - \lambda}{A_{IE}} .$$

The second equality leads to

$$\lambda = \frac{1}{2}(A_{EE} + A_{II}) \pm \frac{j}{2}\sqrt{-(A_{EE} - A_{II})^2 - 4A_{EI}A_{IE}} .$$

We rewrite the eigenvalues in the compact form

$$\lambda = -\nu \pm j\omega_0 \tag{3.18}$$

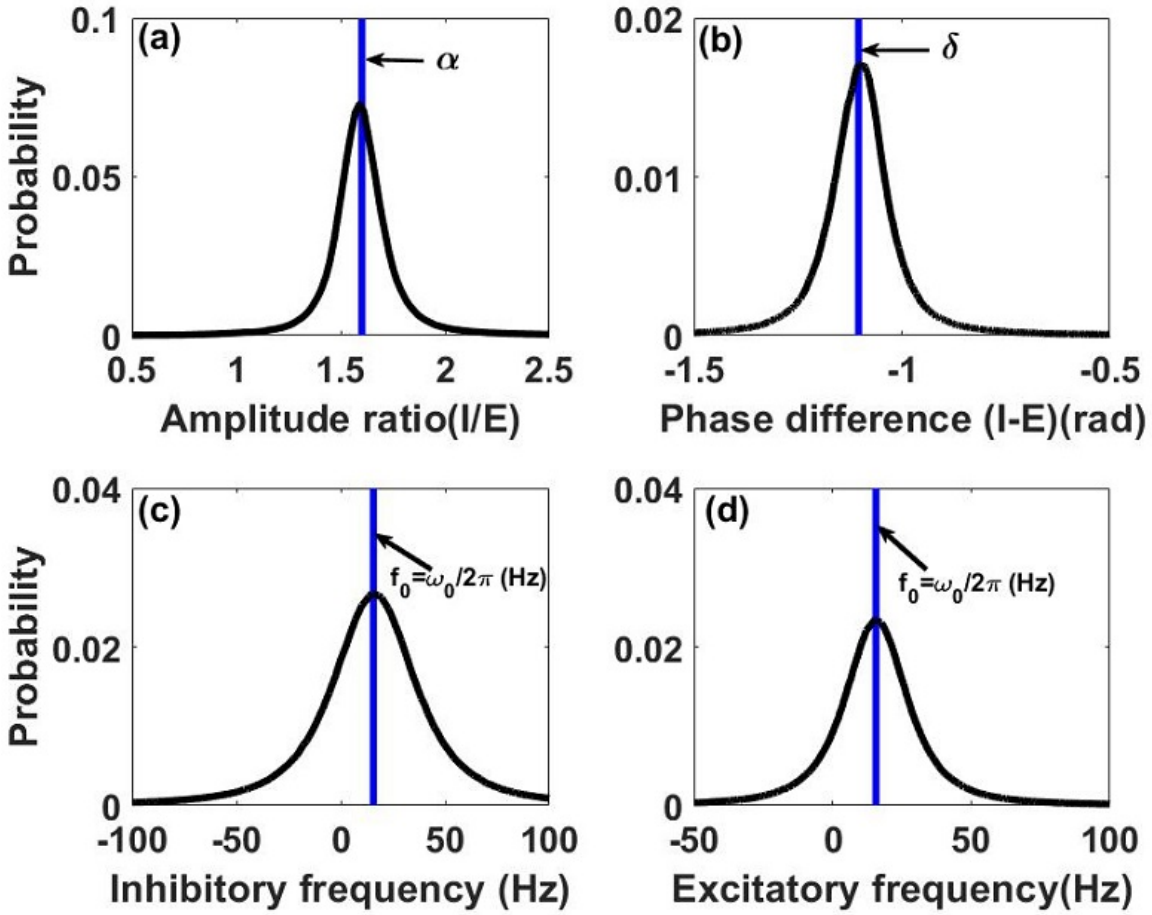

Figure 3.3: **Properties of the quasi-cycle regime.** Amplitude ratio density **(a)**, phase difference density **(b)**, and density of oscillation frequencies of the **(c)** inhibitory and **(d)** excitatory and populations frequencies are nearly Gaussian, with means near their predicted theoretical values (very near to the imaginary part $\omega_0/2\pi$ of the eigenvalues in the case of the frequencies). Black curves are the results of numerical simulations of Eqs.(3.16)-(3.17). Amplitudes, phases and frequencies used to construct the shown densities of these quantities were extracted through the Hilbert transform Eq.(3.21). Vertical blue lines are theoretical values obtained through linear stability analysis. The parameters are $W_{IE} = 21$ and $\sigma_I = 0.1$, with other parameters as in Fig.3.2.

with

$$\nu = -\frac{A_{EE}+A_{II}}{2} \tag{3.19}$$

$$\omega_0 = \frac{1}{2}\sqrt{-(A_{EE}-A_{II})^2-4A_{EI}A_{IE}}\,. \tag{3.20}$$

This leads to the exact expression of the amplitude ratio α between the inhibitory and excitatory LFPs:

$$\alpha = \left|\frac{\tilde{B_I}}{\tilde{B_E}}\right| = \frac{B_I}{B_E} = \sqrt{\frac{A_{IE}}{-A_{EI}}}.$$

Similarly, the phase difference δ can be obtained using the following relation

$$\delta = \theta_I - \theta_E = Arg\left(\frac{\tilde{B_I}}{\tilde{B_E}}\right).$$

For the parameters used here, we found

$$\delta = \theta_I - \theta_E = \arctan\left(\frac{-2\omega_0}{A_{EE}-A_{II}}\right).$$

The symbols $||$ and Arg are respectively the modulus and the argument of the complex number $\frac{\tilde{B}_I}{\tilde{B}_I}$. Note that, in the absence of noise, the time-dependent amplitudes both go to zero exponentially with characteristic time ν^{-1}. One can nevertheless compute the ratio of amplitudes as above. However, in the presence of noise, one can compute the ratio from simulated time series using the analytic signal technique. The amplitudes ratio and the phase difference are obtained by the following approximations:

$$\alpha = \frac{B_I}{B_E} \approx \left\langle \frac{Env\big[V_I(t)\big]}{Env\big[V_E(t)\big]} \right\rangle$$

and

$$\delta = \theta_I - \theta_E \approx \left\langle Arg\big[V_I(t)\big] - Arg\big[V_E(t)\big] \right\rangle.$$

Here $\langle . \rangle$ can be considered a time average of the stochastic process in Eqs.(3.16)-(3.17). Env is defined as the envelope of the analytic signal associated with the LFP. For example, the analytic

signal corresponding to $V_E(t)$ is $V_E(t) + jH\big[V_E(t)\big]$, with the Hilbert transform H defined as

$$H[x] = \frac{1}{\pi} P \int_{-\infty}^{\infty} \frac{x(\tau)}{t-\tau} d\tau \tag{3.21}$$

where P signifies the Cauchy principal value. The envelope of the stochastic signal is then $Env[V_E] = \sqrt{V_E^2 + H^2[V_E]}$. Likewise, the phase angle of the analytic signal is defined as $Arg[V_E] = \arctan\big[H[V_E]/V_E\big]$. We next derive an expression for the dynamics governing the time evolution of the envelopes of the E and I stochastic processes themselves.

3.3 Envelope-phase decomposition of LFP with multiplicative noise

3.3.1 Stochastic Averaging Method

In the quasi-cycle regime, oscillations appear as short epochs of synchrony called bursts. The appearance and duration of such beta bursts are random. They correspond to epochs of high values of the amplitude of the envelope of the LFP's V_E and V_I. The knowledge of the envelope dynamics is necessary to better characterize burst properties like their duration, although here we focus on the distribution of the envelope amplitudes. The envelope dynamics can be obtained through an envelope-phase decomposition of the E and I LFPs described in Eqs.(3.16)-(3.17). The novelty compared to [102, 182] is the multiplicative noise. We define the E and I LFPs in envelope form as follows:

$$V_E = Z_E \cos\big(\omega_0 t + \phi_E\big) \tag{3.22}$$

$$V_I = \alpha Z_E \cos\big(\omega_0 t + \phi_E + \delta\big), \tag{3.23}$$

where Z_E and ϕ_E represent the stochastic envelope and phase of the excitatory LFP. The idea is to extract the dynamics of the envelope Z_E and the phase ϕ_E of the excitatory LFP. This form is inspired by the properties of constant amplitude ratio and phase difference between E and I LFPs, as well as the peak mean frequency that can be approximated by the value of the imaginary part of the rightmost complex conjugate eigenvalues. We reason that these deterministic relations are approximately preserved in the noisy case. The effect of noise is mainly to induce deviations

around the deterministic values of the amplitude ratio, phase difference and mean frequency. This is supported by the results in Fig. 3.3. This assumption holds more effectively for weak values of the noise and when the dynamics are close to the Hopf bifurcation. We then inserted Eqs.(3.22) into Eqs.(3.16) and (3.17) and obtained the following envelope-phase dynamics:

$$\frac{dZ_E}{dt} = F_1\big(Z_E,\phi_E\big) + G_1\big(Z_E,\phi_E,\xi_E,\xi_I\big) \tag{3.24}$$

$$\frac{d\phi_E}{dt} = F_2\big(Z_E,\phi_E\big) + G_2\big(Z_E,\phi_E,\xi_E,\xi_I\big) \tag{3.25}$$

with the definitions:

$$F_1\big(Z_E,\phi_E\big) = \frac{1}{\alpha\sin(\delta)}\Big[\alpha f_1\big(Z_E,\phi_E\big)\sin(\omega_0 t+\phi_E+\delta) - f_2\big(Z_E,\phi_E\big)\sin(\omega_0 t+\phi_E)\Big]$$

$$F_2\big(Z_E,\phi_E\big) = \frac{1}{\alpha Z_E\sin(\delta)}\Big[\alpha f_1\big(Z_E,\phi_E\big)\cos(\omega_0 t+\phi_E+\delta) - f_2\big(Z_E,\phi_E\big)\cos(\omega_0 t+\phi_E)\Big]$$

$$G_1\big(Z_E,\phi_E,\xi_E,\xi_I\big) = \frac{1}{\alpha\sin(\delta)}\Big[\alpha g_1\big(Z_E,\phi_E,\xi_E,\xi_I\big)\sin(\omega_0 t+\phi_E+\delta) - g_2\big(Z_E,\phi_E,\xi_E,\xi_I\big)\sin(\omega_0 t+\phi_E)\Big]$$

$$G_2\big(Z_E,\phi_E,\xi_E,\xi_I\big) = \frac{1}{\alpha Z_E\sin(\delta)}\Big[\alpha g_1\big(Z_E,\phi_E,\xi_E,\xi_I\big)\cos(\omega_0 t+\phi_E+\delta) - g_2\big(Z_E,\phi_E,\xi_E,\xi_I\big)\cos(\omega_0 t+\phi_E)\Big]$$

$$f_1\big(Z_E,\phi_E\big) = \omega_0 Z_E\sin(\omega_0 t+\phi_E) + A_{EE}Z_E\cos(\omega_0 t+\phi_E) + A_{EI}\alpha Z_E\cos(\omega_0 t+\phi_E+\delta)$$

$$f_2\big(Z_E,\phi_E\big) = \alpha\omega_0 Z_E\sin(\omega_0 t+\phi_E+\delta) + A_{IE}Z_E\cos(\omega_0 t+\phi_E) + A_{II}\alpha Z_E\cos(\omega_0 t+\phi_E+\delta)$$

$$g_1\big(Z_E,\phi_E,\xi_E,\xi_I\big) = \Big[\sigma_E^1 + \sigma_E^2 Z_E\cos(\omega_0 t+\phi_E)\Big]\xi_E(t); \quad g_2\big(Z_E,\phi_E,\xi_E(t),\xi_I\big) = \Big[\sigma_I^1 + \sigma_I^2\alpha Z_E\cos(\omega_0 t+\phi_E+\delta)\Big]\xi_I(t).$$

To obtain reduced dynamics for the envelope and phase of the E-LFP, we applied the Stochastic Averaging Method (SAM) [187, 6]. The SAM stipulates that the system of equations (3.24) and (3.25) can under certain conditions (which apply here, such as broadband noise and underdamped oscillatory deterministic behaviour) be approximated to a two-dimensional Markov process given by:

$$d\begin{bmatrix} Z_E(t) \\ \phi_E(t) \end{bmatrix} = \begin{bmatrix} m_1 \\ m_2 \end{bmatrix} dt + \begin{bmatrix} h_{11} & h_{12} \\ h_{21} & h_{22} \end{bmatrix}\begin{bmatrix} dW_1^0(t) \\ dW_2^0(t) \end{bmatrix}, \tag{3.26}$$

$$m = T^{av}\left(E\big\{F\big\} + \int_{-\infty}^{0} E\left\{\left(\frac{\partial G}{\partial X}\right)_t (G)_{t+\tau}\right\}d\tau\right),$$

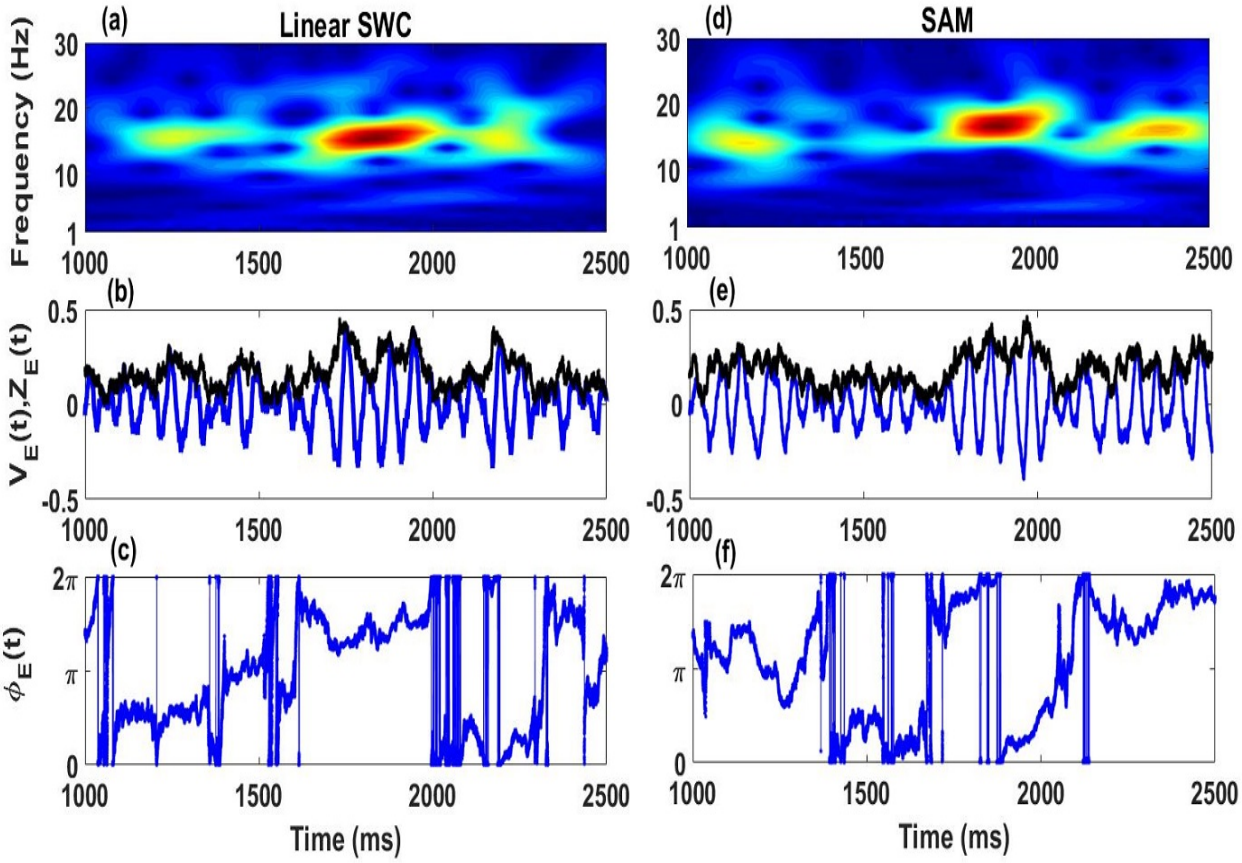

Figure 3.4: **Envelope-phase dynamics through the Stochastic Averaging Method (SAM)**. Time-frequency representation of beta oscillations obtained through the linear SWC dynamics Eqs. (3.16)-(3.17) with additive and multiplicative noise **(a)**. Beta oscillation (blue) its envelope (black) **(b)**, and its stochastic phase **(c)**. The envelope and stochastic phase dynamics are obtained through the Hilbert transform. **(d,e,f)** Same as in **(a,b,c)** but using envelope-phase dynamics Eqs.(3.33)-(3.34) resulting from the SAM method. The envelope-phase dynamics obtained through the SAM technique displays similar bursting structure to that observed for the simulation of the SWC model. The parameters are $W_{IE} = 27$ and $\sigma_I = 2.5$.

$$hh^{'} = T^{av}\bigg(\int_{-\infty}^{\infty} E\big\{(G)_t(G^{'})_{t+\tau}\big\}d\tau\bigg).$$

Here ($'$) denotes transposition, $h\,h'$ is the product of the matrix h with its transpose, the h_{ij} are the elements of the matrix h, and $\left(\frac{\partial G}{\partial X}\right)_t$ is a 2x2 Jacobian matrix. The functions m and h are, respectively, $O(\epsilon^2)$ and $O(\epsilon)$ where ϵ is a small number. This number can be seen as being proportional to the rate of attenuation $-\nu$ of the oscillation below the Hopf bifurcation, which itself must satisfy $\nu/\omega_0 < 1$ to guarantee an underdamped relaxation to the fixed point. Moreover, $E.$ denotes the expectation operator and T^{av} is the time averaging operator defined by

$$T^{av}(.) = \frac{1}{T_0}\int_{t0}^{t0+T0}(.)dt\,.$$

After some calculations we end up with the following expressions:

$$\begin{aligned}
m_1 &= -\big(\nu - \nu_1\big)Z_E(t) + \frac{D_0}{2Z_E(t)};\quad m_2 = -\eta \\
h_{11}^2 + h_{12}^2 &= D_0 + D_1 Z_E^2(t) \\
h_{11}h_{21} + h_{12}h_{22} &= \frac{\cos(\delta)}{16\sin(\delta)}\Big[(\sigma_E^2)^2 - (\sigma_I^2)^2\Big]Z_E(t) \\
h_{21}^2 + h_{22}^2 &= D_2 + \frac{D_0}{Z_E^2(t)}
\end{aligned}$$

with the following definitions:

$$\begin{aligned}
\nu &= -\frac{A_{EE} + A_{II}}{2};\quad D_0 = \frac{(\sigma_I^1)^2 + (\alpha\sigma_E^1)^2}{2\alpha^2\sin^2(\delta)};\quad D_1 = \frac{\big[1 + 2\sin^2(\delta)\big]\big[(\sigma_I^2)^2 + (\sigma_E^2)^2\big]}{8\sin^2(\delta)} \\
D_2 &= \frac{\big[1 + 2\cos^2(\delta)\big]\big[(\sigma_I^2)^2 + (\sigma_E^2)^2\big]}{8\sin^2(\delta)};\quad \eta = \frac{\big((\sigma_I^2)^2 + (\sigma_E^2)^2\big)}{8\sin^2(\delta)} \\
\nu_1 &= \frac{3\big[(\sigma_E^2)^2 + (\sigma_I^2)^2\big] + 2\big[(\cos(\delta)\sigma_E^2)^2 + (\sin(\delta)\sigma_I^2)^2\big]}{16\sin^2(\delta)}\,.
\end{aligned}$$

The coefficients h_{ij} $i,j = 1,2$ of the matrix h are the solutions of a nonlinear 4-dimensional system of equations (see equations in h_{ij} above) and the corresponding envelope-phase dynamics are given

by:

$$dZ_E(t) = m_1(t)dt + h_{11}dW_1^0(t) + h_{12}dW_2^0(t)$$
$$d\phi_E(t) = m_2(t)dt + h_{12}dW_1^0(t) + h_{22}dW_2^0(t).$$

This system of coupled equations can be approximated as follows

$$dZ_E(t) = m_1(t)dt + \sqrt{h_{11}^2 + h_{12}^2}dW_1(t)$$
$$d\phi_E(t) = m_2(t)dt + \sqrt{h_{12}^2 + h_{22}^2}dW_2(t).$$

The noise terms $h_{11}dW_1^0(t)+h_{12}dW_2^0(t)$ and $h_{12}dW_1^0(t)+h_{22}^0dW_2(t)$ are replaced by $\sqrt{h_{11}^2 + h_{12}^2}dW_1(t)$ and $\sqrt{h_{12}^2 + h_{22}^2}dW_2(t)$ respectively, where $W_1(t)$ and $W_2(t)$ are two independent Wiener processes. The new noise coefficients depend only on the diagonal elements of the matrix $G_tG_{t+\tau}^{'}$. This avoids solving the nonlinear 4-dimensional equations in h_{ij} and allows an easy derivation of the envelope-phase dynamics since the quantities $\sqrt{h_{11}^2 + h_{12}^2}$ and $\sqrt{h_{12}^2 + h_{22}^2}$ are available from direct integration of the diagonal coefficients of the matrix $G_tG_{t+\tau}^{'}$ (see equations in h_{ij} above). In this work, we impose the condition (see Eqs.3.15):

$$\sigma_E^2 = \sigma_I^2\,. \tag{3.27}$$

It can be further expressed as:

$$\sigma_E = \frac{\beta_I f^{'}(s_{I_0})}{\beta_E f^{'}(s_{E_0})}\sigma_I\,. \tag{3.28}$$

Then all the noise intensities can be simultaneously altered by only adjusting the value of σ_I. We have made this choice throughout our paper. The condition Eq.(3.27) further reduces the expression of some coefficients to:

$$D_1 = \frac{\big(1 + 2\sin^2(\delta)\big)(\sigma_I^2)^2}{4\sin^2(\delta)} \tag{3.29}$$

$$D_2 = \frac{\big(1 + 2\cos^2(\delta)\big)(\sigma_I^2)^2}{4\sin^2(\delta)} \tag{3.30}$$

$$\eta = \frac{(\sigma_I^2)^2}{4\sin^2(\delta)} \tag{3.31}$$

$$\nu_1 = \frac{(\sigma_I^2)^2}{2\sin^2(\delta)}\,. \tag{3.32}$$

We then obtain the following dynamics for the envelope-phase dynamics:

$$dZ_E(t) = \left[-\nu_{ef} Z_E(t) + \frac{D_0}{2Z_E(t)} \right] dt + \left[D_0 + D_1 Z_E^2(t) \right]^{\frac{1}{2}} dW_1(t) \tag{3.33}$$

$$d\phi_E(t) = -\eta dt + \left[D_2 + \frac{D_0}{Z_E^2(t)} \right]^{\frac{1}{2}} dW_2(t)\,, \tag{3.34}$$

where $\nu_{ef} \equiv \nu - \nu_1$ (in the Itô interpretation). To verify the validity of our envelope-phase model obtained through the SAM technique, we compute the envelope and phase dynamics and the corresponding LFPs Fig. 3.4-(e,f). We also computed the time-frequency representation which allows the visualization of the frequency content of the oscillation as time evolves (Fig. 3.4-(d)). It also reveals bursts in the oscillations as red hot spots. We compared theses quantities to those obtained through the linear SWC Eqs.(3.16)-(3.17), see Figs. 3.4-(a,b,c). We can observe that the envelope-phase dynamics capture well the bursting structure observed in the linear SWC model. Thus, the spectral properties present in the linear SWC model are also contained in the envelope-phase dynamics.

To further analyze the spectral behavior of our envelope-phase dynamics, we computed the power spectral densities of the LFPs and their envelopes for both the linear SWC equations and envelope-phase ones Figs. 3.5. We found that the envelope-phase dynamics capture well the power spectral densities present in the linear SWC equations. This is observed for both the LFPs and their envelopes. In summary, the envelope-phase dynamics presented here can be considered as good candidates for low frequency ET oscillations.

As for the case of additive noise only, the envelope dynamics are not coupled with the phase dynamics. However, multiplicative noises induce additional terms both in the drift and diffusion coefficients of the two processes. The diffusion coefficient of the envelope dynamics becomes a function of Z_E. The coefficients induced by the multiplicative noise are ν_1,D_1,D_2 and η. We remark that the coefficient $\nu_{ef} = \nu - \nu_1$ can be seen as the effective real part of the complex conjugate eigenvalues. The coefficient ν_1 is induced by the multiplicative noise. Importantly, the

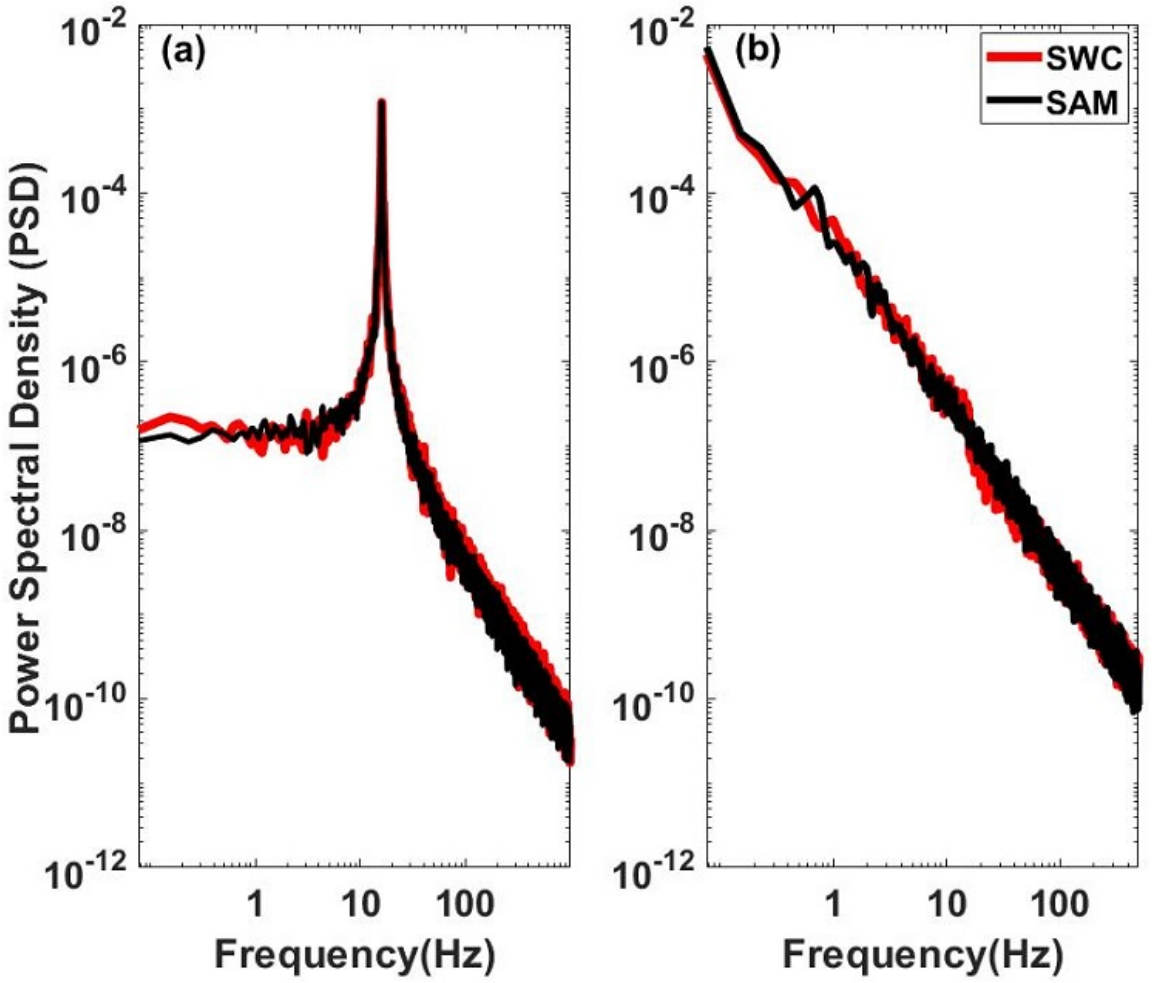

Figure 3.5: **Power spectra of the LFPs and the corresponding envelopes.(a)** Power spectra of the LFPs, i.e. fluctuations around the fixed point. Dynamics from the SWC Eqs.(3.16)-(3.17) (red) are compared to those of the envelope Eqs. (3.33) obtained from the SAM method and substituted into the LFPs Eqs.(3.22). **(b)** Power spectra of the envelope dynamics only, both from the SWC using the Hilbert transform (red), and from simulation of our envelope dynamics Eq.(3.33) (black). Excellent agreement is found in both panels. For all panels, we have used the Pwelch Matlab function for the spectral computations. Numerical simulations in this figure and the following figures 3.6-3.7 were performed during a total duration of 100 s. The parameters are $W_{IE} = 21$ and $\sigma_I = 0.1$.

effective real part is smaller than the true real part, *suggesting that multiplicative noise enhances the synchronization of the oscillations*. In fact the value of the real part of the eigenvalue gives the synchronization strength and the level of oscillations amplitude.

The fact that multiplicative noise reduces this value corresponds to bringing the model nearer

to the Hopf bifurcation and therefore to produce more synchrony. This can be seen in Fig. 3.2-(a) where it is clear that the level of synchronization increases as the value of the noises does. Of course, this is the combined effect of additive and multiplicative noise. The phase dynamics also contain a term which is induced by the multiplicative noise. This term is negative and acts to reduce the mean frequency of the oscillations. When these coefficients are equal to zero, we recover the former case of additive noise only studied in [102, 182].

3.3.2 Envelope density

The decoupling of the envelope dynamics from the phase dynamics allows a tractable analytical treatment. We first look at the envelope probability density using the associated Fokker-Planck equation

$$\frac{\partial P(Z_E,t)}{\partial t} = -\frac{\partial}{\partial Z_E}\left[\left(-\nu_{ef}Z_E + \frac{D_0}{2Z_E}\right)P(Z_E,t)\right] + \frac{\partial^2}{\partial Z_E^2}\left[\left(\frac{D_0+D_1Z_E^2}{2}\right)P(Z_E,t)\right]. \quad (3.35)$$

In the stationary limit, the above equation reduces to

$$-\frac{d}{dZ_E}\left[\left(-\nu_{ef}Z_E + \frac{D_0}{2Z_E}\right)P_s(Z_E)\right] + \frac{d^2}{dZ_E^2}\left[\left(\frac{D_0+D_1Z_E^2}{2}\right)P_s(Z_E)\right] = 0\,.$$

This leads to the normalized expression of $P_s(Z_E)$:

$$P_s(Z_E) = \frac{2\gamma D_1 D_0^{\gamma} Z_E}{\left(D_0 + D_1 Z_E^2\right)^{\gamma+1}} \quad (3.36)$$

where $\gamma = \nu_{ef}/D_1 + 1/2$. This density peaks at

$$Z_E^* = \sqrt{\frac{D_0}{2\big(D_1+\nu_{ef}\big)}}\,. \quad (3.37)$$

The probability density of the I population and its corresponding peak can be recovered by taking into account the amplitude ratio and phase difference between the two processes. We observe an excellent match between the envelopes pdf and their peaks computed from the analytical expression Eqs. (3.36)-(3.37) and those extracted through Hilbert transform performed on the simulated time

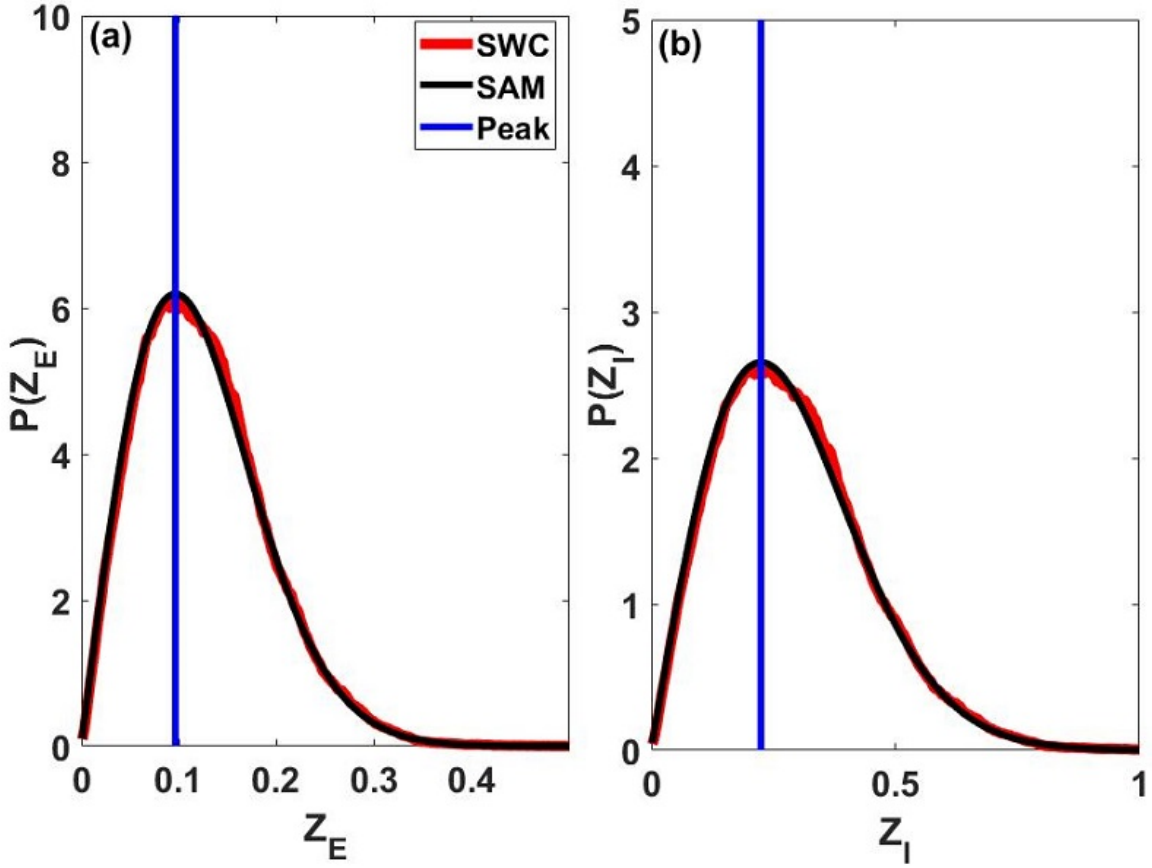

Figure 3.6: Probability densities of envelope fluctuations obtained through the SAM Eq.(3.36) (black) and from simulations of the SWC Eqs.(3.16)-(3.17) (red). The vertical blue lines are the peaks computed from the analytically determined SAM densities (Eq.(3.37)). Excitatory envelope fluctuations $P(Z_E)$ are shown in **(a)**, and inhibitory ones $P(Z_I)$ in **(b)**. The parameters are $W_{IE} = 24$ and $\sigma_I = 0.5$.

series Eqs.(3.16)-(3.17) (see Fig. 3.6). This expression for $P_s(Z_E)$ is valid as long as $\gamma > 0$, i.e. $\nu_{ef} > -D_1/2$; otherwise, the envelope realizations will diverge. The condition $\gamma > 0$, or $-\nu_{ef} < D_1/2$ with $D_1 > 0$ implies that the envelope dynamics Eq.(3.33) also describes the case $-\nu_{ef} > 0$ which corresponds to the virtual limit-cycle previously mentioned. Then, the term "virtual limit-cycle" only refers to the fact that the effective real part of the complex conjugate eigenvalue becomes positive. The reader should not confuse this term with the usual limit cycle. The expression of the density (Eq.(3.36)) for the multiplicative case here is not a Rayleigh distribution as in the case of only additive noise. The peak Z_E^* is also different from that case [182]. There is an additional term

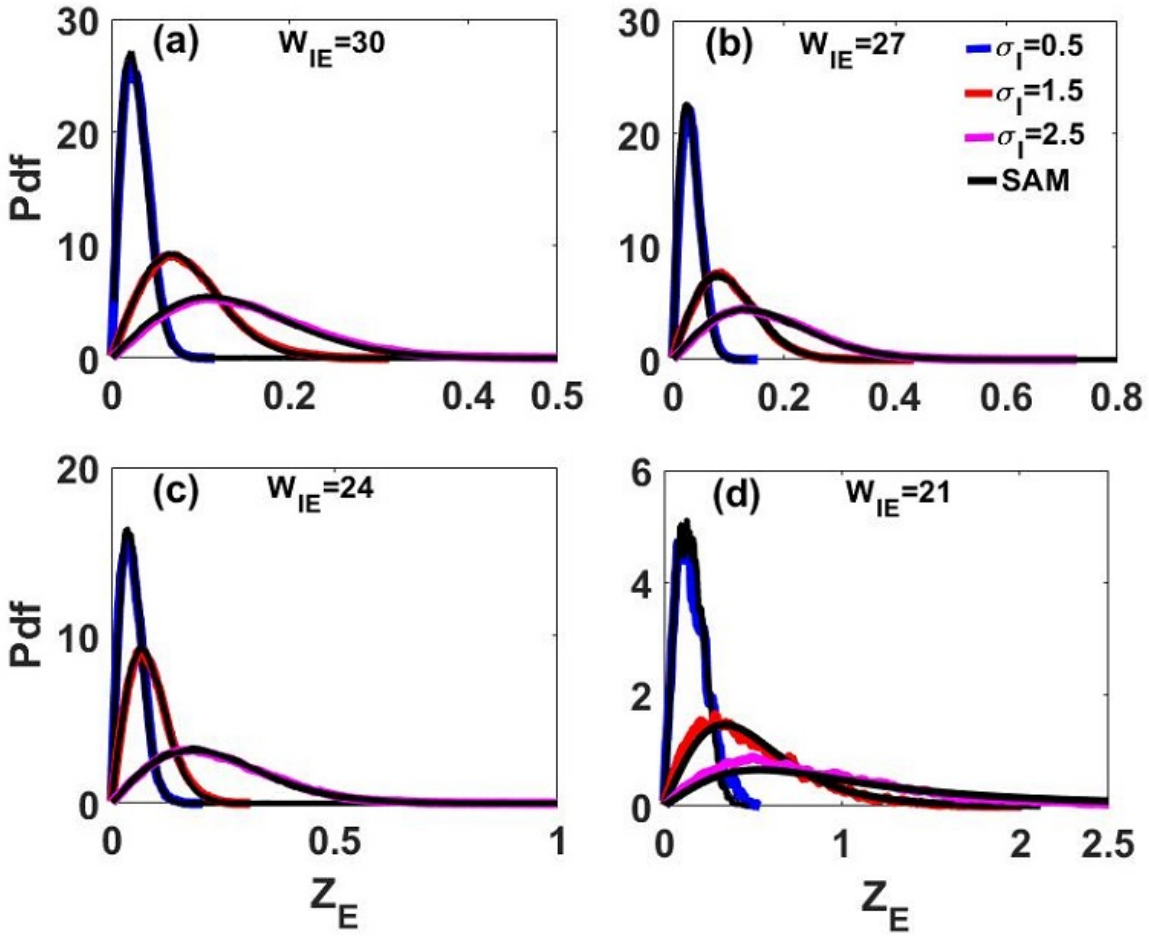

Figure 3.7: **Effect of noise and the distance to the bifurcation on the envelope probability densities.** Black curves correspond to the probability densities obtained through the SAM method Eqs. (3.33) and (3.36), and colored curves to the linear SWC Eqs.(3.16)-(3.17) with corresponding noise intensities. **(a)** Regime far from the Hopf bifurcation. **(b-c)** Regime at an intermediate distance to the Hopf bifurcation. Notice that envelope values are larger for higher noise intensities. **(d)** Regime very close to the bifurcation. The amplitudes of the envelope increase when the distance to the bifurcation is reduced. Higher noise intensities also increase the amplitude of the envelope processes in all regimes. For a point at a fixed distance to the bifurcation, increasing noise has the same effect as reducing the distance to the bifurcation.

D_1 in the denominator of the square-root, and the absolute value of the complex conjugate real part is now replaced by its effective value. This expression suggests that multiplicative noise has two opposite effects. The first effect acts through ν_{ef} to synchronize the network in a "deterministic" way. The second effect via D_1 is to desynchronize the network in a "stochastic" manner.

To further understand the dynamics of the envelope, we investigate the effect of both the noise intensity and the distance to the Hopf bifurcation in Fig. 3.7. For that we both vary the bifurcation parameter W_{IE} and the noise intensity σ_I. We observe that reducing the distance to the Hopf bifurcation synchronizes the system by reducing the deterministic real part of the complex conjugate eigenvalues - this is similar to what happens in a deterministic system near a Hopf bifurcation. We also reported analog behaviour in a previous study on gamma bursts [182]. The new mechanism is the noise-induced synchronization in a "deterministic" way through the coefficient ν_1, which reduces the deterministic eigenvalue ν via the relation $\nu_{ef} = \nu - \nu_1$.

These phenomena are showed in Fig. 3.7. Noise and the vicinity of the bifurcation act together to synchronize the system in a "deterministic" way. There are also the roles played by the multiplicative noise through D_1 and the additive noise through D_0; however such roles are difficult to interpret by a simple visual inspection of the densities in Fig. 3.7. To better understand the role of these latter parameters, it is appropriate to refer to Eq.(3.37). The role of D_0 has been previously discussed: its main effect is to increase the amplitude of the envelope by creating bursts. The role of D_1 should be to prevent the system from synchronizing too fast. However, we remark that the effect of the effective real part of the complex conjugate eigenvalues is more prominent. It is clear that the peak increases with the noise intensity, i.e. higher noise produces larger envelopes, as does the approach of the bifurcation (here by decreasing W_{IE}). The fact that the effective real part of the complex conjugate eigenvalues is higher than the true deterministic real part implies that the system can act "virtually" as a limit cycle despite the fact that its true complex conjugate eigenvalues have negative real part. To investigate the possibility of such behavior, we consider a point close to the Hopf bifurcation and vary the noise intensity. The result is the transition of the real part from negative, to less negative, and eventually to positive. This suggests that the system acts as a limit cycle (see Fig. 3.8). Multiplicative noise-induced synchronization is therefore a new mechanism which is absent in the case of only additive noise, and may be part of the operation of neural systems that generate rhythms.

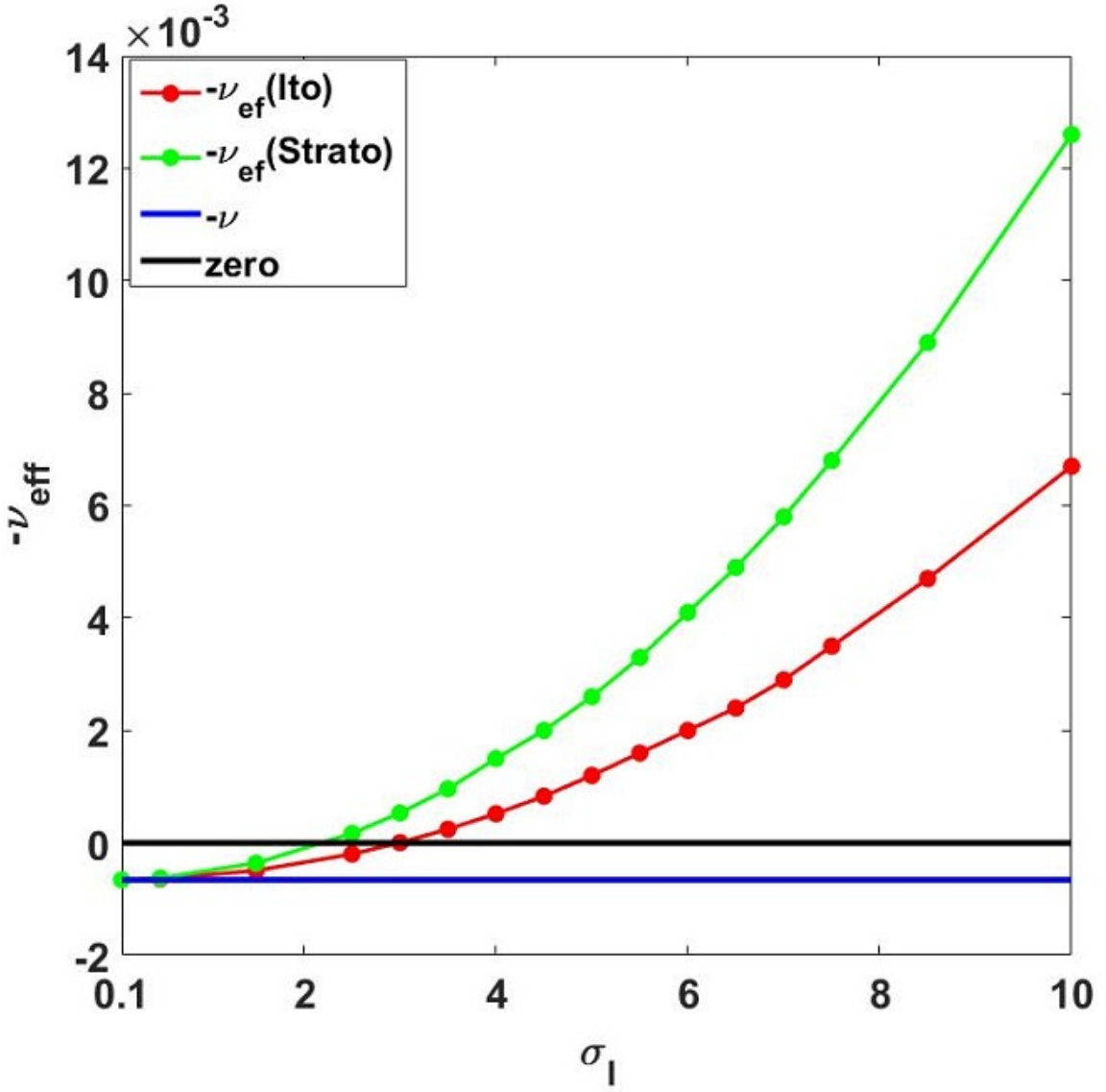

Figure 3.8: **Noise-induced virtual limit cycle**. Effective real part of the complex conjugate eigenvalues as the noise intensity σ_I increases. For lower intensity, one observes the usual quasi-cycle behaviour. A sufficiently strong noise intensity induces a virtual limit cycle by increasing the effective eigenvalue from negative to positive. The Stratonovich interpretation enables this sign change for even smaller noise. The value of the feedback excitation $W_{IE} = 21$ as in Figure 3.7-(b).

3.3.3 Envelope-Phase dynamics in the Stratonovich interpretation

The calculations using the SAM can readily be performed in the Stratonovich interpretation of the nonlinear dynamics with additive and multiplicative noise. The results is that two of the coefficients of the linear part of the dynamics (i.e. drift coefficients) become :

$$A_{EE}^{strato} = A_{EE} + \frac{1}{2}\big(\sigma_E^2\big)^2; \quad A_{II}^{strato} = A_{II} + \frac{1}{2}\big(\sigma_I^2\big)^2 . \tag{3.38}$$

Consequently, the real part of the eigenvalue in the envelope dynamics in Eq.(3.33) becomes:

$$\begin{aligned} -\nu^{strato} =& \frac{\big(A_{EE}^{strato} + A_{II}^{strato}\big)}{2} \quad (see \quad linear \quad stability) \\ =& -\nu + \frac{1}{4}\big((\sigma_E^2)^2 + (\sigma_I^2)^2\big) \quad (\nu = \nu^{ito}) \\ =& -\nu^{ito} + \frac{1}{4}\big((\sigma_E^2)^2 + (\sigma_I^2)^2\big) . \end{aligned}$$

Therefore,

$$\begin{aligned} -\nu_{ef}^{strato} =& -\nu_{ef} + \frac{1}{4}\big((\sigma_E^2)^2 + (\sigma_I^2)^2\big) \quad (\nu_{ef} = \nu_{ef}^{ito}) \\ =& -\nu_{ef}^{ito} + \frac{1}{4}\big((\sigma_E^2)^2 + (\sigma_I^2)^2\big) . \end{aligned}$$

Finally,

$$\nu_{ef}^{strato} = \nu_{ef}^{ito} - \frac{1}{4}\big((\sigma_E^2)^2 + (\sigma_I^2)^2\big) . \tag{3.39}$$

In the Stratonovitch interpretation, one just has to replace the $\nu_{ef} = \nu_{ef}^{ito}$ in Eq.(3.33) by ν_{ef}^{strato} derived in Eq.(3.39). A comparison of the Itô and Stratonovich approaches is seen in Fig. 3.8, where the negative of the effective damping rate is plotted versus noise intensity. It is seen that the Stratonovich interpretation causes the effective damping to become positive at a smaller noise intensity than in the Itô case. For small noise such as $\sigma_I = 0.1$, numerical simulations will barely differ from those in the Itô interpretation (not shown). A higher noise will allow the virtual limit cycle to be reached more quickly. In essence, the effects we have discussed up to now survive, and in fact are even stronger in the Stratonovich interpretation.

3.4 Discussion

In summary, we have built a model of bursty oscillations in the beta frequency range. Oscillations are assumed to be triggered by stochastic synaptic inputs driving individual neurons, and that without this noise, the dynamics are a simple stable focus. To lowest order, this leads to LFP dynamics that are linear SDEs subject to both additive and multiplicative noises. The choice of the linear Stochastic Wilson Cowan dynamics is motivated by a recent study [71] which showed that such a linear model is a good candidate to explain abnormal oscillations recorded *in vivo* relating to essential tremor. An envelope-phase analysis of these equations was then performed using the SAM method in the regime of underdamped oscillation, i.e. below but near the Hopf bifurcation.

With additive noise only, it has been shown that the envelope variable undergoes a random walk in a nonlinear potential, being attracted to zero (i.e. no rhythm) with a relaxation rate $-\nu$, and being driven away from zero by a term that scales with the additive noise intensity (D_o). Including the noise in the firing function rather than additively results in envelope-phase dynamics that contain two additional terms ν_1 and D_1 that scale up with noise intensity, and that are purely induced by the excitatory and inhibitory multiplicative noises.

The first term is added to the drift term and decreases the magnitude of the real part of the complex conjugate eigenvalues. As this part determines the relaxation rate of the envelope to zero, a smaller real part means that the envelope amplitude will be larger on average. In other words, the multiplicative noise brings on more synchronization. At moderate noise, it is even possible for the relaxation rate to change sign as shown in Fig. 3.8. However, the nonlinear envelope dynamics are derived from the linear WC dynamics in Eqs.(3.16)-(3.17), and actually diverge when the effective relaxation rate $-\nu_{ef}$ becomes greater than $D_1/2$. The second term appears in the diffusion coefficient and is proportional to the square of the envelope dynamics. This means that the envelope fluctuates more strongly when it is larger. The envelope dynamics thus have additional features compared to the pure additive noise case.

The phase dynamics Eq.(3.34) also contain two new terms that are absent in the purely additive noise case. The first term actually creates a drift component, i.e. it induces a rotation at a noise intensity dependent mean frequency η. This results in an effective, noise-induced imaginary part of the complex conjugate eigenvalues. The last term is added on the diffusion coefficient and is just a

constant term that increases the phase noise intensity.

With the extra multiplicative noise, the envelope is still uni-directionally coupled to the phase to lowest order, as was the case with additive noise only. This allowed an analytically tractable steady state solution to the Fokker-Planck equation for the envelope density in terms of all system parameters, including the synaptic strength W_{IE} and noise intensities. We limited our analysis to these two parameters as they generically reflected what can be expected from the dynamics. Other combinations could of course be considered. In fact our theory contains all parameters, but for simulations we choose the value of $W_{II} = 0$ [173, 71]. While more work would be needed to make a more general statement, the essential ingredient for the added synchrony caused by multiplicative noise may simply be the operation of the stochastic rate model near but below a Hopf bifurcation. And the condition $W_{II} = 0$ is not essential according to preliminary simulations and inspection of the theory.

Thus, in all the cases we have looked at, an increase in the noise intensities acting on the firing functions of E and I cells brings the network closer to the Hopf bifurcation, thereby increasing the synchronization level of the network. This can be viewed as multiplicative noise boosting a coherence resonance-type effect [150, 180] already present in the additive noise-induced oscillation that constitutes the quasi-cycle.

And close enough to the bifurcation, increasing the amount of noise actually changes the sign of the envelope decay rate, making the system act like a limit cycle - termed here a virtual limit cycle - despite the fact that the underlying fast E-I system has stable complex conjugate eigenvalues. This noise-induced transition can already be seen in the envelope dynamics Eq.(3.33), since the condition of existence of the envelope dynamics is $-\nu_e f < D_1/2$ with $D_1 > 0$ which implies that a value of $-\nu_e f > 0$ can meet such condition and therefore describes the envelope dynamics Eq.(3.33). However a full and proper analysis of the virtual limit cycle is more appropriate from the nonlinear fast dynamics Eqs.(3.12)-(3.13), rather than the linear dynamics Eqs.(3.16)-(3.17) as done here.

The synchronization enhancement by multiplicative noise may underlie some of the aberrant synchronization observed in patients suffering from motor dysfunctions. It may also be seen in the gamma range where the same mechanism operates; a simple change in the model time constants could produce such a move to higher rhythm frequency. Our study shows how this relates to the

more precise modeling of noise, and to the EI coupling strength. Our assumption of $W_{II} = 0$ was motivated by a recent study [71] of essential tremor based on thalamic circuitry, and slightly simplified our analysis.

In contrast, while there are a number of models for different aspects of Parkinson's diseases, those generally assume $W_{EE} = 0$ at the level of the sub-thalamic nuclei (STN), and $W_{II} > 0$ at the level of the globus pallidus-e (GPe). Including the feedback loop from STN to cortex and back actually amounts to a self-inhibition of STN, yet the interaction of oscillatory mechanisms complicate the matter further. State-of-the-art models of PD also consider firing function nonlinearity, bursting dynamics, and delayed feedback between brain nuclei, including to the cortex and back [177, 190]. It would be interesting to investigate how beta bursts arise in these models, and whether the enhanced synchronization discussed here for multiplicative noise appears and can be linked to symptoms. In fact it is possible to extend the SAM approach to delayed connectivity to obtain envelope-phase dynamics with delays [183]. These extensions may then lead to further insights into DBS.

Finally, if the multiplicative noise intensities are set to zero, we recover the case of only additive noise for which an optimal range of parameters, at an intermediate distance to the Hopf bifurcation, produces spectra and bursts similar to those seen in healthy *in vivo* preparations [228, 182]. As multiplicative noise promotes synchronization, its inclusion may result in the optimal range being shifted further from the Hopf boundary. This and the other predictions of our study could be further verified using a large scale network model of spiking neurons wired together to generate rhythms.

Chapter 4

Phase Dynamics of Delay-Coupled Quasi-Cycles with Application to Brain Rhythms

Abstract

We consider the phase locking of two delay-coupled quasi-cycles. A coupled envelope-phase system obtained via stochastic averaging enables a stability analysis. While for deterministic limit cycle oscillators the coupling can produce in-phase, anti-phase and the intermediate "out-of-phase" locking (OPL) behaviour via spontaneous symmetry breaking, such outcomes for the quasi-cycle case are shown to require instead both noise and coupling delay. The theory, which applies the stochastic averaging method to delayed dynamics, generates stochastic stability functions that predict the numerically observed OPL behaviour as a function of all the system parameters. OPL for coupled quasi-cycles occurs for additive or multiplicative noise, and for coupled E-I as well as I-I networks. Our theory also predicts that the bifurcation at which the in-phase state becomes unstable lies at smaller delays for stronger noise. The noise produces the realistic quasi-cycle rhythms and out-of-phase behaviour, all the while causing random reversals of the phase leader. Asymmetry in the coupling between networks, as well as heterogeneity within each network, also allows for quasi-cycle OPL, although it produces asymmetric bifurcations that bias the leadership towards one of the networks. These results are relevant to communication between brain and other networks that rely on noise-induced rather than noise-perturbed rhythms.

4.1 Introduction

Noisy oscillations are observed in a wide variety of systems. Our understanding of the behaviour of these systems in isolation and in networks is governed by the underlying dynamical origin of the oscillation. The case in which the system possesses a deterministic limit cycle which is perturbed by noise has received much attention [179, 1, 210]. Much is known about the synchronization properties of noise-perturbed limit cycle systems, such as their ability to lock in-phase (IP), in anti-phase (AP), or at phase differences in between, i.e. out-of-phase locking (OPL). In contrast, there may be no underlying deterministic limit cycle, and the generation of the observed oscillations relies on noise. Although studied to a much lesser extent, these noise-induced oscillations, known as "quasi-cycles", arise in an increasing number of contexts, from semiconductor lasers to brain dynamics and epidemics [114, 27, 161, 192]. Theory is particularly lacking for coupled quasi-cycles, thought to enable e.g. oscillation (or "rhythm")-based communication between brain areas [192, 175].

In this work, the stochastic averaging method (SAM) is used to obtain an envelope-phase description for coupled quasi-cycles. It reveals a novel mechanism for OPL. Delays are included as they are often non-negligible compared to other system time scales [69, 141].

Although the findings below apply generally, we are particularly motivated by the communication between brain areas, thought to require the phase difference between two rhythms in separate areas being constant over some time interval [219]. The sign of this difference reveals the leadership and direction of the information flow between the areas [152]. For identical, symmetrically coupled networks the available theory, based on deterministic oscillators, invokes spontaneous symmetry breaking (SSB) to explain OPL. SSB is a deterministic effect where the two-oscillator system loses symmetry beyond a critical parameter value, with one becoming the leader and the other the laggard [14, 72]. Flexible, reversible bi-directional communication can then be achieved with brief external pulses that reverse the leadership [16, 134, 226].

However, there is increasing evidence that many brain rhythms are noise-induced and manifest only in brief epochs of random duration [141, 228, 175, 182]. OPL can also be seen, but phase locking of quasi-cycles is not well understood, a specific motivator for our work. While SSB is here shown to not occur for coupled quasi-cycles, OPL can arise thanks both to delays and the smoothing by noise of the bifurcation between IP and AP.

Two dominant mechanisms for rhythms in the higher "gamma" frequency range have been reported in the experimental and theoretical neuroscience literature: PING, which involves reciprocally and self-coupled excitatory and inhibitory neurons (EI), and ING which sees inhibitory neurons coupled to one another, often with a delay (II). The mechanism of delay and noise-induced OPL in coupled quasi-cycles is shown below to be present in two coupled EI networks (our main focus), as well as in two coupled II networks. In both cases, this OPL persists even if the networks are heterogeneous but symmetrically coupled, or identical but asymmetrically coupled. This suggests a strong and robust mechanism which could underlie some of the dynamic functional connectivity observed in the brain of several species at rest and when performing certain tasks [117, 118, 100]. These coupled dynamics, in which each network exhibits quasi-cycle behaviour in isolation, also enable bidirectional exchanges of information between networks [175]. The leadership can then alternate randomly between the two networks following fluctuations in the random inputs, as well as be biased by external pulses as in the case of the coupled oscillator dynamics. We thus extend to noise-induced rhythms the property of communication through coherence [83, 85] and its expanded version with propagation delay [12].

After presentation of the general PING model with noise, we derive the envelope-phase dynamics by extending the SAM technique to delayed coupling. Analysis of the symmetric case reveals the delay-and-noise-induced OPL phenomenon in the coupled quasi-cycles. This is followed by an extension to the asymmetric and heterogeneous cases. We complete our study of coupled quasi-cycles by considering the alternative ING model in the same cases, and end with a discussion and outlook onto future works.

4.2 Model of coupled E-I networks

We are motivated by the work on stochastic EI networks in [220], in which all neurons in each population are simulated as two-state systems that are either quiescent or active. This leads to a two-dimensional Wilson-Cowan-type rate model with an E and an I population each with their own finite size fluctuations. This formalism can also model sparse connectivity through an appropriate scaling of the mean synaptic coupling coefficients. To set the scene, we describe their model in the microscopic, multi-neuron context with specific neuron numbers. However, all the analytical and

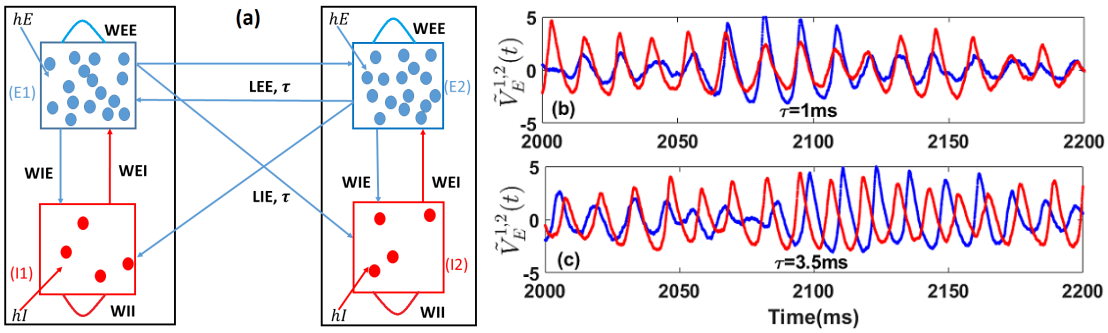

Figure 4.1: **Model.** (a) Two delay-coupled E-I networks.
(b-c) Fluctuation timeseries of E_1 (blue) and E_2 (red) around their equilibrium points, modelling local field potentials (LFPs), from simulations of the SWC system Eqs.(4.1) with $L_{EE} = 2.0$, $L_{IE} = 0.5$. The in-phase synchronization seen in (b) for $\tau = 1ms$ is replaced by out-of-phase behaviour (OPL) for $\tau = 3.5ms$ in (c). Other parameters are $W_{EE} = 27.4, W_{II} = 1.3, W_{IE} = 32, W_{EI} = 26.3, h_E = -3.8, h_I = -8, \alpha_E = 0.1ms^{-1}, \alpha_I = 0.2ms^{-1}, \beta_E = 1, \beta_I = 2, \sigma = 0.006ms^{-1/2}$. All simulations in our paper are done with the Euler-Maruyama method with time step 0.05 ms, except for Fig.4.3 where the time step is shorter. A second-order butterworth bandpass filter was applied to the fluctuations in Fig.1(b,c) to limit frequencies to the gamma band [30-100] Hz.

numerical work will be done on the associated two-variable model.

Each of the two networks has N_E excitatory (E) and N_I inhibitory (I) neurons with $N_E = 4N_I$, as is typical for cortical circuitry, coupled to produce oscillations near but below a Hopf bifurcation. These two networks are further symmetrically coupled via long-range excitatory connections with propagation delay as in Fig.4.1. The state variables are the mean activity of the neurons in each population, i.e. E_i and I_i, $i = 1, 2$. The coefficients W_{EE}, W_{II} are respectively the recurrent excitatory and inhibitory synaptic coupling, while W_{IE}, W_{EI} are, respectively, the feedback excitatory and inhibitory synaptic coupling in each network. In addition, each population in each network receives a constant external input (h_E and h_I, respectively). The long-range excitatory synaptic coupling between the two E populations is L_{EE}, and between the E population of one network and the I population of the other network is L_{IE}. The activity of a neuron in one network is felt by the other network after a delay τ.

The model is schematized in Fig.4.1(a) and described by the stochastic Wilson-Cowan (SWC) equations [220]:

$$
\begin{aligned}
\dot{E}_i(t) &= -\alpha_E E_i(t) + (1 - E_i(t))\beta_E f(s_{E_i}(t)) + g_1 \xi_{E_i}(t) \\
\dot{I}_i(t) &= -\alpha_I I_i(t) + (1 - I_i(t))\beta_I f(s_{I_i}(t)) + g_2 \xi_{I_i}(t) \\
s_{E_i}(t) &= W_{EE} E_i(t) - W_{EI} I_i(t) + h_E + L_{EE}^{i,j} E_j(t - \tau) \\
s_{I_i}(t) &= W_{IE} E_i(t) - W_{II} I_i(t) + h_I^i + L_{IE}^{i,j} E_j(t - \tau)
\end{aligned} \tag{4.1}
$$

for identical and symmetrically coupled networks described in this section, $L_{EE}^{i,j} = L_{EE}$, $L_{IE}^{i,j} = L_{IE}$ and h_I^i with $i, j = 1, 2$ and $i \neq j$, $s_{E_i}(t)$ and $s_{I_i}(t)$, $i = 1, 2$, the total synaptic inputs to E and I populations in each network, $f(x) = 1/(1 + exp(-x))$ the sigmoidal response of a neuron to its total input, $\xi_{E_i}(t)$ and $\xi_{I_i}(t)$ independent Gaussian white noises, and g_1 and g_2 are population-size-dependent multiplicative noise intensities,

$$
\begin{aligned}
g_1(E_i, I_i) &= \sqrt{\frac{(1 - E_i(t))\beta_E f(s_{E_i}(t)) + \alpha_E E_i(t)}{N_E}} \\
g_2(E_i, I_i) &= \sqrt{\frac{(1 - I_i(t))\beta_I f(s_{I_i}(t)) + \alpha_I I_i(t)}{N_I}}\,.
\end{aligned} \tag{4.2}
$$

We define the noise intensities as:

$$
\sigma_E \equiv \left\langle \Big(g_1(E_i, I_i) \Big) \right\rangle \qquad \sigma_I \equiv \left\langle \Big(g_2(E_i, I_i) \Big) \right\rangle,
$$

where $\langle\rangle$ means the time average. Simulations reveal that the distributions of these multiplicative noise intensities are very close to Gaussians, and the values of σ_E and σ_I are close to the means of these distributions. We then defined the total noise as

$$
\sigma \equiv \sqrt{\sigma_E^2 + \sigma_I^2}\,. \tag{4.3}
$$

Our results below also hold for constant functions $g_1(E_i, I_i) = \sigma_E$ and $g_2(E_i, I_i) = \sigma_I$ (additive noise).

The rightmost eigenvalues of the deterministic part of Eqs.(4.1) are complex conjugate with negative real part ($\lambda = -\nu \pm j\omega_0, \quad \nu > 0$), and imaginary part in the gamma band ($30Hz < \omega_0/(2\pi) < 100Hz$). Without noise, activities converge to a fixed point $(E_{10}, I_{10}, E_{20}, I_{20})$. We focus on fluctuations around this point: $\tilde{V}_E^i(t) = c_E(E_i(t) - E_{i0})$ and $\tilde{V}_I^i(t) = c_I(I_i(t) - I_{i0})$ where $c_E = \sqrt{N_E}$ and $c_I = \sqrt{N_I}$ for the case of the multiplicative noise and $c_E = c_I = 1$ for additive noise. Time series of these local field potentials (LFPs) are illustrated in Fig.4.1(b,c) with IP behaviour for the smaller delay and OPL for the slightly larger one.

4.3 Envelope-phase decomposition

In contrast to the case $\nu < 0$ where the limit cycle envelopes are almost constant (in the weak noise limit), in the quasi-cycle regime the envelopes and phases (and therefore frequencies) fluctuate over a larger range. We extend a recent single quasi-cycle analysis using the SAM approximation [187, 182] to the coupled case of interest here, noting that the coupled system still has a deterministic fixed point. A synchronization transition study for a population of coupled quasi-cycles was recently done in this regime using a different method [103]. We write the E and I LFPs as

$$\begin{aligned} V_E^1(t) &= Z_1(t)\cos(\omega_0 t + \phi_1(t)); \quad V_I^1(t) = \alpha_1 Z_1(t)\cos(\omega_0 t + \phi_1(t) + \delta_1) \\ V_E^2(t) &= Z_2(t)\cos(\omega_0 t + \phi_2(t)); \quad V_I^2(t) = \alpha_2 Z_2(t)\cos(\omega_0 t + \phi_2(t) + \delta_2)\,. \end{aligned} \tag{4.4}$$

These trial solutions are motivated by our previous study [182] where the results using these solutions yielded good agreement with simulations both near and far from the Hopf bifurcation, and reproduced many features of the data (stochastic behavior with short and random epochs of synchrony called gamma bursts, highly variable frequency ...[228]). In fact, this choice is an extension to two networks of a previous model for one E-I network which was shown to reproduce the bursting behavior of gamma rhythms *in vivo* [182]. The system to which this trial solution is applied to (see Appendix, Eqs.4.14) is also linear and stochastic, and thus harmonic solutions are a good place to start. An alternate form could be used if one wishes that a certain feature of the data needs to be reflected in the model. Inserting these expressions in the dynamics of the LFPs sustained by

noise and applying the stochastic Averaging Method (SAM) we obtain the following dynamics for the amplitude and phase dynamics

$$
\begin{aligned}
dZ_1(t) &= \Big(-\lambda_1 Z_1(t) + \frac{D_1}{2Z_1(t)} + M_1^1\big[\phi_1(t) - \phi_2(t-\tau)\big] Z_2(t-\tau) \Big) dt + \sqrt{D_1} dW_{Z_1}(t) \\
d\phi_1(t) &= \left(\Omega_1 + M_1^2\big[\phi_1(t) - \phi_2(t-\tau)\big] \frac{Z_2(t-\tau)}{Z_1(t)} \right) dt + \frac{\sqrt{D_1}}{Z_1(t)} dW_{\phi_1(t)} \\
dZ_2(t) &= \Big(-\lambda_2 Z_2(t) + \frac{D_2}{2Z_2(t)} + M_2^1\big[\phi_2(t) - \phi_1(t-\tau)\big] Z_1(t-\tau) \Big) dt + \sqrt{D_2} dW_{Z_2}(t) \\
d\phi_2(t) &= \left(\Omega_2 + M_2^2\big[\phi_2(t) - \phi_1(t-\tau)\big] \frac{Z_1(t-\tau)}{Z_2(t)} \right) dt + \frac{\sqrt{D_2}}{Z_2(t)} dW_{\phi_2}(t)\,,
\end{aligned}
\tag{4.5}
$$

where the functions M_1^1, M_1^2, M_2^1 and M_2^2 are given by

$$
M_1^1[x] = \gamma_1 \Big[\alpha_1 C_{EE}^{12} \sin(x + \omega_0\tau + \delta_1) - C_{IE}^{12} \sin(x + \omega_0\tau) \Big]; \quad M_1^2[x] = \gamma_1 \Big[\alpha_1 C_{EE}^{12} \cos(x + \omega_0\tau + \delta_1) - C_{IE}^{12} \cos(x + \omega_0\tau) \Big]
$$

$$
M_2^1[x] = \gamma_2 \Big[\alpha_2 C_{EE}^{21} \sin(x + \omega_0\tau + \delta_2) - C_{IE}^{21} \sin(x + \omega_0\tau) \Big]; \quad M_2^2[x] = \gamma_2 \Big[\alpha_2 C_{EE}^{21} \cos(x + \omega_0\tau + \delta_2) - C_{IE}^{21} \cos(x + \omega_0\tau) \Big]
$$

with the coefficients

$$
\lambda_1 = -\frac{A_{EE}^1 + A_{II}^1}{2}; \quad \lambda_2 = -\frac{A_{EE}^2 + A_{II}^2}{2}; \quad \gamma_1 = \frac{1}{2\alpha_1 \sin(\delta_1)}; \quad \gamma_2 = \frac{1}{2\alpha_2 \sin(\delta_2)}
$$

and

$$
\begin{aligned}
D_1 &= \frac{\alpha_1^2 \sigma_{E_1}^2 + \sigma_{I_1}^2}{2(\alpha_1 \sin(\delta_1))^2}; \quad D_2 = \frac{\alpha_2^2 \sigma_{E_2}^2 + \sigma_{I_2}^2}{2(\alpha_2 \sin(\delta_2))^2} \\
\Omega_1 &= -\omega_0 + \gamma_1 \big(\alpha_1 \cos(\delta_1)(A_{EE}^1 - A_{II}^1) + \alpha_1^2 A_{EI}^1 - A_{IE}^1 \big) \\
\Omega_2 &= -\omega_0 + \gamma_2 \big(\alpha_2 \cos(\delta_2)(A_{EE}^2 - A_{II}^2) + \alpha_2^2 A_{EI}^2 - A_{IE}^2 \big)\,.
\end{aligned}
\tag{4.6}
$$

Here $dW_k, k = Z_{1,2}, \phi_{1,2}$ are independent Brownian motions, and the parameters $\lambda_{1,2}, \Omega_{1,2}, \delta_{1,2}, \alpha_{1,2}, C_{EE}^{12}, C_{EE}^{21}$ and C_{IE}^{12}, C_{IE}^{21} depend on the network parameters described above (see Appendix). Specifically, $\alpha_{1,2}$ and $\delta_{1,2}$ are the amplitude ratio and phase difference between the I and E populations in networks 1 and 2, respectively.

The dependencies of the parameters of the envelope-phase equations on those in the original SWC system are not trivial, as their definitions that follow Eqs.4.14 in the full derivation in the Appendix reveal. And a number of parameters depend on the fixed point, which is a function of all the parameters. For the symmetric case, we have: $\alpha_1 = \alpha_2 = \alpha$; $\delta_1 = \delta_2 = \delta$; $\lambda_1 = \lambda_2$; $\Omega_1 = \Omega_2 = \Omega_0$; $D_1 = D_2 = D$; $C_{EE}^{12} = C_{EE}^{21} = C_{EE}$; $C_{IE}^{12} = C_{IE}^{21} = C_{IE}$. The envelope-phase dynamics therefore simplify to:

$$\begin{aligned}
\frac{dZ_1}{dt} &= -\lambda_1 Z_1 + \frac{D}{2Z_1} + M_1\big[\phi_1 - \phi_{2\tau}\big] Z_{2\tau} + \sqrt{D}\xi_{Z_1} \\
\frac{d\phi_1}{dt} &= \Omega_0 + M_2\big[\phi_1 - \phi_{2\tau}\big]\frac{Z_{2\tau}}{Z_1} + \frac{\sqrt{D}}{Z_1}\xi_{\phi_1} \\
\frac{dZ_2}{dt} &= -\lambda_1 Z_2 + \frac{D}{2Z_2} + M_1\big[\phi_2 - \phi_{1\tau}\big] Z_{1\tau} + \sqrt{D}\xi_{Z_2} \\
\frac{d\phi_2}{dt} &= \Omega_0 + M_2\big[\phi_2 - \phi_{1\tau}\big]\frac{Z_{1\tau}}{Z_2} + \frac{\sqrt{D}}{Z_2}\xi_{\phi_2}\,,
\end{aligned} \tag{4.7}$$

where $\phi_{i\tau} \equiv \phi_i(t-\tau)$, $Z_{i\tau} \equiv Z_i(t-\tau)$, and

$$\begin{aligned}
M_1 &= \tfrac{1}{2\alpha\sin(\delta)}\Big[\alpha C_{EE}\sin(x+\omega_0\tau+\delta) - C_{IE}\sin(x+\omega_0\tau)\Big] \\
M_2 &= \tfrac{1}{2\alpha\sin(\delta)}\Big[\alpha C_{EE}\cos(x+\omega_0\tau+\delta) - C_{IE}\cos(x+\omega_0\tau)\Big]
\end{aligned}$$

Here again, $\lambda_1, D, \Omega_0, C_{EE}$ and C_{IE} depend on network parameters and are the same for both networks, but ξ_k, $k = \{Z_{1,2}, \phi_{1,2}\}$ are again independent Gaussian white noises as in the general case above.

The E envelopes and phases from Eqs.(4.7) are shown in Fig.4.2(a-d). In Fig.4.2(e,f), good agreement is found between probability distributions of the envelopes and phases from simulations of the SAM Eqs.(4.7) and of the SWC Eqs.(4.1). Agreement improves for weaker noise and closer proximity to the Hopf bifurcation. The phase dynamics $\phi_i(t)$ here differs from that of the usual Hilbert transform by the deterministic rotation $\omega_0 t$. The phase difference $\Delta\phi(t) = \phi_1(t) - \phi_2(t)$ describes the same quantity than the difference of the phases extracted using the Hilbert transform.

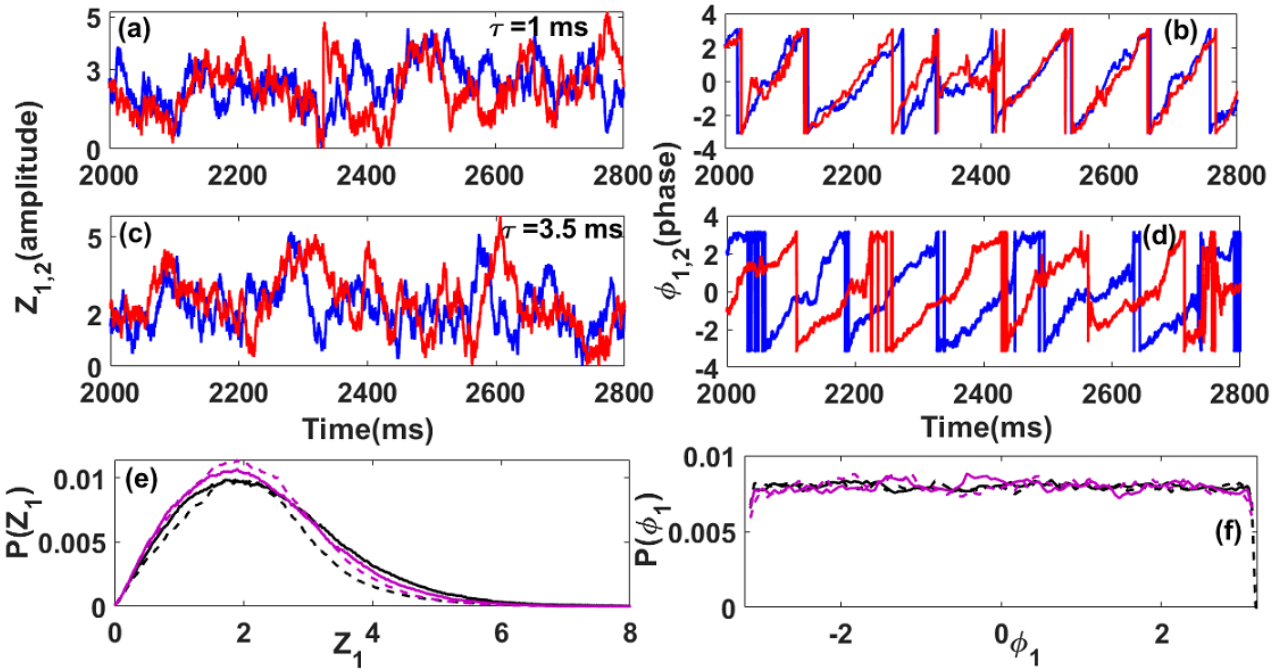

Figure 4.2: **Coupled envelope and phase dynamics.** Envelope time series for E_1 (blue) and E_2 (red) populations for coupling $L_{EE} = 2.0$, $L_{IE} = 0.5$ and delay (a) $\tau = 1ms$ and (c) $3.5ms$. Corresponding phase dynamics are shown in (b) and (d). In-phase locking is seen for $\tau = 1ms$, and out-of-phase locking for $\tau = 3.5ms$ as in Fig.4.1-(b-c). Envelope (e) and phase (f) probability distributions from simulations of the SWC model (Eqs.4.1, solid lines) through the Hilbert transform and the SAM theory (Eqs.4.7, dashed), for $\tau = 1ms$ (magenta) and $\tau = 3.5ms$ (black). Parameters are as in Fig.4.1.

4.4 Quasi-cycle Phase Synchronization

We first derive phase-locking dynamics from the envelope-phase system Eqs.4.7 using $\Delta\phi(t) \equiv \phi_1(t) - \phi_2(t)$, $\theta(t) \equiv \phi_1(t) + \phi_2(t)$, $X \equiv (\theta(t) - \theta(t-\tau))/2$, $Y \equiv (\Delta\phi(t) + \Delta\phi(t-\tau))/2$:

$$\begin{aligned} d\Delta\phi(t) &= -2M_1[X(t)]\sin[Y(t)]\,dt + \frac{\sqrt{D}}{Z_1(t)}dW_1(t) \\ d\theta(t) &= 2\big(\Omega_0 + M_2[X(t)]\cos[Y(t)]\,\big)dt + \frac{\sqrt{D}}{Z_1(t)}dW_2(t) \end{aligned} \tag{4.8}$$

where we assumed $Z_1 \sim Z_2$, $W_1 = W_{\phi_1} - W_{\phi_2}$, and $W_2 = W_{\phi_1} + W_{\phi_2}$. Following [140], we seek the deterministic solutions of Eqs. (4.8) in the form $(\Delta\phi(t), \theta(t)) = (\Delta\phi^*, \Omega t)$. Stability is governed by:

$$F(\Delta\phi^*) = -2M_1[\Omega\tau/2]\sin(\Delta\phi^*) \tag{4.9}$$

where Ω is a solution to $\Omega = 2(\Omega_0 + M_2[\frac{\Omega\tau}{2}]\cos(\Delta\phi^*))$, $C_{IE}, C_{EE}, \omega_0, \tau \geq 0$ and $\delta \leq 0$. Either IP or AP stable solutions exist, depending on $C_{IE}, C_{EE}, \omega_0, \tau$ and δ. The transition between IP and AP occurs at a critical delay

$$\tau^* = (2/(2\omega_0 + \Omega))atan\left[\left(\frac{-\alpha\sin(\delta)C_{EE}}{\alpha C_{EE}\cos(\delta) - C_{IE}}\right)\right].$$

This implies the necessary condition $C_{EE} > C_{IE}/(\alpha\cos(\delta))$ for the existence of AP solutions. For $\tau = 0$, the deterministic stability function is reduced to

$$F(\Delta\phi^*) = -\big[C_{EE}\big]\sin[\Delta\phi^*].$$

The only stable solutions correspond to IP. The noise-free quasi-cycle phase dynamics converge to a fixed point, and thus do not allow spontaneous symmetry breaking. SAM theory leads to the stochastic stability function:

$$\tilde{F}(\Delta\phi) = M_2\big[\phi_1 - \phi_{2\tau}\big]\frac{Z_{2\tau}}{Z_1} - M_2\big[\phi_2 - \phi_{1\tau}\big]\frac{Z_{1\tau}}{Z_2} \tag{4.10}$$

which can be evaluated from simulations. Figs.4.3 (d,e) reveal that for weak delay, the stochastic and deterministic stability functions have the same stable fixed points, which correspond to IP states. But for the larger delay in Fig.4.3 (f), $\tilde{F}$ exhibits two symmetric stable fixed points at locations $\Delta\phi^* = -\beta, \beta$ with $0 < |\beta| < \pi$, corresponding to OPL states. Thus, for quasi-cycles, OPL relies on both delay and noise.

4.5 Delay and noise induce Out of Phase Locking

4.5.1 Out of Phase Locking in E-I networks

Limit cycle regime. The delay and noise intensity are now varied to reveal their effect on phase-locking. We first confirm previously published findings that OPL occurs via SSB in the limit cycle

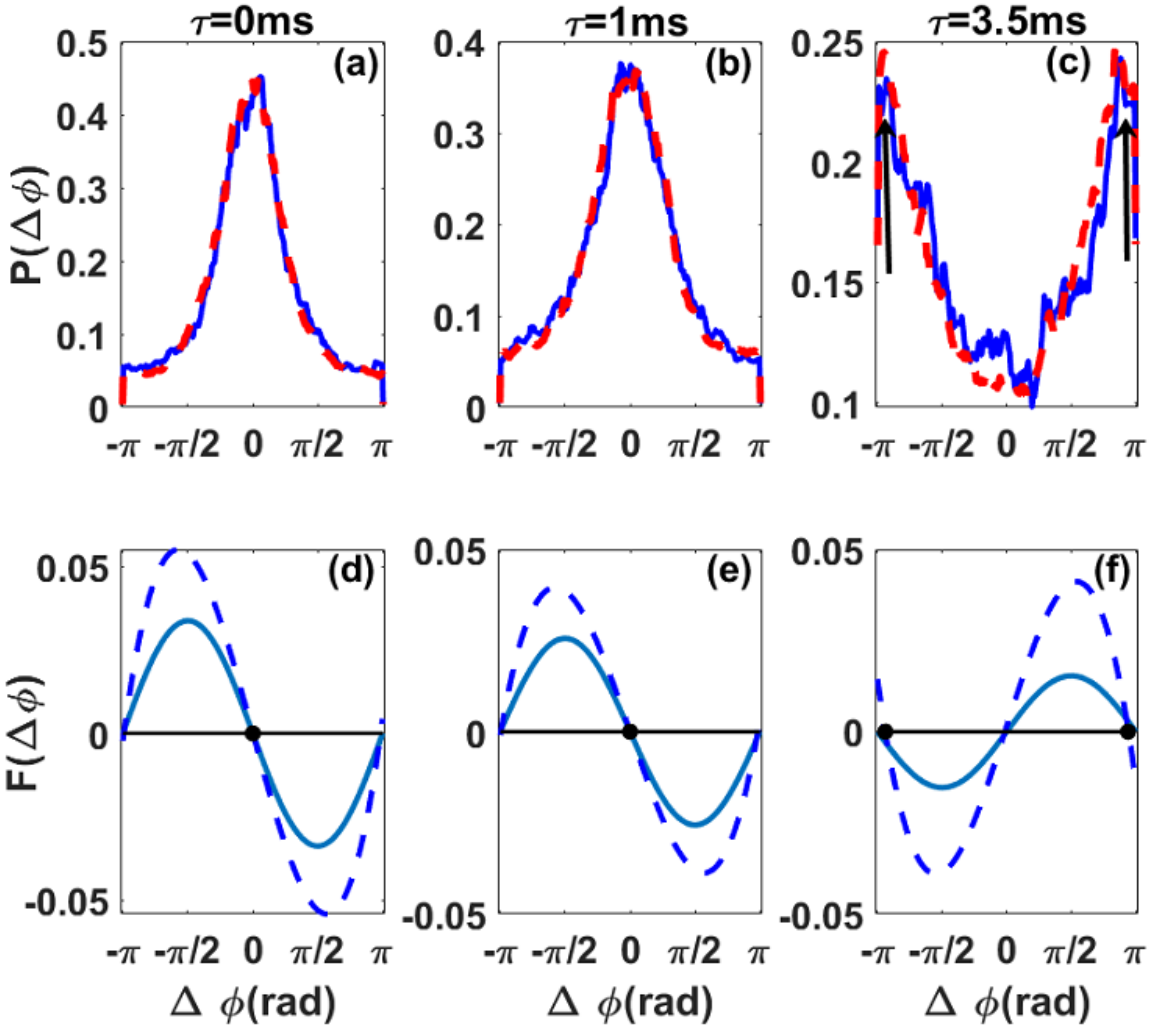

Figure 4.3: **OPL for quasi-cycles.** (a-c) Phase difference probability distributions for $\tau = 0, 1, 3.5$ ms from SAM theory (solid blue) and Hilbert transforms of simulations of SWC Eqs.4.1 (dashed red). For small τ (a-b), densities peak at $\Delta\phi = 0$ (IP), while for larger τ (c) OPL is seen with two symmetric peaks away from zero (IP) and $\pm\pi$ (AP) (see vertical black arrows). Good agreement is seen in all cases. d-f) Stability functions for, respectively, panels (a-c). Deterministic stability functions Eq.(4.9) (solid blue) with stable fixed points (black dots) located at zero for IP (d,e) and at $\pm\pi$ for AP (f). The stochastic stability function Eq.(4.10) (dashed blue) evaluated from simulations with noise, followed by smoothing with a third degree polynomial, show the same fixed points for (d,e), but OPL instead of AP for (f) as in (c). Parameters are as in Fig.4.1, except that the time step has been reduced to 0.01 ms for both the SAM and SWC simulations.

regime [72, 14] in Fig.4.4(a). This is done by looking at the deterministic situation where each network is in the limit-cycle regime prior to its coupling to the other network. The coupling induces OPL at a critical value of the delay $\tau_{crit} \approx 1.6ms$ (Fig.4.4(a)-black dots). One network becomes the leader and the other the laggard, the identity of which one depends on the initial conditions. There is no need for noise to observe such OPL states, i.e. OPL is a deterministic nonlinear phenomenon [14, 72].

However, there is no reversal of leadership unless there is an external intervention to induce it [16, 72]. Such lack of leadership exchange is thought to be problematic for inter-areal brain communication, since information is preferentially shared when one network leads the other, and dynamic exchange of leadership is required for an efficient bidirectional communication between areas [175]. The main effect of noise on the deterministic SSB property is to postpone the transition between the IP and OPL regimes, in proportion to the noise intensity, as well as induce changes in leadership. The initial condition will bias the solution towards one leader. At low noise, leadership changes can occur but are increasingly rare as τ moves further beyond the deterministic bifurcation point τ_{crit}.

Quasi-cycle regime. The underlying deterministic dynamics of the quasi-cycles decay to the fixed point in an underdamped manner, but a phase relationship between the two networks can nevertheless be computed during such decays. Then, only IP and AP are seen, with a transition from IP to AP at a critical delay $\tau = \tau^*$. This is shown in Fig.4.4(b) using linear stability analysis of the SWC system (solid black dots), as well as the SAM-derived stability function $F(\Delta\phi^*)$ in Eq.(4.9) (black circles). Noise then shifts the trivial IP and AP locations and induces OPL. The noise allows the dynamics to sample both the IP and the neighbouring AP attractors, yielding on average two OPL states. At τ^*, the noise samples each attractor similarly, with OPL around $\pm\pi/2$. Below τ^*, the IP attractor in the full SWC simulations appears destabilized by noise, but it is difficult to resolve whether this also represents an advancement of the bifurcation. This is due to critical slowing down near the bifurcation, which makes the simulations converge prohibitively slowly to pinpoint the bifurcation exactly in the presence of noise. But clearly the situation differs qualitatively from the postponement observed in Fig.4.4(a) for the limit cycles.

Beyond τ^*, the noise increasingly samples the AP attractor. The OPL asymptotically tends to

the deterministic AP value $\Delta\phi^* = |\pi|$ in a time proportional to noise strength. The abrupt IP-AP transition observed in the transient deterministic dynamics is smoothed by the noise and arises for smaller delays. It is important to mention that when the delay is varied in Fig.4.4, the intrinsic frequency of the networks remains almost constant. The main effect of the propagation delay is to induce AP states which are smoothed by noise to give rise to OPL states.

Such OPL attractors reflect a noise-induced transition where the parameter range for OPL increases with noise intensity. The networks also exchange leadership over time due to the noise, without external pulses, yielding a "dynamic OPL" for quasi-cycles. This suggests that coupled quasi-cycles are good candidates for flexible inter-areal network communication. OPL states are also excitation-dependent, since the aforementioned necessary condition implies that strong L_{EE} and weak L_{IE} values promote OPL.

Additive rather than multiplicative noises in the model formulation lead to similar results (not shown), as can be verified by replacing $g_1(E_i, I_i)$ and $g_2(E_i, I_i)$ by their respective numerically-determined means σ_E and σ_I (these densities are approximately Gaussian).

The mechanism of OPL in the coupled quasi-cycle regime is thus different from the one in the limit-cycle regime. The presence of noise is critical for OPL. The noise also allows a continual random exchange of leadership between the two networks - in fact, since the noise is required for sustained quasi-cycle behaviour, OPL is always present. As in the coupled limit cycle case, the initial condition will bias the leadership towards one network, and subsequent leadership exchanges are increasingly rare as the delay moves beyond the bifurcation point, or when the noise intensity is small. But in principle, each network spends half the time being the leader, as could be verified with long simulations (and perhaps unreasonably long when the noise is small or the delay is large). This has already been observed in another purely computational study [175].

Figure 4.4(b) also shows that the SAM theory predicts OPL states in the quasi-cycle regime. Further, it shows that the bifurcation is advanced to smaller and smaller delay values the stronger the noise is; this contrasts with what is seen in the coupled limit cycle case. More extensive simulations of the full network SWC equations are needed (i.e. more closed symbols closer to the zero axis need to be computed from very long simulations in Fig.4.4(b)) to determine whether advancement occurs, and if so, how well it agrees with the SAM theory. The advancement here also contrasts with other

delay-differential equations where additive or multiplicative noise postpones a Hopf bifurcation [149].

The Dip test for bimodality was performed on the $\Delta\phi(t) = \phi_1(t) - \phi_2(t)$ timeseries (Fig.4.5(a)). It is a statistical test that measures the level of multimodality of the density of a given timeseries (see Appendix). A value near zero indicates an unimodal timeseries, while increasing values of the Dip statistic is associated with more than one mode in the density. We observe an increase of the Dip values close to the deterministic transition between IP and AP locking. This shows the presence of multimodality (bimodality in this specific case) in the distribution of phase-difference values in the timeseries, and therefore the presence of OPL. In fact, it exposes a transition from zero to non-zero Dip values very near the same points as in Fig.4.4, as well as in Fig.4.3,(c) with modes located at $0 < |\beta| < |\pi|$. The Dip statistic thus corroborates the conclusion of bimodality, and therefore OPL. We also computed the Phase locking value (PLV) to measure the synchronization strength ([152] - see Appendix). Higher values of the PLV correspond to strong synchronization. The PLV is seen to capture well the transition between IP and OPL. PLV analysis reveals that the synchronization strength increases away from the IP-AP bifurcation in either direction (Fig.4.5(b)). The PLV is non-zero, and shows a minimum near the same transition points as in Fig.4.4 (b). We also observe a discrepancy between the SAM and the Hilbert transform at large noise intensity for both the Dip value and the PLV.

We finally note that the coupling delay has little effect on the oscillation frequency of each network. The frequency of the coupled-network is mainly determined by the parameters of each network and the connection coefficients.

4.5.2 Effect of Asymmetric Coupling and Network Heterogeneity

The case we have considered so far involves two identical networks that are coupled reciprocally using the same delays and coupling strengths. This is an oversimplification, as real neural networks are never identical and the connectivity is rarely symmetric. Is the mechanism of delay and noise-induced OPL still present when symmetry and homogeneity conditions are not present? Much work is required to fully address these issues. Our immediate, more restricted goal here is to show a generic effect of relaxing the requirement of symmetric coupling or network homogeneity. Specifically, we first consider the case where identical networks are asymmetrically coupled. Afterwards, we look at

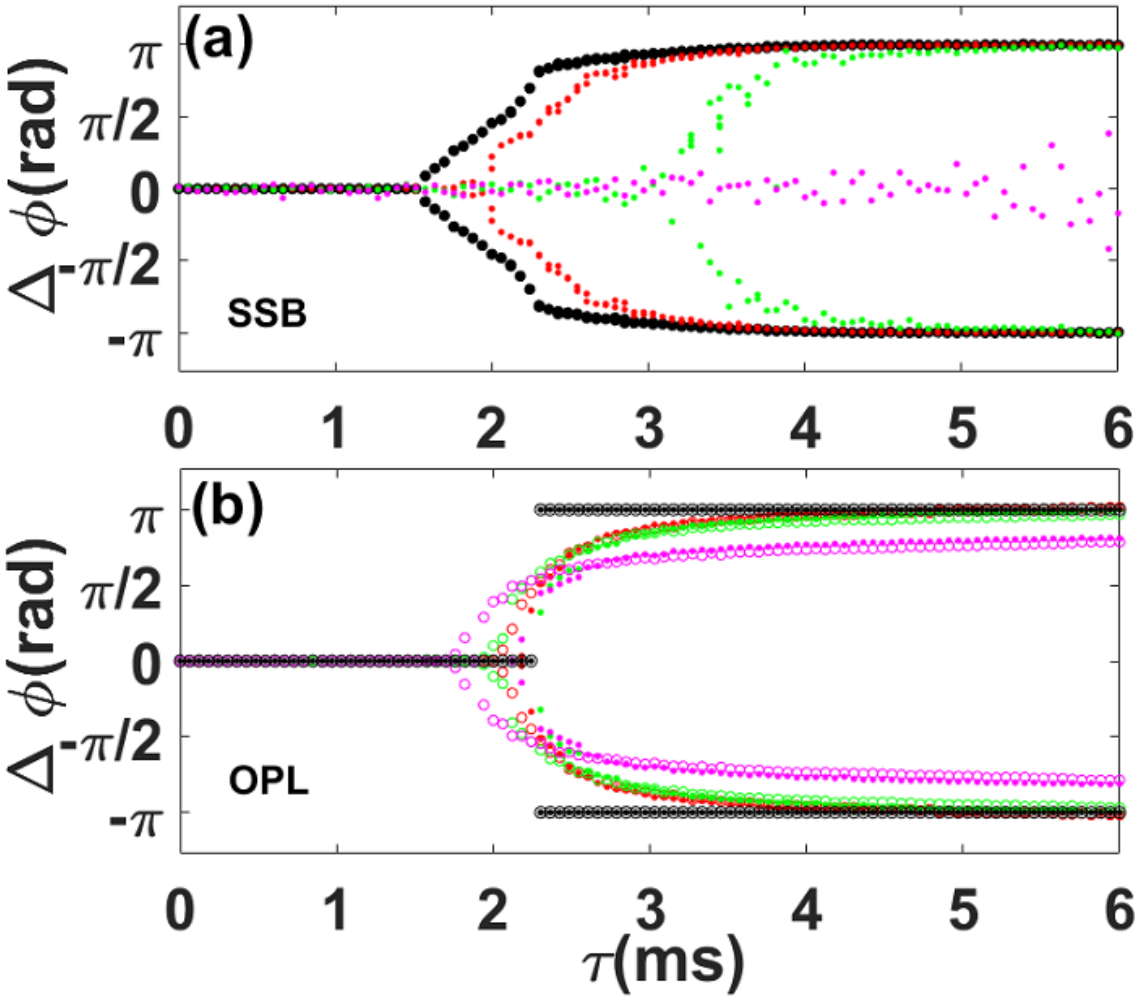

Figure 4.4: **Noise and delay-induced OPL.** (a) Coupled limit cycles. In the deterministic case ($\sigma = \sqrt{\sigma_E^2 + \sigma_I^2} = 0$, solid black dots), a bifurcation occurs from IP to OPL via spontaneous symmetry breaking at a critical delay value. OPL is further delayed (and IP stabilized) as σ increases (red: 0.0006, green: 0.0018, magenta: 0.0156). (b) Coupled quasi-cycles. Only a bifurcation from IP to AP is seen for $\sigma = 0$ (black). OPL is observed only in the noisy case. Phase differences are computed by applying Hilbert transforms to simulations of the SWC system (Eqs.4.1) (solid dots in (a) and (b), except for the black dots in (b)) and from the solutions of the SAM theory (open circles in (b)). Parameters for (a) are $L_{EE} = 1; L_{IE} = 0.5$ and $W_{EE} = 30.4$. In (b), we have $L_{EE} = 2, L_{IE} = 0.5$ and $W_{EE} = 27.4$. Other parameters are as in Fig.4.1. Due to the transient synchrony nature of the oscillations, phase differences were computed using the correlation function in (b) and other bifurcation diagrams below.

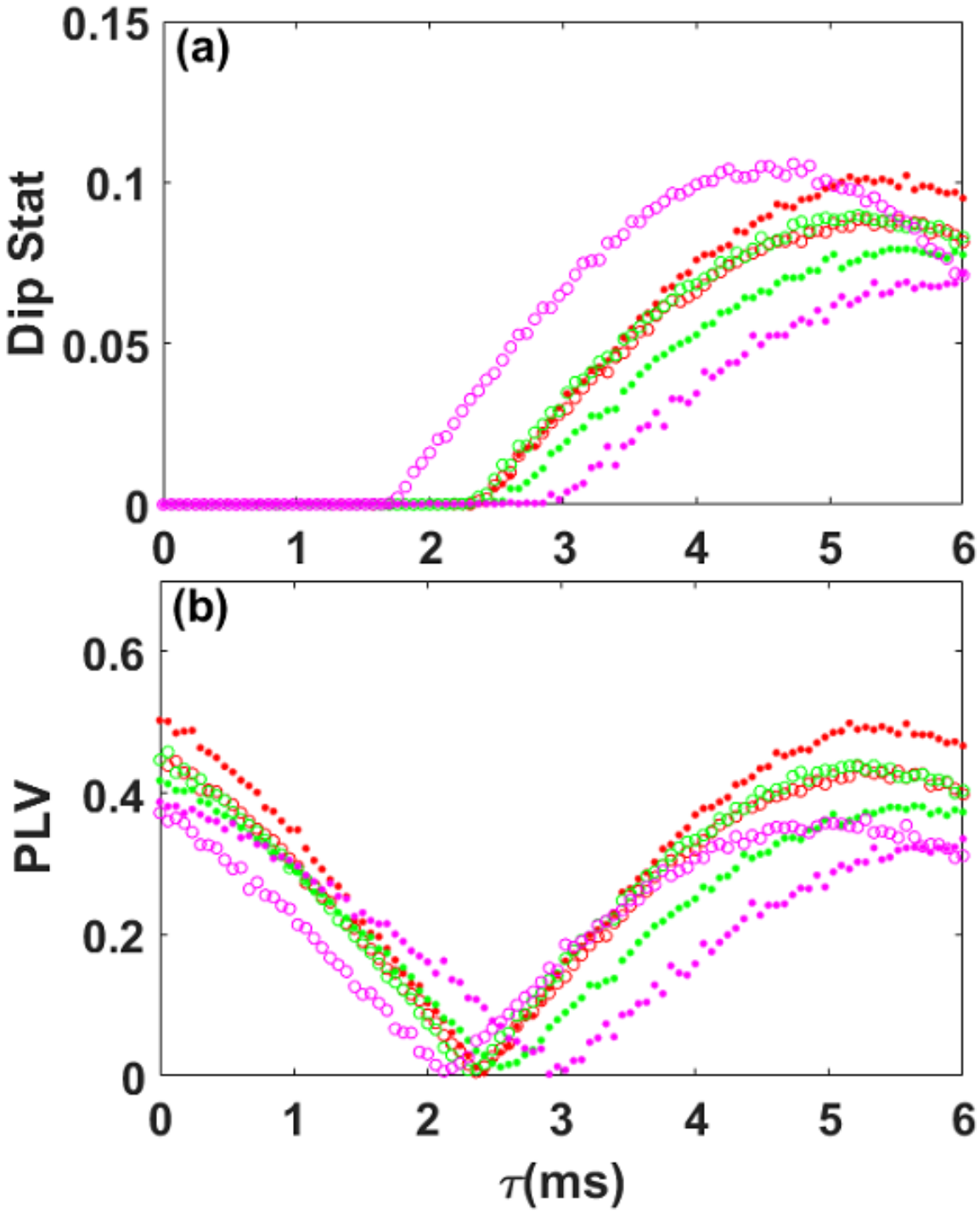

Figure 4.5: **Dip statistic and Phase-Locking-Value show signatures of OPL.** (a) Dip statistic versus lag assesses the presence of bimodality in the density of the time series, which is agreement with the appearance of OPL in Figs.4.3 and 4.4. (b) Phase-Locking-Value versus lag measures the degree of phase synchronization between two timeseries. The PLV was computed from the phase timeseries $\phi_1(t)$ and $\phi_2(t)$ using both the Hilbert transform (solid dots) and the SAM (circles). The PLV values are weaker at the transition between IP and AP locking, revealing the appearance of OPL states. All the parameters are the same as in Fig.4.4 (b).

the heterogeneous case when non-identical networks are symmetrically coupled.

The asymmetric case is set up by slightly decreasing the excitatory coupling from the first to the second network ($L_{EE}^{21} = 1.5; L_{EE}^{12} = 2$). Figure 4.6(a) shows that the asymmetry induces a small phase difference between the two networks even for the smallest delays, leading to a dominant directionality. Nevertheless, the mechanism of delay- and noise-induced OPL is still present, although with an intrinsic bias compared to the symmetric case. When the delay increases, a second branch eventually appears, i.e. another OPL state is induced. As in all the bifurcation diagrams up to now for stochastic dynamics, we plotted only the local extrema of the phase difference distribution. For a given delay, the two states are not symmetric as in the former case, but rather, one state is more stable than the other.

In the heterogeneous case in Fig.4.6(b), the external inhibitory input to the second network is slightly increased, but the connectivity coefficients are symmetric, and all other parameters identical. As in the asymmetric case, this also induces a phase difference between the networks. The mechanism of noise and delay-induced OPL is still present, but again with a bias. The heterogeneous case is qualitatively similar to the asymmetric case. All branches in(de)crease towards $\pm\pi$ when the delay is large.

Hence, for both of these specific examples of asymmetry and heterogeneity, the mechanism of delay and noise-induced occurs, along with dynamical changes in leadership. However, the amount of time one network leads the other is not the same as in the homogeneous and symmetric case. In fact one network leads the other one most of the time depending on the phase relation induced by the asymmetry or the heterogeneity. This mechanism is observed and persists when the asymmetry is weak and the heterogeneous networks are nearly identical. If the asymmetry is strong or the two networks are too different, the phase relation will be imposed by such asymmetry or heterogeneity. Then, one network will almost always be the leader, as the noise will rarely induce switches to the less stable state. Dynamic OPL is revealed using numerical simulations of Eqs.4.1 followed by Hilbert transforms, as well as the SAM Eqs.5 (for the heterogeneous and asymmetric case) and 7 (symmetric and homogeneous case).

Results from the Hilbert transform and the SAM are in good agreement for weak and intermediate values of the noise intensity (see red, green solid dots and circles in Fig.4.6). From the large noise

intensity, the results for the SAM and the Hilbert transform start to diverge as observed in the magenta solid dots and circles in Fig.4.6. The dynamics derived from the SAM Eqs.5,7 provide a good approximation for the envelope and phase of the LFPs derived in Eqs.4.1 for weak and intermediate values of the noise for the E-I network. However, quasi-cycles are also present in purely inhibitory networks. A natural question will be to understand the phase locking mechanism of such quasi-cycles.

4.5.3 OPL in inhibitory networks.

We finally considered two coupled identical inhibitory (I-I) networks. Each isolated I-I population with its all-to-all delayed inhibition can also exhibit either a noisy limit cycle or quasi-cycle [69, 141, 73, 132]. We coupled the two I-I populations with delayed long-range excitatory connections in the quasi-cycle regime as for the E-I networks discussed until now. The dynamics of the model is given by:

$$\begin{aligned}
\frac{dI_1(t)}{dt} &= -\alpha_I I_1(t) + \big[1 - I_1(t)\big]\beta_I f(s_{I_1}(t)) + g_1(I_1)\xi_{I_1}(t) \\
\frac{dI_2(t)}{dt} &= -\alpha_I I_2(t) + \big[1 - I_2(t)\big]\beta_I f(s_{I_2}(t)) + g_2(I_2)\xi_{I_2}(t) \\
s_{I_1}(t) &= h_1 - W I_1(t-\hat{\tau}) + L_1 I_2(t-\tau) \\
s_{I_2}(t) &= h_2 - W I_2(t-\hat{\tau}) + L_2 I_1(t-\tau)
\end{aligned} \tag{4.11}$$

$$\begin{aligned}
g_1(I_1) &= \sqrt{\frac{\alpha_I I_1(t) + \big[1 - I_1(t)\big]\beta_I f(s_{I_1}(t))}{N}} \\
g_2(I_2) &= \sqrt{\frac{\alpha_I I_2(t) + \big[1 - I_2(t)\big]\beta_I f(s_{I_2}(t))}{N}}\,.
\end{aligned} \tag{4.12}$$

As in the case of the coupled E-I networks, we define the noise intensities for each network as:

$$\sigma_1 = \left\langle \Big(g_1(I_1) \Big) \right\rangle \quad and \quad \sigma_2 = \left\langle \Big(g_2(I_2) \Big) \right\rangle .$$

For this case, an envelope-phase decomposition using the SAM as in the case of the coupled E-I networks is not yet available. We thus only consider numerical simulations and linear stability

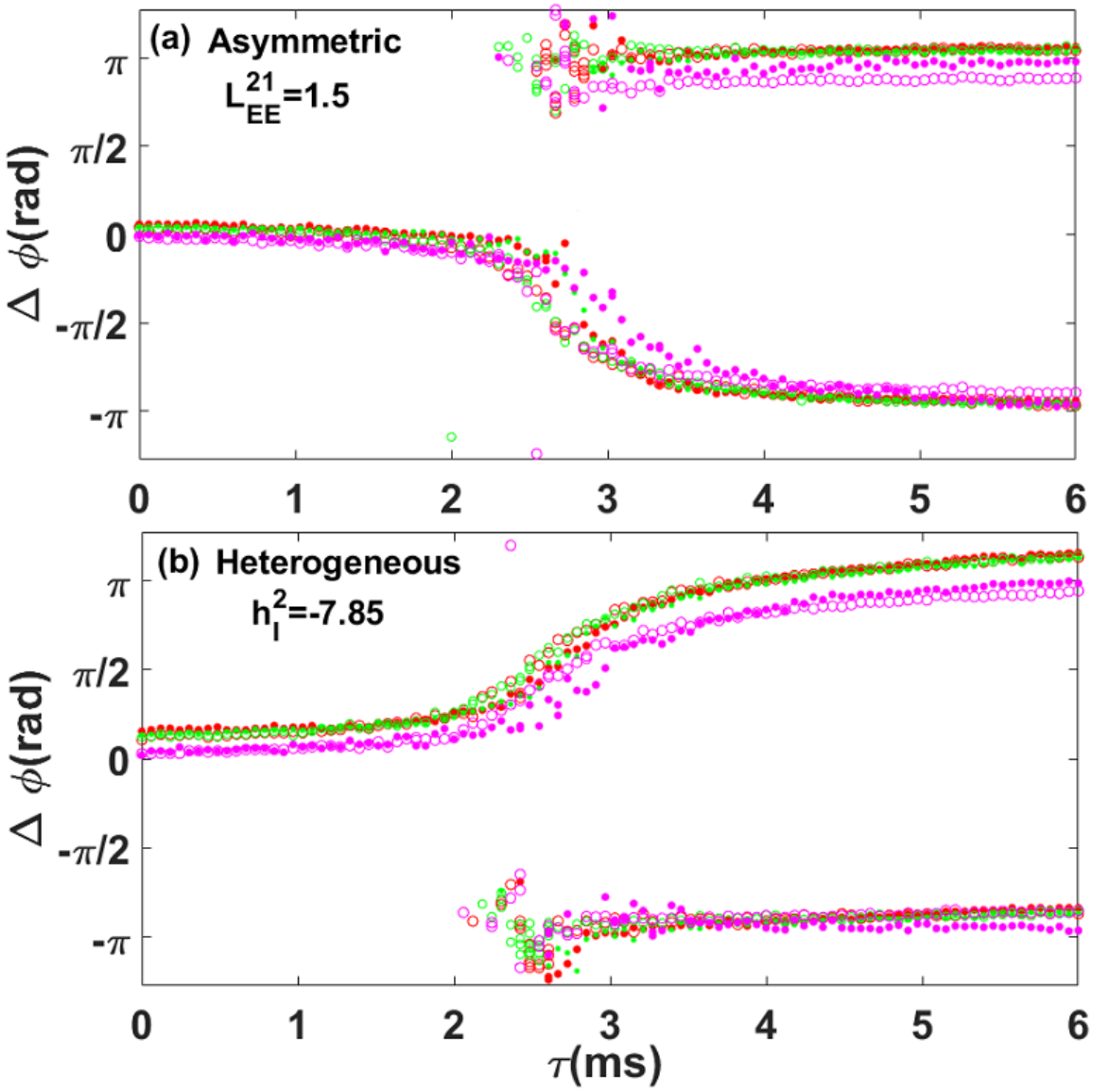

Figure 4.6: **Noise and delay-induced OPL in asymmetrically coupled, or heterogeneous but symmetrically coupled E-I networks.** **(a)** The asymmetric case where the excitatory connectivity from the first to second network is slightly decreased compared to the reverse excitatory connectivity ($L_{EE}^{21} = 1.5$; $L_{EE}^{12} = 2$). The other parameters are identical for the two networks. **(b)** The heterogeneous case where the inhibitory input to the second network is slightly increased compared to the same input applied in the first network ($h_I^1 = -8$; $h_I^2 = -7.85$). Connectivities are kept symmetric as previously in Fig.4.4. For all panels and figures, solid dots are phase locking states obtained using the Hilbert transform, while circles are obtained through Stochastic Averaging Method (SAM) Eqs 5. Red corresponds to weak, green intermediate and magenta strong values of the noise intensity (values are as in Fig.4.4).

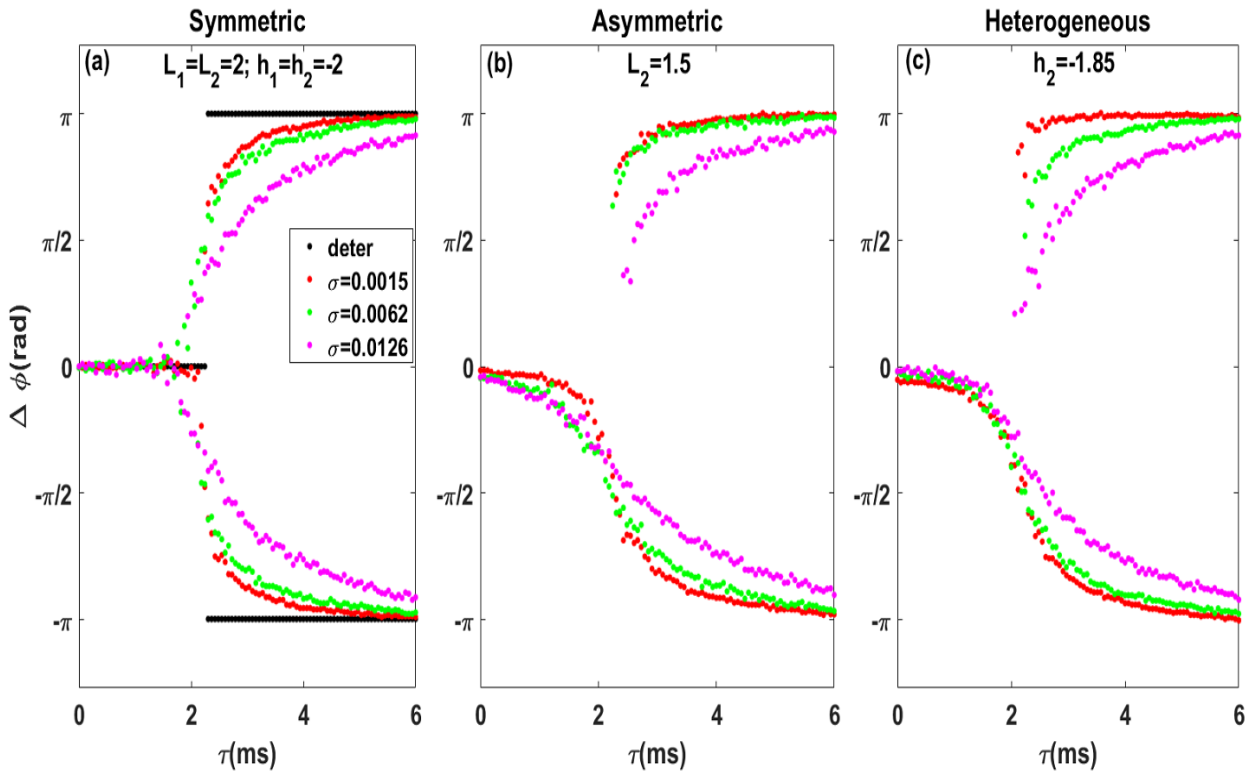

Figure 4.7: **Noise-induced Out of Phase locking in two purely inhibitory networks coupled via long-range delayed excitatory connections (ING mechanism).** For all curves, red corresponds to weak, green to intermediate and magenta to strong noise. The respective values of the noise intensities are specified in the legend of the left panel. **(a)** The symmetric case with black dots correspond to the deterministic phase locking computed through linear stability analysis. **(b)** The asymmetric case where the connectivity is enhanced in one direction compared to the other. **(c)** The heterogeneous case where the external current applied to the second network is slightly greater. We observe that noise and delay induce out of phase locking, phase locking persist for the asymmetric and heterogeneous cases. Simulations are performed using the phase signal extracted through Hilbert transform. For the symmetric case, the parameters are chosen as follows: $\alpha_I = 0.1$, $\beta_I = 2$, $W = 30$, $\hat{\tau} = 5.5ms$, $h_1 = h_2 = -2$, $L_1 = L_2 = 2$. For the asymmetric case, we have slightly decreased L_2 to 1.5 and for the heterogeneous case we have increased h_2 to -7.85. The noise intensities are $\sigma \approx \sigma_1 \approx \sigma_2$.

analysis. We define the local field potential (LFPs) as $\tilde{V}_{I_1}(t) = c(I_1(t) - I_{10})$ $\tilde{V}_{I_2}(t) = c(I_2(t) - I_{20})$ where I_{10} and I_{20} are the stable fixed points of network 1 and 2, $c = \sqrt{N}$ for the case of the multiplicative noise and $c = 1$ for the additive noise. The phase difference is again $\Delta\phi(t) = \phi_1(t) - \phi_2(t)$, where $\phi_1(t)$ is the phase of the signal $\tilde{V}_{I_1}(t)$ and $\phi_2(t)$ the one of $\tilde{V}_{I_2}(t)$, both extracted through the Hilbert transform. We perform the same analysis as in the case of the coupled E-I networks.

We first consider the symmetric case, choosing the delay as the bifurcation parameter for different noise intensities σ. We observe in Fig.4.7 that the mechanism of delay and noise-induced OPL is qualitatively the same to that observed in the case of coupled E-I networks. The noise smooths the abrupt transition between the deterministic IP and AP locking states, and induces OPL states. We also consider the symmetric and heterogeneous cases as previously described for the coupled E-I networks. The mechanism of delay and noise induced OPL again survives these losses of symmetry, but with a bias compared to the symmetric case. The presence of this mechanism in the case of purely inhibitory networks suggests that it only depends on the dynamical regime of the oscillations in each network, ie on their noise-induced nature. We then expect to observe similar delay and noise-induced OPL more generally if the corresponding networks in isolation exhibit quasi-cycles.

4.6 Discussion

In summary, a robust noise-induced, delay-dependent OPL mechanism was revealed by an envelope-phase decomposition of the coupled quasi-cycle dynamics. Although no spontaneous symmetry breaking arises, the noise samples attractor dynamics corresponding to both IP and AP dynamics, leading to OPL well before the deterministic bifurcation point. The lead-lag relationship displays random reversals, an intrinsic property of the coupled system. This mechanism is observed in both coupled PING and ING type systems. It persists but with a bias when the networks are weakly asymmetrically coupled, or when they are heterogeneous but nearly identical.

The SAM used here requires underdamped oscillatory motion in each network prior to coupling. It has been extended here to include delays. It allows an accurate description of the envelope and phase dynamics of the nonlinear PING LFPs for weak and intermediate value of the noise. It constitutes a new appropriate theoretical framework for the study of phase synchronization in quasi-cycles. However, we found that for strong values of the noise intensity, the agreement with

the Hilbert transform was not so good. There may be many reasons for discrepancy. Firstly, we compare the SAM equations which are derived from the linear equations sustained by noise (see Appendix, Eqs.4.14) with the full SWC which is a stochastic nonlinear model. Neglecting nonlinear terms to calculate the SAM could lead to some discrepancy. In fact, for high values of the noise intensity, the agreement between the network frequencies from the full nonlinear SWC model and the LNA dynamics significantly worsens (not shown). Since the phase relation depends on the network frequencies, the immediate consequence is a disagreement between the SAM and the full nonlinear SWC model.

Secondly, we found that numerical simulations of the envelope-phase dynamics obtained via the SAM can be problematic. The classical Euler-Maruyama iterative scheme was inaccurate in the sense that the envelope process could be negative during the simulation process. To deal with this pathological issue, we consider a very small time-step, and replace the envelope processes by their absolute values at each simulation time-step. This allows the processes to remain positive. This numerical scheme may cause convergence inaccuracies when the amplitude process is close to zero, particularly for strong noise.

Despite these limitations, the SAM method remains a good theoretical framework for the study of envelope and phase dynamics of isolated and coupled quasi-cycles. It exhibits all the qualitative behavior of phase and amplitude dynamics present in the full nonlinear SWC model. The mechanism of delay-dependent, noise-induced out of phase locking exposed here through the SAM and the Hilbert transform of Eqs.4.1 is robust, flexible and general for rhythm-based communication purposes. The potential ability to communicate under the realistic conditions reported here opens the way for information transfer studies to obtain deeper insights into activity coordination in complex networks. This would require extending the methods used here to dimensions greater than two and with the necessary network topology. Also, the inclusion of more realistic external signals, such as correlated noise or periodic inputs, promises to yield interesting phenomena.

4.7 Appendix

4.7.1 Linear Noise approximation

We first consider the deterministic part of Eqs.4.1 ($g_i = 0$, i=1,2). Their corresponding fixed points $(E_{10}, I_{10}, E_{20}, I_{20})$ can be obtained as the solutions of the following system:

$$\begin{aligned} -\alpha_E E_{10} + (1 - E_{10})\beta_E f(s_{E_{10}}) &= 0 \\ -\alpha_I I_{10} + (1 - I_{10})\beta_I f(s_{I_{10}}) &= 0 \\ -\alpha_E E_{20} + (1 - E_{20})\beta_E f(s_{E_{20}}) &= 0 \\ -\alpha_I I_{20} + (1 - I_{20})\beta_I f(s_{I_{20}}) &= 0 \end{aligned} \tag{4.13}$$

with

$$\begin{aligned} s_{E_{10}} &= W_{EE}E_{10} - W_{EI}I_{10} + h_E + L^{12}_{EE}E_{20}; \quad s_{I_{10}} = W_{IE}E_{10} - W_{II}I_{10} + h^1_I + L^{12}_{IE}E_{20} \\ s_{E_{20}} &= W_{EE}E_{20} - W_{EI}I_{20} + h_E + L^{21}_{EE}E_{10}; \quad s_{I_{20}} = W_{IE}E_{20} - W_{II}I_{20} + h^2_I + L^{21}_{IE}E_{10}\,. \end{aligned}$$

We are interested in the parameter regime where such a fixed point is a stable focus. The dynamics therefore converge in a decaying oscillatory manner toward the fixed point in the absence of noise. When noise is added, the dynamics are fluctuations around the fixed points. Following the system size-expansion [217, 172, 28, 19], these fluctuations can be sought in the following form:

$$\tilde{V}^i_E = \sqrt{N_E}\big(E_i - E_{i0}\big),\;\; \tilde{V}^i_I = \sqrt{N_I}\big(I_i - I_{i0}\big),\;\; i = 1, 2\,.$$

Plugging theses expressions into Eqs.4.1, and keeping terms of order $O\big(\sqrt{N_{E,I}}\big)$, we obtain the following dynamics for the local field potential (LFPs) fluctuations:

$$\begin{aligned} \frac{d\tilde{V}^1_E}{dt} &= A^1_{EE}\tilde{V}^1_E(t) + A^1_{EI}\tilde{V}^1_I(t) + C^{12}_{EE}\tilde{V}^2_E(t-\tau) + \sigma_{E_1}\xi_{E_1} \\ \frac{d\tilde{V}^1_I}{dt} &= A^1_{IE}\tilde{V}^1_E(t) + A^1_{II}\tilde{V}^1_I(t) + C^{12}_{IE}\tilde{V}^2_E(t-\tau) + \sigma_{I_1}\xi_{I_1} \end{aligned} \tag{4.14}$$

$$\frac{d\tilde{V}_E^2}{dt} = A_{EE}^2\tilde{V}_E^2(t) + A_{EI}^2\tilde{V}_I^2(t) + C_{EE}^{21}\tilde{V}_E^1(t-\tau) + \sigma_{E_2}\xi_{E_2}$$
$$\frac{d\tilde{V}_I^2}{dt} = A_{IE}^2\tilde{V}_E^2(t) + A_{II}^2\tilde{V}_I^2(t) + C_{IE}^{21}\tilde{V}_E^1(t-\tau) + \sigma_{I_2}\xi_{I_2}\,,$$

where the parameters of each network are given by:

$$A_{EE}^1 = -\alpha_E - \beta_E f\big(s_{E_{10}}\big) + \big(1-E_{10}\big)\beta_E f^{'}\big(s_{E_{10}}\big)W_{EE}$$
$$A_{EI}^1 = -c_{EI}\big(1-E_{10}\big)\beta_E f^{'}\big(s_{E_{10}}\big)W_{EI};\quad A_{IE}^1 = c_{IE}\big(1-I_{10}\big)\beta_I f^{'}\big(s_{I_{10}}\big)W_{IE}$$
$$A_{II}^1 = -\alpha_I - \beta_I f\big(s_{I_{10}}\big) - \big(1-I_{10}\big)\beta_I f^{'}\big(s_{I_{10}}\big)W_{II}$$
$$A_{EE}^2 = -\alpha_E - \beta_E f\big(s_{E_{20}}\big) + \big(1-E_{20}\big)\beta_E f^{'}\big(s_{E_{20}}\big)W_{EE}$$
$$A_{EI}^2 = -c_{EI}\big(1-E_{20}\big)\beta_E f^{'}\big(s_{E_{20}}\big)W_{EI};\quad A_{IE}^2 = c_{IE}\big(1-I_{20}\big)\beta_I f^{'}\big(s_{I_{20}}\big)W_{IE}$$
$$A_{II}^2 = -\alpha_I - \beta_I f\big(s_{I_{20}}\big) - \big(1-I_{20}\big)\beta_I f^{'}\big(s_{I_{20}}\big)W_{II}$$

and

$$\sigma_{E_1} = \sqrt{2\alpha_E E_{10}}\quad \sigma_{I_1} = \sqrt{2\alpha_I I_{10}}\quad \sigma_{E_2} = \sqrt{2\alpha_E E_{20}}\quad \sigma_{I_2} = \sqrt{2\alpha_I I_{20}}\quad c_{EI} = \sqrt{N_E/N_I}\quad c_{IE} = \sqrt{N_I/N_E}\,.$$

The effective couplings are:

$$C_{EE}^{12} = \big(1-E_{10}\big)\beta_E f^{'}\big(s_{E_{10}}\big)L_{EE}^{12};\quad C_{IE}^{12} = c_{IE}\big(1-I_{10}\big)\beta_I f^{'}\big(s_{I_{10}}\big)L_{IE}^{12}$$
$$C_{EE}^{21} = \big(1-E_{20}\big)\beta_E f^{'}\big(s_{E_{20}}\big)L_{EE}^{21};\quad C_{IE}^{21} = c_{IE}\big(1-I_{20}\big)\beta_I f^{'}\big(s_{I_{20}}\big)L_{IE}^{21}\,.$$

This system of four linear equations sustained by noise is a good representation of the dynamics of excitatory and inhibitory LFPs in the quasi-cycle regime. This can be seen as a system of two connected networks of excitatory and inhibitory populations with effective intra-population connectivity coefficients $A_{EE}^i, A_{EI}^i, A_{IE}^i$ and $A_{II}^i, i = 1, 2$. The noise intensities in the E and I populations are, respectively, σ_{E_i} and $\sigma_{I_i}, i = 1, 2$. The effective long range excitatory connections from the first network to the E and I populations of the second network are C_{EE}^{21} and C_{IE}^{21}, respectively, while the effective long range excitatory connections from the second network to the excitatory and inhibitory populations of the first network are respectively C_{EE}^{12} and C_{IE}^{12}. Following the expressions

of the effective long range excitatory connections C_{EE}^{ij} and $C_{IE}^{ij}, i \neq j = 1, 2$, the two networks have effective connectivities that are different from the anatomical connectivity since $C_{EE}^{ij} \neq L_{EE}^{ij}$ and $C_{IE}^{ij} \neq L_{IE}^{ij}$. Moreover, $C_{EE}^{12} \neq C_{EE}^{21}$ and $C_{IE}^{12} \neq C_{EE}^{21}$ for the asymmetric and heterogeneous cases.

4.7.2 Linear stability

In the quasi-cycle regime, the dynamics of the LFPs converge to zero in the absence of noise. However we can still extract important properties from the deterministic decay dynamics. Here, we investigate the properties of the decay dynamics in the absence of noise. The dynamics of such decays are given by ($\sigma_{E_1} = \sigma_{E_2} = \sigma_{I_1} = \sigma_{I_2} = 0$):

$$\begin{aligned}
\frac{d\tilde{V}_E^1(t)}{dt} &= A_{EE}^1 \tilde{V}_E^1(t) + A_{EI}^1 \tilde{V}_I^1(t) + C_{EE}^{12} \tilde{V}_E^2(t-\tau) \\
\frac{d\tilde{V}_I^1(t)}{dt} &= A_{IE}^1 \tilde{V}_E^1(t) + A_{II}^1 \tilde{V}_I^1(t) + C_{IE}^{12} \tilde{V}_E^2(t-\tau) \\
\frac{d\tilde{V}_E^2(t)}{dt} &= A_{EE}^2 \tilde{V}_E^2(t) + A_{EI}^2 \tilde{V}_I^2(t) + C_{EE}^{21} \tilde{V}_E^1(t-\tau) \\
\frac{d\tilde{V}_I^2(t)}{dt} &= A_{IE}^2 \tilde{V}_E^2(t) + A_{II}^2 \tilde{V}_I^2(t) + C_{IE}^{21} \tilde{V}_E^1(t-\tau).
\end{aligned} \tag{4.15}$$

We look for solutions of these equations in the form of exponential decays:

$$\begin{aligned}
\tilde{V}_E^1(t) &= \tilde{A}_E^1 \exp\big(\lambda t\big), \quad \tilde{V}_I^1(t) = \tilde{A}_I^1 \exp\big(\lambda t\big) \\
\tilde{V}_E^2(t) &= \tilde{A}_E^2 \exp\big(\lambda t\big), \quad \tilde{V}_I^2(t) = \tilde{A}_I^2 \exp\big(\lambda t\big).
\end{aligned}$$

Replacing these expressions into the noise-free dynamics Eqs.4.15 above yields the following relationships:

$$\begin{aligned}
\tilde{\alpha}_{IE}^1 &= \frac{\tilde{A}_I^1}{\tilde{A}_E^1} = \frac{A_{IE}^1 C_{EE}^{12} - C_{IE}^{12}\big(A_{EE}^1 - \lambda\big)}{A_{EI}^1 C_{IE}^{12} - C_{EE}^{12}\big(A_{II}^1 - \lambda\big)} \\
\tilde{\alpha}_E^{21} &= \frac{\tilde{A}_E^2}{\tilde{A}_E^1} = \frac{\big(A_{EE}^1 - \lambda\big)\big(A_{II}^1 - \lambda\big) - A_{IE}^1 A_{EI}^1}{A_{EI}^1 C_{IE}^{12} - C_{EE}^{12}\big(A_{II}^1 - \lambda\big)} \cdot \exp(\lambda\tau) \\
\tilde{\alpha}_{IE}^2 &= \frac{\tilde{A}_I^2}{\tilde{A}_E^2} = \frac{A_{IE}^2 C_{EE}^{21} - C_{IE}^{21}\big(A_{EE}^2 - \lambda\big)}{A_{EI}^2 C_{IE}^{21} - C_{EE}^{21}\big(A_{II}^2 - \lambda\big)} \\
\tilde{\alpha}_E^{12} &= \frac{\tilde{A}_E^1}{\tilde{A}_E^2} = \frac{\big(A_{EE}^2 - \lambda\big)\big(A_{II}^2 - \lambda\big) - A_{IE}^2 A_{EI}^2}{A_{EI}^2 C_{IE}^{21} - C_{EE}^{21}\big(A_{II}^2 - \lambda\big)} \cdot \exp(\lambda\tau).
\end{aligned}$$

Using the relation $\tilde{\alpha}_E^{12} = (\tilde{\alpha}_E^{21})^{-1}$ we obtain the following characteristic equation:

$$\Big[\big(A_{II}^2 - \lambda\big)\big(A_{EE}^2 - \lambda\big) - A_{EI}^2 A_{IE}^2\Big]\Big[\big(A_{II}^1 - \lambda\big)\big(A_{EE}^1 - \lambda\big) - A_{EI}^1 A_{IE}^1\Big] = e^{-2\lambda\tau}\Big[A_{EI}^1 C_{IE}^{12} - C_{EE}^{12}\big(A_{II}^1 - \lambda\big)\Big]\Big[A_{EI}^2 C_{IE}^{21} - C_{EE}^{21}\big(A_{II}^2 - \lambda\big)\Big].$$

The value of the amplitude ratio can be obtained by first solving the characteristic equation. The solution of interest is the eigenvalue with the largest real part (note that this real part should be negative since we are in the quasi-cycle regime). Replacing this particular eigenvalue in the expression of the amplitude ratio above allows us to obtain the right expression for these ratios. Note that the ratios are complex quantities and can therefore be put in exponential form, with the argument of the exponential being the phase difference and its modulus the real amplitude ratio. We then obtain the amplitude ratio and phase difference between the inhibitory and excitatory LFPs in each network as:

$$\alpha_1 = abs(\tilde{\alpha}_{IE}^1) \quad \alpha_2 = abs(\tilde{\alpha}_{IE}^2) \tag{4.16}$$

$$\delta_1 = arg(\tilde{\alpha}_{IE}^1) \quad \delta_2 = arg(\tilde{\alpha}_{IE}^2) \tag{4.17}$$

and the phase difference between excitatory populations of different networks (1 and 2 respectively) as:

$$\Delta\phi = arg\big(\tilde{\alpha}_E^{12}\big)\,. \tag{4.18}$$

Similar analysis was done for the case of purely inhibitory populations (not shown here) to compute the deterministic phase difference in solid black dots Fig.4.7-(a).

4.7.3 Stochastic Averaging Method (SAM) and Envelope-Phase Decomposition

We are interested in the fluctuations from the baseline activities (LNA): $\tilde{V}_E^i(t) = c_E\big(E_i(t) - E_{i0}\big)$; $\tilde{V}_I^i(t) = c_I\big(I_i(t) - I_{i0}\big)$ where E_{0i} and I_{0i} are the deterministic fixed point activities. We are further interested in the slow envelope and phase dynamics of the fluctuations. For that, we seek solutions in the form of Eqs.4.4 and plug these expressions in the equations for the LFPs, Eqs.4.14.

This yields a system of differential equations in terms of Z_1, Z_2, ϕ_1 and ϕ_2 as follows:

$$\begin{aligned}
\dot{Z}_1(t) &= F_1^1\left(Z_{1,2},\phi_{1,2}\right) + G_1^1\left(Z_{1,2},\phi_{1,2},\xi_{E_{1,2}},\xi_{I_{1,2}}\right)\\
\dot{\phi}_1(t) &= F_2^1\left(Z_{1,2},\phi_{1,2}\right) + G_2^1\left(Z_{1,2},\phi_{1,2},\xi_{E_{1,2}},\xi_{I_{1,2}}\right)\\
\dot{Z}_2(t) &= F_1^2\left(Z_{1,2},\phi_{1,2}\right) + G_1^2\left(Z_{1,2},\phi_{1,2},\xi_{E_{1,2}},\xi_{I_{1,2}}\right)\\
\dot{\phi}_2(t) &= F_2^2\left(Z_{1,2},\phi_{1,2}\right) + G_2^2\left(Z_{1,2},\phi_{1,2},\xi_{E_{1,2}},\xi_{I_{1,2}}\right)
\end{aligned} \tag{4.19}$$

where

$$F_1^1\left(Z_{1,2},\phi_{1,2}\right) = \frac{1}{\alpha_1\sin(\delta_1)}\left[\alpha_1 f_1^1\left(Z_{1,2},\phi_{1,2}\right)\sin(\omega_0 t+\phi_1(t)+\delta_1) - f_2^1\left(Z_{1,2},\phi_{1,2}\right)\sin(\omega_0 t+\phi_1(t))\right]$$

$$F_2^1\left(Z_{1,2},\phi_{1,2}\right) = \frac{1}{\alpha_1 Z_1\sin(\delta_1)}\left[\alpha_1 f_1^1\left(Z_{1,2},\phi_{1,2}\right)\cos(\omega_0 t+\phi_1(t)+\delta_1) - f_2^1\left(Z_{1,2},\phi_{1,2}\right)\cos(\omega_0 t+\phi_1(t))\right]$$

$$F_1^2\left(Z_{1,2},\phi_{1,2}\right) = \frac{1}{\alpha_2\sin(\delta_2)}\left[\alpha_2 f_1^2\left(Z_{1,2},\phi_{1,2}\right)\sin(\omega_0 t+\phi_2(t)+\delta_2) - f_2^2\left(Z_{1,2},\phi_{1,2}\right)\sin(\omega_0 t+\phi_2(t))\right]$$

$$F_2^2\left(Z_{1,2},\phi_{1,2}\right) = \frac{1}{\alpha_2 Z_2\sin(\delta_2)}\left[\alpha_2 f_1^2\left(Z_{1,2},\phi_{1,2}\right)\cos(\omega_0 t+\phi_2(t)+\delta_2) - f_2^2\left(Z_{1,2},\phi_{1,2}\right)\cos(\omega_0 t+\phi_2(t))\right]$$

$$G_1^1\left(Z_{1,2},\phi_{1,2},\xi_{E,I_{1,2}}\right) = \frac{1}{\alpha_1\sin(\delta_1)}\left[\alpha_1 g_1^1\left(Z_{1,2},\phi_{1,2},\xi_{E,I_{1,2}}\right)\sin(\omega_0 t+\phi_1(t)+\delta_1) - g_2^1\left(Z_{1,2},\phi_{1,2},\xi_{E,I_{1,2}}\right)\sin(\omega_0 t+\phi_1(t))\right]$$

$$G_2^1\left(Z_{1,2},\phi_{1,2},\xi_{E,I_{1,2}}\right) = \frac{1}{\alpha_1 Z_1\sin(\delta_1)}\left[\alpha_1 g_1^1\left(Z_{1,2},\phi_{1,2},\xi_{E,I_{1,2}}\right)\cos(\omega_0 t+\phi_1(t)+\delta_1) - g_2^1\left(Z_{1,2},\phi_{1,2},\xi_{E,I_{1,2}}\right)\cos(\omega_0 t+\phi_1(t))\right]$$

$$G_1^2\left(Z_{1,2},\phi_{1,2},\xi_{E,I_{1,2}}\right) = \frac{1}{\alpha_2\sin(\delta_2)}\left[\alpha_2 g_1^2\left(Z_{1,2},\phi_{1,2},\xi_{E,I_{1,2}}\right)\sin(\omega_0 t+\phi_2(t)+\delta_2) - g_2^2\left(Z_{1,2},\phi_{1,2},\xi_{E,I_{1,2}}\right)\sin(\omega_0 t+\phi_2(t))\right]$$

$$G_2^2\left(Z_{1,2},\phi_{1,2},\xi_{E,I_{1,2}}\right) = \frac{1}{\alpha_2 Z_2\sin(\delta_2)}\left[\alpha_2 g_1^2\left(Z_{1,2},\phi_{1,2},\xi_{E,I_{1,2}}\right)\cos(\omega_0 t+\phi_2(t)+\delta_2) - g_2^2\left(Z_{1,2},\phi_{1,2},\xi_{E,I_{1,2}}\right)\cos(\omega_0 t+\phi_2(t))\right]$$

$$\begin{aligned}
f_1^1\left(Z_{1,2},\phi_{1,2}\right) &= \omega_0 Z_1(t)\sin(\omega_0 t+\phi_1(t)) + A_{EE}^1 Z_1\cos(\omega_0 t+\phi_1(t)) + A_{EI}^1\alpha_1 Z_1\cos(\omega_0 t+\phi_1(t)+\delta_1)\\
&\quad + C_{EE}^{12} Z_2(t-\tau)\cos(\omega_0 t-\omega_0\tau+\phi_2(t-\tau))\\
f_2^1\left(Z_{1,2},\phi_{1,2}\right) &= \alpha_1\omega_0 Z_1(t)\sin(\omega_0 t+\phi_1(t)+\delta_1) + A_{IE}^1 Z_1\cos(\omega_0 t+\phi_1(t)) + A_{II}^1\alpha_1 Z_1\cos(\omega_0 t+\phi_1(t)+\delta_1)\\
&\quad + C_{IE}^{12} Z_2(t-\tau)\cos(\omega_0 t-\omega_0\tau+\phi_2(t-\tau))\\
f_1^2\left(Z_{1,2},\phi_{1,2}\right) &= \omega_0 Z_2(t)\sin(\omega_0 t+\phi_2(t)) + A_{EE}^2 Z_2\cos(\omega_0 t+\phi_2(t)) + A_{EI}^2\alpha_2 Z_2\cos(\omega_0 t+\phi_2(t)+\delta_2)\\
&\quad + C_{EE}^{21} Z_1(t-\tau)\cos(\omega_0 t-\omega_0\tau+\phi_1(t-\tau))\\
f_2^2\left(Z_{1,2},\phi_{1,2}\right) &= \alpha_2\omega_0 Z_2(t)\sin(\omega_0 t+\phi_2(t)+\delta_2) + A_{IE}^2 Z_2\cos(\omega_0 t+\phi_2(t)) + A_{II}^2\alpha_2 Z_2\cos(\omega_0 t+\phi_2(t)+\delta_2)\\
&\quad + C_{IE}^{21} Z_1(t-\tau)\cos(\omega_0 t-\omega_0\tau+\phi_1(t-\tau))
\end{aligned}$$

$$g_1^1\left(Z_{1,2},\phi_{1,2},\xi_{E_{1,2}},\xi_{I_{1,2}}\right) = \sigma_{E_1}\xi_{E_1}(t); \quad g_2^1\left(Z_{1,2},\phi_{1,2},\xi_{E_{1,2}},\xi_{I_{1,2}}\right) = \sigma_{I_1}\xi_{I_1}(t);$$

$$g_1^2\left(Z_{1,2},\phi_{1,2},\xi_{E_{1,2}},\xi_{I_{1,2}}\right) = \sigma_{E_2}\xi_{E_2}(t); \quad g_2^2\left(Z_{1,2},\phi_{1,2},\xi_{E_{1,2}},\xi_{I_{1,2}}\right) = \sigma_{I_2}\xi_{I_2}(t).$$

The envelope and phase dynamics described by Eqs.4.19 are hard to visualize and analyze. To simplify their dynamics, we apply the Stochastic Averaging Method (SAM). The SAM states that, under certain conditions (usually met for regular functions like F_1^i, F_2^i and G_1^i, G_2^i, i=1,2), the above system of four stochastic differential equations can be approximated by the following 4-dimensional Markov process [187, 6]:

$$dX(t) = m(X)dt + h(X)dW(t)\,, \tag{4.20}$$

where $X(t) = \Big[Z_1(t); \phi_1(t); Z_2(t); \phi_2(t)\Big]^{'}$, m is a 4x1 matrix, h is a 4x4 matrix and $W(t)$ denotes a 4-dimensional vector of independent Wiener processes with unit variance. Also, m and h are respectively $O(\epsilon^2)$ and $O(\epsilon)$ functions defined as:

$$m = T^{av}\Big(E\big\{F\big\} + \int_{-\infty}^{0} E\Big\{\Big(\frac{\partial G}{\partial X}\Big)_t (G)_{t+z}\Big\}dz\Big)$$

$$hh^{'} = T^{av}\Big(\int_{-\infty}^{\infty} E\big\{(G)_t (G^{'})_{t+z}\big\}dz\Big)$$

where ϵ is a small parameter which can be assumed proportional to the real part of the most unstable eigenvalue. Here $(')$ denotes transposition, and $\Big(\frac{\partial G}{\partial X}\Big)_t$ is a 4x4 Jacobian matrix. Moreover, $E.$ denotes the expectation operator and T^{av} is the time averaging operator defined by

$$T^{av}(.) = \frac{1}{T_0}\int_{t0}^{t0+T0} (.)dt$$

where $T_0 = \frac{2\pi}{\omega_0}$ is the period of an oscillation cycle. When evaluating the expectations in the stochastic averages formula, the elements of X are treated as constants. The result of these calculations leads to the coupled envelope-phase dynamics Eqs.5.

4.7.4 Dip Statistic and Phase-Locking-Value

The Dip value is a measure of multimodality of a given timeseries. It computes the maximum difference, over all points of the timeseries, between the empirical distribution and the unimodal distribution that minimizes that maximum difference. The uniform distribution is chosen as the unimodal distribution when performing the dip test for multimodality [107]. The dip value approaches

asymptotically zero for an unimodal distribution and a positive constant for a multimodal distribution. We used a Matlab version of the program already written by the authors [108] to produce Fig.4.5(a). The increase of the Dip value as the delay increases is a signature of the multimodality of the phase difference timeseries. In our case, this multimodality is a bimodality corresponding to the two symmetric out of phase states present. The Dip test therefore confirms the presence of OPL.

To measure the strength of phase synchronization between the two networks, we also computed the Phase-Locking-Value (PLV) [219, 152] as the delay varies. The PLV is a quantity to measure the strength of the phase-synchronization and is defined as

$$PLV = \frac{1}{n}\left|\sum_{k=1}^{n} e^{-j\Delta\phi_k}\right| \tag{4.21}$$

where $j = \sqrt{-1}$, n the total number of points and $\Delta\phi_k = \Delta\phi(t_k) = \phi_1(t_k) - \phi_2(t_k)$. The PLV is computed in Fig.4.5(b) and captures well the transition between unimodal and bimodal behaviour in the phase difference.

Chapter 5

Amplitude-Phase Description of Stochastic Neural Oscillators Across the Hopf Bifurcation

Abstract

We derive a unified amplitude-phase decomposition for both noisy limit cycles and quasi-cycles; in the latter case, the oscillatory motion has no deterministic counterpart. We extend a previous amplitude-phase decomposition approach using the stochastic averaging method (SAM) for quasi-cycles by taking into account nonlinear terms up to order 3. We further take into account the case of coupled networks where each isolated network can be in a quasi- or noisy limit cycle regime. The method is illustrated on two models which exhibit a deterministic supercritical Hopf bifurcation: the Stochastic Wilson-Cowan model of neural rhythms, and the Stochastic Stuart-Landau model in physics. At the level of a single oscillatory network, the amplitude process of each of these models decouples from the phase process to the lowest order, allowing a Fokker-Planck estimate of the amplitude probability density. The peak of this density captures well the transition between the two regimes. The model describes accurately the effect of Gaussian white noise as well as of correlated noise. Bursting epochs in the limit cycle regime are in fact favoured by noise with shorter correlation time or stronger intensity. Quasi-cycle and noisy limit-cycle dynamics are associated with, respectively, Rayleigh-type and Gaussian-like amplitude densities. This may provide an additional tool to distinguish quasi-cycle from limit-cycle origins of bursty rhythms. The case of multiple oscillatory networks with excitatory all-to-all delayed coupling results in a system of stochastic coupled amplitude-phase equations that keeps all the biological or physical parameters of the initial

networks and again works across the Hopf bifurcation. The theory is illustrated for a small number of heterogeneous coupled networks. Numerical simulations of the amplitude-phase dynamics obtained through the SAM are in good agreement with those of the original oscillatory networks. In the deterministic and nearly identical oscillators limits, the Stochastic Stuart-Landau model leads to the Kuramoto model of interacting phases. The approach can be tailored to networks with different frequency, topology, and stochastic inputs, thus providing a general and flexible framework to analyze noisy oscillations continuously across the underlying deterministic bifurcation.

5.1 Introduction

Limit cycle oscillations have been studied in many areas ranging from biology [145, 151, 152], ecology[157, 109] and laser physics [137]. Biological limit cycles in particular have been the subject of numerous papers over the past decades in the context of biochemical oscillations [96, 97, 98, 160, 171], circadian rhythms [10, 18], genetic oscillations [59, 214, 204, 68, 165], cardiac rhythms [95, 105], calcium oscillations[70, 199], epidemic and ecological oscillations [5, 189, 164, 161], neural rhythms [41, 42, 11, 125, 220] and hair cell motion [191, 77]. These rhythms often display strong fluctuations, or are seen during brief, randomly recurring epochs. In certain systems such as circadian rhythms, the oscillations are known to be an essential part of their function. In neural systems, slow (delta,alpha)[176, 57] and fast (beta, gamma)[79, 42, 135] rhythms are believed to support cognitive processes such as perception [143], attention [25], cognition [83], working memory [231, 154], or communication between brain areas [85, 175]. Abnormal or dysfunctional rhythms have been linked to neurological disorders like epilepsy, Alzheimer Disease (AD), and Parkinson's disease (PD) [32, 106, 113] just to mention a few.

Amplitude-phase descriptions of limit cycle oscillations have been investigated using a variety of techniques [221, 8, 198, 156, 21, 23, 22] following early studies of noise-induced and noise-perturbed oscillations [75, 88, 128]. The focus has been mainly on the phase, as studies often assume weak noise which leads to small amplitude variations. Thus, the amplitude-phase description is often reduced to a simple phase description of the noisy limit cycle oscillations [31]. Recently, descriptions in terms of the slow amplitude fluctuations and phase, referred henceforth as amplitude-phase, have been applied to the quasi-cycle regime and their random bursts [102, 182]. Bursts correspond to epochs

of higher amplitude values. In this regime, a simple phase description of the oscillation is unable to capture the bursting features, and thus taking the amplitude into account is necessary. Our goal is to provide a framework for computing amplitude-phase equations across the Hopf bifurcation for single oscillatory modules, driven by white or colored noise processes, and to generalize this approach to networks of delay-coupled modules. This will pave the way to understand communication with bursts across brain areas.

There is increasing evidence that fast rhythms in certain neural systems are induced rather than perturbed by noise [228, 170, 38, 182]. Similar observations have been made for predator-prey ecological systems, whose overall cyclical activity has been suggested to require demographic noise [161]. The vicinity of the transition between noisy limit cycles and noise-induced limit cycles known as "quasi-cycles" is thus worthy of attention as systems may drift over this boundary.

The modelling of stochastic oscillations thus involves the distinction between noisy limit cycles and quasi-cycles, depending on weather one suspects the deterministic dynamics to lie below or beyond a bifurcation from a fixed point to a limit cycle. Noisy limit cycles are self-sustained oscillations which exist independently of their noisy environment, i.e. are a manifestation of operation beyond the bifurcation. They are modelled as single or coupled oscillators. Quasi-cycles on the other hand are induced and sustained by their stochastic surroundings, in the absence of which trajectories decay to a fixed point. Models for quasi-cycles assume stable complex eigenvalues around this fixed point [102].

A unified framework which smoothly meshes together these two classes of stochastic models at the level of single as well as coupled networks is of interest, in particular when the focus is a decomposition into their time-dependent amplitude and phase. Previous studies have described the normal form dynamics of the Hopf bifurcation with additive and multiplicative noise [144, 128], including the multi-scale behaviour known to occur in the vicinity of the bifurcation [233]. The seminal study in [54] does perform a transformation of a system of arbitrary dimension near a Hopf bifurcation into a set of dynamical equations for the complex mode amplitudes; further work would then be required to convert such a system into an amplitude-phase description as is our end goal here. It also does not produce a slower amplitude dynamics which is of interest to eventually characterize bursting. Our work below starts instead with additive colored noise and different noise

on the components, and derives slow amplitude dynamics. Further it goes beyond considering a single oscillatory system; although each system is in 2D, we develop the theory for several delay-coupled 2D systems. In contrast, in the context of neural rhythms, current models that describe quasi-cycles and their coupled counterparts are based simply on linear equations driven by noise and are confined below the Hopf bifurcation [102, 182, 184, 103, 183]. Thus, we are not aware of any method that directly yields an amplitude-phase representation of coupled neural networks that is accurate across the Hopf bifurcation, let alone one that can handle colored noise and delay coupling.

Our study derives a decomposition that bridges the gap across this boundary, i.e. across the Hopf bifurcation for both single and coupled networks. The slow amplitude that emerges from our analysis quantifies the temporal evolution of the cycle to cycle amplitude of the rhythm, while the phase contains information about its regularity. This is done by extending a previous amplitude-phase decomposition of quasi-cycles oscillation to noisy limit cycles by considering nonlinear terms up to order three in the fast dynamics. This involves lengthier calculations using the stochastic averaging method (SAM) [187]. While the Taylor expansion of sigmoidal nonlinearities like those of the neural response functions converge slowly, our immediate goal is only to obtain the next order corrections to our previous nonlinear amplitude-phase equations derived from linear dynamics. Our method can accurately describe noisy oscillations over a range of frequencies. It can also accommodate different types of noise across a range of intensities. In fact the general theory in our work also considers quasi-cycle and limit cycle dynamics driven by Ornstein-Uhlenbeck (OU) noise.

We develop our theory using two models of rhythm generation, namely, the Stochastic Wilson Cowan model (SWC) of neural rhythms [224, 220], and the Stochastic Stuart Landau model (SSL) used to describe oscillations in various areas including physics and neuroscience. Each two-dimensional model system describes the interaction of a first variable (E or x) with a second variable (I or y). Multiple such systems have been used to study the emergence and coupling of rhythms across brain areas [48]. The results of such analyses have even been shown to account for features of real data [62, 64, 126]. Both models exhibit a supercritical Hopf bifurcation; in fact the Stuart Landau model in polar coordinates is the normal form for this bifurcation [206]. Thus our illustrative examples are taken from the field of neural rhythms and physics, but are more generally applicable.

We further generalize our results for a two-population E-I network model to super-networks

whose unit building blocks are such E-I modules, each of which can oscillate on its own in either the quasi or limit cycle regime. Our amplitude-phase model goes beyond purely phase-coupled oscillator models to describe both the quasi-cycle and noisy limit cycle dynamics with a higher level of biophysical realism. It also allows moderate noise and coupling strength. The model is adaptable to different frequency bands, and can be simplified to obtain a representation in terms of coupled Kuramoto oscillators.

We focus our work on the amplitude dynamics, showing good agreement with the original nonlinear model in both the quasi- and limit cycles regimes. Coupled rhythm-generating networks have been considered in the context of the activity arising from the brain connectome [64], as well as genetic and biochemical networks [96]. The modelling of such networks has mostly been limit cycle-based in the deterministic or weak noise limit, and assumed weakly coupled and nearly identical oscillators. In such limits, the influence of the amplitudes of the oscillators is usually neglected and the only important variables are the phases of the oscillatory units. Such interacting phase models do not describe coupled quasi-cycles whose behaviour is strongly amplitude-dependent. We note however a recent study of coupled quasi-cycles that involves amplitude-phase coupling [103]. In contrast, our study of super-networks in the last part of our paper involves quasi-cycle dynamics and noisy limit-cycles.

We first present the nonlinear version of the stochastic Wilson-Cowan model, and derive the amplitude-phase approximation that agrees well with the numerics of the original model across the Hopf bifurcation. We then perform a similar calculation for the stochastic Stuart-Landau model. Finally, super-networks of such models are considered. Our theory is developed assuming that these systems are driven by OU noise. For simplicity, most of our simulations are compared with the theory for the white noise case; the exceptions are Figures (5.10) and (5.11) where the effect of the noise correlation time on amplitudes densities is highlighted.

5.2 Stochastic Wilson-Cowan Model

We consider a stochastic version [220] of the seminal Wilson-Cowan model [224] for oscillation generation. The two-dimensional model with additive noise mimics a population of excitatory (E) and of inhibitory (I) cells. The mean synaptic coupling from E cells to themselves, and from E cells

to I cells, are given respectively by W_{EE} and W_{IE}. Similarly, the mean synaptic coupling from I cells to themselves and from I cells to E cells are W_{II} and W_{EI}. The E cell population receives a constant external stimulus h_E, while the I cell population is driven by the constant external current h_I. Additive noise is assumed to arise mainly from random synaptic events. Defining the fraction of excitatory cells that are firing at a given time by E(t), and of inhibitory cells I(t), yields the stochastic WC model (SWC):

$$\frac{dE(t)}{dt} = -\alpha_E E(t) + \big(1 - E(t)\big)\beta_E f(s_E(t)) + \eta_E(t) \tag{5.1}$$

$$\frac{dI(t)}{dt} = -\alpha_I I(t) + \big(1 - I(t)\big)\beta_I f(s_I(t)) + \eta_I(t)\,. \tag{5.2}$$

The sigmoid function is $f(x) = (1 + e^{-x})^{-1}$ and the total excitatory $s_E(t)$ and inhibitory $s_I(t)$ synaptic inputs to a neuron are given respectively by

$$s_E(t) = W_{EE}E(t) - W_{EI}I(t) + h_E \tag{5.3}$$

$$s_I(t) = W_{IE}E(t) - W_{II}I(t) + h_I\,. \tag{5.4}$$

We choose $\eta_{E,I}(t)$ as two independent Ornstein-Uhlenbeck (OU) [90] processes given by:

$$\frac{d\eta_E(t)}{dt} = -\frac{\eta_E(t)}{\tau_E} + \sqrt{\frac{2\sigma_E^2}{\tau_E}}\xi_E(t) \tag{5.5}$$

$$\frac{d\eta_I(t)}{dt} = -\frac{\eta_I(t)}{\tau_I} + \sqrt{\frac{2\sigma_I^2}{\tau_I}}\xi_I(t) \tag{5.6}$$

where $\xi_{E,I}$ are two independent Gaussian white noises with the following properties:

$$< \xi_{E,I}(t) > = 0, \quad < \xi_E(t)\xi_I(t) >= 0$$

$$< \xi_E(t^{'})\xi_E(t) > =< \xi_I(t^{'})\xi_I(t) >= \delta(t - t^{'})\,.$$

The variances of these OU processes are $\sigma^2_{E,I}$, their autocorrelations are given by:

$$\langle \eta_E(t)\eta_E(s)\rangle = \sigma^2_E \exp(-|t-s|/\tau_E) \tag{5.7}$$

$$\langle \eta_I(t)\eta_I(s)\rangle = \sigma^2_I \exp(-|t-s|/\tau_I)\,, \tag{5.8}$$

and their intensities (integrals of the autocorrelation functions) are $Q_{E,I} = \tau_{E,I}\sigma^2_{E,I}$. Further in our work, we will investigate the effect of the noise correlation time on the dynamics, while maintaining the noise intensity fixed. In other words, we will fix $Q_{E,I}$, and vary $\tau_{E,I}$ while changing $\sigma^2_{E,I}$ [115]. However, for the stochastic Wilson Cowan model in the first part of our paper, we will consider stochastic forcing by Gaussian white noises.

The noise-free ($\sigma_E = \sigma_I = 0$) dynamics has a fixed point (E_0, I_0) (for the parameter values chosen in our work) which can be a stable or an unstable focus. If the fixed point is a stable focus, deviations from the fixed point converge to zero. The noise slowly erases the memory of the initial conditions, and induces deviations from the fixed point that relax in a noisy oscillatory manner [102, 182]. Adding noise to this regime leads to noise-induced oscillations or quasi-cycles. If the system undergoes a Hopf bifurcation to a stable limit cycle, then the fixed point becomes an unstable focus. The noise then yields a stochastic limit cycle [58, 196] by perturbing the amplitude, frequency and phase of the deterministic oscillation.

5.2.1 Dynamics of the fluctuations

We wish to characterize the fast and slow features of the deviations from the fixed point and the limit cycle with a unique dynamical description no matter if their corresponding dynamics is a quasi-cycle or a noisy limit cycle. We look for solutions of Eqs.(5.1-5.2) in the form:

$$E(t) = E_0 + V_E(t) \qquad\qquad I(t) = I_0 + V_I(t) \tag{5.9}$$

where the fixed points E_0 and I_0 solve the deterministic equations:

$$\begin{aligned} -\alpha_E E_0 + \big(1 - E_0\big)\beta_E f(s_{E_0}) = 0 \\ -\alpha_I I_0 + \big(1 - I_0\big)\beta_I f(s_{I_0}) = 0\,, \end{aligned} \tag{5.10}$$

with the definitions

$$s_{E_0} = W_{EE}E_0 - W_{EI}I_0 + h_E \quad and \quad s_{I_0} = W_{IE}E_0 - W_{II}I_0 + h_I\,.$$

Note that we have restricted our analysis to the parameter regime most relevant to brain rhythms, namely the one where the system has only one deterministic fixed point. We inserted Eqs. (5.9) into Eqs. (5.1-5.2) and used the following Taylor expansion of the sigmoid function:

$$\begin{aligned} f(s_E(t)) &= f(s_{E_0} + \delta s_E(t)) \\ &= f(s_{E_0}) + \delta s_E(t) f^{'}(s_{E_0}) + \frac{1}{2}(\delta s_E(t))^2 f^{''}(s_{E_0}) \\ f(s_I(t)) &= f(s_{I_0} + \delta s_I(t)) \\ &= f(s_{I_0}) + \delta s_I(t) f^{'}(s_{I_0}) + \frac{1}{2}(\delta s_I(t))^2 f^{''}(s_{I_0}) \end{aligned} \tag{5.11}$$

where

$$\delta s_E(t) = W_{EE}V_E(t) - W_{EI}V_I(t); \quad \delta s_I(t) = W_{IE}V_E(t) - W_{II}V_I(t). \tag{5.12}$$

We note that the Taylor expansion made above in Eqs. (5.11) is accurate for small deviations in Eqs. (5.12). If these quantities become too large, this approximation converges poorly which may lead to incorrect results.

The fluctuations $V_E(t)$ and $V_I(t)$ are considered as local field potentials (LFP) in the context of brain dynamics [102, 182]. These LFPs are dimensionless in the Wilson-Cowan modeling framework since they are simply deviations from the steady state fractions E_0 and I_0; they are nevertheless

interpreted as potentials [228]. They are approximately governed by:

$$\frac{dV_E(t)}{dt} = A_{EE}V_E(t) + A_{EI}V_I(t) + L_{EE}V_E^2(t) + L_{EI}V_E(t)V_I(t) + M_{EI}V_I^2(t) + B_{1E}V_E^3(t) \quad (5.13)$$
$$+ B_{2E}V_EV_I^2(t) + B_{3E}V_IV_E^2(t) + B_{4E}V_I^3(t) + \eta_E(t)$$
$$\frac{dV_I(t)}{dt} = A_{IE}V_E(t) + A_{II}V_I(t) + L_{II}V_I^2(t) + L_{IE}V_E(t)V_I(t) + M_{IE}V_E^2(t) + B_{1I}V_I^3(t) \quad (5.14)$$
$$+ B_{2I}V_EV_I^2(t) + B_{3I}V_IV_E^2(t) + B_{4I}V_E^3(t) + \eta_I(t)\,,$$

with the following parameter definitions:

$$\begin{aligned}
A_{EE} &= -\big[\alpha_E + \beta_E f(s_{E_0}) - (1-E_0)\beta_E f^{'}(s_{E_0})W_{EE}\big] \\
A_{II} &= -\big[\alpha_I + \beta_I f(s_{I_0}) + (1-I_0)\beta_I f^{'}(s_{I_0})W_{II}\big] \\
A_{EI} &= -(1-E_0)\beta_E f^{'}(s_{E_0})W_{EI}, \quad A_{IE} = (1-I_0)\beta_I f^{'}(s_{I_0})W_{IE} \\
L_{EE} &= -\beta_E f^{'}(s_{E_0})W_{EE}, \quad L_{EI} = \beta_E f^{'}(s_{E_0})W_{EI} \\
L_{IE} &= -\beta_I f^{'}(s_{I_0})W_{IE}, \quad L_{II} = \beta_I f^{'}(s_{I_0})W_{II} \\
M_{EI} &= 0, \qquad M_{IE} = 0, \qquad B_{4E} = 0, \qquad B_{4I} = 0. \\
B_{1E} &= -\frac{1}{2}\beta_E f^{''}(s_{E_0})W_{EE}^2, \quad B_{2E} = -\frac{1}{2}\beta_E f^{''}(s_{E_0})W_{EI}^2 \\
B_{3E} &= \beta_E f^{''}(s_{E_0})W_{EE}W_{EI}, \quad B_{1I} = -\frac{1}{2}\beta_I f^{''}(s_{I_0})W_{II}^2 \\
B_{2I} &= \beta_I f^{''}(s_{I_0})W_{IE}W_{II}, \quad B_{3I} = -\frac{1}{2}\beta_I f^{''}(s_{I_0})W_{IE}^2\,.
\end{aligned}$$

Note that to obtain Eqs. (5.13-5.14) we have used the fixed point condition Eqs.5.10. The Taylor expansion for this stochastic WC model leads to the four parameters $M_{EI} = M_{IE} = 0$ and $B_{4E} = B_{4I} = 0$. The values of the first parameters ($M_{EI} = M_{IE} = 0$) is a consequence of a specific choice of some terms which leads to a better convergence to the former Wilson-Cowan dynamics as we show in the Appendix Fig.5.14. The second relation $B_{4E} = B_{4I} = 0$ follows because the Taylor expansion of the sigmoid function was truncated at the second order (see Appendix). These terms could be different from zero for a different choice of parameters or in other models. For our analytic work, we will use Eqs. (5.13-5.14) instead of Eqs. (5.1-5.2). Equations (5.13-5.14) are the approximate fluctuation dynamics to order O(3) of the stochastic Wilson-Cowan model, denoted henceforth as

SWC3 (see further below in Fig. (5.3) for time series from this model). We focus on this system and investigate its ability to generate oscillations and amplitude-phase dynamics across the Hopf boundary in the presence of noise.

Nonlinear Fluctuation Dynamics: Numerical Analysis

We first simulate Eqs. (5.13-5.14) without stochastic inputs ($\sigma_E = 0$ and $\sigma_I = 0$). Then we use Eqs. 5.9 to compute the synchronization level of any existing long-life oscillations of the excitatory activity $E(t)$. The synchronization level was defined as the mean of the amplitude between each trough and the successive peak, computed using a very long simulation time. It can also be seen as the mean of the cycle-to-cycle amplitudes of the oscillatory process after transients have decayed. We plotted this synchronization level in the (W_{EE}, W_{II}) parameter space in Fig. 5.1(a), which reveals the emergence of oscillations after a Hopf bifurcation. The level of synchronization increases smoothly for parameters deeper into the limit cycle regime. Accordingly, the mean amplitude of the limit cycle increases with the real part of the complex conjugate eigenvalues at that fixed point.

We now take stochastic inputs into account. We first consider only white noises $\eta_{E,I}(t) = \sigma_{E,I}\xi_{E,I}(t)$ and define the total noise strength as:

$$\sigma = \sqrt{\sigma_E^2 + \sigma_I^2}. \tag{5.15}$$

For weak noise, quasi-cycle oscillations emerge (Fig. 5.1(b)). In the limit cycle regime, the oscillation amplitude is larger at higher noise (Fig.5.1(c)) compared to the lower noise (Figs.5.1(b)) and deterministic (Figs.5.1(a)) cases. At the higher noise strength in Fig 5.1(c), the oscillations are in fact more prominent in both the quasi-cycle and limit cycle regimes.

The oscillation frequency for weak noise strength is also shown in Fig.5.1(d), where it is apparent that it varies smoothly across the Hopf boundary. The frequency content of the quasi-cycle oscillations can be seen in the spectrogram (Fig.5.1(e)). Oscillations are quite irregular, with epochs of high and low amplitude values. The epochs of high amplitude values are "bursts"; the mean frequency of such bursts is also a random variable. In contrast, in the limit cycle regime (black dot in Fig.5.1(b)) oscillations are more regular, with small fluctuations in amplitude and peak frequency as seen in the corresponding spectrogram (Fig.5.1(f)).

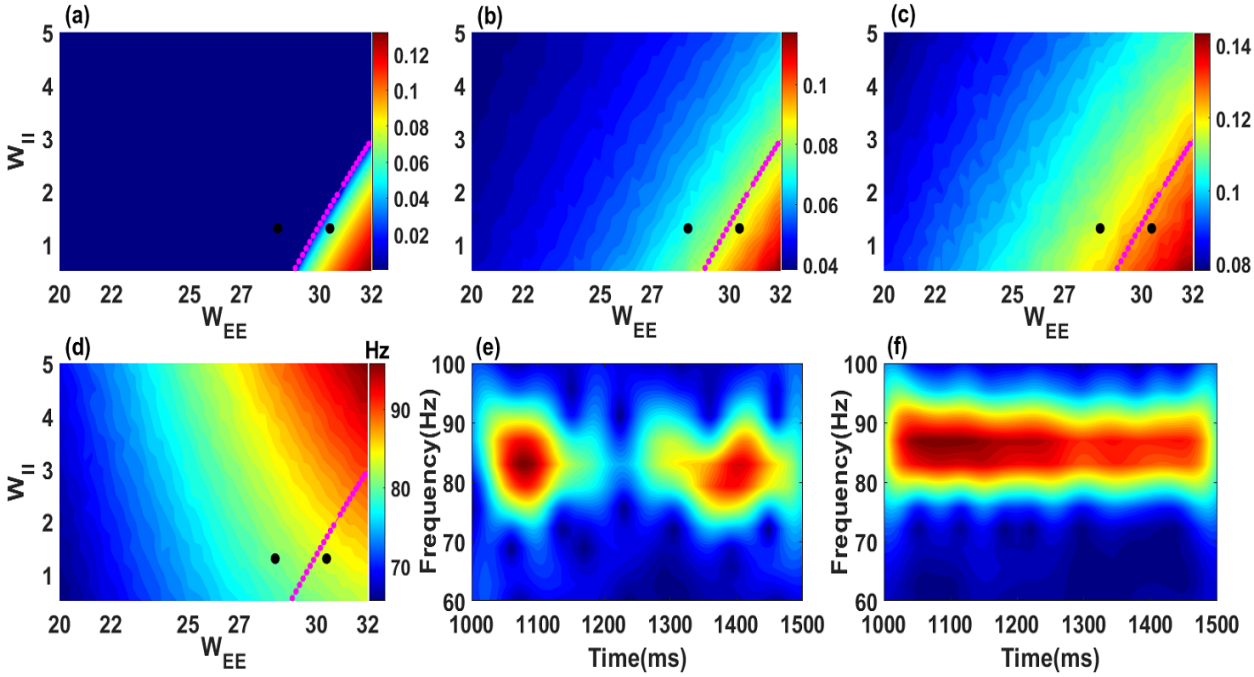

Figure 5.1: **Oscillations in the Stochastic Wilson-Cowan truncated to O(3), i.e. in the SWC3 model.**Top panels: synchronization level of the E cells in the subspace of self-connectivity parameters. The synchronization is measured from numerical simulations of the activities Eqs.5.13 as the average difference between each trough and its successive peak. Specifically, we used a Gaussian filter and the Matlab function "findpeaks" to filter and extract the peaks and troughs of the E activity (Eq.5.9). The curve in magenta represents the Hopf bifurcation boundary computed by setting the real part $-\nu$ of the complex conjugate eigenvalues to zero. The two black dots lie on either side of the Hopf boundary at $W_{II} = 1.3$ and $W_{EE} = 27.4$ (quasi-cycle) or $W_{EE} = 30.4$ (noisy limit cycle). **(a)** No noise: synchronization increases from zero beyond the Hopf bifurcation. **(b)** Weak noise ($\sigma_E = 0.0015ms^{-1}, \sigma_I = 0.005ms^{-1/2}, \sigma = 0.005ms^{-1/2}$) causes "quasi-cycle" oscillations even below the Hopf bifurcation. **(c)** For stronger noise ($\sigma_E = 0.004ms^{-1/2}, \sigma_I = 0.015ms^{-1/2}, \sigma = 0.0155ms^{-1/2}$), noise-induced oscillations are more prominent. **(d)** Frequency of the oscillations generated in **(b)**. **(e)** Spectrogram corresponding to the black dot in the quasi-cycle regime in **(b)**. Oscillations appear as discrete (short) epochs of synchrony called "bursts"; the frequency content also fluctuates from burst to burst. **(f)** Spectrogram for the black dot in the noisy limit-cycle regime in panel **(b)**. Oscillations are now highly coherent with peak power around $f = 88Hz$. Parameters are $W_{EI} = 26.3, W_{IE} = 32, h_E = -3.8, h_I = -8, \alpha_E = 0.1ms^{-1}, \alpha_I = 0.2ms^{-1}, \beta_E = 1, \beta_I = 2$. Panels **(d-f)** use the noise intensities in panel **(b)**. The parameters here are also used in Figs.5.2 to 5.7, unless otherwise stated.

Linear Analysis

Recent studies showed that noise-induced oscillations could be described by linear equations sustained by noise [102, 182]. More interestingly, it was found that the amplitude ratio and the phase difference between inhibitory and excitatory fluctuations were constant in the deterministic limit [102, 182]. In the most general case considered here, the dynamics of excitatory and inhibitory fluctuations are described by nonlinear equations which are sustained by noise when the real part of the eigenvalues is negative and self-sustained when it is positive. We therefore checked whether these properties of the E and I amplitudes and phases are conserved in the regime of self-sustained oscillations. For that, we perform the linear analysis of Eqs. (5.13-5.14). The associated noise-free linear system of Eqs. (5.13-5.14) can be written in the following matrix form:

$$\frac{dV^0(t)}{dt} = AV^0(t)$$

where

$$V^0(t) = \begin{bmatrix} V_E^0(t) \\ V_I^0(t) \end{bmatrix} \quad and \quad A = \begin{bmatrix} A_{EE} & A_{EI} \\ A_{IE} & A_{II} \end{bmatrix} .$$

We look for a trial solution in the form:

$$\begin{bmatrix} V_E^0(t) \\ V_I^0(t) \end{bmatrix} = \begin{bmatrix} \tilde{B_E} \\ \tilde{B_I} \end{bmatrix} e^{\lambda t}$$

where $\tilde{B_E} = B_E e^{j\theta_E}$ and $\tilde{B_I} = B_I e^{j\theta_I}$. The eigenvalue λ of the associated matrix A is found by substituting the trial solution into the linear system, yielding

$$\frac{\tilde{B_I}}{\tilde{B_E}} = \frac{A_{EE} - \lambda}{-A_{EI}} = -\frac{A_{IE}}{A_{II} - \lambda} .$$

The second equality leads to

$$\lambda = \frac{1}{2}(A_{EE} + A_{II}) \pm \frac{j}{2}\sqrt{-(A_{EE} - A_{II})^2 - 4A_{EI}A_{IE}} .$$

We rewrite the eigenvalue in the compact form

$$\lambda = -\nu \pm j\omega_0$$

with

$$\nu = -\frac{A_{EE} + A_{II}}{2}; \;\; \omega_0 = \frac{1}{2}\sqrt{-(A_{EE} - A_{II})^2 - 4A_{EI}A_{IE}}\,.$$

This leads to the exact expression of the amplitude ratio between the I and E fluctuations for the linearized SWC3 system:

$$\alpha = \left|\frac{\tilde{B}_I}{\tilde{B}_E}\right| = \frac{B_I}{B_E} = \sqrt{\frac{A_{IE}}{-A_{EI}}} \tag{5.16}$$

Similarly, the phase difference δ can be obtained from the relation

$$\delta = \theta_I - \theta_E = Arg\left(\frac{\tilde{B}_I}{\tilde{B}_E}\right). \tag{5.17}$$

For the parameters used here, we found

$$\delta = \theta_I - \theta_E = \arctan\left(\frac{-2\omega_0}{A_{EE} - A_{II}}\right). \tag{5.18}$$

In Eqs. 5.16-5.17, $||$ and Arg are respectively the modulus and the argument of the complex number $\frac{\tilde{B}_I}{\tilde{B}_E}$. In the presence of noise, one can compute amplitudes and phases of the E and I fluctuations from simulated time series using the analytic signal technique. The amplitude ratio and the phase difference are obtained by the following approximations:

$$\alpha = \frac{B_I}{B_E} \approx \left\langle \frac{Env\big[V_I(t)\big]}{Env\big[V_E(t)\big]} \right\rangle$$

and

$$\delta = \theta_I - \theta_E \approx \left\langle Arg\big[V_I(t)\big] - Arg\big[V_E(t)\big] \right\rangle.$$

Here $\langle . \rangle$ can be considered a time average of the stochastic process in Eqs. (5.13-5.14). Env is defined as the amplitude of the analytic signal associated with the LFP. For example, the analytic signal corresponding to $V_E(t)$ is $V_E(t) + jH\big[V_E(t)\big]$, with the Hilbert transform H defined as

$$H[x] = \frac{1}{\pi} P \int_{-\infty}^{\infty} \frac{x(\tau)}{t - \tau} d\tau\,,$$

where P signifies the Cauchy principal value. The amplitude of the stochastic signal is then $Env[V_E] = \sqrt{V_E^2 + H^2[V_E]}$. Likewise, the phase angle of the analytic signal is defined as $Arg[V_E] =$

arctan $\left[H[V_E]/V_E\right]$. The transition between noise-induced and self-sustained oscillations happens when the real part of the eigenvalue is zero. This condition is expressed as

$$-\frac{\alpha_E}{1-E_0}+\alpha_E E_0\left[1-\frac{\alpha_E E_0}{(1-E_0)\beta_E}\right]W_{EE}-\frac{\alpha_I}{1-I_0}-\alpha_I I_0\left[1-\frac{\alpha_I I_0}{(1-I_0)\beta_I}\right]W_{II}=0\,. \tag{5.19}$$

Note that to obtain this equation we have used the expressions of $f(s_{E_0})$ and $f(s_{I_0})$ obtained from the fixed points condition Eqs.5.10 and replaced them in the expressions of coefficients A_{EE} and A_{II}. We also used the relation between f and its derivative: $f^{'}=f(1-f)$. This analytical expression of the Hopf bifurcation (Eq.5.19) is in good agreement with numerical simulations (Fig. 5.1(a)). The stability boundary is shown as dots in magenta, and is reproduced in Figs. 5.1(b-d). We also computed the amplitude ratio, phase difference and excitatory and inhibitory frequency distributions from the simulated nonlinear Eqs. (5.13-5.14). The results show approximate Gaussian distributions around the mean values provided by the linear stability analysis in Eqs. (5.16-5.18) (see Figs. 5.2), in spite of the nonlinearities in Eqs. (5.13-5.14). The noise basically spreads the delta distributions of the deterministic case to yield approximately Gaussian distributions. The standard deviations of the distributions increase with noise. Similar results have been previously obtained in the quasi-cycle regime [182]. Numerically computed means of the frequency content are close to the imaginary part of the complex conjugate eigenvalues since the system is close to the Hopf bifurcation (black dot in Figs.5.1). Moving away from this boundary slowly diminishes the agreement as the frequency depends on the amplitude.

5.2.2 Amplitude-phase decomposition of SWC3

Our goal now is to derive an amplitude-phase dynamics that carries over from the quasi-cycle to the limit cycle regime, rather than having two separate dynamics. Our hope is that it will account for phase-amplitude coupling over a range of noise strengths including the high noise-induced bursts in the limit cycle regime. We first seek analytical expressions of the E and I fluctuations in the following forms [182]:

$$V_E=Z_E\cos\left(\omega_0 t+\phi_E\right);\quad V_I=\alpha Z_E\cos\left(\omega_0 t+\phi_E+\delta\right) \tag{5.20}$$

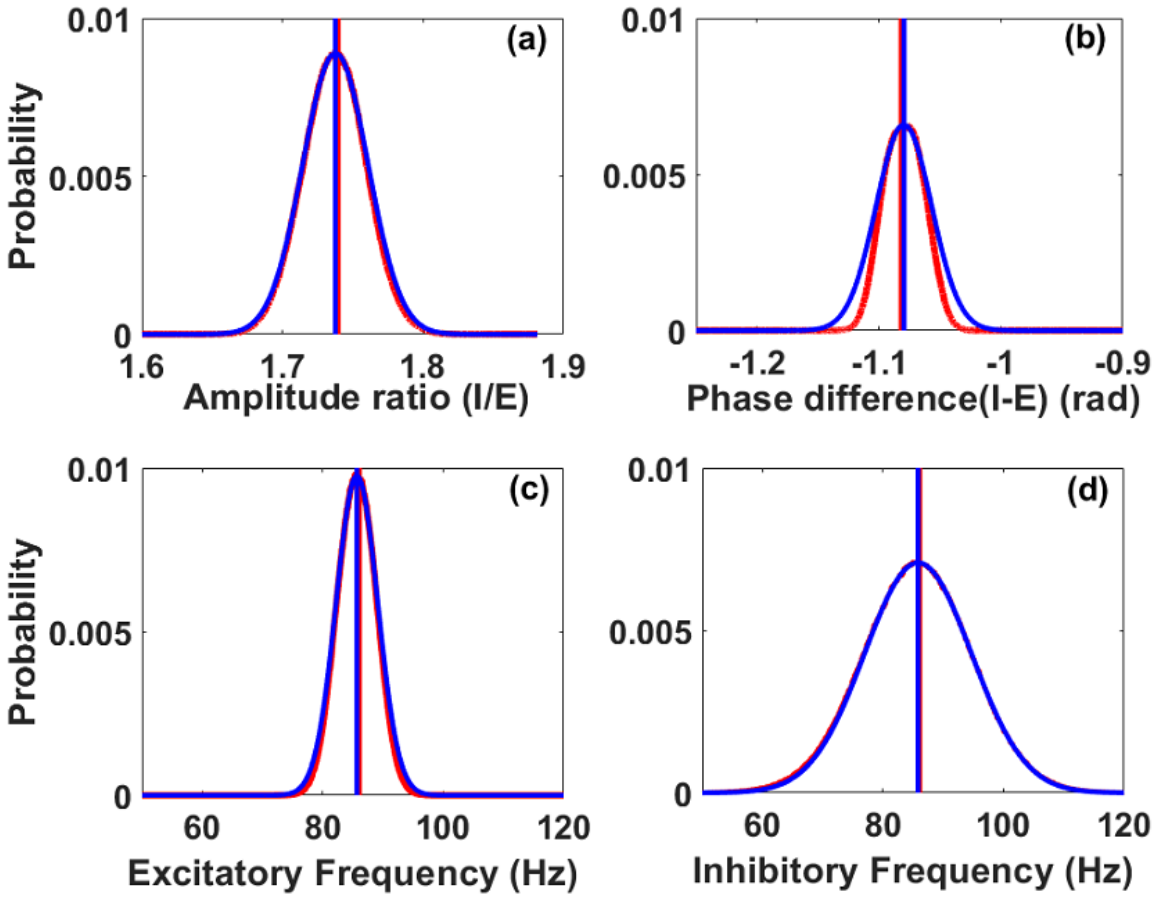

Figure 5.2: **I/E amplitude ratio, I-E phase difference and peak frequencies in the noisy limit cycle regime**. **(a)** Probability distribution of the amplitude ratio between inhibitory and excitatory fluctuations from Eq.5.16. **(b)** Probability distribution of the phase difference between inhibitory and excitatory fluctuations from Eq.5.18. **(c)** Excitatory frequency probability distribution. **(d)** Inhibitory frequency probability distribution. For all the figures, **(blue)** curves correspond to the probability distributions computed numerically; the corresponding vertical lines are computed analytically from linear stability analysis Eqs. (5.16-5.18). The **red** curves are Gaussian fits to the blue curves, while the vertical red lines are the means of the red Gaussian distributions. Parameters are as in Fig.5.1 with $W_{EE} = 30.4$. Noise intensities are $\sigma_E = 0.0002ms^{-1/2}, \sigma_I = 0.0006ms^{-1/2}, \sigma = 0.0007ms^{-1/2}$. Other parameters are as in Fig.5.1.

where Z_E and ϕ_E represent the stochastic amplitude and phase of the E fluctuations. The idea is to compute the dynamics of the slow amplitude fluctuations of the cycle to cycle amplitude, Z_E, and the phase ϕ_E of the E fluctuations. The parameters α, δ and ω_0 are the amplitude ratio, phase difference and frequency computed from the linear stability analysis Eqs. (5.16-5.18) (see Fig. 5.2). We then insert these expressions into Eqs. (5.13-5.14) and obtain:

$$\frac{dZ_E}{dt} = F_1\big(Z_E,\phi_E\big) + G_1\big(Z_E,\phi_E,\eta_E,\eta_I\big) \tag{5.21}$$

$$\frac{d\phi_E}{dt} = F_2\big(Z_E,\phi_E\big) + G_2\big(Z_E,\phi_E,\eta_E,\eta_I\big) \tag{5.22}$$

with the following functions:

$$F_1\big(Z_E,\phi_E\big) = \frac{1}{\alpha\sin(\delta)}\Big[\alpha f_1\big(Z_E,\phi_E\big)\sin(\omega_0 t+\phi_E+\delta) - f_2\big(Z_E,\phi_E\big)\sin(\omega_0 t+\phi_E)\Big]$$

$$F_2\big(Z_E,\phi_E\big) = \frac{1}{\alpha Z_E\sin(\delta)}\Big[\alpha f_1\big(Z_E,\phi_E\big)\cos(\omega_0 t+\phi_E+\delta) - f_2\big(Z_E,\phi_E\big)\cos(\omega_0 t+\phi_E)\Big]$$

$$G_1\big(Z_E,\phi_E,\eta_E,\eta_I\big) = \frac{1}{\alpha\sin(\delta)}\Big[\alpha g_1\big(Z_E,\phi_E,\eta_E,\eta_I\big)\sin(\omega_0 t+\phi_E+\delta) - g_2\big(Z_E,\phi_E,\eta_E,\eta_I\big)\sin(\omega_0 t+\phi_E)\Big]$$

$$G_2\big(Z_E,\phi_E,\eta_E,\eta_I\big) = \frac{1}{\alpha Z_E\sin(\delta)}\Big[\alpha g_1\big(Z_E,\phi_E,\eta_E,\eta_I\big)\cos(\omega_0 t+\phi_E+\delta) - g_2\big(Z_E,\phi_E,\eta_E,\eta_I\big)\cos(\omega_0 t+\phi_E)\Big]$$

$$\begin{aligned} f_1\big(Z_E,\phi_E\big) &= \omega_0 Z_E\sin(\omega_0 t+\phi_E) + A_{EE}Z_E\cos(\omega_0 t+\phi_E) + A_{EI}\alpha Z_E\cos(\omega_0 t+\phi_E+\delta) + L_{EE}Z_E^2\times \\ &\quad \cos^2(\omega_0 t+\phi_E) + L_{EI}\alpha Z_E^2\cos(\omega_0 t+\phi_E)\cos(\omega_0 t+\phi_E+\delta) + M_{EI}\alpha^2 Z_E^2\cos(\omega_0 t+\phi_E+\delta) \\ &\quad + B_{1E}Z_E^3\cos^3(\omega_0 t+\phi_E) + B_{2E}\alpha^2 Z_E^3\cos(\omega_0 t+\phi_E)\cos^2(\omega_0 t+\phi_E+\delta) + B_{3E}\alpha Z_E^3\times \\ &\quad \cos^2(\omega_0 t+\phi_E)\cos(\omega_0 t+\phi_E+\delta) + B_{4E}\alpha^3 Z_E^3\cos^3(\omega_0 t+\phi_E+\delta) \end{aligned}$$

$$\begin{aligned} f_2\big(Z_E,\phi_E\big) &= \alpha\omega_0 Z_E\sin(\omega_0 t+\phi_E+\delta) + A_{IE}Z_E\cos(\omega_0 t+\phi_E) + A_{II}\alpha Z_E\cos(\omega_0 t+\phi_E+\delta) + L_{II}\alpha^2 Z_E^2\times \\ &\quad \cos^2(\omega_0 t+\phi_E+\delta) + L_{IE}\alpha Z_E^2\cos(\omega_0 t+\phi_E)\cos(\omega_0 t+\phi_E+\delta) + M_{IE}Z_E^2\cos^2(\omega_0 t+\phi_E) + \\ &\quad B_{1I}\alpha^3 Z_E^3\cos^3(\omega_0 t+\phi_E+\delta) + B_{2I}\alpha^2 Z_E^3\cos(\omega_0 t+\phi_E)\cos^2(\omega_0 t+\phi_E+\delta) + \\ &\quad B_{3I}\alpha Z_E^3\cos(\omega_0 t+\phi_E+\delta)\cos^2(\omega_0 t+\phi_E) + B_{4I}Z_E^3\cos^3(\omega_0 t+\phi_E) \end{aligned}$$

$$g_1\big(Z_E,\phi_E,\eta_E,\eta_I\big) = \eta_E(t)$$

$$g_2\big(Z_E,\phi_E,\eta_E,\eta_I\big) = \eta_I(t).$$

However, such equations are cumbersome and difficult to analyze since the amplitude and phase are coupled in a complicated manner. We need simpler equations for a suitable analysis of amplitude dynamics, which we now determine.

Stochastic Averaging Method (SAM)

To simplify the amplitude-phase dynamics in Eqs. 5.21 and 5.22, we make use of the Stochastic Averaging Method (SAM) [187, 6], which stipulates that the system can be approximated by a two-dimensional Markov process given by:

$$d\begin{pmatrix} Z_E(t) \\ \phi_E(t) \end{pmatrix} = \begin{pmatrix} m_1(t) \\ m_2(t) \end{pmatrix} dt + \begin{pmatrix} h_{11}(t) & h_{12}(t) \\ h_{21}(t) & h_{22}(t) \end{pmatrix} \begin{pmatrix} dW_1(t) \\ dW_2(t) \end{pmatrix}$$

$$m = T^{av}\Big(E\big\{F\big\} + \int_{-\infty}^{0} E\Big\{ \Big(\frac{\partial G}{\partial X}\Big)_t (G)_{t+\tau} \Big\} d\tau \Big)$$

$$h\,h^{'} = T^{av}\Big(\int_{-\infty}^{\infty} E\big\{ (G)_t (G^{'})_{t+\tau} \big\} d\tau \Big)\,.$$

Here $m = \begin{pmatrix} m_1(t) \\ m_2(t) \end{pmatrix}$, $F = \begin{pmatrix} F_1(t) \\ F_2(t) \end{pmatrix}$, $G = \begin{pmatrix} G_1(t) \\ G_2(t) \end{pmatrix}$ h is the matrix made up of the elements h_{ij}, $(h\,h')$ is the product of h and its transpose, and

$$\Big(\frac{\partial G}{\partial X}\Big)_t \equiv \begin{pmatrix} \frac{\partial G_1}{\partial Z_E} & \frac{\partial G_1}{\partial \phi_E} \\ \\ \frac{\partial G_2}{\partial Z_E} & \frac{\partial G_2}{\partial \phi_E} \end{pmatrix}$$

is a 2x2 Jacobian matrix. Moreover, $E.$ denotes the expectation operator (i.e. average over realizations), and T^{av} is the time averaging operator defined by

$$T^{av}(.) = \frac{1}{T_0} \int_{t_0}^{t_0+T_0} (.) dt\,.$$

The subscript t and $t+\tau$ mean that the elements of the corresponding vectors and matrix are evaluated at these times. The SAM further assumes that the 2-dimensional functions $F(Z_E, \phi_E)$

and $G(Z_E, \phi_E, \xi_E, \xi_I)$ are respectively of order $\mathrm{O}(\epsilon)$ and $\mathrm{O}(\epsilon^2)$, where ϵ is a small parameter. The averaging in the SAM procedure assumes that the functions $Z_E(t)$ and $\phi_E(t)$ are constant during the period $T_0 = 2\pi/\omega_0$ of the underlying deterministic oscillation (ω_0 also varies with system parameters). After some calculations, we end up with the following amplitude-phase dynamics:

$$dZ_E = \left[-\nu Z_E + B_1 Z_E^3 + \frac{D}{2Z_E} \right] dt + \sqrt{D} dW_1 \tag{5.23}$$

$$d\phi_E = B_2 Z_E^2 \, dt + \frac{\sqrt{D}}{Z_E} dW_2 \tag{5.24}$$

If we further make the change of variable $\theta_E(t) = \omega_0 t + \phi_E(t)$, the dynamics of the fast phase $\theta_E(t)$ is obtained from Eq. 5.24 as

$$d\theta_E = \left[\omega_0 + B_2 Z_E^2 \right] dt + \frac{\sqrt{D}}{Z_E} dW_2 \tag{5.25}$$

with the following expressions:

$$\begin{aligned}
B_1 &= \frac{1}{8}\Big[3B_{1E} + B_{3I} + \alpha^2(B_{2E} + 3B_{1I}) + 2\alpha\cos(\delta)(B_{3E} + B_{2I})\Big] \\
B_2 &= \frac{1}{8\sin(\delta)}\Big[2\alpha(B_{3E} - B_{2I}) + 3(B_{1E} - B_{3I})\cos(\delta) + 3\alpha^2(B_{2E} - B_{1I})\cos(\delta) + \alpha(B_{3E} - B_{2I})\cos(2\delta) + \\
&\quad \frac{3}{\alpha}\big(\alpha^4 B_{4E} - B_{4I}\big)\Big] \\
D &= \frac{1}{2\alpha^2\sin^2(\delta)}\left[\frac{2\tau_E(\alpha\sigma_E)^2}{1 + (\omega_0\tau_E)^2} + \frac{2\tau_I(\sigma_I)^2}{1 + (\omega_0\tau_I)^2}\right].
\end{aligned} \tag{5.26}$$

Here $W_1(t)$ and $W_2(t)$ are two independent Wiener processes. We found that the coefficient B_1 is negative, which implies that the amplitude Z_E remains finite, i.e. deviations from the fixed point remain bounded. Taking into account the power spectra at ω_0,

$$S_{\eta_{E,I}}(\omega_0) = \frac{2\tau_{E,I}(\sigma_{E,I})^2}{2\pi\big[1 + (\omega_0\tau_{E,I})^2\big]},$$

of the OU processes $\eta_E(t)$ and $\eta_I(t)$ applied respectively on the E and I dynamics, we find that the effective noise strength D of the amplitude-phase dynamics is a weighted sum of these power

spectra:

$$D = \frac{\pi}{\alpha^2 \sin^2(\delta)} \Big[\alpha^2 S_{\eta_E}(\omega_0) + S_{\eta_I}(\omega_0) \Big]. \tag{5.27}$$

Different noise processes can be handled by substituting the proper power spectra in this expression for D.

Most of our simulations in this work consider additive Gaussian white noise on the SWC3 model Eqs. (5.13-5.14) and further below on the SSL model, although we do later explore the effect of the noise correlation time in the SSL model in Figs. (5.10-5.11). For the white noise case $\eta_{E,I}(t) = \sigma_{E,I}\xi_{E,I}(t)$, the above amplitude-phase dynamics apply with the definition of D based on the white noise power spectra $S(\omega_0) = \frac{\sigma^2_{E,I}}{2\pi}$ that is,

$$D = \frac{(\sigma_I)^2 + (\alpha\sigma_E)^2}{2\alpha^2 \sin^2(\delta)}\,. \tag{5.28}$$

Further, since the noise is only additive, there is no need to distinguish between Itô and Stratonovich calculus; the SAM method itself was developed using Itô calculus [187].

As for the case of the quasi-cycle oscillations [182], the amplitude dynamics is uncoupled from the phase dynamics. In contrast however, a new term $B_1 Z_E^3$ appears in the amplitude dynamics. This term is at the origin of the stabilization of the growth of the amplitude when the real part of the complex conjugate eigenvalues becomes positive beyond the Hopf bifurcation. The phase dynamics also has a new deterministic term $B_2 Z_E^2$. This causes the deterministic frequency to depend on the amplitude magnitude. This contrasts with the quasi-cycle regime obtained with the linear WC system, where the term B_2 was absent.

Next, we compute spectrograms and time-series of the fluctuations $V_{E,I}(t)$, their amplitudes $Z_{E,I}(t)$ and their phases $\phi_{E,I}(t)$ both for the quasi-cycle and noisy limit-cycle regimes (Fig. 5.3). We observe that our amplitude-phase representation describes well the dynamics of E and I fluctuations for both quasi-cycles (left panels) and noisy limit cycles (right panels). Our model can thus account for both noise-induced oscillations and noise-perturbed oscillations. It produces bursting epochs for quasi-cycles and self-sustained oscillations of long duration for the noisy limit cycles.

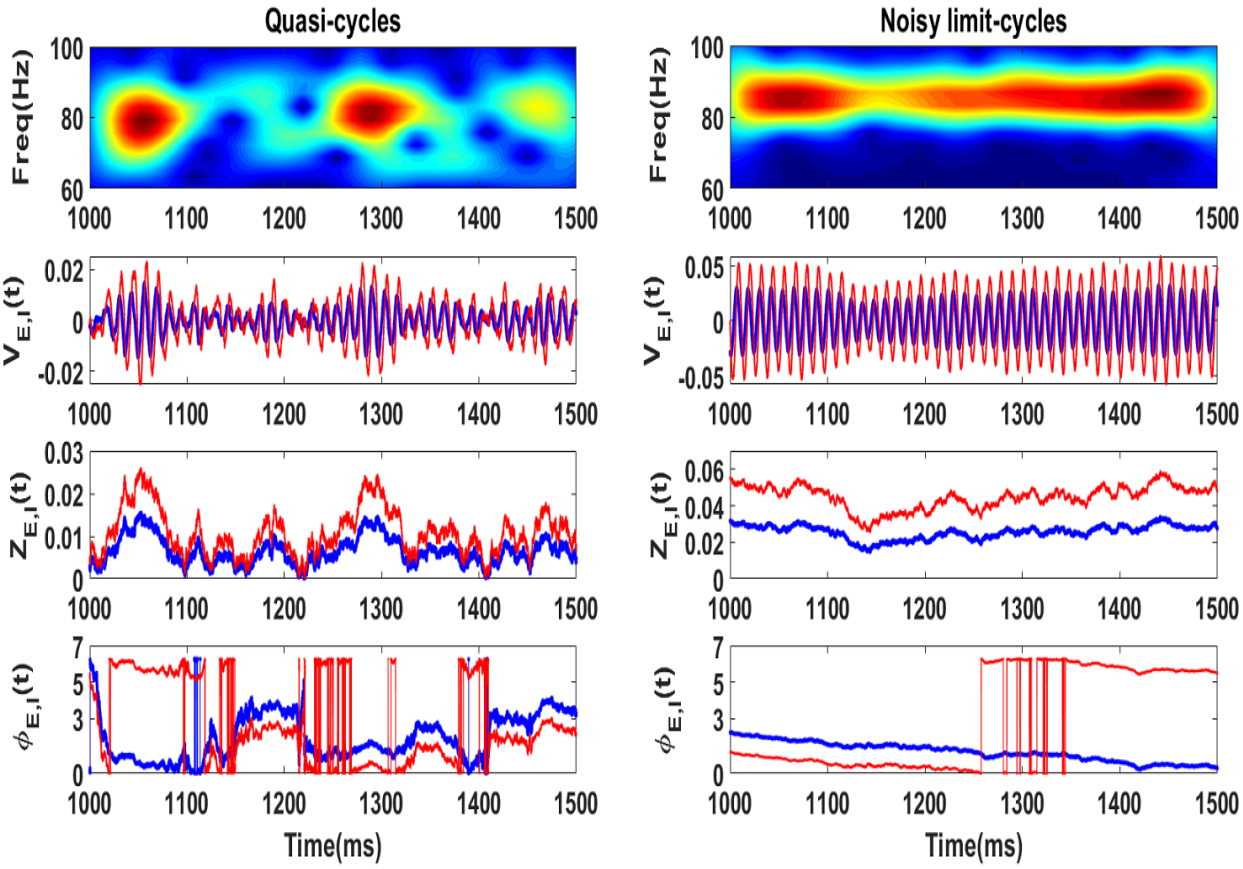

Figure 5.3: **Quasi-cycle and noisy limit cycle properties using the SAM approximation.** From top to bottom: Spectrogram, activity timeseries, amplitudes and phases of the excitatory (blue) and inhibitory (blue) populations simulated using the dynamics Eqs. (5.23-5.24) computed using the SAM analysis. **Left**: quasi-cycle regime with its characteristic bursting structure. Fluctuations, amplitudes and phases resemble dynamics obtained with linear equations driven by noise [102, 182]. **Right**: self-sustained oscillations perturbed by noise, with almost constant envelope, phase and frequency characteristic of noisy limit cycles. Quasi-cycle parameters are as for the left black dot in Fig.5.1(b), i.e. $W_{EE} = 27.4$. Limit cycle parameters are as for the right black dot in Fig.5.1(b), i.e. $W_{EE} = 30.4$. The noise strengths are $\sigma_E = 0.0015ms^{-1/2}, \sigma_I = 0.005ms^{-1/2}, \sigma = 0.005ms^{-1/2}$. Other parameters are as in Fig.5.1(e,f).

Deterministic analysis of the amplitude dynamics

We focus on the deterministic case $D = 0$, for which the amplitude dynamics are:

$$\frac{dZ_E^0}{dt} = -\nu Z_E^0 + B_1 (Z_E^0)^3 \,. \tag{5.29}$$

Let us define $F_0(Z_E) \equiv -\nu Z_E + B_1 (Z_E)^3$ and its derivative $F_0^{'}(Z_E) = -\nu + 3B_1 (Z_E)^2$. The solutions of $F(Z_E^0) = 0$ are the fixed points of the deterministic amplitude dynamics Eq. (5.29). Their stability is given by the sign of the corresponding value of $F'(Z_E^0)$. The existence and the number of the solutions of $F(Z_E^0) = 0$ depend on whether the system lies below or above the Hopf bifurcation.

- Stable focus ($\nu > 0$): The only fixed point is $Z_E^0 = 0$. This fixed point is stable since $F^{'}(0) = -\nu < 0$. This is in agreement with previous results, since in the deterministic limit and below the Hopf bifurcation, the amplitude of a perturbation from the fixed point converges to zero.

- Limit-cycle ($\nu < 0$): We have two fixed points $Z_E^0 = 0$ and $Z_E^0 = \sqrt{\frac{\nu}{B_1}}$. But the only stable fixed point is $Z_E^0 = \sqrt{\frac{\nu}{B_1}}$ since $F^{'}(0) = -\nu > 0$ and $F^{'}\left(\sqrt{\frac{\nu}{B_1}}\right) = 2\nu < 0$. The value of this fixed point represents the amplitude of the oscillation. The size of the limit cycle thus varies as $\sqrt{\nu}$ as expected from the normal form of the supercritical Hopf bifurcation [206].

Now, we turn to the effect of the noise on this deterministic picture.

Stochastic analysis of the amplitude dynamics ($D > 0$)

To perform the stochastic analysis of the amplitude process, we consider the corresponding stationary Fokker-Planck equation of (5.23) [90]:

$$-\frac{d}{dZ_E}\left[\left(-\nu Z_E + \frac{D}{2Z_E} + B_1 Z_E^3\right) P_E\right] + \frac{D}{2}\frac{d^2 P_E}{dZ_E^2} = 0 \tag{5.30}$$

where $P_E\big(Z_E\big)$ represents the stationary probability density function of the amplitude process $Z_E(t)$. The normalized solution $\left(\int_0^\infty P_E(Z_E) = 1\right)$ of this second order differential equation is given by

$$P_E(Z_E) = \frac{4a}{\sqrt{\pi} erfc(ba)} Z_E \exp\left[- a^2(Z_E^2 + b)^2 \right]. \tag{5.31}$$

By using the relation between the amplitude of excitatory and inhibitory LFPs ($Z_I = \alpha Z_E$), we obtain the stationary probability density function for the inhibitory amplitude process:

$$P_I(Z_I) = \frac{4a}{\alpha^2\sqrt{\pi} erfc(ba)} Z_I \exp\left[- (a/\alpha)^2(Z_I^2 + \alpha^2 b)^2 \right] \tag{5.32}$$

where the parameters a and b are defined as

$$a = \sqrt{\tfrac{-B_1}{2D}} \quad \text{and} \quad b = \frac{-\nu}{B_1}$$

and $ercf$ denotes the complementary error function defined as: $erfc(x) = \frac{2}{\sqrt{\pi}} \int_x^\infty e^{-t^2} dt$. The peak of the stationary density, which represents the most probable value taken by the stochastic amplitude process, is given by

$$\frac{dP_E(Z_E)}{dZ_E} = 0 \ .$$

This relation leads to the following equation

$$1 - 4a^2 b Z_E^2 - 4a^2 Z_E^4 = 0 \, . \tag{5.33}$$

The solution of this equation can be obtained for the two distinct regimes:

- Quasi-cycle regime ($\nu > 0, \quad b > 0$):

  The solution is given by

  $$Z_E^2 = -\frac{b}{2} + \frac{b}{2}\left(1 + \frac{1}{(ab)^2}\right)^{1/2} . \tag{5.34}$$

  The approximate expressions for the location of the peaks of the E and I amplitude probability densities are then:

  $$Z_E^* \approx \sqrt{\frac{D}{2\nu}} \quad and \quad Z_I^* \approx \alpha\sqrt{\frac{D}{2\nu}} \, . \tag{5.35}$$

We observe that the peak values of the stationary probability densities are in agreement with the previous results reported for the linearized Wilson-Cowan equations driven by additive noise [182]. Moreover, in the limit $B_1 = 0$ using $b \to \infty, a \to 0, ab \to \infty$, the E stationary probability density can be written as (we drop the subscript E for the sake of readability):

$$\begin{aligned} P_E(Z) &= \frac{4a}{ercf(ba)\sqrt{\pi}} Z \exp\left[- a^2(Z^2+b)^2 \right] \\ &= \frac{4a}{\sqrt{\pi}}(1 - erf(ba))^{-1} Z e^{-(ab)^2} e^{-a^2 Z^4} e^{-2ba^2 Z^2} \\ &\approx \frac{4a}{\sqrt{\pi}}(1 - erf(ba))^{-1} Z e^{-(ab)^2} e^{-2ba^2 Z^2} . \end{aligned}$$

Expanding the error function as

$$erf(ab) \approx 1 - e^{-(ab)^2} . \frac{1}{\sqrt{\pi}} \left(\frac{1}{ab} - \frac{1}{2(ab)^3} + ... \right) \tag{5.36}$$

we then obtain

$$\begin{aligned} P_E(Z) &\approx \frac{4a}{\sqrt{\pi}} \left(e^{-(ab)^2} . \frac{1}{\sqrt{\pi}} \frac{1}{ab} \right)^{-1} Z e^{-(ab)^2} e^{-2ba^2 Z^2} \\ &\approx 4a^2 b Z \exp\left(-\frac{\nu}{D} Z^2 \right) . \end{aligned}$$

We thus recover the expressions of the probability densities obtained in the case of linear equations driven by additive noise [182], namely

$$P_E(Z_E) = \tfrac{2\nu}{D} Z_E \exp\left(- \tfrac{\nu}{D} Z_E^2 \right)$$

for the excitatory amplitude process and

$$P_I(Z_I) = \tfrac{2\alpha\nu}{D} Z_I \exp\left(- \tfrac{\alpha^2\nu}{D} Z_I^2 \right)$$

for the inhibitory amplitude process.

- Noisy limit-cycle regime ($\nu < 0, \quad b < 0$):

  The solution is given by:

$$Z_E^2 = -\frac{b}{2} - \frac{b}{2} \left(1 + \frac{1}{(ab)^2} \right)^{1/2} . \tag{5.37}$$

This leads to the following approximate expressions obtained in weak noise limit:

$$Z_E^* \approx \sqrt{\frac{\nu}{B_1} + \frac{D}{2(-\nu)}} \quad and \quad Z_I^* \approx \alpha \sqrt{\frac{\nu}{B_1} + \frac{D}{2(-\nu)}}\,. \tag{5.38}$$

We should mention that the approximations in Eq. (5.35) and Eq. (5.38) are valid for weak noise and away from the Hopf bifurcation. They were derived to get an idea of the role of noise on the limit cycle dynamics. The accurate expression for the peak of the amplitude probability density is determined by Eq. (5.33).

We see that for $D = 0$, we recover the result previously obtained in the deterministic analysis. Importantly, for $D > 0$ the most probable amplitude value for the noisy limit cycle is greater than that for the deterministic case. There is an additional term which is proportional to the strength of the noise D and inversely proportional to the real part of the eigenvalues. This is a noise-induced term which shows how noise shapes the amplitude of the limit cycle by increasing its magnitude.

We plot the densities of the E and I amplitude processes for the quasi-cycles and noisy limit cycles in Fig. 5.4(a,c) and Fig. 5.4(b,d), respectively. We find an excellent match between analytical expressions from Eqs. (5.31 and 5.32) (black curves) and numerical simulations of Eqs. (5.13-5.14) (magenta curves). Also we found excellent agreement with the values of the means (vertical blue lines) computed from the stochastic analysis Eqs. (5.38) in both regimes.

In the following, we mostly focus on the dynamics of the noisy limit cycle since the case of the quasi-cycle has already been investigated in a previous study [182], and the results here with the extra nonlinearity are qualitatively the same. Can strong noise induce bursting structures in the limit cycle regime like those seen for quasi-cycles? If so, how can we discriminate between these two dynamical origins for the burst epochs?

Dynamics of the noisy limit cycle

We investigate the effect that different noise strengths can have on the amplitudes of limit cycle oscillations. We consider the limit cycle regime close to the supercritical Hopf bifurcation (black dot, figures 5.1), where the system is weakly nonlinear and the amplitude of the deterministic limit cycle is small. The amplitude density shows little variation with noise strength in the weak noise

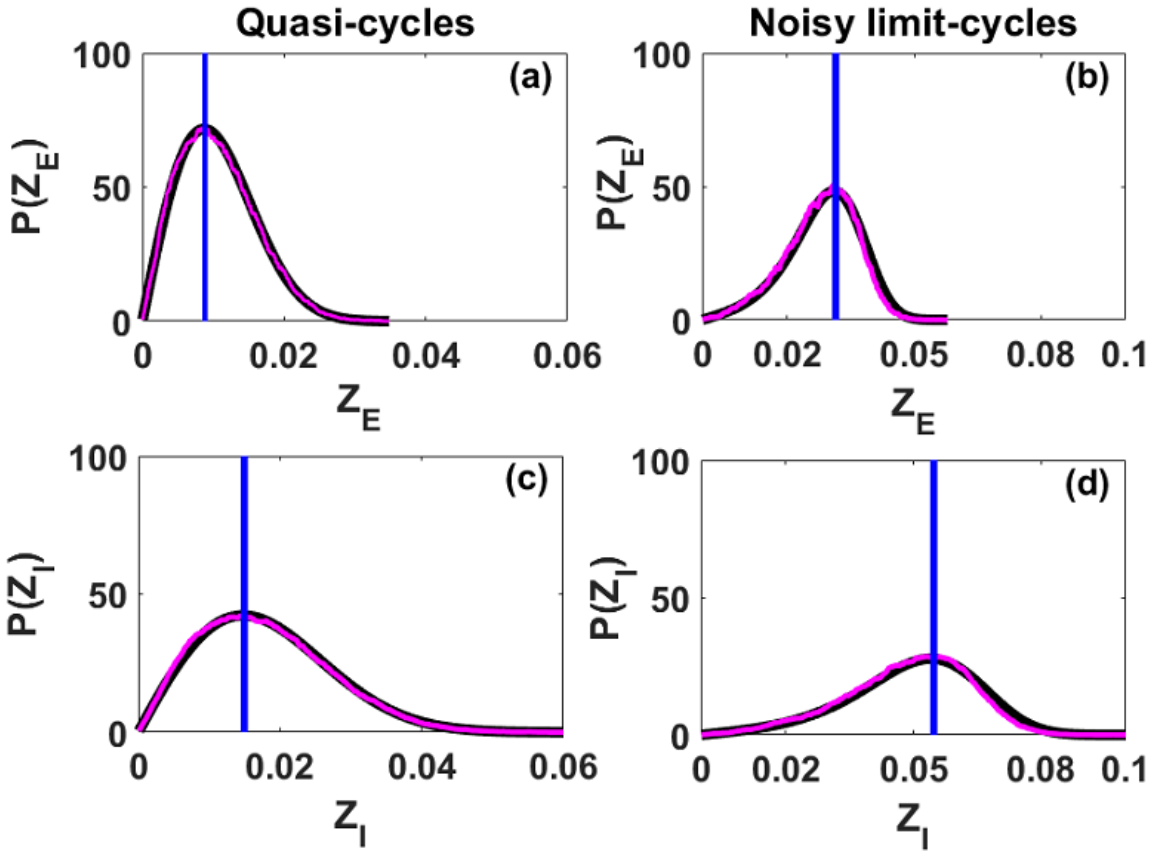

Figure 5.4: **Probability densities of excitatory and inhibitory amplitude processes. Left panels**: Probability densities of excitatory (top) and inhibitory (bottom) amplitude processes in the quasi-cycle regime. **Right panels**: Probability densities of excitatory (top) and inhibitory (bottom) amplitude processes in the noisy limit cycle regime. The black curves correspond to analytical results (equations 5.31 and 5.32) and the magenta curves are from numerical simulations of Eqs. (5.13-5.14). The vertical blue lines are analytical values of the probability density peak locations computed from Eq. (5.35) for the quasi-cycle (left panels) and from Eq. (5.38) for the limit cycle regimes (right panels). Theory matches up very well with numerical simulations. We also note a transition of the density shape from Rayleigh in the quasi-cycle case to approximately Gaussian in the noisy limit cycle case. Quasi-cycles (a,c): $W_{EE} = 27.4$. Noisy limit cycles (b,d): $W_{EE} = 30.4$. Noise strengths are $\sigma_E = 0.0015, \sigma_I = 0.005, \sigma = 0.005$ in $ms^{-1/2}$, and other parameters are as in Fig.5.1.

limit. The corresponding probability densities in Fig. 5.5(a,b), red curves) are close to Gaussian with small variance; their means can be predicted from the theoretical expressions in Eqs. (5.38).

The small variance causes long segments of uninterrupted strong oscillations, i.e. minimal bursting, in contrast to what is observed for the quasi-cycles. As we further increase the noise strength, the mean and variance of the amplitude values increase. For strong noise (Figs. 5.5(a,b), blues curves) the mean amplitude values are high with corresponding large variance. The fact that amplitude values near zero are now more probable compared to the weak noise limit suggests that bursts are favoured under these conditions. To unveil the interplay between the noise and the size of the limit cycle, we now increase the size of the limit cycle using larger recurrent excitation strengths W_{EE} as suggested by Fig. (5.1), as well as vary the noise strength.

For weak noise in Fig.5.6(a,b), increasing W_{EE} increases the mean value of the oscillation amplitude and decreases its variance. This suggests that bursting decreases moving further beyond the bifurcation. Intermediate noise in Fig.5.6(c,d) increases the variance, thus causing bursts, as is seen for all limit cycle sizes over this range of W_{EE}. The effect of noise on the mean amplitude is more significant close to the Hopf bifurcation. Strong noise in Fig. 5.6(e,f) increases variance for all limit cycle sizes, but increases the mean mostly near the Hopf bifurcation. This can be understood from Eqs. (5.38). Close to the Hopf bifurcation, $|\nu|$ is small and the effect of the term $\frac{D}{2(-\nu)}$ dominates. Far from the bifurcation however, $|\nu|$ is larger and $\frac{D}{2(-\nu)}$ is now less important. The mean amplitude thus depends less on D and instead varies mostly as $\frac{\nu}{B_1}$.

We next directly characterize the effect of noise on the peak of the probability density given by the solution of Eq. (5.33). This can now be done for both the quasi- and limit cycle regimes. Figure (5.7) shows that increasing noise strength produces more smoothing of the bifurcation and higher most probable values. The results computed by the SAM are in good agreement with numerical simulations obtained through the Hilbert transform performed on the SWC3 dynamics. This speaks to the predictive power of the SAM technique in this system, as it provides a theoretical handle on amplitude strength as a function of the intrinsic network parameters and the external noise. The most probable amplitude value is also an indirect measure of level of network synchronization, and can be seen as an order parameter for the stochastic bifurcation as Fig. (5.7) reveals.

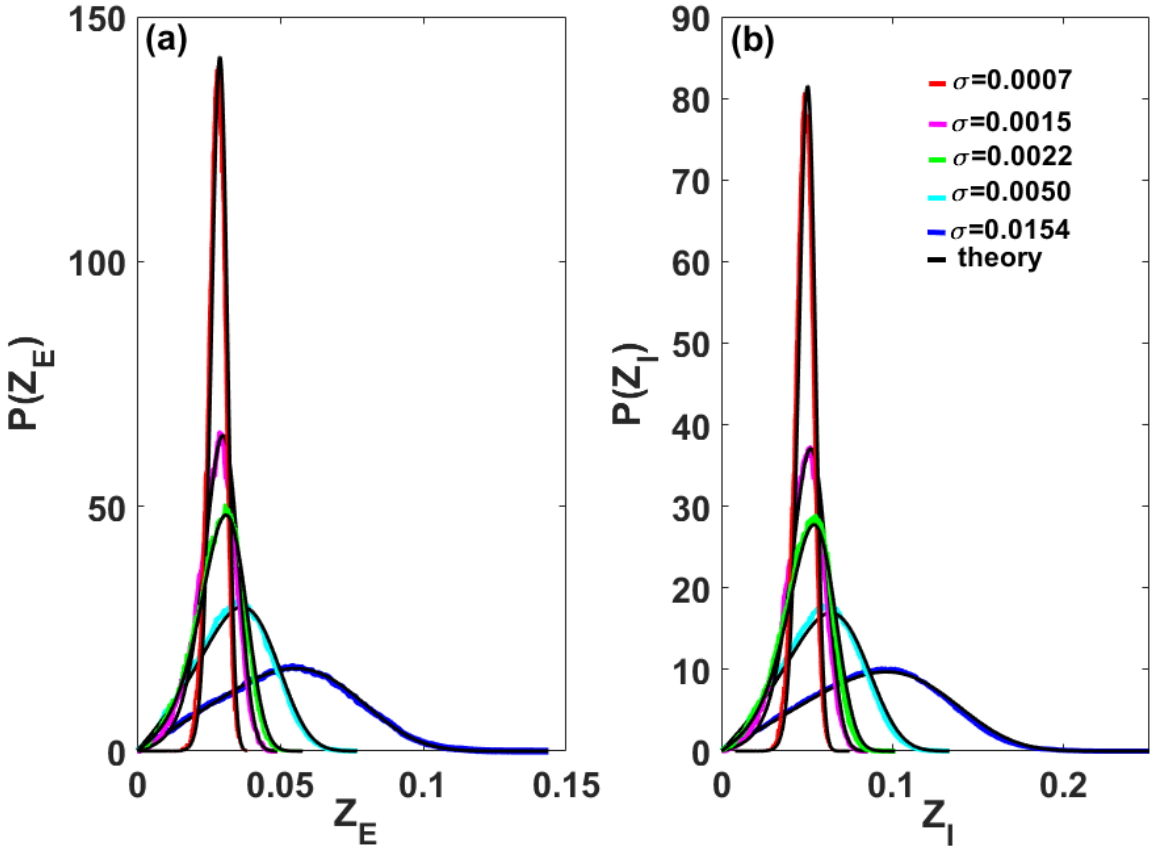

Figure 5.5: **Effect of noise on the limit cycle oscillations**. We consider the limit cycle regime just beyond the Hopf bifurcation (see Fig. 5.1) and look at the effect of the noise strength on the dynamics of the E **(a)** and I **(b)** amplitudes. High noise increases the overall amplitude values but also increases their variability, enabling oscillatory bursts. Black curves correspond to theory while other colours correspond to numerical simulations at different noise strengths as specified in the legend to panel (**b**). In detail, blue: $\sigma_E = 0.004ms^{-1/2}, \sigma_I = 0.015ms^{-1/2}, \sigma = 0.0154ms^{-1/2}$; cyan: $\sigma_E = 0.0015ms^{-1/2}, \sigma_I = 0.005ms^{-1/2}, \sigma = 0.005$; green: $\sigma_E = 0.0006, \sigma_I = 0.002, \sigma = 0.0022$; magenta: $\sigma_E = 0.00045, \sigma_I = 0.0015, \sigma = 0.0015$; red: $\sigma_E = 0.0002, \sigma_I = 0.0006, \sigma = 0.0007$. The units of the noise intensities are $ms^{-1/2}$. In all cases, there is good agreement between theory and numerics.

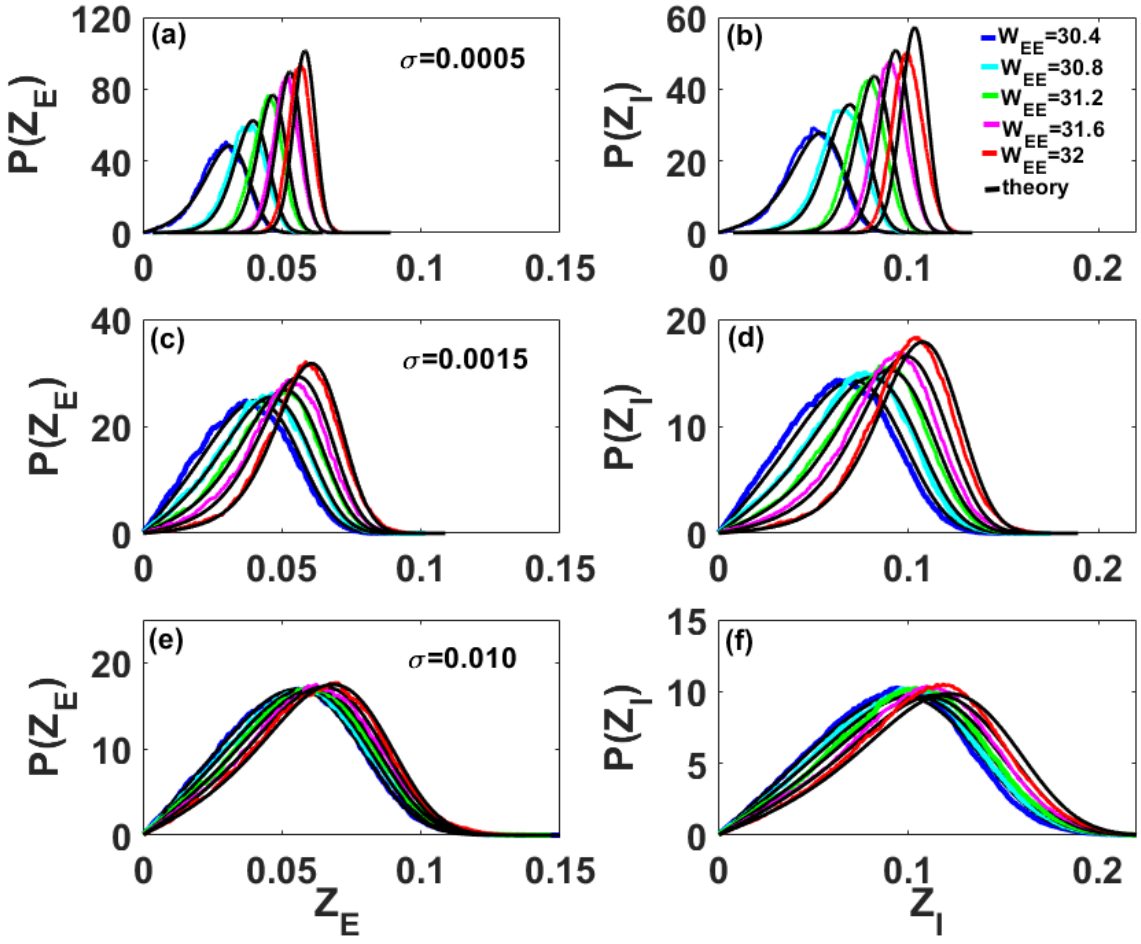

Figure 5.6: **Interplay between noise and limit cycle amplitude density**. For weak noise (a-b), moving beyond the Hopf bifurcation by increasing W_{EE} leads to an increase in the mean amplitude and a reduction of its variability. For intermediate noise (c-d), an increase in variability is visible for all values of W_{EE}. The effect of noise strength on increasing the mean amplitude of the oscillations is prominent near the Hopf bifurcation (weak values of W_{EE}), but very weak far from it. For strong noise (e-f), the amplitude mean and variability increase again for all W_{EE}. The units of the noise intensities in the figures are $ms^{-1/2}$.Other parameters are as in Fig.5.1.

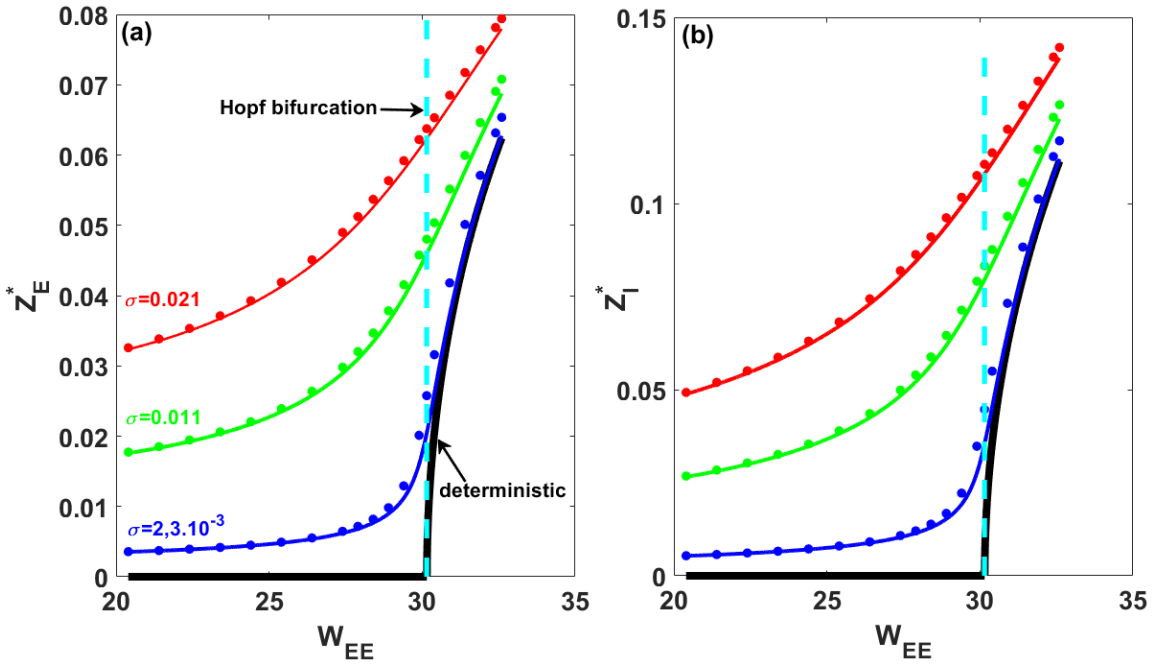

Figure 5.7: **Bifurcation diagram of the SWC3 model.** Peaks of the probability densities of the E **(a)** and I **(b)** amplitude fluctuations as a function of the recurrent excitatory coupling. Noise smoothes the sharp Hopf bifurcation and increases the mean amplitude, i.e. it induces the quasi-cycles. However, these densities does not reveal the regularity or coherence of the oscillation. For all the curves, the solid lines correspond to the theoretical expression of the peak amplitude, while the dots are the result of numerical simulation which are in good agreement with the SAM theory. Other parameters are as in Fig.5.1.

Our analysis also shows that noise shapes the mean and burstiness of the limit cycle amplitude. In particular, strong noise can create bursts even in the limit cycle regime. Quasi-cycle bursts are a signature of an induced oscillation, but in the limit cycle regime, they are a sign of strong noise. It is difficult to differentiate between these two cases just by looking at the spectrograms. But this can be helped by also considering the envelope probability densities. If the density is closer to Rayleigh than Gaussian, the spectrogram is likely the result of quasi-cycle dynamics; a better fit to a Gaussian points instead to a noisy limit cycle.

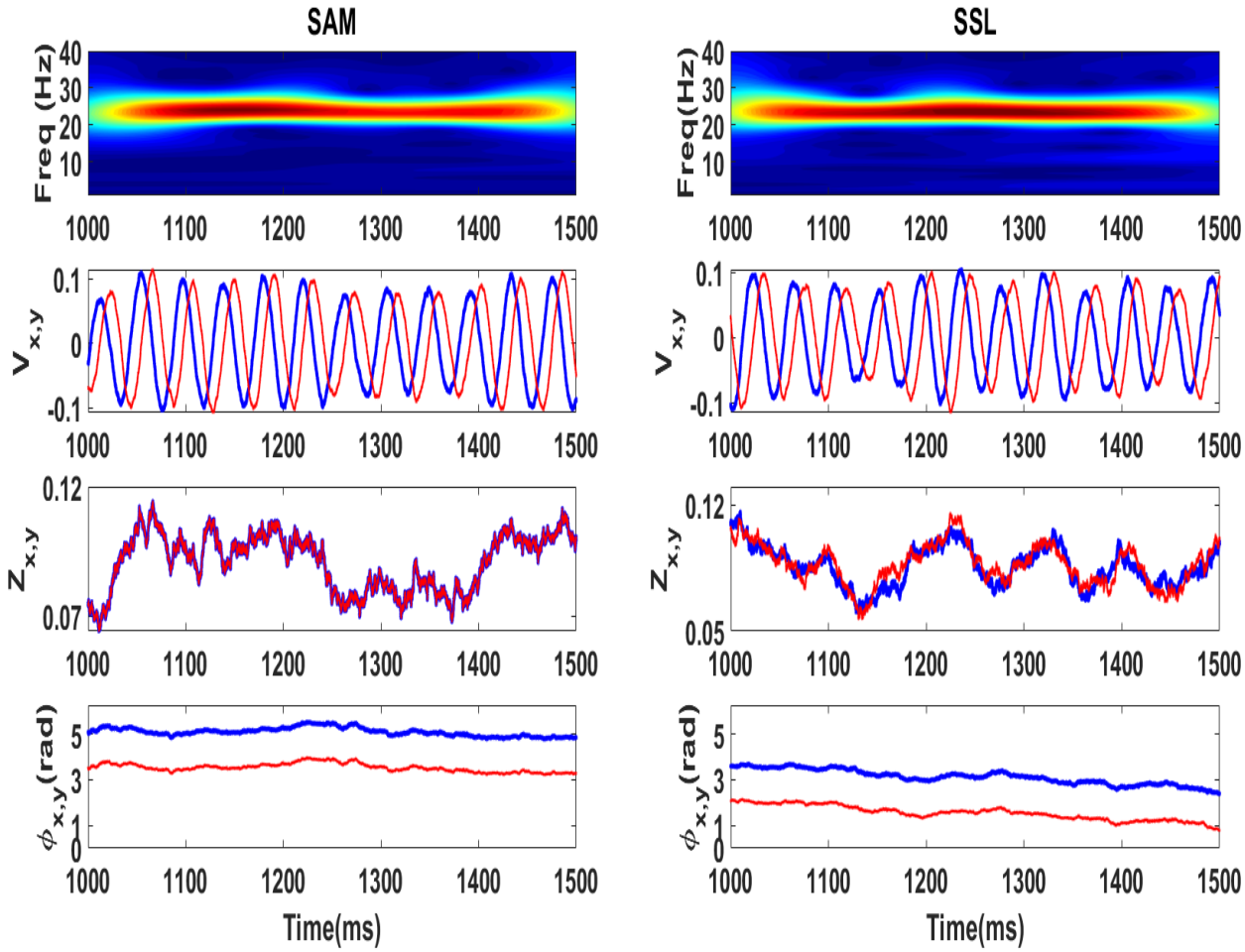

Figure 5.8: **Spectrogram, x and y fluctuations, amplitudes and phases computed from the SAM and from the SSL using the Hilbert transform.** From top to bottom: Spectrogram, x and y fluctuations, amplitudes and phases of the x (blue) and y (red) populations computed from the SAM analysis (left panels) and from the Hilbert transform (right panels) performed on numerical solutions of the SSL model. The SAM results match well with the numerical results obtained through the Hilbert transform. Parameters are $a_0 = 0.01ms^{-1}, \omega_0 = 0.150ms^{-1}, \sigma_x = \sigma_y = \sigma = 0.002ms^{-1/2}$. We have consider a Gaussian white noises applied on x and y variables.

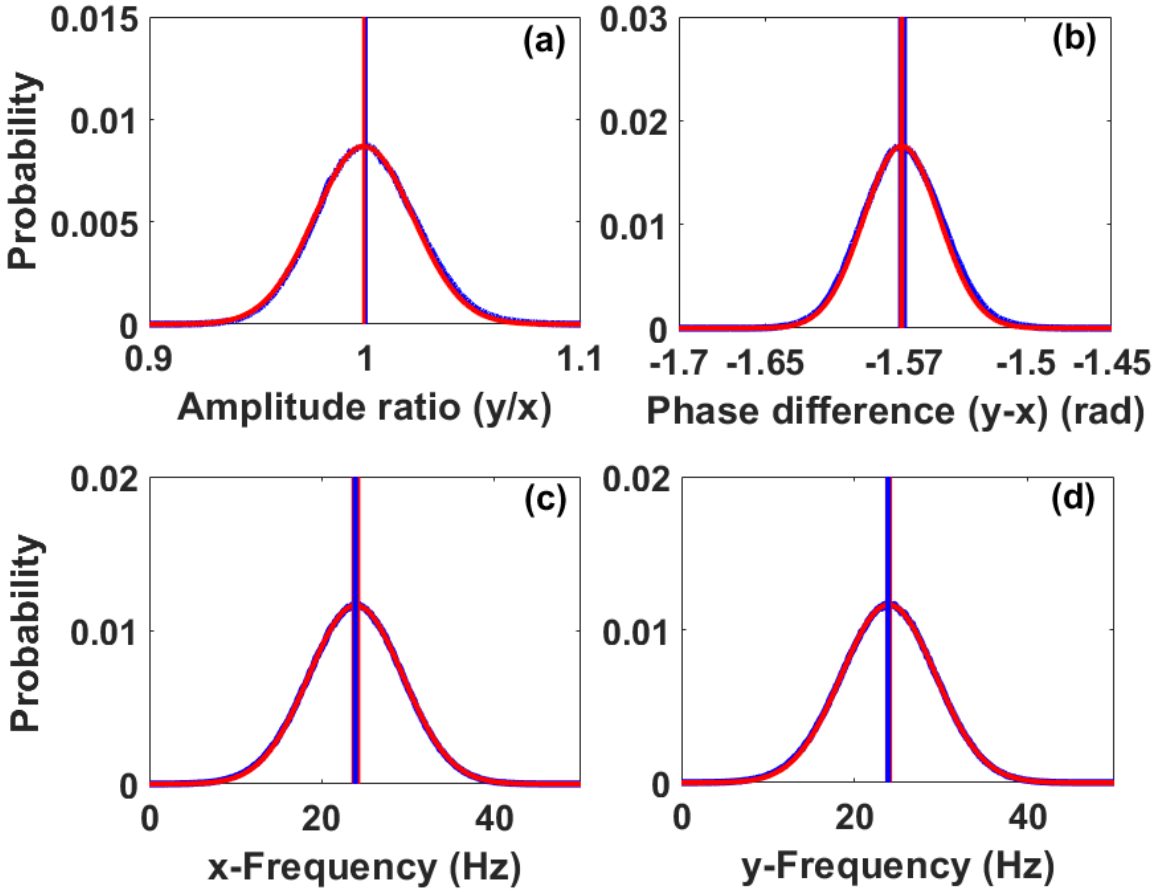

Figure 5.9: **Amplitude ratio, phase difference between y and x fluctuations, along with their frequency, in the noisy limit cycle regime.** As for the SWC3 case, the amplitude ratio is plotted (red curve-(a)) along with the corresponding Gaussian distribution (blue curve-(a)). The vertical red line is the result of the linear stability, while the vertical blue line corresponds to the mean of the Gaussian distribution. Similar results hold for panels (b-d). The probability distributions of the fixed ratio and phase difference are Gaussian distributed. The x and y frequencies are also Gaussian distributed with their mean value at ω_0. The values of ω_0 were converted to be in the beta range. Parameters are as in Fig.5.8.

5.3 Stochastic Stuart-Landau Model

To assess the generality of our amplitude-phase decomposition across the bifurcation, we now turn to the stochastic Stuart-Landau (SSL) model [206]. Its deterministic dynamics is the canonical form of the supercritical Hopf bifurcation. We perform an amplitude-phase decomposition and pay particular attention to the noisy limit cycle regime and the effect of correlated noise. The dynamics is given as:

$$\dot{x}(t) = a_0 x(t) - \omega_0 y(t) - x(t)\big[x^2(t) + y^2(t)\big] + \eta_x(t) \tag{5.39}$$

$$\dot{y}(t) = \omega_0 x(t) + a_0 y(t) - y(t)\big[x^2(t) + y^2(t)\big] + \eta_y(t)\,. \tag{5.40}$$

The eigenvalues around the origin are given by $\lambda = a_0 \pm j\omega_0$, and the supercritical Hopf bifurcation happens at $a_0 = 0$. Quasi-cycles exist in the region $(a_0 < 0; \omega_0 > 0)$ and noisy limit cycles are defined in the region $(a_0 > 0; \omega_0 > 0)$. We proceed as in the case of SWC3 equations. We first separate the dynamics of the model into its fixed point and the corresponding fluctuations as $x(t) = x_0 + V_x(t)$ and $y(t) = y_0 + V_y(t)$. Note that for the Stuart-Landau model, the fixed point is the origin $(x_0 = y_0 = 0)$. However, we will keep the notations x_0 and y_0 to easily make the connection with the analysis done in the SWC3 model. By identification with the analysis done in the case of the SWC3 system in Eqs. (5.13-5.14), we obtain the following coefficients for the dynamics of the fluctuations (with subscripts E and I replaced by x and y respectively):

$$\begin{aligned}
&A_{xx} = a_0 - \big(3x_0^2 + y_0^2\big); \quad A_{yy} = a_0 - \big(x_0^2 + 3y_0^2\big),\\
&A_{xy} = -\big(\omega_0 + 2x_0 y_0\big); \quad A_{yx} = \omega_0 - 2x_0 y_0,\\
&L_{xx} = -3x_0; \quad L_{xy} = -2y_0; \quad L_{yx} = -2x_0; \quad L_{yy} = -3y_0,\\
&M_{xy} = -x_0; \quad M_{yx} = -y_0; \quad B_{1x} = -1; \quad B_{2x} = -1,\\
&B_{3x} = 0; \quad B_{1y} = -1; \quad B_{2y} = 0; \quad B_{3y} = -1; \quad B_{4x} = 0; \quad B_{4y} = 0.
\end{aligned}$$

The fixed amplitude ratio and phase difference between x and y components are also obtained similarly, with ω_o again considered as the oscillation frequency. However, in the case of the SSL model, the amplitude ratio computed through linear stability analysis is $\alpha = 1$ (Fig. 5.9(a)) and the

phase difference is $\delta = -\frac{\pi}{2}$ (Fig. 5.9(b)). Therefore the solution can be sought in the form:

$$V_x = Z(t)\cos(\omega_0 t + \phi(t)); \quad V_y = Z(t)\sin(\omega_0 t + \phi(t))\,. \tag{5.41}$$

We have assumed $Z_x = Z$ for readability. We then applied the SAM using the above expressions and obtained:

$$dZ(t) = \left[a_0 Z(t) - Z^3(t) + \frac{D}{2Z(t)}\right]dt + \sqrt{D}dW_1(t) \tag{5.42}$$

$$d\phi(t) = B_2 Z^2(t)dt + \frac{\sqrt{D}}{Z(t)}dW_2(t)\,. \tag{5.43}$$

For the case of the SSL model, the coefficient $B_1 = -1$ and $B_2 = 0$. We choose to replace B_1 by its value to show the specificity of the SSL model, and to keep B_2 to show the general dependence of the phase on the envelope amplitude for noisy limit cycles; the fact that $B_2 = 0$ is just a specific property of the SSL model. We focus on the noisy limit cycle regime, comparing our amplitude-phase dynamics with the SAM to those extracted using the Hilbert transform. Figure (5.8) shows good agreement between the two. Note that we have chosen parameters such that the peak frequency is lower than for the SWC3 model, placing it more in the beta range in the context of brain rhythms. Similar analyses can be performed at higher (gamma) or lower frequencies such as in the delta and theta ranges.

Unlike the SWC3 case, here we have independent correlated OU noise inputs to the x and y components. We computed the density $P(Z)$ for different correlation times $\tau = \tau_x = \tau_y$ (varied while keeping the noise intensity fixed pour both inputs), and this was repeated for four noise intensities. Figure (5.10) shows that shorter noise correlation time and larger intensity, and especially their combination, cause significant probability at small amplitudes, which is a sign of bursting. For small τ, the inputs approach white noise, and the behavior of the amplitude can be understood from the analysis of the SWC3 above. We also observed a good match between the SAM theory and numerical simulations for all correlation times.

As for the SWC3 model, we computed the peak of the probability density of the amplitude process for different τ values at a low and a high noise strength (Figs.5.11). Like previously observed, the noise and correlation strength increase the overall amplitude mean as they smoothe out (i.e.

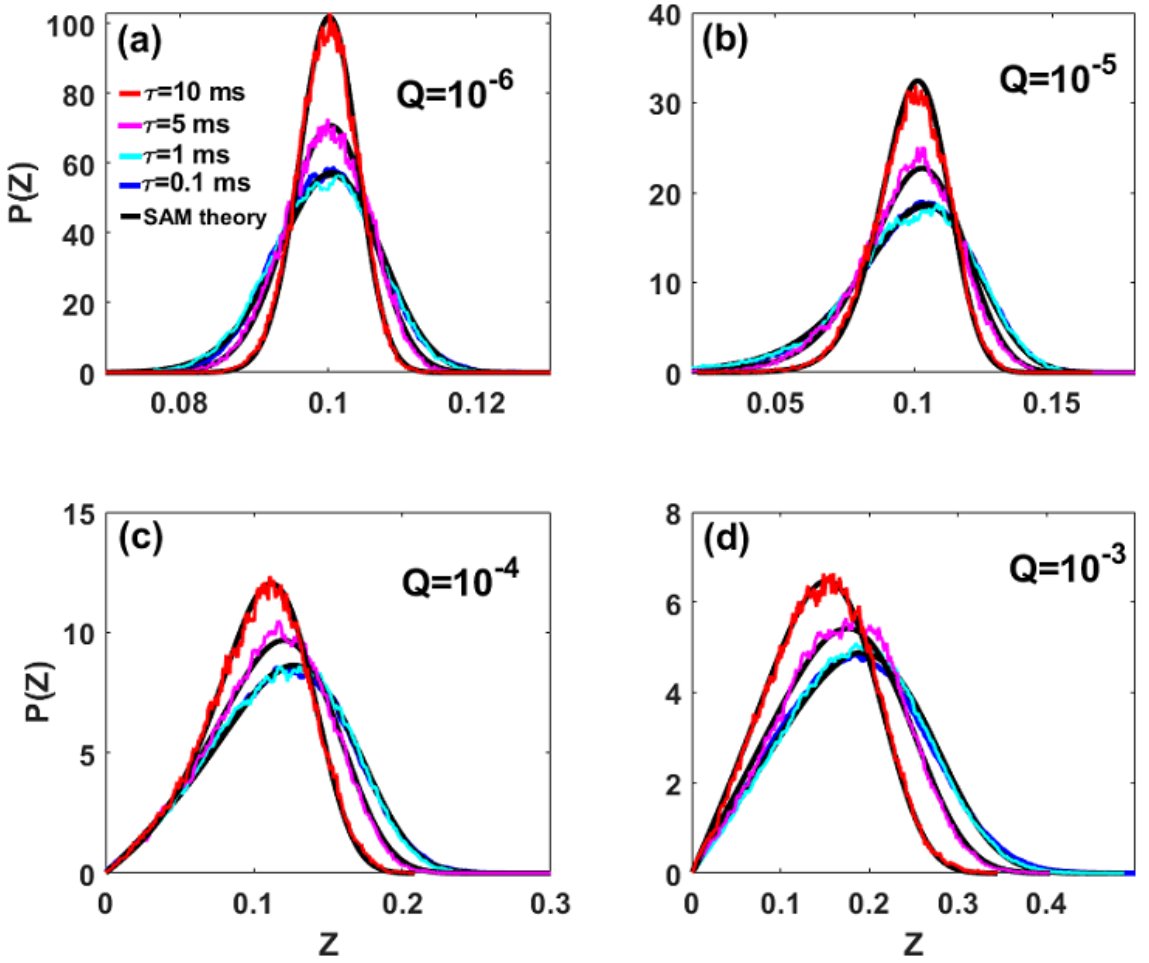

Figure 5.10: **Effect of noise correlation time and intensity on the SSL amplitude-phase dynamics.** The probability densities of the amplitudes of the SSL for correlation times $\tau = \tau_x = \tau_y$ of the OU processes were computed for **(a)** weak noise, **(b-c)** intermediate noise and **(d)** strong noise intensity. We observe that for all intensities and correlation times, the density for the amplitude processes computed numerically through the Hilbert transform (**colored curves**) match with those calculated theoretically (**black curves**) using Eqs. 5.31 and 5.26, with $\sigma_E = \sigma_x = \sigma; \sigma_I = \sigma_y = \sigma$ and $Q = \tau\sigma^2$. For weak values of τ and large intensities, the corresponding densities are broader. For large intensities, the densities have higher mean amplitude; weak values of τ also increase the mean amplitude. Parameters are as in Fig.5.9 unless otherwise specified here.

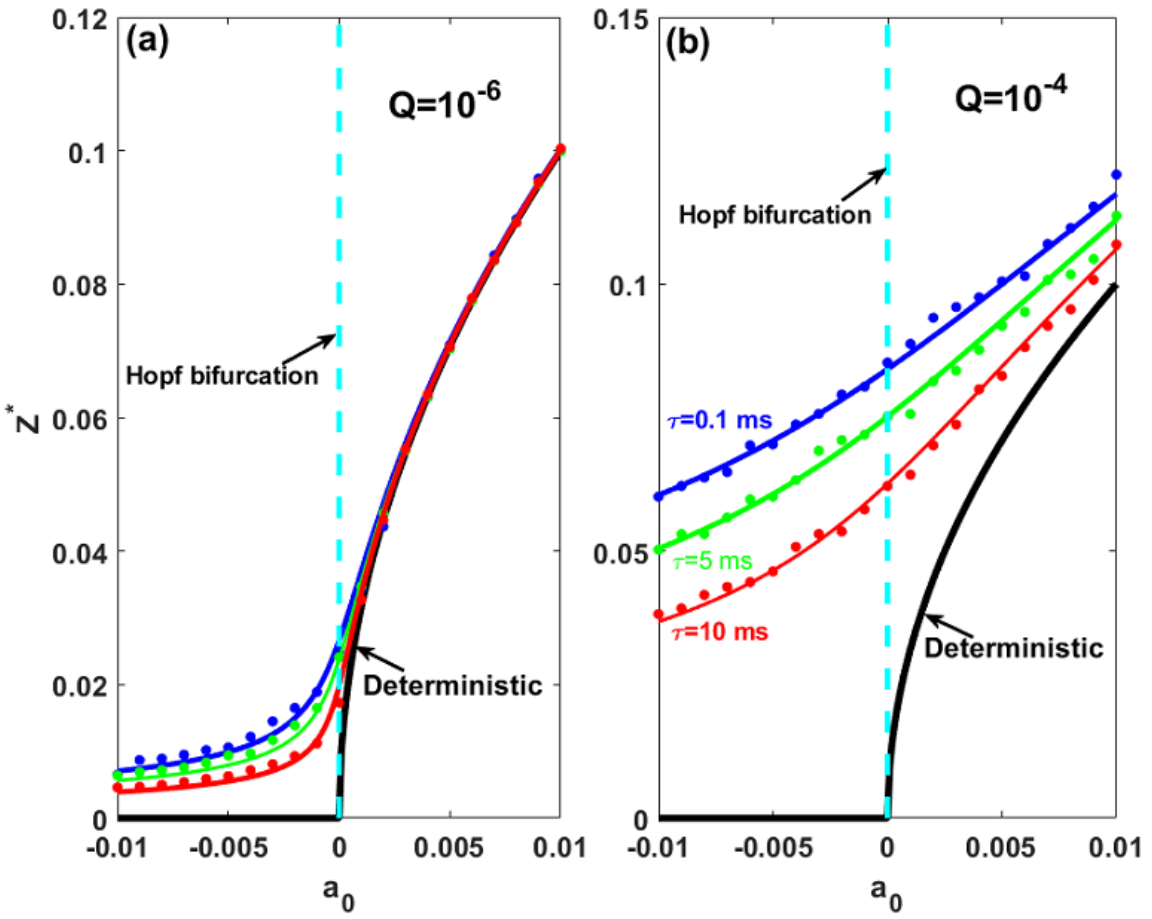

Figure 5.11: **Bifurcation diagram of the SSL model.** The peak of the amplitude probability density is plotted as a function of the bifurcation parameter a. The noise is the OU process with different $\tau = \tau_x = \tau_y$. The noise strength is $Q = \tau\sigma^2 = 10^{-6}$ in **(a)** and $Q = \tau\sigma^2 = 10^{-4}$ **(b)**. Increasing Q and τ increases the peak amplitude value. Solid curves correspond to SAM theory while dots are from numerical simulations. For all cases, a good match between theory and numerical results is seen. Parameters are as in Fig.5.9 unless otherwise specified.

linearize) the supercritical Hopf bifurcation. The SAM approximation continues to work well even for the stronger correlation case.

Next we compare our amplitude-phase decomposition with previous decomposition of the SSL model using the change of variable $\theta(t) = \omega_0 t + \phi(t)$, leading to:

$$d\theta(t) = \omega_0 \, dt + \frac{\sqrt{D}}{Z(t)} dW_2(t) \, . \tag{5.44}$$

In the deterministic limit $D = 0$, Eqs. (5.42) and 5.44 correspond to the polar normal form of the supercritical Hopf bifurcation [206]. In the stochastic case however, the noise appears in a non-trivial manner in both the Z and ϕ (or θ) equations, and is a general amplitude-phase description of noisy oscillators around a supercritical Hopf bifurcation. By taking into account the amplitude ratio and phase difference between the two components, it provides a good description of the quasi-ellipsoid form of the quasi-cycle or of the stochastic noisy limit cycle (the deterministic limit cycle is a quasi-ellipsoid for the WC model); its complements other averaging approaches that consider the component amplitudes to be the same [58, 178].

5.4 Amplitude-Phase Decomposition for Networks

Finally we extend our theory to interconnected networks of E-I units described by the SWC3 or SSL nonlinear rate models. One application of such amplitude-phase decomposition may be the study of the functional connectivity between brain areas [64, 58, 62]. We only consider the case where the network frequencies belong to the same band and therefore avoid the case of cross-frequency coupling where faster rhythms are coupled with slower ones [122].

5.4.1 Network of Stochastic Wilson-Cowan units

We consider a network of SWC3 units coupled through long-range excitatory connections:

$$\frac{dE_k(t)}{dt} = -\alpha_E E_k + \big(1 - E_k\big)\beta_E f(s_{E_k}) + \eta_{E_k} \tag{5.45}$$

$$\frac{dI_k(t)}{dt} = -\alpha_I I_k + \big(1 - I_k\big)\beta_I f(s_{I_k}) + \eta_{I_k} \tag{5.46}$$

The total excitatory $s_{E_k}(t)$ and inhibitory $s_{I_k}(t)$ synaptic inputs to a neuron population are given by

$$s_{E_k}(t) = W_{EE}^k E_k - W_{EI}^k I_k + h_E^k + \sum_{l=1, l\neq k}^{N} S_{EE}^{kl} E_l(t-\tau_{kl}) \tag{5.47}$$

$$s_{I_k}(t) = W_{IE}^k E_k - W_{II}^k I_k + h_I^k + \sum_{l=1, l\neq k}^{N} S_{IE}^{kl} E_l(t-\tau_{kl})\,. \tag{5.48}$$

The coefficient S_{EE}^{kl} denotes the long-range excitatory weight from excitatory population l to excitatory population k, while S_{IE}^{kl} accounts for the weight from excitatory population l to inhibitory population k. As for the case of the single E-I units, we look at the fluctuations of each unit as follows:

$$E_k(t) = E_0^k + V_{E_k}(t) \quad \textit{and} \quad I_k(t) = I_0^k + V_{I_k}(t)\,. \tag{5.49}$$

Each basic E-I units behaves as above, but for simplicity, we keep only the linear coupling terms because we consider weak coupling coefficients S_{EE}^{kl} and S_{IE}^{kl}. In this limit, keeping only linear terms is a reasonable approximation since nonlinear terms will be small and contribute little compared to the linear terms. Also, this simplifies the analytical treatment. Therefore, the only difference is the fact that the coefficients of the single unit analysis now have the index k which characterizes the heterogeneity of each network. But the form of the coefficients of the deviations dynamics are similar. Specifically, the fixed points (E_0^k, I_0^k) now depend on the coupling terms. The fluctuation dynamics are given by the $2N$-dimensional system:

$$\begin{aligned}\frac{dV_{E_k}}{dt} &= A_{EE}^k V_{E_k} + A_{EI}^k V_{I_k} + L_{EE}^k V_{E_k}^2 + L_{EI}^k V_{E_k}(t) V_{I_k} + M_{EI}^k V_{I_k}^2 + B_{1E}^k V_{E_k}^3 \\ &\quad + B_{2E}^k V_{E_k} V_{I_k}^2 + B_{3E}^k V_{I_k} V_{E_k}^2 + B_{4E}^k V_{I_k}^3 + \sum_{l=1, l\neq k}^{N} C_{EE}^{kl} V_{E_l}(t-\tau_{kl}) + \eta_{E_k}\end{aligned} \tag{5.50}$$

$$\begin{aligned}\frac{dV_{I_k}}{dt} &= A_{IE}^k V_{E_k} + A_{II}^k V_{I_k} + L_{II}^k V_{I_k}^2 + L_{IE}^k V_{E_k} V_{I_k} + M_{IE}^k V_{E_k}^2 + B_{1I}^k V_{I_k}^3 \\ &\quad + B_{2I}^k V_{E_k} V_{I_k}^2 + B_{3I}^k V_{I_k} V_{E_k}^2 + B_{4I}^k V_{E_k}^3 + \sum_{l=1, l\neq k}^{N} C_{IE}^{kl} V_{E_l}(t-\tau_{kl}) + \eta_{I_k}\,.\end{aligned} \tag{5.51}$$

The effective coupling coefficients C_{EE}^{kl} and C_{EE}^{kl} are:

$$C_{EE}^{kl} = (1 - E_0^k)\beta_E f^{'}(s_{E_0^k}) S_{EE}^{kl} \quad and \quad C_{IE}^{kl} = (1 - I_0^k)\beta_I f^{'}(s_{I_0^k}) S_{IE}^{kl} \tag{5.52}$$

with the following expressions for the inputs to each population of the k-th unit:

$$s_{E_0^k} = W_{EE}^k E_0^k - W_{EI}^k I_0^k + h_E^k + \sum_{l=1, l\neq k}^{N} S_{EE}^{kl} E_0^l$$
$$s_{I_0^k} = W_{IE}^k E_0^k - W_{II}^k I_0^k + h_I^k + \sum_{l=1, l\neq k}^{N} S_{IE}^{kl} E_0^l \,.$$

Here $(E_0^k, I_0^k), k = 1...N$ are the fixed points of the stationary noise-free Eqs. (5.45-5.46). The coefficients of Eqs. (5.50-5.51) have the same form as in the single unit case; however the expressions for (s_{E_0}, s_{I_0}) are now replaced by $(s_{E_0^k}, s_{I_0^k}, k = 1...N)$. Similarly, (E_0, I_0) is replaced by $(E_0^k, I_0^k, k = 1...N)$.

As in the case of the single unit, linear stability analysis suggests a fixed amplitude ratio and phase difference between the E and I components of each unit. However, the determination of these quantities is different from the single unit case. To find the frequency, amplitude ratio and phase difference, these steps are followed:

- From the linear stability analysis, compute the eigenvalues of the corresponding $2N$-dimensional linear system associated with Eqs. (5.50-5.51). The number of eigenvalues is infinite when the propagation delay is considered, and is equal to $2N$ otherwise. The imaginary part ω_0 of the eigenvalue with the largest real part is considered as the mean frequency of the system.

- Consider the eigenvalue with the largest real part ($\lambda = \nu_{max} + j\omega_0$) and solve the following $N \times N$ system of equations for the amplitude ratios derived from the linear stability analysis:

$$A_{EI}^k \tilde{\alpha}_{kk} + \sum_{l=1, l\neq k}^{N} C_{EE}^{kl} \exp(-\lambda\tau_{kl})\tilde{\alpha}_{kl} = \lambda - A_{EE}^k$$
$$\sum_{l=1, l\neq k}^{N} C_{IE}^{kl} \exp(-\lambda\tau_{kl})\tilde{\alpha}_{kl} + (A_{II}^k - \lambda)\tilde{\alpha}_{kk} = -A_{IE}^k$$
$$\tilde{\alpha}_{kl} = \left(\tilde{\alpha}_{lk}\right)^{-1}, \quad k, \neq l = 1, ..., N$$

where

$$\tilde{\alpha}_{kk} = \frac{\tilde{B}_{I_k}}{\tilde{B}_{E_k}}, \quad \tilde{\alpha}_{kl} = \frac{\tilde{B}_{E_l}}{\tilde{B}_{E_k}}, \quad k, \neq l = 1, ..., N\,. \tag{5.53}$$

- The amplitude ratio and phase difference between inhibitory and excitatory fluctuations are therefore given by:

$$\alpha_k = \left|\tilde{\alpha}_{kk}\right| \quad ; \delta_k = Arg\big(\tilde{\alpha}_{kk}\big),\, k = 1, ..., N$$

where $||$ and Arg are respectively the modulus and the argument of a complex number.

As in the case of single unit, we can look for solutions of excitatory and inhibitory fluctuation dynamics for each population in each unit in the form:

$$V_{E_k}(t) = Z_k(t)\cos\big(\omega_0 t + \phi_k(t)\big) \quad and \quad V_{I_k}(t) = \alpha_k Z_k(t)\cos\big(\omega_0 t + \phi_k(t) + \delta_k\big)\,. \tag{5.54}$$

We have dropped the subscript E for the variables Z and ϕ for the sake of readability. We then plugged these expressions in the system of $2N$-dimensional Eqs. (5.50-5.51) and obtained the final system of $2N$-dimensional equations for the amplitudes Z_k and phases ϕ_k:

$$\frac{dZ_k}{dt} = F_1^k\big(Z_k, \phi_k\big) + G_1^k\big(Z_k, \phi_k, \eta_{E_k}, \eta_{I_k}\big) \tag{5.55}$$

$$\frac{d\phi_k}{dt} = F_2^k\big(Z_k, \phi_k\big) + G_2^k\big(Z_k, \phi_k, \eta_{E_k}, \eta_{I_k}\big) \tag{5.56}$$

with the following functions:

$$F_1^k\big(Z_k,\phi_k\big) = \frac{1}{\alpha_k \sin(\delta_k)}\Big[\alpha_k f_1^k\big(Z_k,\phi_k\big)\sin(\omega_0 t+\phi_k+\delta_k) - f_2^k\big(Z_k,\phi_k\big)\sin(\omega_0 t+\phi_k)\Big]$$

$$F_2^k\big(Z_k,\phi_k\big) = \frac{1}{\alpha_k Z_k \sin(\delta_k)}\Big[\alpha_k f_1^k\big(Z_k,\phi_k\big)\cos(\omega_0 t+\phi_k+\delta_k) - f_2^k\big(Z_k,\phi_k\big)\cos(\omega_0 t+\phi_k)\Big]$$

$$G_1^k\big(Z_k,\phi_k,\eta_{E_k},\eta_{I_k}\big) = \frac{1}{\alpha_k \sin(\delta_k)}\Big[\alpha_k g_1^k\big(Z_k,\phi_k,\eta_{E_k},\eta_{I_k}\big)\sin(\omega_0 t+\phi_k+\delta_k) - g_2^k\big(Z_k,\phi_k,\eta_{E_k},\eta_{I_k}\big)\sin(\omega_0 t+\phi_k)\Big]$$

$$G_2^k\big(Z_k,\phi_k,\eta_{E_k},\eta_{I_k}\big) = \frac{1}{\alpha_k Z_k \sin(\delta_k)}\Big[\alpha_k g_1^k\big(Z_k,\phi_k,\eta_{E_k},\eta_{I_k}\big)\cos(\omega_0 t+\phi_k+\delta_k) - g_2^k\big(Z_k,\phi_k,\eta_{E_k},\eta_{I_k}\big)\cos(\omega_0 t+\phi_k)\Big]$$

$$\begin{aligned} f_1^k\big(Z_k,\phi_k\big) &= \omega_0 Z_k \sin(\omega_0 t+\phi_k) + A_{EE}^k Z_k \cos(\omega_0 t+\phi_k) + A_{EI}^k \alpha_k Z_k \cos(\omega_0 t+\phi_k+\delta_k) + L_{EE}^k Z_k^2 \times \\ &\cos^2(\omega_0 t+\phi_k) + L_{EI}^k \alpha_k Z_k^2 \cos(\omega_0 t+\phi_k)\cos(\omega_0 t+\phi_k+\delta_k) + M_{EI}^k \alpha_k^2 Z_k^2 \cos^2(\omega_0 t+\phi_k+\delta) + \\ &B_{1E}^k Z_k^3 \cos^3(\omega_0 t+\phi_k) + B_{2E}^k \alpha_k^2 Z_k^3 \cos(\omega_0 t+\phi_k)\cos^2(\omega_0 t+\phi_k+\delta_k) + B_{3E}^k \alpha_k Z_k^3 \times \\ &\cos^2(\omega_0 t+\phi_k)\cos(\omega_0 t+\phi_k+\delta_k) + B_{4E}^k \alpha_k^3 Z_k^3 \cos^3(\omega_0 t+\phi_k+\delta_k) \\ &+ \sum_{l=1,l\neq k}^{N} C_{EE}^{kl} Z_l(t-\tau_{kl})\cos[\omega_0 t - \omega_0\tau_{kl} + \phi_l(t-\tau_{kl})], \end{aligned}$$

$$\begin{aligned} f_2^k\big(Z_k,\phi_k\big) &= \alpha_k\omega_0 Z_k \sin(\omega_0 t+\phi_k+\delta_k) + A_{IE}^k Z_k \cos(\omega_0 t+\phi_k) + A_{II}^k \alpha_k Z_k \cos(\omega_0 t+\phi_k+\delta_k) \\ &+ L_{II}^k \alpha_k^2 Z_k^2 \cos^2(\omega_0 t+\phi_k+\delta_k) + L_{IE}^k \alpha_k Z_k^2 \cos(\omega_0 t+\phi_k)\cos(\omega_0 t+\phi_k+\delta_k) \\ &+ M_{IE}^k Z_k^2 \cos^2(\omega_0 t+\phi_k) + B_{1I}^k \alpha_k^3 Z_k^3 \cos^3(\omega_0 t+\phi_k+\delta_k) + B_{2I}^k \alpha_k^2 Z_k^3 \cos(\omega_0 t+\phi_k)\times \\ &\cos^2(\omega_0 t+\phi_k+\delta_k) + B_{3I}^k \alpha_k Z_k^3 \cos^2(\omega_0 t+\phi_k)\cos(\omega_0 t+\phi_k+\delta_k) + B_{4I}^k Z_k^3 \cos^3(\omega_0 t+\phi_k) \\ &+ \sum_{l=1,l\neq k}^{N} C_{IE}^{kl} Z_l(t-\tau_{kl})\cos[\omega_0 t - \omega_0\tau_{kl} + \phi_l(t-\tau_{kl})], \end{aligned}$$

$$g_1^k\big(Z_k,\phi_k,\xi_{E_k},\xi_{I_k}\big) = \eta_{E_k}(t); \quad g_2^k\big(Z_k,\phi_k,\xi_{E_k},\xi_{I_k}\big) = \eta_{I_k}(t).$$

Applying the SAM method to the $2N$-dimensional system (Eqs. 5.55-5.56) leads to the following amplitude-phase equations for the networks of SWC3 units:

$$dZ_k(t) = \Big\{ -\lambda_k Z_k(t) + B_1^k Z_k^3(t) + \frac{D_k}{2Z_k(t)} + \frac{1}{2\alpha_k \sin(\delta_k)} \sum_{l=1, l\neq k}^{N} \Big[\alpha_k C_{EE}^{kl} \sin\big(\phi_k(t) - \phi_l(t-\tau_{kl}) + \omega_0 \tau_{kl} + \delta_k\big) - C_{IE}^{kl} \sin\big(\phi_k(t) - \phi_l(t-\tau_{kl}) + \omega_0 \tau_{kl}\big) \Big] Z_l(t-\tau_{kl}) \Big\} dt + \sqrt{D_k}\, dW_1^k(t) \tag{5.57}$$

$$d\phi_k(t) = \Big\{ \Omega_k + B_2^k Z_k^2(t) + \frac{1}{2\alpha_k \sin(\delta_k)} \sum_{l=1, l\neq k}^{N} \Big[\alpha_k C_{EE}^{kl} \cos\big(\phi_k(t) - \phi_l(t-\tau_{kl}) + \omega_0 \tau_{kl} + \delta_k\big) - C_{IE}^{kl} \cos\big(\phi_k(t) - \phi_l(t-\tau_{kl}) + \omega_0 \tau_{kl}\big) \Big] \frac{Z_l(t-\tau_{kl})}{Z_k(t)} \Big\} dt + \frac{\sqrt{D_k}}{Z_k(t)}\, dW_2^k(t)\,. \tag{5.58}$$

The coefficients in these expressions are defined by:

$$B_1^k = \frac{1}{8}\Big[3B_{1E}^k + B_{3I}^k + \alpha_k^2 (B_{2E}^k + 3B_{1I}^k) + 2\alpha_k \cos(\delta_k)(B_{3E}^k + B_{2I}^k) \Big] \tag{5.59}$$

as well as

$$B_2^k = \frac{1}{8\sin(\delta_k)} \Big[2\alpha_k (B_{3E}^k - B_{2I}^k) + 3(B_{1E}^k - B_{3I}^k)\cos(\delta_k) + 3\alpha_k^2 (B_{2E}^k - B_{1I}^k)\cos(\delta_k) + \alpha_k (B_{3E}^k - B_{2I}^k)\cos(2\delta_k) + \frac{3}{\alpha_k}\big(\alpha_k^4 B_{4E}^k - B_{4I}^k\big) \Big] \tag{5.60}$$

with the definitions

$$\begin{aligned}
\lambda_k &= -\frac{A_{EE}^k + A_{II}^k}{2} \\
\Omega_k &= -\omega_0 + \frac{\alpha_k \cos(\delta_k)(A_{EE}^k - A_{II}^k) + \alpha_k^2 A_{EI}^k - A_{IE}^k}{2\alpha_k \sin(\delta_k)} \\
D_k &= \frac{1}{2\alpha_k^2 \sin^2(\delta_k)} \left[\frac{2\tau_{E_k} (\alpha_k \sigma_{E_k})^2}{1 + (\omega_0 \tau_{E_k})^2} + \frac{2\tau_{I_k} (\sigma_{I_k})^2}{1 + (\omega_0 \tau_{I_k})^2} \right] \\
&= \frac{\pi}{\alpha_k^2 \sin^2(\delta_k)} \Big[\alpha_k^2 S_{\xi_{E_k}}(\omega_0) + S_{\xi_{I_k}}(\omega_0) \Big]\,.
\end{aligned}$$

We have thus derived an amplitude-phase decomposition of connected SWC3 E-I units through the SAM by extending the technique used for an isolated E-I network. The result is a set of $2 \times N$ stochastic differential equations for the amplitudes and phases of each unit. The connectivity between the amplitude and phase are made through sinusoidal coupling functions. Unfortunately,

the amplitude equation is not uncoupled from that for the phase as was the case for a single unit. A Fokker-Planck analysis is therefore difficult to conduct.

However, we performed numerical simulations of this network of amplitude-phase dynamics (Eqs. 5.57-5.58) and their original fluctuations variables (Eqs. 5.50-5.51) and found good agreement between the two. This was done for the quasi-cycle regimes as well as for the noisy limit cycle regime in Figs.(5.12a,b). For each regime, we made sure that a single isolated E-I unit was in the regime of interest (quasi- or limit cycle), and that the connectivity between units kept the network in the same regime of each isolated unit. In other words, the connectivity does not induce a change of regime.

We represented the probability densities of the amplitude $Z_k, k = 1, 2, 3$ for three selected units in a minimal heterogeneous network of 5 units and the corresponding excitatory amplitudes extracted using the Hilbert transform for Eqs. (5.50-5.51) and found good agreement between the two methods. In Figs. (5.12a,b), the black curves are the result of the SAM approximation, while the coloured curves correspond to the Hilbert transform computation. Our amplitude-phase approach across the Hopf bifurcation is therefore generally applicable to both single units and heterogeneous networks of units in both the quasi- and limit cycle regimes.

To recover the common fast phase variable usually used and associated to the Hilbert transform, it suffices to consider the change of variable $\theta_k(t) = \omega_0 t + \phi_k(t)$. This leads to the following amplitude-phase dynamics

$$dZ_k(t) = \Big\{ -\lambda_k Z_k(t) + B_1^k Z_k^3(t) + \frac{D_k}{2Z_k(t)} + \frac{1}{2\alpha_k \sin(\delta_k)} \sum_{l=1, l\neq k}^{N} \Big[\alpha_k C_{EE}^{kl} \sin\big(\theta_k(t) - \theta_l(t-\tau_{kl}) + \delta_k\big) - C_{IE}^{kl} \sin\big(\theta_k(t) - \theta_l(t-\tau_{kl})\big) \Big] Z_l(t-\tau_{kl}) \Big\} dt + \sqrt{D_k}\, dW_1^k(t) \tag{5.61}$$

$$d\theta_k(t) = \Big\{ \omega_k + B_2^k Z_k^2(t) + \frac{1}{2\alpha_k \sin(\delta_k)} \sum_{l=1, l\neq k}^{N} \Big[\alpha_k C_{EE}^{kl} \cos\big(\theta_k(t) - \theta_l(t-\tau_{kl}) + \delta_k\big) - C_{IE}^{kl} \cos\big(\theta_k(t) - \theta_l(t-\tau_{kl})\big) \Big] \frac{Z_l(t-\tau_{kl})}{Z_k(t)} \Big\} dt + \frac{\sqrt{D_k}}{Z_k(t)}\, dW_2^k(t)\,. \tag{5.62}$$

The new parameter ω_k is related to Ω_k and depends on the intrinsic parameter of each network,

as following

$$\omega_k = \Omega_k + \omega_0 = \frac{\alpha_k \cos(\delta_k)(A^k_{EE} - A^k_{II}) + \alpha_k^2 A^k_{EI} - A^k_{IE}}{2\alpha_k \sin(\delta_k)}.$$

It is related to the deterministic frequency of the oscillator k and coincides with the imaginary part of the complex conjugate eigenvalues ω_0 for a single oscillator. However, we found that the complete deterministic frequency is generally amplitude-dependent as shown by the two first terms in right side of the equality of Eq. 5.62. The new dynamics Eqs.(5.61-5.62) represent a general model for the interaction of oscillators in the slow $Z_k(t)$ and fast $\theta_k(t)$ variables framework. The major difference with the previous amplitude-phase dynamics Eqs. (5.57-5.58) is the timescale of the new phase variable $\theta_k(t)$ which now evolves on a faster time scale compared to the amplitude $Z_k(t)$ which remain in a slow timescale. This new framework is usually adopted when defining the interaction of oscillators in the amplitude-phase representation.

5.4.2 Networks of Stochastic Stuart-Landau units

General Case

We now consider a network of coupled SSL units. The coupling is a linear coupling, the model is described as:

$$\dot{x}_k(t) = a_k x_k(t) - \omega_0^k y_k(t) - x_k(t)\big[x_k^2(t) + y_k^2(t)\big] + \sum_{l=1, l\neq k}^{N} C_{kl}\big[x_l(t-\tau_{kl}) - x_k(t)\big] + \eta_x^k(t) \quad (5.63)$$

$$\dot{y}_k(t) = \omega_0^k x_k(t) + a_k y_k(t) - y_k(t)\big[x_k^2(t) + y_k^2(t)\big] + \sum_{l=1, l\neq k}^{N} C_{kl}\big[y_l(t-\tau_{kl}) - y_k(t)\big] + \eta_y^k(t)\,. \quad (5.64)$$

We perform the same analysis as for the case of the network of SWC3 units. The fluctuations from the fixed points are therefore sought in the form:

$$V_x^k(t) = Z_k(t)\cos\big[\omega_0 t + \phi_k(t)\big] \quad and \quad V_y^k(t) = \alpha_k Z_k(t)\cos\big[\omega_0 t + \phi_k(t) + \delta_k\big]\,. \quad (5.65)$$

The same steps as for the SWC3 units lead to amplitude-phase equations for the network of coupled SSL units:

$$dZ_k = \Big\{ -\lambda_k Z_k(t) + B_1^k Z_k^3(t) + \frac{D_k}{2Z_k(t)} + \frac{1}{2\alpha_k \sin(\delta_k)} \sum_{l=1, l\neq k}^{N} C_{kl} \Big[\alpha_k \big(Z_l(t-\tau_{kl}) \times$$

$$\sin\big(\phi_k(t) - \phi_l(t-\tau_{kl}) + \omega_0 \tau_{kl} + \delta_k\big) - Z_k(t)\sin(\delta_k)\big) \tag{5.66}$$

$$+ \big(\alpha_l Z_l(t-\tau_{kl}) \sin\big(\phi_l(t-\tau_{kl}) - \omega_0\tau_{kl} - \phi_k(t) + \delta_l\big) - \alpha_k Z_k(t)\sin(\delta_k)\big)\Big]\Big\} dt + \sqrt{D_k} dW_1^k(t)$$

$$d\phi_k = \Big\{ \Omega_k + B_2^k Z_k^2(t) + \frac{1}{2\alpha_k \sin(\delta_k)} \sum_{l=1, l\neq k}^{N} C_{kl} \Big[\alpha_k \cos\big(\phi_k(t) - \phi_l(t-\tau_{kl}) + \omega_0\tau_{kl} + \delta_k\big) -$$

$$\alpha_l \cos\big(\phi_l(t-\tau_{kl}) - \omega_0\tau_{kl} - \phi_k(t) + \delta_l\big)\Big] \frac{Z_l(t-\tau_{kl})}{Z_k(t)} \Big\} dt + \frac{\sqrt{D_k}}{Z_k(t)} dW_2^k(t)\,. \tag{5.67}$$

The amplitude equations are now coupled with the phase equations, making it now difficult to perform a Fokker-Planck analysis in contrast to the case of the isolated unit. Figure 5.13 shows results from numerical simulations of the amplitude-phase equations for a small all-to-all connected heterogeneous network of five units. Only the parameters a_k differ amongst the units. The parameters a_k are such that each isolated unit is in the quasi-cycle regime. The connectivity coefficient is then chosen to ensure that the connected network remains in the quasi-cycle regime. The same approach is used for the limit cycle regime. The results of numerical simulations in Figs. (5.13) show good agreement between the envelopes computed on the original SSL model using the Hilbert transform (colored curves) and those simulated from the SAM dynamics (black curves). Our analysis thus works well for a single unit for a different model than SWC3, for different types of stochastic input, for low and high frequency bands, and for networks of several units. As for the case of the SWC3, we can rewritte the dynamics Eqs. (5.66-5.67) in the framework of the slow amplitude and fast phase by using the change of variable $\theta_k(t) = \omega_0 t + \phi_k(t)$,

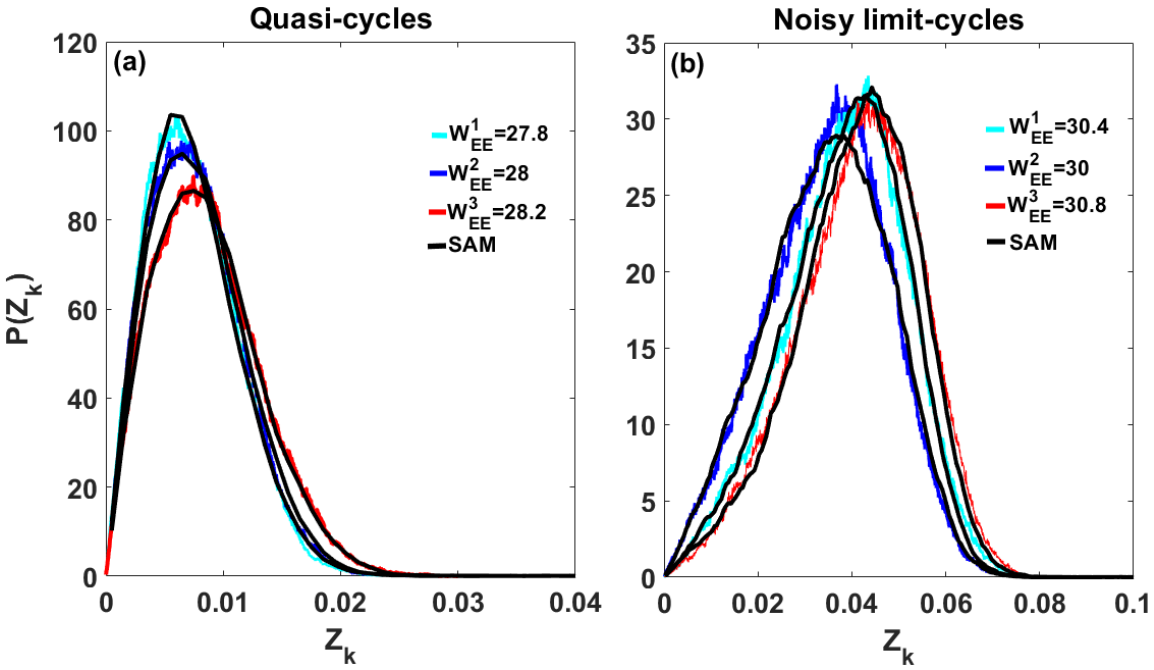

Figure 5.12: **Envelope probability densities of 3 selected units in a heterogeneous network of 5 SWC3 units.** Numerical simulations of the SWC3 network of units (Eqs. 5.50-5.51) followed by Hilbert transforms to obtain the amplitude density, along with numerical simulations of the corresponding amplitude-phase decomposition obtained through the SAM (Eqs. 5.57-5.58). **(a)** Quasi-cycle regime. Each unit is in this regime when isolated or coupled. Parameters are $W^k_{EE} = 27.8, 28, 28.2, 27.6, 28.4, k = 1, ..., 5$. The network is all-to-all connected with $C^{kl}_{IE} = C_{IE} = 0$, $\tau_{kl} = 0$ and $C^{kl}_{EE} = C_{EE} = 2/5$. **(b)** Noisy limit cycle regime. Each isolated network is in the limit cycle regime and remains so when connected. Parameters are $W^k_{EE} = 30.4, 30, 30.8, 30.6, 30.4, k = 1, ..., 5$. The connectivity is all-to-all with $C^{kl}_{IE} = C_{IE} = 0$, $\tau_{kl} = 0$ and $C^{kl}_{EE} = C_{EE} = 1/5$. Black curves correspond to the SAM approximation Eqs. (5.57-5.58); colored curves correspond to the approximate SWC3. An excellent match is seen between the amplitude densities computed from the SAM and the original model for both regimes. Noise parameters for each unit are: $\sigma_E = 0.0014, \sigma_I = 0.0048, \sigma \approx 0.005$ in $ms^{-1/2}$. Other parameters are specified in Fig.5.1. All the equations involving the stochastic Wilson-Cowan model and its truncated version (SWC3) were integrated using the stochastic version of the fourth order Runge-Kutta algorithm [131] with a time-step dt= 0.025 ms.

$$dZ_k(t) = \Big\{ -\lambda_k Z_k(t) + B_1^k Z_k^3(t) + \frac{D_k}{2Z_k(t)} + \frac{1}{2\alpha_k \sin(\delta_k)} \sum_{l=1,l\neq k}^{N} C_{kl} \Big[\alpha_k \big(Z_l(t-\tau_{kl}) \sin\big(\theta_k(t) - \theta_l(t-\tau_{kl}) + \delta_k\big) - Z_k(t)\sin(\delta_k)\big) + \big(\alpha_l Z_l(t-\tau_{kl}) \sin\big(\theta_l(t-\tau_{kl}) - \theta_k(t) + \delta_l\big) - \alpha_k Z_k(t)\sin(\delta_k)\big) \Big] \Big\} dt + \sqrt{D_k} dW_1^k(t) \tag{5.68}$$

$$d\theta_k(t) = \Big\{ \omega_k + B_2^k Z_k^2(t) + \frac{1}{2\alpha_k \sin(\delta_k)} \sum_{l=1,l\neq k}^{N} C_{kl} \Big[\alpha_k \cos\big(\theta_k(t) - \theta_l(t-\tau_{kl}) + \delta_k\big) - \alpha_l \cos\big(\theta_l(t-\tau_{kl}) - \theta_k(t) + \delta_l\big) \Big] \frac{Z_l(t-\tau_{kl})}{Z_k(t)} \Big\} dt + \frac{\sqrt{D_k}}{Z_k(t)} dW_2^k(t)\,. \tag{5.69}$$

Near identical, weakly coupled limit cycles with low noise

Let us consider the fast phase dynamics of the network of SSL units extracted used the SAM and the change of variable $\theta_k(t) = \omega_0 t + \phi_k(t)$ in Eq. (5.69). If the units are nearly identical, weakly coupled and subject to small noise ($D_k << 1$), we can make the following approximations:

- $\alpha_k \sim \alpha_l$; $\delta_k \sim \delta_l$
- $Z_k(t) \sim Z_l(t) \sim Z_l(t-\tau_{kl}) \sim \big\langle Z_k(t) \big\rangle = c_0$

where c_0 is a constant. The first approximation comes from the fact that the networks are nearly identical. It reduces the coupling function of the fast phase dynamics Eq. (5.69) to $C_{kl} \frac{Z_l(t-\tau_{kl})}{Z_k(t)} \sin[\theta_l(t-\tau_{kl}) - \theta_k(t)]$. The second approximation can be made because the units are nearly identical, weakly coupled and the noise is small. The amplitudes then vary slightly over time and we can replace them by a constant. We choose this constant here to be the mean amplitude over the period of a unit and is thus the same for every unit. Such an approximation further reduces the coupling to $C_{kl}\sin[\theta_l(t-\tau_{kl}) - \theta_k(t)]$, and the stochastic terms to $\sqrt{D_k^0} = \sqrt{D_k}/c_0$. We recall that for the case of the SL model the coefficients of the squared amplitude in the phase dynamics are always zero ($B_2^k = 0$). This leads to the following equation for the phase dynamics:

$$\frac{d\theta_k}{dt} = \omega_k + \sum_{l=1,l\neq k}^{N} C_{kl} \sin\big(\theta_l(t-\tau_{kl}) - \theta_k(t)\big) + \sqrt{D_k^0}\xi_2^k \tag{5.70}$$

where

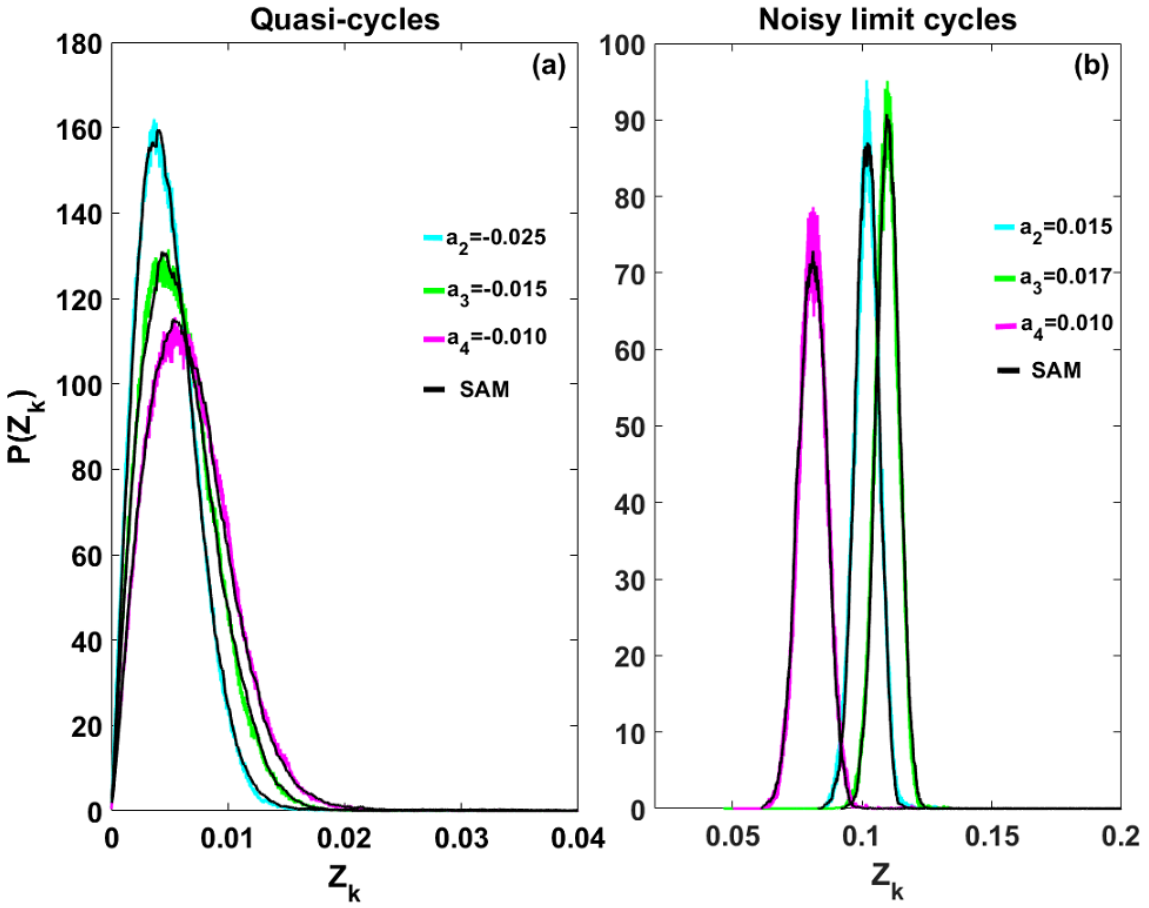

Figure 5.13: **Amplitude probability densities of 3 selected units in a network of 5 SSL units.** Numerical simulations of the amplitude equations obtained from the SAM Eqs.5.66-5.67 and of the Hilbert transform extracted from simulations of the SSL model. **(a)** Quasi-cycle regime. Each unit is in this regime when isolated or coupled. Parameters are $a_k = -0.01, -0.025, -0.015, -0.01, -0.01, k = 1, ..., 5$. The network is all-to-all connected with $C_{kl} = K/N = 0.01/5$ and $\tau_{kl} = 0$. **(b)** Noisy limit cycle regime. Each isolated or coupled network is in the limit cycle regime. Parameters are $a_k = 0.010, 0.015, 0.015, 0.01, 0.01, k = 1, ..., 5$. The connectivity is all-to-all with $C_{kl} = K/N = 0.01/5$ and $\tau_{kl} = 0$. Black curves correspond to the SAM Eqs. (5.66-5.67) and colored curves to the original SSL dynamics. An excellent match is again seen between the two envelope dynamics in both regimes. Noise parameters for each unit are: $\sigma_x = \sigma_y = \sigma = 0.01$ and the parameter b_0 is set to 0.15. For the two regimes, the coupling C_{kl} is applied only on the x variable for simplicity. Other parameters are specified in Fig.5.8. All the equations involving the stochastic Stuart-Landau model were integrated using the Euler-Maruyama algorithm with a time-step dt= 0.025 ms.

$$\omega_k = \omega_0 + \Omega_k = \frac{\alpha_k \cos(\delta_k)(A^k_{xx} - A^k_{yy}) + \alpha_k^2 A^k_{xy} - A^k_{yx}}{2\alpha_k \sin(\delta_k)} .$$

For the SSL model, it is found that the value of the frequency ω_k coincides with the frequency ω_k^0 of each isolated unit. Equation (5.70) is the delayed [195] and stochastic [169, 168] version of the Kuramoto phase model.

No propagation delay: The Kuramoto model

If we further neglect the propagation delays ($\tau_{kl} = 0$) and the noise $D_k = 0$, we recover the Kuramoto phase model of coupled phase oscillators [139, 2]:

$$\frac{d\theta_k(t)}{dt} = \omega_k + \sum_{l=1}^{N} C_{kl} \sin\big(\theta_l(t) - \theta_k(t)\big) . \tag{5.71}$$

Note that our amplitude-phase model derived above also displays interesting phase synchronization properties that will be studied elsewhere, since our focus here has been on illustrating the amplitude dynamics. The generality of our model is highlighted by this relation to the well-known deterministic Kuramoto model in specific limits.

5.5 Discussion

In this work, we have addressed the problem of amplitude-phase decomposition of noisy oscillations. The quantities of interest are the fluctuations from the fixed points. Our approach consists in first performing a linear stability analysis to extract the amplitude ratio, phase difference and mean frequency. Second, solutions in a sinusoidal form are sought that take into account these properties. And finally the Stochastic Averaging Method (SAM) is applied to obtain the dynamics of the amplitude and phase processes. The method was shown to work well on two different models that span the Hopf bifurcation from the quasi-cycle to the limit cycle regimes, as well as for colored noise or Gaussian white noise. It complements previous approaches that treat these two regimes with separate models by providing a unified approach across regimes, and further extends the method to several delay-coupled oscillatory networks.

We first considered a single E-I network in the SWC model case, or a single Hopf oscillator in the SSL case. The amplitude dynamics is then uncoupled from the phase dynamics. We then

applied a Fokker-Planck analysis to compute the stationary probability densities of the amplitude variables. The peak of the probability densities can be extracted and used as bifurcation parameter. The bifurcation diagram computed with the peak probability density captures the transition from quasi- to limit cycle oscillations. It shows how noise properties (strength, correlation time) shape the behaviour of the oscillations.

Larger noise intensities and shorter noise correlation times increase the mean of the amplitude of the fast oscillation. In the limit cycle case, the variance of the envelope process also increases, making bursting epochs - i.e. segments where the amplitude process is large - more prominent. This novel result highlights a benefit of considering the amplitude process rather than just the phase when modelling limit cycle oscillations. The phase dynamics is coupled to the amplitude dynamics. The strength of the noise perturbation on the phase process depends on the amplitude process. Hence during such bursts, the effect of noise weakens (due to the $1/Z(t)$ dependence). However, during epochs of low amplitude between bursts, the phase fluctuates more strongly. The amplitude process therefore plays an important role in the phase dynamics, especially for moderate to strong noise.

We extended our method to several coupled units of the Stochastic Wilson Cowan (SWC) and the Stochastic Stuart Landau (SSL) models. Such super-networks of units have been invoked to model brain connectivity [58, 64]. Our analysis allowed us to also derive an amplitude-phase model for coupled units. Unlike the single unit network, the amplitude processes are now reciprocally connected with the phase processes of the units. A Fokker-Planck analysis of the system of coupled units is beyond the scope of our study and poses serious challenges. We are not aware of any analytical method able to provide exact quantities like the probability density functions of the envelope processes. We therefore presented only numerical simulations. But nevertheless the amplitude-phase dynamics provide a new tool to understand amplitude-phase coupling of rhythms that are either autonomous or owe their existence to noise.

As for the case of a single oscillating unit, the SAM method applied to these networks of units of nonlinear oscillators is accurate across the Hopf bifurcation. Future work could investigate the case of a mixture of quasi-cycle and limit cycle units and the one where the coupling actually alters the dynamical regime seen in the isolated units. Also, we mostly focused on the dynamics of the amplitude process of an isolated unit since we were mostly interested in the ability of noise in creating

bursts. But for the coupled network of oscillators, phase synchronization is also of interest. This behavior is present in our coupled models. It is likely that other exciting phenomena such as chimera will be revealed in these networks, even in the quasi-cycle regime.

Note that in the WC framework, the amplitude of the oscillation is a reasonable proxy for the synchronization of an actual network consisting of many noisy excitatory and inhibitory neurons, as established in [220]. This correspondence will nevertheless miss out on effects such as synchrony without oscillation or strongly synchronous oscillations at low firing rate in deterministic networks [44], a direction we leave for future study.

Although we developed our theory of networks of coupled units with delays using the SAM approach, we have illustrated our results only for zero delays due to space limitations. Recent work shows that interesting phenomena in two coupled quasi-cycles relate to these delays, such as states of phase locking with phase difference between $-\pi$ and π and random changes in the identity of the quasi-cycle that leads the other [183]. Thus an extension to explore the effects of propagation delays is warranted, which will provide a closer match to the biophysical situation. Our formalism also enables the inclusion of external periodic inputs, which will also be the focus of future work.

Our results point to a possible discrimination between bursting behaviors from two dynamical origins: in quasi-cycles at low to moderate noise, and in limit cycles at stronger noise. While the spectrograms may be similar, the different shapes of the amplitude density - Rayleigh in the former case and almost Gaussian in the latter - can help distinguish between these two cases. It is possible that further differentiation can be made upon substituting colored noise in the place of Gaussian white noise. The SAM requires the noise to be broadband in order for it to work accurately; Ornstein-Uhlenbeck noise for example would have to be sufficiently broadband. We have also investigated this question over a limited volume of the whole parameter space. It may be easier to discriminate the two kinds of burst dynamics in the neural context of amplitudes of lower frequency rhythms such as in the beta band (13-30Hz), in contrast to our focus on the gamma band. Other model topologies than the generic E-I one considered here may also be better suited to such rhythms.

Moreover, the discrimination between data from quasi-cycle and noisy limit cycle origins is a fundamental question for modeling purposes. If the data have a quasi-cycle origin, the modeling could be simplified by avoiding the nonlinearities in the envelope-phase dynamics [182]. If instead

the data have a limit cycle origin, nonlinearities have to be included in the model (Eqs.5.23-5.24). The knowledge of the proper dynamical regime could also be important for therapeutic goals. In fact, if the data recorded from a specific region of the brain are pathological with exaggerated bursts [182], they might also have a limit cycle origin. Stimulation techniques should therefore have the goal to first identify the location of the Hopf bifurcation and to shift the system (e.g the part of the brain where the data are recorded) from a limit cycle to a quasi-cycle with healthy bursts. The investigation of the amplitude-phase dynamics of such models across the Hopf bifurcation with different types of noises, following the methods described here, is certainly an interesting direction to pursue.

5.6 Appendix

5.6.1 Derivation of the SWC3 model

We consider the Wilson Cowan equations Eqs.5.1-5.2 in the deterministic limit:

$$\frac{dE(t)}{dt} = -\alpha_E E(t) + \big(1 - E(t)\big)\beta_E f(s_E(t)) \tag{5.72}$$

$$\frac{dI(t)}{dt} = -\alpha_I I(t) + \big(1 - I(t)\big)\beta_I f(s_I(t))\,. \tag{5.73}$$

The synaptic inputs $s_{E(t)}$ and $s_{I(t)}$ are given by Eqs. 5.3-5.4 respectively. We are interested in the dynamics of the deviations $V_{E(t)}$ and $V_{I(t)}$ when one takes higher order approximations of the sigmoidal firing function. For that, we insert Eqs.5.9 in Eqs.5.72-5.73, which leads to

$$\begin{aligned}
\frac{d(E_0 + V_E)}{dt} &= -\alpha_E(E_0 + V_E) + \big(1 - (E_0 + V_E)\big)\beta_E f(s_E) \\
&= -\alpha_E E_0 - \alpha_E V_E + (1 - E_0)\beta_E f(s_E) - V_E \beta_E f(s_E) \\
\frac{d(I_0 + V_I)}{dt} &= -\alpha_I(I_0 + V_I) + \big(1 - (I_0 + V_I)\big)\beta_I f(s_I) \\
&= -\alpha_I I_0 - \alpha_I V_I + (1 - I_0)\beta_I f(s_I) - V_I \beta_I f(s_I).
\end{aligned}$$

We now replace $f(s_E)$ and $f(s_I)$ by their Taylor expansion at the second order given in Eqs.5.11,

$$
\begin{aligned}
\frac{d(E_0+V_E)}{dt} &= -\alpha_E(E_0+V_E) + \Big(1-(E_0+V_E)\Big)\beta_E f(s_E) \\
&= -\alpha_E E_0 - \alpha_E V_E + (1-E_0)\beta_E f(s_E) - V_E\beta_E f(s_E) \\
&= -\alpha_E E_0 - \alpha_E V_E + (1-E_0)\beta_E\Big(f(s_{E_0}) + \delta s_E f^{'}(s_{E_0}) + \frac{1}{2}(\delta s_E)^2 f^{''}(s_{E_0})\Big)... \\
&- V_E\beta_E\Big(f(s_{E_0}) + \delta s_E f^{'}(s_{E_0}) + \frac{1}{2}(\delta s_E)^2 f^{''}(s_{E_0})\Big) \\
\frac{d(I_0+V_I)}{dt} &= -\alpha_I(I_0+V_I) + \Big(1-(I_0+V_I)\Big)\beta_I f(s_I) \\
&= -\alpha_I I_0 - \alpha_I V_I + (1-I_0)\beta_I f(s_I) - V_I\beta_E f(s_I) \\
&= -\alpha_I I_0 - \alpha_I V_I + (1-I_0)\beta_I\Big(f(s_{I_0}) + \delta s_I f^{'}(s_{I_0}) + \frac{1}{2}(\delta s_I)^2 f^{''}(s_{I_0})\Big)... \\
&- V_I\beta_I\Big(f(s_{I_0}) + \delta s_I f^{'}(s_{I_0}) + \frac{1}{2}(\delta s_I)^2 f^{''}(s_{I_0})\Big).
\end{aligned}
$$

Taking into account the fixed points solutions Eq.5.10, the equations above are reduced to

$$
\begin{aligned}
\frac{dV_E}{dt} &= -\alpha_E V_E + (1-E_0)\beta_E\Big(\delta s_E f^{'}(s_{E_0}) + \frac{1}{2}(\delta s_E)^2 f^{''}(s_{E_0})\Big) - V_E\beta_E\Big(f(s_{E_0}) + \delta s_E f^{'}(s_{E_0}) + \frac{1}{2}(\delta s_E)^2 f^{''}(s_{E_0})\Big) \\
\frac{dV_I}{dt} &= -\alpha_I V_I + (1-I_0)\beta_I\Big(\delta s_I f^{'}(s_{I_0}) + \frac{1}{2}(\delta s_I)^2 f^{''}(s_{I_0})\Big) - V_I\beta_I\Big(f(s_{I_0}) + \delta s_I f^{'}(s_{I_0}) + \frac{1}{2}(\delta s_I)^2 f^{''}(s_{I_0})\Big).
\end{aligned}
$$

We now group the terms of the equations according to different orders:

$$
\begin{aligned}
\frac{dV_E}{dt} &= -\alpha_E V_E + (1-E_0)\beta_E f^{'}(s_{E_0})\delta s_E - \beta_E f(s_{E_0})V_E + (1-E_0)\beta_E\Big(\frac{1}{2}(\delta s_E)^2 f^{''}(s_{E_0})\Big) - \beta_E V_E\Big(\delta s_E f^{'}(s_{E_0})\Big) \\
&- \beta_E V_E\Big(\frac{1}{2}(\delta s_E)^2 f^{''}(s_{E_0})\Big) \\
\frac{dV_I}{dt} &= -\alpha_I V_I + (1-I_0)\beta_I f^{'}(s_{I_0})\delta s_I - \beta_I f(s_{I_0})V_I + (1-I_0)\beta_I\Big(\frac{1}{2}(\delta s_I)^2 f^{''}(s_{I_0})\Big) - \beta_I V_I\Big(\delta s_I f^{'}(s_{I_0})\Big) \\
&- \beta_I V_I\Big(\frac{1}{2}(\delta s_I)^2 f^{''}(s_{I_0})\Big).
\end{aligned}
$$

We replace δs_E and δs_I by their expressions

$$\frac{dV_E}{dt} = -\alpha_E V_E + (1-E_0)\beta_E f^{'}(s_{E_0})\big(W_{EE}V_E - W_{EI}V_I\big) - \beta_E f(s_{E_0})V_E - \beta_E f^{'}(s_{E_0})V_E\Big(W_{EE}V_E - W_{EI}V_I\Big)$$
$$+ \frac{1}{2}(1-E_0)\beta_E f^{''}(s_{E_0})\Big(W_{EE}^2V_E^2 + W_{EI}^2V_I^2 - 2W_{EE}W_{EI}V_EV_I\Big)$$
$$- \frac{1}{2}\beta_E f^{''}(s_{E_0})V_E\Big(W_{EE}^2V_E^2 + W_{EI}^2V_I^2 - 2W_{EE}W_{EI}V_EV_I\Big) \tag{5.74}$$
$$\frac{dV_I}{dt} = -\alpha_I V_I + (1-I_0)\beta_I f^{'}(s_{I_0})\big(W_{IE}V_E - W_{II}V_I\big) - \beta_I f(s_{I_0})V_I - \beta_I f^{'}(s_{I_0})V_I\Big(W_{IE}V_E - W_{II}V_I)\Big)$$
$$+ \frac{1}{2}(1-I_0)\beta_I f^{''}(s_{I_0})\Big(W_{IE}^2V_E^2 + W_{II}^2V_I^2 - 2W_{IE}W_{II}V_EV_I\Big)$$
$$- \frac{1}{2}\beta_I f^{''}(s_{I_0})V_I\Big(W_{IE}^2V_E^2 + W_{II}^2V_I^2 - 2W_{IE}W_{II}V_EV_I\Big). \tag{5.75}$$

The dynamics of the deviation from the fixed point (E_0, I_0) are composed of terms of three orders. We have terms of order 1 or linear, those of order 2 or quadratic terms and finally terms of order 3 or cubic terms. We are particularly interested in quadratic and cubic terms, since the effect of linear terms have been studied previously. Note that quadratic terms have two origins: some come from the product of two linear terms (Eqs.5.74-5.75,terms in blue) and others from the square of the linear terms δs_E and δs_I (Eqs.5.74-5.75,terms in green). We are looking for a dynamics which approximate the full deterministic Wilson Cowan model (with the sigmoid function) particularly at the vicinity of the Hopf bifurcation. The selected approximation will then be investigated with noise. We compare the bifurcation diagrams of the approximate model Eqs.5.74-5.75 (called the full WC3) derived above and the full Wilson Cowan model Eqs.5.72-5.73 (full WC). We find that the approximate model (Eqs.5.74-5.75) above (green curve, Fig.5.14) does not describe well the full Wilson Cowan (red curve, Fig.5.14) even close to the Hopf bifurcation. We then discard quadratic terms coming from the square of the terms δs_E and δs_I. The new dynamics (Eqs.5.76-5.77, called the WC3) without these terms (blue curve, Fig.5.14) now approximate well the full Wilson Cowan (red curve, Fig.5.14) particularly in the vicinity of the Hopf bifurcation. In this work, we use these new dynamics Eqs.5.76-5.77 since they are a better approximation of the Wilson Cowan for the range of parameters used. To obtain its stochastic version named the SWC3, we add the noise terms η_E and η_I. The resulting dynamics are given by Eqs.5.13-5.14.

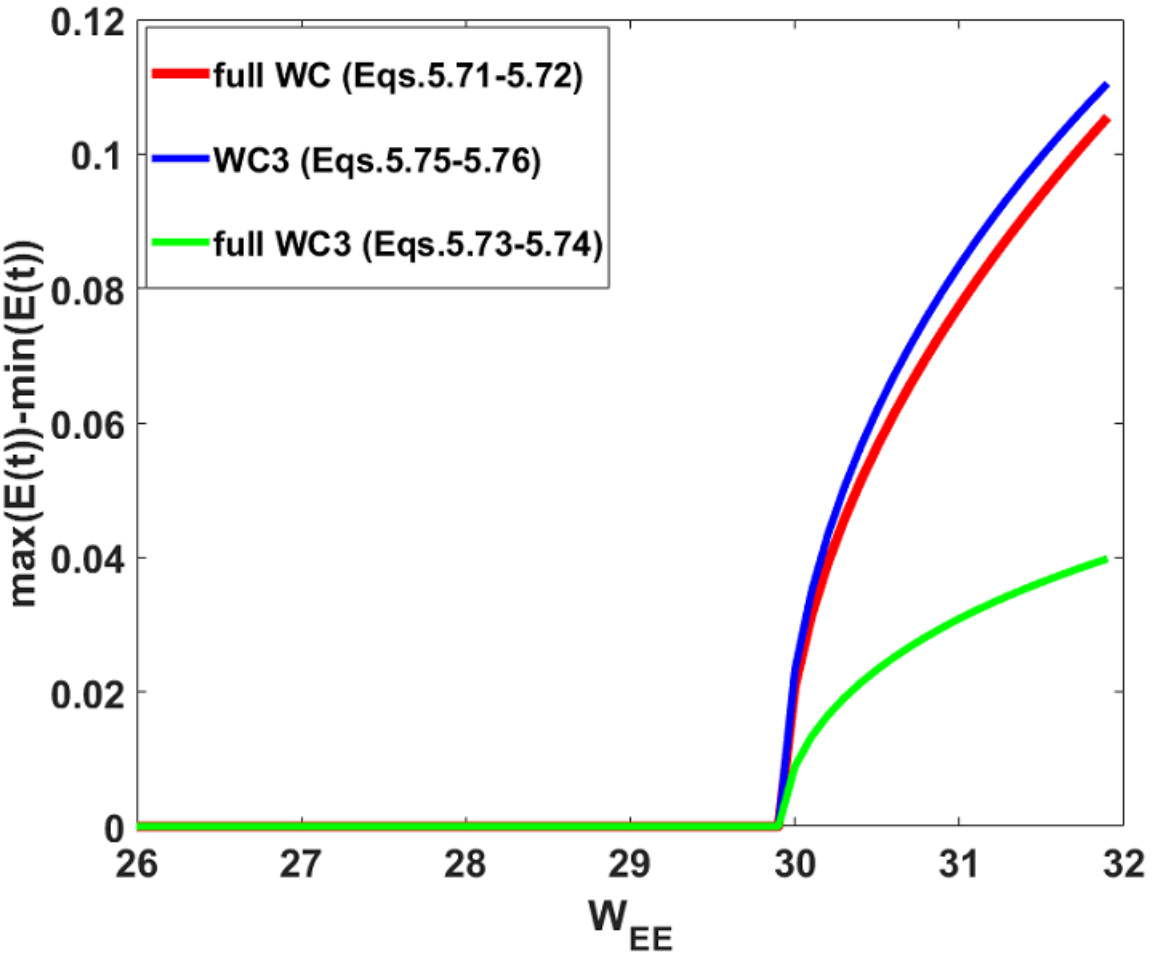

Figure 5.14: **Bifurcation diagram of the full Wilson-Cowan model and its approximate versions obtained after a Taylor expansion of the sigmoid function.** The red curve represents the full (i.e with the sigmoid function) deterministic Wilson Cowan (WC) dynamics (Eqs.5.72-5.73). The green curve is the bifurcation diagram of the approximate Wilson Cowan with the Taylor expansion of the sigmoid function at order 2 (full WC3), Eqs.5.74-5.75. this approximation is already not accurate. Finally, the blue curve is obtained from the full WC3 after discarding the quadratic terms coming from the square of the quantities δs_E and δs_I. (see Eqs.5.76-5.77). This approximation provided a good agreement with the full W.C model over the range of parameters of interest, and was therefore adopted for the stochastic problem. All the curves were obtained using a fourth order Runge-Kutta iterative scheme with timestep dt=0.025 ms.

$$\frac{dV_E}{dt} = -\alpha_E V_E + (1-E_0)\beta_E f^{'}(s_{E_0})\big(W_{EE}V_E - W_{EI}V_I\big) - \beta_E f(s_{E_0})V_E - \beta_E f^{'}(s_{E_0})V_E\Big(W_{EE}V_E - W_{EI}V_I\Big)$$
$$- \frac{1}{2}\beta_E f^{''}(s_{E_0})V_E\Big(W_{EE}^2V_E^2 + W_{EI}^2V_I^2 - 2W_{EE}W_{EI}V_EV_I\Big) \tag{5.76}$$
$$\frac{dV_I}{dt} = -\alpha_I V_I + (1-I_0)\beta_I f^{'}(s_{I_0})\big(W_{IE}V_E - W_{II}V_I\big) - \beta_I f(s_{I_0})V_I - \beta_I f^{'}(s_{I_0})V_I\Big(W_{IE}V_E - W_{II}V_I)\Big)$$
$$- \frac{1}{2}\beta_I f^{''}(s_{I_0})V_I\Big(W_{IE}^2V_E^2 + W_{II}^2V_I^2 - 2W_{IE}W_{II}V_EV_I\Big). \tag{5.77}$$

5.6.2 Expansion of the Stochastic Averaging Method (SAM)

The drift two-dimensional function $m = \begin{pmatrix} m_1(t) \\ m_2(t) \end{pmatrix}$, obtained from the Stochastic Averaging Method (SAM) can be expanded as follows:

$$m_1(t) = T^{av}\Big(E\big\{F_1(t)\big\} + \int_{-\infty}^{0} E\Big\{\frac{\partial G_1(t)}{\partial Z_E}G_1(t+\tau)\Big\}d\tau + \int_{-\infty}^{0} E\Big\{\frac{\partial G_1(t)}{\partial \phi_E}G_2(t+\tau)\Big\}d\tau\Big),$$
$$m_2(t) = T^{av}\Big(E\big\{F_2(t)\big\} + \int_{-\infty}^{0} E\Big\{\frac{\partial G_2(t)}{\partial Z_E}G_1(t+\tau)\Big\}d\tau + \int_{-\infty}^{0} E\Big\{\frac{\partial G_2(t)}{\partial \phi_E}G_2(t+\tau)\Big\}d\tau\Big).$$

The coefficients h_{ij} of the diffusion matrix h can also be obtained as

$$h_{11}^2 + h_{12}^2 = T^{av}\Big(\int_{-\infty}^{\infty} E\big\{G_1(t)G_1(t+\tau)\big\}d\tau\Big)$$
$$h_{11}h_{21} + h_{12}h_{22} = T^{av}\Big(\int_{-\infty}^{\infty} E\big\{G_1(t)G_2(t+\tau)\big\}d\tau\Big)$$
$$h_{11}h_{21} + h_{12}h_{22} = T^{av}\Big(\int_{-\infty}^{\infty} E\big\{G_2(t)G_1(t+\tau)\big\}d\tau\Big)$$
$$h_{21}^2 + h_{22}^2 = T^{av}\Big(\int_{-\infty}^{\infty} E\big\{G_2(t)G_2(t+\tau)\big\}d\tau\Big).$$

When the noises acting on the two variables are uncorrelated and only additive, an easy choice for the non-diagonal components of the matrix h can be made ($h_{12} = h_{21} = 0$). This leads to

$$h_{11}^2 = T^{av}\Big(\int_{-\infty}^{\infty} E\big\{G_1(t)G_1(t+\tau)\big\}d\tau\Big),$$
$$h_{12} = 0,$$
$$h_{21} = 0,$$
$$h_{22}^2 = T^{av}\Big(\int_{-\infty}^{\infty} E\big\{G_2(t)G_2(t+\tau)\big\}d\tau\Big).$$

If instead the noises are correlated or multiplicative, such an easy choice could not be made. This will lead to the following system

$$dZ_E(t) = m_1(t)dt + h_{11}dW_1(t) + h_{12}dW_2(t)$$
$$d\phi_E(t) = m_2(t)dt + h_{12}dW_1(t) + h_{22}dW_2(t).$$

This system of coupled equations can be approximated as follows

$$dZ_E(t) = m_1(t)dt + \sqrt{h_{11}^2 + h_{12}^2}dW_3(t)$$
$$d\phi_E(t) = m_2(t)dt + \sqrt{h_{12}^2 + h_{22}^2}dW_4(t).$$

The noises terms $h_{11}dW_1(t)+h_{12}dW_2(t)$ and $h_{12}dW_1(t)+h_{22}dW_2(t)$ are replaced by $\sqrt{h_{11}^2 + h_{12}^2}dW_3(t)$ and $\sqrt{h_{12}^2 + h_{22}^2}dW_4(t)$ respectively, where $W_3(t)$ and $W_4(t)$ are two independent Wiener processes. The new noise coefficients depend only on the diagonal elements of the matrix $G_tG'_{t+\tau}$. This avoids solving the nonlinear 4-dimensional equations in h_{ij} and allows an easy derivation of the envelope and phase dynamics. The functions $F = \begin{pmatrix} F_1(t) \\ F_2(t) \end{pmatrix}$ and $G = \begin{pmatrix} G_1(t) \\ G_2(t) \end{pmatrix}$ are defined in Eqs.5.21-5.22. The functions F and G are replaced by F^k and G^k defined in Eqs.5.55-5.56 for the case of networks. We recall that T^{av} is the time averaging operator defined as

$$T^{av}(.) = \frac{1}{T_0}\int_{t_0}^{t_0+T_0}(.)dt$$

and $E.$ denotes the expectation operator (i.e. average over realizations).

5.6.3 Accuracy of the amplitude-phase equations obtained from the Stochastic Averaging Method (SAM)

The Stochastic Averaging Method (SAM) can be interpreted as a proper stochastic averaging operation through the operator E and a deterministic averaging through the operator T^{av}. In this work, the deterministic averaging operation is an averaging throughout an oscillation. The result of such operation depends on the trial solutions which we have chosen to be sinusoidal (Eqs. 5.20,5.41,5.54,5.65). In the quasi-cycle regime, the envelope and phase dynamics obtained describe very well those of the former dynamics (linear equations sustained by noise). In the limit cycle regime, however, the results may depend on the specificity of each system. In fact we found that the quadratic terms in the nonlinear deviation dynamics (Eqs.5.13-5.14; Eqs.5.50-5.51) are not present in the corresponding envelope-phase dynamics (Eqs.5.23-5.24; Eqs.5.57-5.58) obtained through the SAM. This means that including them would not have chnaged the envelope-phase description obtained via the SAM. This could lead to important differences between the SAM envelope-phase dynamics and their former counterparts (directly extracted through the Hilbert transform) particularly if the quadratic nonlinearity is strong. We also found that all the cubic terms are not present in the saturation parameter $B_1(B_1^k)$ of the envelope dynamics obtained through the SAM. The absence of the quadratic and some cubic terms may be seen as the consequence of the choice of trial solutions in a sinusoidal form and may cause divergence of the SAM envelope from the Hilbert envelope.

Another limitation of the SAM exposed here is the fact that it only takes into account the primary frequency of the system. Therefore,it does not take into account higher-order harmonics which may be present in the system because of the nonlinearity and the delay. This is due to the deterministic periodic averaging procedure ($T^{av}(.)$) over the faster primary frequency (ω_0) of the system. To take into account higher-order harmonics, a trial solution in the form of a truncated Fourier series that includes higher harmonics could be a better choice. Such an approach may be more complex than what we have done in this thesis, but, it will be a more general solution.

Concerning numerical simulations, we found that the envelope process was pathological. In fact, numerical simulations of the envelope process (which is a positive quantity) gave negative values

because of the term $\frac{1}{Z(t)}$. In chapter 2 (see Methods), we used the fact that the envelope process was equal to the square-root of two standard independent Ornstein-Uhlenbeck (OU) processes to obtain a positive envelope process. For other chapters (3,4 and 5) where such equality can not be made, we maintain the envelope process positive by taking its absolute value at each time-step of the simulation. This allows the envelope process to remain positive and gives good results since excellent agreement was found with the corresponding theory.

Chapter 6

Summary and Conclusion

In this thesis, we considered dynamical and functional properties of fast brain oscillations known as gamma and beta rhythms. We derived dynamical models of stochastic brain oscillations in terms of slow envelope and phase which reproduce the transient nature of *in vivo* data. Oscillations can be generated by two distinct mechanisms. The first, which is the most common assumes a deterministic stable limit cycle attractor. Noise has a weak effect on the envelope and phase dynamics of stochastic oscillations in this regime unless its intensity is strong. This produces noisy limit cycle oscillations. The second mechanism is stochastic and does not have a deterministic analog. Oscillations in this regime are known as noise-induced or quasi-cycle oscillations. The envelope and phase vary strongly depending on the noise intensity. The work in this thesis has focused mainly on this latter model of stochastic oscillations which are studied in chapters 2, 3, and 4. We used the envelope-phase representation to investigate the ability of such models to communicate with one another by studying their phase-locking properties. Finally, we extended the modeling to produce a unified model that spans both regimes and to go from an isolated stochastic oscillatory network to several networks coupled via long-range excitatory connections.

6.0.1 Summary

The main focus of this thesis has been the origin and the properties of the bursts of high amplitude activity brain rhythms. In the second chapter, we considered a network of reciprocally coupled excitatory and inhibitory neurons subject to fluctuations caused by the finite-size effect of the network. The model is a stochastic version of the well-known Wilson-Cowan model where the intensities of

the noises are related to the size of the excitatory and inhibitory populations. We focused on the limit where oscillations are induced by noise known as the quasi-cycle regime. Without noise, only decaying oscillations towards a fixed point are seen. We used the linear noise approximation to obtain linear equations driven by additive noise. This equations act like as Local field Potentials (LFPs). Their dynamics show transient epochs of the sustained activity known as gamma bursts as often observed *in vivo*. The Stochastic Averaging Method (SAM) was used to derive dynamics for the slow envelope and phase of the stochastic LFP equations. This adds to previous work, based on a different method [102], by providing a full parametrization of these dynamics in terms of the quantities in the detailed Wilson-Cowan model. The SAM was adapted to take into account the amplitude ratio and phase difference between inhibitory and excitatory LFPs. In the envelope-phase framework, a burst is defined as the epoch where the envelope is sustained above a given threshold. We find that the whole problem of burst dynamics is governed by two meta-parameters.

Since the envelope equation obtained is uncoupled from the phase equation, it is easy to derive the stationary probability density of the envelope from Fokker-Planck analysis. Moreover, we were able to obtain a theoretical expression of the mean burst duration by conducting a First passage time analysis. Analyzing the envelope dynamics in the parameter space allows us to uncover an optimal region where the dynamics and statistics (mean burst duration, burst-peak-frequency) of the envelope-phase model match with *in vivo* recordings. Deviation from this optimal range can be associated with pathologies as epilepsy and Alzheimer's diseases.

In Chapter 3, we considered the same Wilson-Cowan system as in Chapter 2, but with alternative modeling where noise in the system comes from the constant synaptic bombardment from surrounding neurons rather than from finite-size effects. This amounts to include noisy inputs inside the response function of a single neuron. Taylor's expansion of the sigmoid response function leads to an effective Wilson-Cowan model driven by both additive and multiplicative noises. As in the previous chapter, we then focused on the quasi-cycle regime, where oscillations are induced by the noise. The dynamics of the excitatory and inhibitory LFPs are again linear equations, but now driven by both additive and multiplicative noises. We further calibrated the model such that the mean frequency of the oscillations falls inside the lower beta range. To investigate the bursting dynamics of the LFPs and the effect of the multiplicative noise, the envelope-phase decomposition

was performed using the SAM.

The corresponding envelope dynamics is again uncoupled from the phase as in Chapter 2, however, the multiplicative noise terms give rise to two additional parameters compared to the case with only additive noise in Chapter 2. The first is a positive coefficient which appears in the drift function and results in a greater effective real part of the complex conjugate eigenvalues. This induces a stronger mean oscillation amplitude than in the case with only additive noise. Furthermore, for sufficiently strong multiplicative noise intensity , the system can virtually behave as a noisy limit cycle even if its deterministic parameters describe a quasi-cycle. The second parameter appears in the diffusion function of the envelope process and has a diffusive role. In the phase dynamics, multiplicative noise also induces additional terms in the drift and diffusion function. This makes the mean frequency depend on the size of the multiplicative noise. However such coefficients are small and do not induce significant changes in the phase dynamics compare to the case with only additive noise. The main effect of the multiplicative noise is therefore to induce a stronger rhythm. This may explain a component of the excess synchronization observed in pathologies like Parkinson's disease.

Chapters 2 and 3 are about the modeling of stochastic oscillations with bursting behavior in terms of an envelope-phase representation. The focus is on the dynamics and statistics of the envelope process since it is directly related to the notion of a burst. In Chapter 4, we investigated the capability of this class of noise-induced oscillations (quasi-cycle oscillations) to sustain robust out-of-phase locking. This is an essential functional property directly linked to inter-areal brain communication. We extended the analysis to two identical connected Stochastic Wilson-Cowan networks driven by finite-size noise as in Chapter 2. The connection is made with long-range excitatory projections involving a propagation delay. Restricting the study to a noise-induced regime and applying a Linear noise approximation leads to delayed-stochastic linear equations driven by additive noise. We then applied the SAM to these dynamics and obtained novel delayed envelope-phase dynamics. This is an extension to two delayed coupled networks of the single envelope-phase description performed in Chapter 2.

The dynamics of the envelope and phase are now mutually coupled, making hard a Fokker-Planck analysis as in Chapters 2 and 3. We focused on the phase dynamics and more precisely on the dynamics of the phase difference. Making some approximations, we found that the vanishing

of the deterministic dynamics towards the stable fixed point only admits In-phase and anti-phase locking behavior. The transition between In-phase and anti-phase locking happens for a critical value of the propagation delay. Without propagation delay, the only phase-locking happens when the phase difference is zero, representing a trivial In-phase locking. This shows the importance of the propagation delay for the appearance of both In and Anti-phase locking states.

Then performing numerical simulations of the noisy envelope-phase dynamics obtained through the SAM as well as of the original Stochastic Wilson-Cowan equations reveals that symmetric out-phase-locking behavior can be observed. This happens around the deterministic transition between In-phase and Anti-phase locking states. The noise smoothes the abrupt deterministic transition between In-phase and Anti-phase locking states and therefore creates symmetric out-of-phase locking states, where one network leads the other during an epoch of time and then loses the leadership in favor of the other and so on. In contrast, to the limit cycle regime where out-of-phase locking states are the consequence of spontaneous symmetry breaking due to the nonlinearity, in the quasi-cycle regime such states are purely induced by noise. Their precise phase difference values and their robustness depend on the intensity of noise. The leadership between the two networks is exchanged dynamically by the noise, but each of the two networks leads the other fifty percent of the time for a sufficiently long simulation time. The mechanism persists even for identical and asymmetrically coupled networks, and heterogeneous symmetrically coupled networks, but with a bias towards one of the two networks. The same mechanism is further observed in delay-coupled networks of purely inhibitory neurons, in the perfectly identical symmetrically coupled, identical asymmetrically coupled, and heterogeneous symmetrically coupled cases. This attests to the generality of the mechanism where coupling-delay and noise induce episodes of robust out-of-phase locking in coupled quasi-cycles. Information can be shared from one network to the other during an episode of out-of-phase locking. It is believed that information is shared from leader to the laggard [134, 175]. Then, the results obtained in this chapter suggest that oscillations in the noise-induced regime are good candidates for inter-areal brain oscillations. Brain oscillations by quasi-cycle oscillations, rather than the usual noisy limit cycle oscillations should thus be considered a serious mechanism for phase locking and coherence-based communication brain areas.

Finally, in Chapter 5, we extended the SAM to include nonlinear terms to obtain a unified

description of the envelope-phase dynamics in both regimes. First, we considered the case of an isolated Stochastic Wilson Cowan model subject to additive white or temporally correlated noises. The resulting envelope dynamics is uncoupled from the phase dynamics and possesses an additional nonlinear term compared to the linear dynamics in Chapter 2. This allowed a description of stochastic oscillations across the Hopf bifurcation from quasi-cycles to noisy limit cycles oscillations, thereby providing a theory that encompasses both regimes that may exist in real brain. The Fokker-Planck analysis was conducted on the envelope dynamics and allowed the derivation of its stationary probability density. The theory uses more general correlated noise of Ornstein-Uhlenbeck (OU) type, but numerics are performed using only Gaussian white noises. Good agreement was found between the probability densities obtained from the SAM and those computed numerically from the original Stochastic Wilson Cowan model for both quasi-cycle and noisy limit cycle regimes.

The same analysis was applied to another model, namely the Stochastic Stuart Landau system, but this time we also considered correlated Ornstein-Uhlenbeck (OU) noise for numerical simulations. The results of the SAM theory match well with numerical simulations for different values of the noise correlation times. This makes the SAM flexible also for different types of noise. In the quasi-cycle regime, the probability density of the envelope process is close to a Rayleigh distribution, while in the noisy limit cycle regime it was better described by a Gaussian distribution. This difference may allow pinpointing the regime responsible for noisy oscillations recorded *in vivo*.

We further extended the SAM to several networks connected through delayed long-range excitatory connections. This results in a set of delayed envelope-phase equations representing the envelope and phase dynamics of coupled oscillatory networks across the Hopf Bifurcation. The extension was considered for both the Stochastic Wilson and the Stochastic Stuart landau models. For limit cycle oscillators, in the deterministic and nearly identical oscillator limit, the Stuart-Landau model leads to the well-known Kuramoto model of interacting phase oscillators. The approach can be applied to other types of networks with different topologies and various stochastic inputs. This shows the generality and the flexibility of the SAM in extracting the envelope and phase processes of a large class of stochastic oscillatory processes.

6.0.2 Future Work

The investigations concerning the modeling of stochastic oscillations in the gamma and other frequency bands presented in this thesis are certainly of great interest, but more work needs to be done to better understand fast brain oscillations and their functions.

When modeling gamma oscillations in Chapter 2, we have investigated how the envelope dynamics and related bursts change in the parameter space. However, we have only investigated the change of a single parameter, namely the recurrent excitation of the E-I network. Specifically, when the result is an increase of the real part of the complex conjugate eigenvalues. This leads to a correlated change of the burst duration and amplitude. When the recurrent excitation is changed, the duration of the bursts and their amplitude change simultaneously in the same direction. This is known as normal amplification [213, 111]. It can also be achieved through other parameter changes with qualitatively similar results. Future work should therefore focus on an alternative amplification which changes the amplitude of bursts without changing their duration. This latter amplification is called non-normal amplification [213, 111] and could be another relevant mechanism by which healthy bursts are generated in the brain. The possibly different characteristics of bursts should then be explored.

We have also suggested that there exists an optimal region in the parameter space which generates burst dynamics similar to what has been observed in monkeys data and healthy patients. However, it not clear what is the meaning of such an optimal region. Is this region related to the critical dynamics of the brain? This idea has to be investigated using a statistical analysis of the envelope processes both for single and coupled oscillatory networks derived in Chapters 2 and 5. Such an analysis could be done to investigate the presence of long-range power-law correlations in the envelope process, their avalanche behavior, and related behavior corresponding to criticality.

Another key result of the Thesis was the theoretical expression for the mean burst duration in Chapter 2 as function of all system parameters contained in the meta-parameters that we have uncovered. However, this theoretical expression has been obtained using several approximations concerning the beginning, the maximum amplitude, and the end of a burst. A recent publication [7] has proposed a framework for first passage time calculation from a threshold back to the same threshold. The mean burst duration may then be calculated without any approximations. It will be a promising avenue to continue the investigation of burst duration by computing its closed form.

This may also be done using the envelope dynamics obtained in Chapter 5.

Very long burst durations have been associated with neurological dysfunction like epilepsy, and short burst durations with Alzheimer's disease. For the case of very long burst durations, therapeutical techniques should be able to desynchronize the corresponding oscillatory neural activity and therefore reduce the lengths of the bursts such that their mean value falls inside the healthy range of [65 150 ms] [228, 80]. The therapy could be reversed for short burst durations. The goal should be to synchronize the oscillatory neural activity such that the duration of the bursts is sufficiently increased and their mean falls inside the healthy range. A common way to achieve these two therapeutical goals is to target the associated neural activity with periodic stimulation. The amplitude, frequency and shape of the external periodic stimulus need to be adapted depending on these two scenarios. The SAM presented here could therefore be adapted to take into account external periodic inputs. Analytical results from the SAM could allow inferring optimal parameters of the external periodic input which can induce or suppress bursts. This may have a significant impact on the treatment of people suffering from these pathologies and other such as Parkinson. External periodic input to shape bursts in the brain is already used in the beta frequency band which is relevant to the treatment of Parkinson's disease. This deep brain stimulation technique, where a fast frequency external periodic input is used to target slower beta rhythm and reduce their burstiness, stands to benefit from the expansion of our work to a stimulation context.

But before any external intervention, a data-driven analysis could be done to extract the meta-parameters related to our envelope-phase dynamics. The knowledge of these parameters from real data recorded from human brains along with proper modifications to the model to account for the structures involved, will allow identifying the proper envelope-phase dynamics corresponding to the brain state under consideration. For the gamma-band, the data-driven analysis could be limited to the envelope-phase dynamics in chapter 2, since sufficient experimental evidence is showing that LFPs in this frequency band are well described by linear equations driven by additive noise. However, gamma-band oscillations could be generated by a network of purely inhibitory neurons, known as the ING mechanism. For this case, envelope-phase dynamics is not available yet. Then it is important to adapt the SAM or any other methods with the ambition of extracting similar envelope-phase dynamics for the ING case as done here for the PING case of E-I networks. This will complement

the repertoire of envelope-phase dynamics for fast gamma-band neural oscillations.

Concerning phase synchronization studied in Chapter 4, the next steps should be to investigate information sharing between connected networks depending on the underlying phase relation, and to document how external inputs are routed given the local relationship between the networks [175]. Such studies are of great interest to elucidate the problem of information propagation in the brain. Along the same line, the set of envelope-phase dynamics obtained in Chapter 5 could be adapted from real data to mimic known brain architecture.

In fact, the study of the whole brain connectivity is a fundamental step to understand the brain functioning. The investigation of the brain connectivity has gained much more attention these last years because of the publicly available large amount of data from the brain of many species at rest or performing some cognitive tasks. An important step is to be able to close the gap between theoretical models and existing data. This could be done by building data-constrained models of the whole brain connectivity. Such an approach has been adopted recently with success in several works[138, 64, 62, 66].

However, the model used to mimic the brain activity is the Stuart-Landau (Chapter 5), which is a canonical model of the Hopf bifurcation and does not contain biophysical parameters as the Wilson-Cowan model does. The use of the Stuart-Landau model is motivated by the fact that it has few parameters (two for a single network) and is therefore more appropriate for data-driven analysis. Here, our envelope-phase decomposition allows to reduce a large amount of parameters to only two meta-parameters for a single network. Like the Stuart-landau, our dynamics thus become suitable for data-driven analysis and in addition, it can be related to biophysical parameters. Our modelling approach of the brain connectivity through the SAM could thus be more appropriate for data modelling of the complete brain structure from a biophysical point.

In fact, the parameters such as the local bifurcation parameter λ_k and the mean-frequency ω_k of each brain area could be extracted from the data as in previous studies [64, 62, 66]. The connectivity matrix C_{kl} could also be extracted from neuroimaging data as well as the conduction delays τ_{kl}. This makes our modelling suitable to incorporate brain connectivity. The question of information propagation in the brain may be therefore investigated from a biophysical informed models (Wilson-Cowan network) following our approach (envelope-phase modelling of the complete brain structure

through the SAM) rather than the canonical normal-form of the Hopf bifurcation [66].

Bibliography

[1] Juan A. Acebron, L.L. Bonilla, Conrad J. Perez Vicente, Felix Ritort, and Renato Spigler. The Kuramoto model: A simple paradigm for synchronization phenomena. *Rev. Mod. Phys.*, 77:137–185, 2005.

[2] Juan A Acebrón, Luis L Bonilla, Conrad J Pérez Vicente, Félix Ritort, and Renato Spigler. The kuramoto model: A simple paradigm for synchronization phenomena. *Reviews of modern physics*, 77(1):137, 2005.

[3] Peyman Adjamian, Ian E Holliday, Gareth R Barnes, Arjan Hillebrand, Avgis Hadjipapas, and Krish D Singh. Induced visual illusions and gamma oscillations in human primary visual cortex. *European Journal of Neuroscience*, 20(2):587–592, 2004.

[4] Gonzalo Alarcon, CD Binnie, RDC Elwes, and CE Polkey. Power spectrum and intracranial eeg patterns at seizure onset in partial epilepsy. *Electroencephalography and clinical neurophysiology*, 94(5):326–337, 1995.

[5] Juan Pablo Aparicio and Hernán Gustavo Solari. Sustained oscillations in stochastic systems. *Mathematical biosciences*, 169(1):15–25, 2001.

[6] ST Ariaratnam and TK Srikantaiah. Parametric instabilities in elastic structures under stochastic loading. *Journal of Structural Mechanics*, 6(4):349–365, 1978.

[7] Oriol Artime, Nagi Khalil, Raúl Toral, and Maxi San Miguel. First-passage distributions for the one-dimensional fokker-planck equation. *Physical Review E*, 98(4):042143, 2018.

[8] Peter Ashwin, Stephen Coombes, and Rachel Nicks. Mathematical frameworks for oscillatory network dynamics in neuroscience. *The Journal of Mathematical Neuroscience*, 6(1):2, 2016.

[9] Bassam V. Atallah and Massimo Scanziani. Instantaneous modulation of gamma oscillation frequency by balancing excitation with inhibition. *Neuron*, 62(4):566 – 577, 2009.

[10] Naama Barkai and Stanislas Leibler. Circadian clocks limited by noise. *Nature*, 403(6767):267–268, 2000.

[11] Marlene Bartos, Imre Vida, and Peter Jonas. Synaptic mechanisms of synchronized gamma oscillations in inhibitory interneuron networks. *Nature reviews neuroscience*, 8(1):45, 2007.

[12] Andre M Bastos, Julien Vezoli, and Pascal Fries. Communication through coherence with inter-areal delays. *Current opinion in neurobiology*, 31:173–180, 2015.

[13] Demian Battaglia, Nicolas Brunel, and David Hansel. Temporal decorrelation of collective oscillations in neural networks with local inhibition and long-range excitation. *Phys. Rev. Lett.*, 99:238106, Dec 2007.

[14] Demian Battaglia, Nicolas Brunel, and David Hansel. Temporal decorrelation of collective oscillations in neural networks with local inhibition and long-range excitation. *Phys. Rev. Lett.*, 99(23):238106, 2007.

[15] Demian Battaglia and David Hansel. Synchronous chaos and broad band gamma rhythm in a minimal multi-layer model of primary visual cortex. *PLoS computational biology*, 7(10):e1002176, 2011.

[16] Demian Battaglia, Annette Witt, Fred Wolf, and Theo Geisel. Dynamic effective connectivity of inter-areal brain circuits. *PLoS Comput. Biol.*, 8(3):e1002438, 2012.

[17] Peter H. Baxendale and Priscilla E. Greenwood. Sustained oscillations for density dependent markov processes. *Journal of Mathematical Biology*, 63(3):433–457, Sep 2011.

[18] Deborah Bell-Pedersen, Vincent M Cassone, David J Earnest, Susan S Golden, Paul E Hardin, Terry L Thomas, and Mark J Zoran. Circadian rhythms from multiple oscillators: lessons from diverse organisms. *Nature Reviews Genetics*, 6(7):544–556, 2005.

[19] Marc Benayoun, Jack D Cowan, Wim van Drongelen, and Edward Wallace. Avalanches in a stochastic model of spiking neurons. *PLoS computational biology*, 6(7):e1000846, 2010.

[20] Boualem Boashash. Estimating and interpreting the instantaneous frequency of a signal. i. fundamentals. *Proceedings of the IEEE*, 80(4):520–538, 1992.

[21] Michele Bonnin. Amplitude and phase dynamics of noisy oscillators. *International Journal of Circuit Theory and Applications*, 45(5):636–659, 2017.

[22] Michele Bonnin, Fabrizio Bonani, and Fabio L Traversa. Kuramoto-like model of noisy oscillators. In *2017 European Conference on Circuit Theory and Design (ECCTD)*, pages 1–4. IEEE, 2017.

[23] Michele Bonnin, Fabio L Traversa, and Fabrizio Bonani. Colored noise in oscillators. phase-amplitude analysis and a method to avoid the ito-stratonovich dilemma. *IEEE Transactions on Circuits and Systems I: Regular Papers*, 66(10):3917–3927, 2019.

[24] Christoph Borgers, Steven Epstein, and Nancy J. Kopell. Gamma oscillations mediate stimulus competition and attentional selection in a cortical network model. *Proceedings of the National Academy of Sciences*, 2008.

[25] Conrado A Bosman, Jan-Mathijs Schoffelen, Nicolas Brunet, Robert Oostenveld, Andre M Bastos, Thilo Womelsdorf, Birthe Rubehn, Thomas Stieglitz, Peter De Weerd, and Pascal Fries. Attentional stimulus selection through selective synchronization between monkey visual areas. *Neuron*, 75(5):875–888, 2012.

[26] Paul C Bressloff. Stochastic neural field theory and the system-size expansion. *SIAM Journal on Applied Mathematics*, 70(5):1488–1521, 2009.

[27] Paul C Bressloff. Metastable states and quasicycles in a stochastic wilson-cowan model of neuronal population dynamics. *Phys. Rev. E*, 82(5):051903, 2010.

[28] Paul C Bressloff. Stochastic neural field theory and the system-size expansion. *SIAM Journal on Applied Mathematics*, 70(5):1488–1521, 2010.

[29] Paul C Bressloff. *Stochastic processes in cell biology*, volume 41. Springer, 2014.

[30] Paul C Bressloff and James MacLaurin. A variational method for analyzing limit cycle oscillations in stochastic hybrid systems. *Chaos: An Interdisciplinary Journal of Nonlinear Science*, 28(6):063105, 2018.

[31] Paul C Bressloff and James N MacLaurin. Phase reduction of stochastic biochemical oscillators. *SIAM Journal on Applied Dynamical Systems*, 19(1):151–180, 2020.

[32] Peter Brown. Abnormal oscillatory synchronisation in the motor system leads to impaired movement. *Current opinion in neurobiology*, 17(6):656–664, 2007.

[33] Nicolas Brunel and Vincent Hakim. Fast global oscillations in networks of integrate-and-fire neurons with low firing rates. *Neural Computation*, 11(7):1621 – 1671, 1999.

[34] Nicolas Brunel and Vincent Hakim. Fast global oscillations in networks of integrate-and-fire neurons with low firing rates. *Neural computation*, 11(7):1621–1671, 1999.

[35] Nicolas Brunel and Xiao-Jing Wang. Effects of neuromodulation in a cortical network model of object working memory dominated by recurrent inhibition. *Journal of Computational Neuroscience*, 11(1):63–85, Jul 2001.

[36] Eberhard H Buhl, Gabor Tamás, and Andre Fisahn. Cholinergic activation and tonic excitation induce persistent gamma oscillations in mouse somatosensory cortex in vitro. *The Journal of physiology*, 513(1):117–126, 1998.

[37] Samuel P. Burns, Dajun Xing, and Robert M. Shapley. Is gamma-band activity in the local field potential of v1 cortex a "clock" or filtered noise? *Journal of Neuroscience*, 31(26):9658–9664, 2011.

[38] Samuel P Burns, Dajun Xing, and Robert M Shapley. Is gamma-band activity in the local field potential of v1 cortex a "clock" or filtered noise? *J. Neurosci.*, 31(26):9658–9664, 2011.

[39] Samuel P Burns, Dajun Xing, Michael J Shelley, and Robert M Shapley. Searching for autocoherence in the cortical network with a time-frequency analysis of the local field potential. *Journal of Neuroscience*, 30(11):4033–4047, 2010.

[40] Samuel P. Burns, Dajun Xing, Michael J. Shelley, and Robert M. Shapley. Searching for autocoherence in the cortical network with a time-frequency analysis of the local field potential. *Journal of Neuroscience*, 30(11):4033–4047, 2010.

[41] Gyorgy Buzsaki. *Rhythms of the Brain*. Oxford University Press, 2006.

[42] György Buzsáki and Xiao-Jing Wang. Mechanisms of gamma oscillations. *Annual review of neuroscience*, 35:203–225, 2012.

[43] György Buzsáki and James J Chrobak. Temporal structure in spatially organized neuronal ensembles: a role for interneuronal networks. *Current Opinion in Neurobiology*, 5(4):504 – 510, 1995.

[44] Áine Byrne, Reuben D O'Dea, Michael Forrester, James Ross, and Stephen Coombes. Next-generation neural mass and field modeling. *Journal of neurophysiology*, 123(2):726–742, 2020.

[45] Joana Cabral, Morten L. Kringelbach, and Gustavo Deco. Exploring the network dynamics underlying brain activity during rest. *Progress in Neurobiology*, 114:102 – 131, 2014.

[46] Joana Cabral, Henry Luckhoo, Mark Woolrich, Morten Joensson, Hamid Mohseni, Adam Baker, Morten L. Kringelbach, and Gustavo Deco. Exploring mechanisms of spontaneous functional connectivity in meg: How delayed network interactions lead to structured amplitude envelopes of band-pass filtered oscillations. *NeuroImage*, 90:423 – 435, 2014.

[47] Hayriye Cagnan, Nicolas Mallet, Christian KE Moll, Alessandro Gulberti, Abbey B Holt, Manfred Westphal, Christian Gerloff, Andreas K Engel, Wolfgang Hamel, Peter J Magill, et al. Temporal evolution of beta bursts in the parkinsonian cortical and basal ganglia network. *Proceedings of the National Academy of Sciences*, 116(32):16095–16104, 2019.

[48] Yuansheng Cao, Hongli Wang, Qi Ouyang, and Yuhai Tu. The free-energy cost of accurate biochemical oscillations. *Nature Physics*, 11(9):772–778, 2015.

[49] Jeremy B Caplan, Joseph R Madsen, Sridhar Raghavachari, and Michael J Kahana. Distinct patterns of brain oscillations underlie two basic parameters of human maze learning. *Journal of Neurophysiology*, 86(1):368–380, 2001.

[50] Jessica A Cardin, Marie Carlén, Konstantinos Meletis, Ulf Knoblich, Feng Zhang, Karl Deisseroth, Li-Huei Tsai, and Christopher I Moore. Driving fast-spiking cells induces gamma rhythm and controls sensory responses. *Nature*, 459(7247):663, 2009.

[51] J. J. Chrobak and G. Buzsáki. Gamma oscillations in the entorhinal cortex of the freely behaving rat. *Journal of Neuroscience*, 18(1):388–398, 1998.

[52] Mike X Cohen. *Analyzing neural time series data: theory and practice*. MIT press, 2014.

[53] Laura Lee Colgin and Edvard I Moser. Gamma oscillations in the hippocampus. *Physiology*, 25(5):319–329, 2010.

[54] PH Coullet, C Elphick, and E Tirapegui. Normal form of a hopf bifurcation with noise. *Physics Letters A*, 111(6):277–282, 1985.

[55] Jozsef Csicsvari, Brian Jamieson, Kensall D Wise, and György Buzsáki. Mechanisms of gamma oscillations in the hippocampus of the behaving rat. *Neuron*, 37(2):311–322, 2003.

[56] Mark O. Cunningham, Ceri H. Davies, Eberhard H. Buhl, Nancy Kopell, and Miles A. Whittington. Gamma oscillations induced by kainate receptor activation in the entorhinal cortex in vitro. *Journal of Neuroscience*, 23(30):9761–9769, 2003.

[57] FH Lopes Da Silva, JP Pijn, D Velis, and PCG Nijssen. Alpha rhythms: noise, dynamics and models. *International Journal of Psychophysiology*, 26(1-3):237–249, 1997.

[58] Andreas Daffertshofer and Bernadette van Wijk. On the influence of amplitude on the connectivity between phases. *Frontiers in neuroinformatics*, 5:6, 2011.

[59] Tal Danino, Octavio Mondragón-Palomino, Lev Tsimring, and Jeff Hasty. A synchronized quorum of genetic clocks. *Nature*, 463(7279):326–330, 2010.

[60] Coralie De Hemptinne, Elena S Ryapolova-Webb, Ellen L Air, Paul A Garcia, Kai J Miller, Jeffrey G Ojemann, Jill L Ostrem, Nicholas B Galifianakis, and Philip A Starr. Exaggerated phase–amplitude coupling in the primary motor cortex in parkinson disease. *Proceedings of the National Academy of Sciences*, 110(12):4780–4785, 2013.

[61] Gustavo Deco, Joana Cabral, Mark W. Woolrich, Angus B.A. Stevner, Tim J. van Hartevelt, and Morten L. Kringelbach. Single or multiple frequency generators in on-going brain activity: A mechanistic whole-brain model of empirical meg data. *NeuroImage*, 152:538 – 550, 2017.

[62] Gustavo Deco, Joana Cabral, Mark W Woolrich, Angus BA Stevner, Tim J Van Hartevelt, and Morten L Kringelbach. Single or multiple frequency generators in on-going brain activity: A mechanistic whole-brain model of empirical meg data. *Neuroimage*, 152:538–550, 2017.

[63] Gustavo Deco and Viktor K. Jirsa. Ongoing cortical activity at rest: Criticality, multistability, and ghost attractors. *Journal of Neuroscience*, 32(10):3366–3375, 2012.

[64] Gustavo Deco, Morten L Kringelbach, Viktor K Jirsa, and Petra Ritter. The dynamics of resting fluctuations in the brain: metastability and its dynamical cortical core. *Scientific reports*, 7(1):1–14, 2017.

[65] Gustavo Deco, Adrián Ponce-Alvarez, Dante Mantini, Gian Luca Romani, Patric Hagmann, and Maurizio Corbetta. Resting-state functional connectivity emerges from structurally and dynamically shaped slow linear fluctuations. *Journal of Neuroscience*, 33(27):11239–11252, 2013.

[66] Gustavo Deco, Diego Vidaurre, and Morten L Kringelbach. Revisiting the global workspace orchestrating the hierarchical organization of the human brain. *Nature Human Behaviour*, pages 1–15, 2021.

[67] Jean-Michel Deniau, Bertrand Degos, Clémentine Bosch, and Nicolas Maurice. Deep brain stimulation mechanisms: beyond the concept of local functional inhibition. *European Journal of Neuroscience*, 32(7):1080–1091, 2010.

[68] M Omar Din, Tal Danino, Arthur Prindle, Matt Skalak, Jangir Selimkhanov, Kaitlin Allen, Ellixis Julio, Eta Atolia, Lev S Tsimring, Sangeeta N Bhatia, et al. Synchronized cycles of bacterial lysis for in vivo delivery. *Nature*, 536(7614):81–85, 2016.

[69] Brent Doiron, Benjamin Lindner, André Longtin, Leonard Maler, and Joseph Bastian. Oscillatory activity in electrosensory neurons increases with the spatial correlation of the stochastic input stimulus. *Phys. Rev. Lett.*, 93(4):048101, 2004.

[70] Ricardo E Dolmetsch, Keli Xu, and Richard S Lewis. Calcium oscillations increase the efficiency and specificity of gene expression. *Nature*, 392(6679):933–936, 1998.

[71] Benoit Duchet, Gihan Weerasinghe, Hayriye Cagnan, Peter Brown, Christian Bick, and Rafal Bogacz. Phase-dependence of response curves to deep brain stimulation and their relationship: from essential tremor patient data to a wilson–cowan model. *The Journal of Mathematical Neuroscience*, 10:1–39, 2020.

[72] Grégory Dumont and Boris Gutkin. Macroscopic phase resetting-curves determine oscillatory coherence and signal transfer in inter-coupled neural circuits. *PLoS Comp.Biol.*, 15(5):e1007019, 2019.

[73] Grégory Dumont, Georg Northoff, and André Longtin. Linear noise approximation for oscillations in a stochastic inhibitory network with delay. *Physical Review E*, 90(1):012702, 2014.

[74] Grégory Dumont, Georg Northoff, and André Longtin. A stochastic model of input effectiveness during irregular gamma rhythms. *Journal of Computational Neuroscience*, 40(1):85–101, Feb 2016.

[75] W Ebeling, H Herzel, and EE Selkov. The influence of noise on an oscillating glycolytic model. *studia biophysica*, 98(3):147–154, 1983.

[76] Alexander S Ecker, Philipp Berens, Georgios A Keliris, Matthias Bethge, Nikos K Logothetis, and Andreas S Tolias. Decorrelated neuronal firing in cortical microcircuits. *science*, 327(5965):584–587, 2010.

[77] Víctor M Eguíluz, Mark Ospeck, Y Choe, AJ Hudspeth, and Marcelo O Magnasco. Essential nonlinearities in hearing. *Physical review letters*, 84(22):5232, 2000.

[78] A Einstein. On the movement of small particles suspended in stationary liquids required by the molecularkinetic theory of heat. *Ann. d. Phys*, 17(549-560):1, 1905.

[79] Andreas K Engel and Pascal Fries. Beta-band oscillations—signalling the status quo? *Current opinion in neurobiology*, 20(2):156–165, 2010.

[80] Joseph Feingold, Daniel J Gibson, Brian DePasquale, and Ann M Graybiel. Bursts of beta oscillation differentiate postperformance activity in the striatum and motor cortex of monkeys performing movement tasks. *Proceedings of the National Academy of Sciences*, 112(44):13687–13692, 2015.

[81] Andre Fisahn, Fenella G Pike, Eberhard H Buhl, and Ole Paulsen. Cholinergic induction of network oscillations at 40 hz in the hippocampus in vitro. *Nature*, 394(6689):186, 1998.

[82] Robert S Fisher, WR Webber, Ronald P Lesser, Santiago Arroyo, and Sumio Uematsu. High-frequency eeg activity at the start of seizures. *Journal of clinical neurophysiology: official publication of the American Electroencephalographic Society*, 9(3):441–448, 1992.

[83] Pascal Fries. A mechanism for cognitive dynamics: neuronal communication through neuronal coherence. *Trends in cognitive sciences*, 9(10):474–480, 2005.

[84] Pascal Fries. A mechanism for cognitive dynamics: neuronal communication through neuronal coherence. *Trends in Cognitive Sciences*, 9(10):474 – 480, 2005.

[85] Pascal Fries. Rhythms for cognition: communication through coherence. *Neuron*, 88(1):220–235, 2015.

[86] Pascal Fries. Rhythms for cognition: Communication through coherence. *Neuron*, 88(1):220 – 235, 2015.

[87] Pascal Fries, Danko Nikolić, and Wolf Singer. The gamma cycle. *Trends in Neurosciences*, 30(7):309 – 316, 2007. July INMED/TINS special issue—Physiogenic and pathogenic oscillations: the beauty and the beast.

[88] LEONE Fronzoni, RICCARDO Mannella, Peter VE McClintock, and Frank Moss. Postponement of hopf bifurcations by multiplicative colored noise. *Physical Review A*, 36(2):834, 1987.

[89] Surya Ganguli, Dongsung Huh, and Haim Sompolinsky. Memory traces in dynamical systems. *Proceedings of the National Academy of Sciences*, 105(48):18970–18975, 2008.

[90] Crispin W Gardiner et al. *Handbook of stochastic methods*, volume 3. springer Berlin, 1985.

[91] C.W. Gardiner. *Handbook of Stochastic Methods for Physics, Chemistry, and the Natural Sciences*. Springer complexity. Springer, 2004.

[92] Wulfram Gerstner and Werner M Kistler. *Spiking neuron models: Single neurons, populations, plasticity*. Cambridge university press, 2002.

[93] Daniel T Gillespie. Exact stochastic simulation of coupled chemical reactions. *The journal of physical chemistry*, 81(25):2340–2361, 1977.

[94] Daniel T Gillespie. The chemical langevin equation. *The Journal of Chemical Physics*, 113(1):297–306, 2000.

[95] Leon Glass. Synchronization and rhythmic processes in physiology. *Nature*, 410(6825):277–284, 2001.

[96] Albert Goldbeter. *Biochemical oscillations and cellular rhythms: the molecular bases of periodic and chaotic behaviour*. Cambridge university press, 1997.

[97] Albert Goldbeter. Modelling biochemical oscillations and cellular rhythms. *Current Science*, pages 933–939, 1997.

[98] Albert Goldbeter. Computational approaches to cellular rhythms. *Nature*, 420(6912):238–245, 2002.

[99] Oscar J Avella Gonzalez, Karlijn I Van Aerde, Ronald AJ Van Elburg, Simon-Shlomo Poil, Huibert D Mansvelder, Klaus Linkenkaer-Hansen, Jaap van Pelt, and Arjen van Ooyen. External drive to inhibitory cells induces alternating episodes of high-and low-amplitude oscillations. *PLoS computational biology*, 8(8):e1002666, 2012.

[100] Javier Gonzalez-Castillo and Peter A Bandettini. Task-based dynamic functional connectivity: Recent findings and open questions. *Neuroimage*, 180:526–533, 2018.

[101] Izrail Solomonovich Gradshteyn and Iosif Moiseevich Ryzhik. *Table of integrals, series, and products*. Academic press, 2014.

[102] Priscilla E Greenwood, Mark D McDonnell, and Lawrence M Ward. Dynamics of gamma bursts in local field potentials. *Neural computation*, 27(1):74–103, 2015.

[103] Priscilla E Greenwood, Mark D McDonnell, and Lawrence M Ward. A kuramoto coupling of quasi-cycle oscillators with application to neural networks. *Journal of Coupled Systems and Multiscale Dynamics*, 4(1):1–13, 2016.

[104] Joachim Gross, Alfons Schnitzler, Lars Timmermann, and Markus Ploner. Gamma oscillations in human primary somatosensory cortex reflect pain perception. *PLoS biology*, 5(5):e133, 2007.

[105] Michael R Guevara, Leon Glass, and Alvin Shrier. Phase locking, period-doubling bifurcations, and irregular dynamics in periodically stimulated cardiac cells. *Science*, 214(4527):1350–1353, 1981.

[106] Constance Hammond, Hagai Bergman, and Peter Brown. Pathological synchronization in parkinson's disease: networks, models and treatments. *Trends in neurosciences*, 30(7):357–364, 2007.

[107] John A Hartigan, Pamela M Hartigan, et al. The dip test of unimodality. *The annals of Statistics*, 13(1):70–84, 1985.

[108] PM Hartigan. Algorithm as 217: Computation of the dip statistic to test for unimodality. *Journal of the Royal Statistical Society. Series C (Applied Statistics)*, 34(3):320–325, 1985.

[109] Alan Hastings, Karen C Abbott, Kim Cuddington, Tessa Francis, Gabriel Gellner, Ying-Cheng Lai, Andrew Morozov, Sergei Petrovskii, Katherine Scranton, and Mary Lou Zeeman. Transient phenomena in ecology. *Science*, 361(6406):eaat6412, 2018.

[110] Guillaume Hennequin, Tim P. Vogels, and Wulfram Gerstner. Non-normal amplification in random balanced neuronal networks. *Phys. Rev. E*, 86:011909, Jul 2012.

[111] Peter Henrici. Bounds for iterates, inverses, spectral variation and fields of values of non-normal matrices. *Numerische Mathematik*, 4(1):24–40, Dec 1962.

[112] Christoph S. Herrmann, Matthias H.J. Munk, and Andreas K. Engel. Cognitive functions of gamma-band activity: memory match and utilization. *Trends in Cognitive Sciences*, 8(8):347 – 355, 2004.

[113] CS Herrmann and T Demiralp. Human eeg gamma oscillations in neuropsychiatric disorders. *Clinical neurophysiology*, 116(12):2719–2733, 2005.

[114] J Hizanidis, AG Balanov, Andreas Amann, and Eckehard Schöll. Noise-induced oscillations and their control in semiconductor superlattices. *Int. J. Bif. Chaos*, 16(06):1701–1710, 2006.

[115] Werner Horsthemke. Noise induced transitions. In *Non-Equilibrium Dynamics in Chemical Systems*, pages 150–160. Springer, 1984.

[116] Marc W Howard, Daniel S Rizzuto, Jeremy B Caplan, Joseph R Madsen, John Lisman, Richard Aschenbrenner-Scheibe, Andreas Schulze-Bonhage, and Michael J Kahana. Gamma oscillations correlate with working memory load in humans. *Cerebral cortex*, 13(12):1369–1374, 2003.

[117] R Matthew Hutchison, Thilo Womelsdorf, Elena A Allen, Peter A Bandettini, Vince D Calhoun, Maurizio Corbetta, Stefania Della Penna, Jeff H Duyn, Gary H Glover, Javier Gonzalez-Castillo, et al. Dynamic functional connectivity: promise, issues, and interpretations. *Neuroimage*, 80:360–378, 2013.

[118] R Matthew Hutchison, Thilo Womelsdorf, Joseph S Gati, Stefan Everling, and Ravi S Menon. Resting-state networks show dynamic functional connectivity in awake humans and anesthetized macaques. *Human brain mapping*, 34(9):2154–2177, 2013.

[119] Axel Hutt and Andre Longtin. Effects of the anesthetic agent propofol on neural populations. *Cognitive neurodynamics*, 4(1):37–59, 2010.

[120] Axel Hutt, Connie Sutherland, and André Longtin. Driving neural oscillations with correlated spatial input and topographic feedback. *Physical Review E*, 78(2):021911, 2008.

[121] Alexandre Hyafil, Anne-Lise Giraud, Lorenzo Fontolan, and Boris Gutkin. Neural cross-frequency coupling: Connecting architectures, mechanisms, and functions. *Trends in Neurosciences*, 38(11):725 – 740, 2015.

[122] Alexandre Hyafil, Anne-Lise Giraud, Lorenzo Fontolan, and Boris Gutkin. Neural cross-frequency coupling: connecting architectures, mechanisms, and functions. *Trends in neurosciences*, 38(11):725–740, 2015.

[123] Jorge Jaramillo, Jorge F Mejias, and Xiao-Jing Wang. Engagement of pulvino-cortical feedforward and feedback pathways in cognitive computations. *Neuron*, 101(2):321–336, 2019.

[124] John G.R Jefferys, Roger D Traub, and Miles A Whittington. Neuronal networks for induced '40 hz' rhythms. *Trends in Neurosciences*, 19(5):202 – 208, 1996.

[125] Xiaoxuan Jia and Adam Kohn. Gamma rhythms in the brain. *PLoS biology*, 9(4), 2011.

[126] Beatrice M Jobst, Rikkert Hindriks, Helmut Laufs, Enzo Tagliazucchi, Gerald Hahn, Adrián Ponce-Alvarez, Angus BA Stevner, Morten L Kringelbach, and Gustavo Deco. Increased stability and breakdown of brain effective connectivity during slow-wave sleep: mechanistic insights from whole-brain computational modelling. *Scientific reports*, 7(1):1–16, 2017.

[127] Madhura R Joglekar, Jorge F Mejias, Guangyu Robert Yang, and Xiao-Jing Wang. Inter-areal balanced amplification enhances signal propagation in a large-scale circuit model of the primate cortex. *Neuron*, 98(1):222–234, 2018.

[128] S Kabashima and T Kawakubo. Observation of a noise-induced phase transition in a parametric oscillator. *Physics letters A*, 70(5-6):375–376, 1979.

[129] Kukjin Kang, Michael Shelley, James Andrew Henrie, and Robert Shapley. Lfp spectral peaks in v1 cortex: network resonance and cortico-cortical feedback. *Journal of computational neuroscience*, 29(3):495–507, 2010.

[130] Kukjin Kang, Michael Shelley, and Haim Sompolinsky. Mexican hats and pinwheels in visual cortex. *Proceedings of the National Academy of Sciences*, 100(5):2848–2853, 2003.

[131] N Jeremy Kasdin. Discrete simulation of colored noise and stochastic processes and 1/f/sup/spl alpha//power law noise generation. *Proceedings of the IEEE*, 83(5):802–827, 1995.

[132] Stephen Keeley, André A. Fenton, and John Rinzel. Modeling fast and slow gamma oscillations with interneurons of different subtype. *J. Neurophysiol.*, 117(0):950–965, 2017.

[133] Rafail Z Khas' minskii. A limit theorem for the solutions of differential equations with random right-hand sides. *Theory of Probability & Its Applications*, 11(3):390–406, 1966.

[134] Christoph Kirst, Marc Timme, and Demian Battaglia. Dynamic information routing in complex networks. *Nature communications*, 7:11061, 2016.

[135] N Kopell, GB Ermentrout, MA Whittington, and RD Traub. Gamma rhythms and beta rhythms have different synchronization properties. *Proceedings of the National Academy of Sciences*, 97(4):1867–1872, 2000.

[136] Andreas K Kreiter and Wolf Singer. Stimulus-dependent synchronization of neuronal responses in the visual cortex of the awake macaque monkey. *Journal of neuroscience*, 16(7):2381–2396, 1996.

[137] Henry Kressel. *Semiconductor Lasers and Herterojunction LEDs*. Elsevier, 2012.

[138] Morten L Kringelbach, Anthony R McIntosh, Petra Ritter, Viktor K Jirsa, and Gustavo Deco. The rediscovery of slowness: exploring the timing of cognition. *Trends in cognitive sciences*, 19(10):616–628, 2015.

[139] Yoshiki Kuramoto. *Chemical oscillations, waves, and turbulence*. Courier Corporation, 2003.

[140] YN Kyrychko, KB Blyuss, and E Schöll. Amplitude and phase dynamics in oscillators with distributed-delay coupling. *Phil. Trans. Roy. Soc. A*, 371(1999):20120466, 2013.

[141] E. Ledoux and N. Brunel. Dynamics of networks of excitatory and inhibitory neurons in response to time-dependent inputs. *Front. Comput. Neurosci.*, 5(0):25, 2011.

[142] Kwang-Hyuk Lee, Leanne Williams, Albert Haig, and Evian Gordon. " gamma (40 hz) phase synchronicity" and symptom dimensions in schizophrenia. *Cognitive Neuropsychiatry*, 8(1):57–71, 2003.

[143] Kwang-Hyuk Lee, Leanne M Williams, Michael Breakspear, and Evian Gordon. Synchronous gamma activity: a review and contribution to an integrative neuroscience model of schizophrenia. *Brain Research Reviews*, 41(1):57–78, 2003.

[144] René Lefever and J Wm Turner. Sensitivity of a hopf bifurcation to multiplicative colored noise. *Physical review letters*, 56(16):1631, 1986.

[145] Benjamin Lindner, Kai Dierkes, and Frank Jülicher. Local exponents of nonlinear compression in periodically driven noisy oscillators. *Physical review letters*, 103(25):250601, 2009.

[146] Simon Little, James Bonaiuto, Gareth Barnes, and Sven Bestmann. Human motor cortical beta bursts relate to movement planning and response errors. *PLoS biology*, 17(10):e3000479, 2019.

[147] Simon Little and Peter Brown. The functional role of beta oscillations in parkinson's disease. *Parkinsonism & related disorders*, 20:S44–S48, 2014.

[148] Roxanne Lofredi, Huiling Tan, Wolf-Julian Neumann, Chien-Hung Yeh, Gerd-Helge Schneider, Andrea A Kühn, and Peter Brown. Beta bursts during continuous movements accompany the velocity decrement in parkinson's disease patients. *Neurobiology of disease*, 127:462–471, 2019.

[149] André Longtin. Noise-induced transitions at a hopf bifurcation in a first-order delay-differential equation. *Physical Review A*, 44(8):4801, 1991.

[150] André Longtin, John G Milton, Jelte E Bos, and Michael C Mackey. Noise and critical behavior of the pupil light reflex at oscillation onset. *Physical Review A*, 41(12):6992, 1990.

[151] Eric Lowet, Mark Roberts, Avgis Hadjipapas, Alina Peter, Jan van der Eerden, and Peter De Weerd. Input-dependent frequency modulation of cortical gamma oscillations shapes spatial synchronization and enables phase coding. *PLoS computational biology*, 11(2), 2015.

[152] Eric Lowet, Mark J Roberts, Alina Peter, Bart Gips, and Peter De Weerd. A quantitative theory of gamma synchronization in macaque v1. *Elife*, 6:e26642, 2017.

[153] Mikael Lundqvist, Pawel Herman, Melissa R Warden, Scott L Brincat, and Earl K Miller. Gamma and beta bursts during working memory readout suggest roles in its volitional control. *Nature communications*, 9(1):394, 2018.

[154] Mikael Lundqvist, Jonas Rose, Pawel Herman, Scott L Brincat, Timothy J Buschman, and Earl K Miller. Gamma and beta bursts underlie working memory. *Neuron*, 90(1):152–164, 2016.

[155] Mikael Lundqvist, Jonas Rose, Pawel Herman, Scott L. Brincat, Timothy J. Buschman, and Earl K. Miller. Gamma and beta bursts underlie working memory. *Neuron*, 90(1):152 – 164, 2016.

[156] Alexandre Mauroy and Igor Mezić. Global computation of phase-amplitude reduction for limit-cycle dynamics. *Chaos: An Interdisciplinary Journal of Nonlinear Science*, 28(7):073108, 2018.

[157] Robert M May. Limit cycles in predator-prey communities. *Science*, 177(4052):900–902, 1972.

[158] A. J. McKane and T. J. Newman. Predator-prey cycles from resonant amplification of demographic stochasticity. *Phys. Rev. Lett.*, 94:218102, Jun 2005.

[159] Alan J McKane and Barbara Drossel. Models of food web evolution. *Ecological networks: linking structure to dynamics in food webs (eds M. Pascual & JA Dunne)*, pages 223–243, 2006.

[160] Alan J McKane, James D Nagy, Timothy J Newman, and Marianne O Stefanini. Amplified biochemical oscillations in cellular systems. *Journal of Statistical Physics*, 128(1-2):165–191, 2007.

[161] Alan J McKane and Timothy J Newman. Predator-prey cycles from resonant amplification of demographic stochasticity. *Phys. Rev. Lett.*, 94(21):218102, 2005.

[162] Jorge F Mejias, John D Murray, Henry Kennedy, and Xiao-Jing Wang. Feedforward and feedback frequency-dependent interactions in a large-scale laminar network of the primate cortex. *Science advances*, 2(11):e1601335, 2016.

[163] Jason W Middleton, André Longtin, Jan Benda, and Leonard Maler. The cellular basis for parallel neural transmission of a high-frequency stimulus and its low-frequency envelope. *Proceedings of the National Academy of Sciences*, 103(39):14596–14601, 2006.

[164] Denis Mollison. Simplifying simple epidemic models. *Nature*, 310(5974):224–225, 1984.

[165] Octavio Mondragón-Palomino, Tal Danino, Jangir Selimkhanov, Lev Tsimring, and Jeff Hasty. Entrainment of a population of synthetic genetic oscillators. *Science*, 333(6047):1315–1319, 2011.

[166] Teresa Montez, Simon-Shlomo Poil, Bethany F Jones, Ilonka Manshanden, Jeroen PA Verbunt, Bob W van Dijk, Arjen B Brussaard, Arjen van Ooyen, Cornelis J Stam, Philip Scheltens, et al. Altered temporal correlations in parietal alpha and prefrontal theta oscillations in early-stage alzheimer disease. *Proceedings of the National Academy of Sciences*, pages pnas–0811699106, 2009.

[167] Brendan K. Murphy and Kenneth D. Miller. Balanced amplification: A new mechanism of selective amplification of neural activity patterns. *Neuron*, 61(4):635 – 648, 2009.

[168] Y Nakamura, F Tominaga, and T Munakata. Clustering behavior of time-delayed nearest-neighbor coupled oscillators. *Physical Review E*, 49(6):4849, 1994.

[169] Ernst Niebur, Heinz G Schuster, and Daniel M Kammen. Collective frequencies and metastability in networks of limit-cycle oscillators with time delay. *Physical review letters*, 67(20):2753, 1991.

[170] Danko Nikolić, Pascal Fries, and Wolf Singer. Gamma oscillations: precise temporal coordination without a metronome. *Trends in cognitive sciences*, 17(2):54–55, 2013.

[171] Béla Novák and John J Tyson. Design principles of biochemical oscillators. *Nature reviews Molecular cell biology*, 9(12):981–991, 2008.

[172] Toru Ohira and Jack D Cowan. Stochastic neurodynamics and the system size expansion. In *Mathematics of neural networks*, pages 290–294. Springer, 1997.

[173] Angela CE Onslow, Matthew W Jones, and Rafal Bogacz. A canonical circuit for generating phase-amplitude coupling. *PloS one*, 9(8):e102591, 2014.

[174] Hirofumi Ozeki, Ian M. Finn, Evan S. Schaffer, Kenneth D. Miller, and David Ferster. Inhibitory stabilization of the cortical network underlies visual surround suppression. *Neuron*, 62(4):578 – 592, 2009.

[175] Agostina Palmigiano, Theo Geisel, Fred Wolf, and Demian Battaglia. Flexible information routing by transient synchrony. *Nature neuroscience*, 20(7):1014, 2017.

[176] Satu Palva and J Matias Palva. New vistas for α-frequency band oscillations. *Trends in neurosciences*, 30(4):150–158, 2007.

[177] Alex Pavlides, S John Hogan, and Rafal Bogacz. Computational models describing possible mechanisms for generation of excessive beta oscillations in parkinson's disease. *PLoS computational biology*, 11(12):e1004609, 2015.

[178] Bastian Pietras. Modeling phase synchronization of interacting neuronal populations. 2018.

[179] Arkady Pikovsky, Michael Rosenblum, and Jürgen Kurths. *Synchronization*. Cambridge University Press, 1 edition, 2001.

[180] Arkady S Pikovsky and Jürgen Kurths. Coherence resonance in a noise-driven excitable system. *Physical Review Letters*, 78(5):775, 1997.

[181] Simon-Shlomo Poil, Rick Jansen, Karlijn van Aerde, Jaap Timmerman, Arjen B Brussaard, Huibert D Mansvelder, and Klaus Linkenkaer-Hansen. Fast network oscillations in vitro exhibit a slow decay of temporal auto-correlations. *European Journal of Neuroscience*, 34(3):394–403, 2011.

[182] Arthur S Powanwe and André Longtin. Determinants of brain rhythm burst statistics. *Scientific Reports*, 9(1):1–23, 2019.

[183] Arthur S Powanwe and André Longtin. Phase dynamics of delay-coupled quasi-cycles with application to brain rhythms. *Physical Review Research*, 2(4):043067, 2020.

[184] Arthur S Powanwe and André Longtin. Brain rhythm bursts are enhanced by multiplicative noise. *Chaos: An Interdisciplinary Journal of Nonlinear Science*, 31(1):013117, 2021.

[185] Supratim Ray and John HR Maunsell. Do gamma oscillations play a role in cerebral cortex? *Trends in cognitive sciences*, 19(2):78–85, 2015.

[186] Alfonso Renart, Jaime De La Rocha, Peter Bartho, Liad Hollender, Néstor Parga, Alex Reyes, and Kenneth D Harris. The asynchronous state in cortical circuits. *science*, 327(5965):587–590, 2010.

[187] JB Roberts and PD Spanos. Stochastic averaging: an approximate method of solving random vibration problems. *International Journal of Non-Linear Mechanics*, 21(2):111–134, 1986.

[188] Francisco A Rodrigues, Thomas K DM Peron, Peng Ji, and Jürgen Kurths. The kuramoto model in complex networks. *Physics Reports*, 610:1–98, 2016.

[189] Ganna Rozhnova and Ana Nunes. Fluctuations and oscillations in a simple epidemic model. *Physical Review E*, 79(4):041922, 2009.

[190] Jonathan E Rubin. Computational models of basal ganglia dysfunction: the dynamics is in the details. *Current opinion in neurobiology*, 46:127–135, 2017.

[191] Joshua D Salvi, Dáibhid Ó Maoiléidigh, and AJ Hudspeth. Identification of bifurcations from observations of noisy biological oscillators. *Biophysical journal*, 111(4):798–812, 2016.

[192] Belen Sancristobal, Beatriz Rebollo, Paul Boada, Maria V. Sanchez-Vives, and Jordi Garcia-Ojalvo. Collective stochastic coherence in recurrent neuronal networks. *Nature Phys.*, 12:881–887, 2016.

[193] Aaron Schurger, Alan Cowey, and Catherine Tallon-Baudry. Induced gamma-band oscillations correlate with awareness in hemianopic patient gy. *Neuropsychologia*, 44(10):1796 – 1803, 2006.

[194] H. G. Schuster and P. Wagner. A model for neuronal oscillations in the visual cortex. *Biological Cybernetics*, 64(1):77–82, Nov 1990.

[195] Heinz Georg Schuster and Peter Wagner. Mutual entrainment of two limit cycle oscillators with time delayed coupling. *Prog. Theor. Physics*, 81(5):939–945, 1989.

[196] HG Schuster and P Wagner. A model for neuronal oscillations in the visual cortex. *Biological cybernetics*, 64(1):77–82, 1990.

[197] Justus TC Schwabedal and Arkady Pikovsky. Phase description of stochastic oscillations. *Physical review letters*, 110(20):204102, 2013.

[198] Sho Shirasaka, Wataru Kurebayashi, and Hiroya Nakao. Phase-amplitude reduction of transient dynamics far from attractors for limit-cycling systems. *Chaos: An Interdisciplinary Journal of Nonlinear Science*, 27(2):023119, 2017.

[199] James Sneyd, Joel Keizer, and Michael J Sanderson. Mechanisms of calcium oscillations and waves: a quantitative analysis. *The FASEB Journal*, 9(14):1463–1472, 1995.

[200] Polychronis-TD Spanos and George P Solomos. Markov approximation to transient vibration. *Journal of Engineering Mechanics*, 109(4):1134–1150, 1983.

[201] Kevin M Spencer, Paul G Nestor, Ruth Perlmutter, Margaret A Niznikiewicz, Meredith C Klump, Melissa Frumin, Martha E Shenton, and Robert W McCarley. Neural synchrony indexes disordered perception and cognition in schizophrenia. *Proceedings of the National Academy of Sciences*, 101(49):17288–17293, 2004.

[202] David Sterratt, Bruce Graham, Andrew Gillies, and David Willshaw. *Principles of computational modelling in neuroscience*. Cambridge University Press, 2011.

[203] Rouslan L Stratonovich. *Topics in the theory of random noise*, volume 2. CRC Press, 1967.

[204] Jesse Stricker, Scott Cookson, Matthew R Bennett, William H Mather, Lev S Tsimring, and Jeff Hasty. A fast, robust and tunable synthetic gene oscillator. *Nature*, 456(7221):516–519, 2008.

[205] S.H. Strogatz. *Nonlinear Dynamics and Chaos: With Applications to Physics, Biology, Chemistry, and Engineering*. Studies in Nonlinearity. Avalon Publishing, 2014.

[206] Stephen Strogatz. Nonlinear dynamics and chaos: with applications to physics, biology, chemistry, and engineering (studies in nonlinearity). 2001.

[207] Jian-Qiao Sun, Albert C J Luo, and George Zaslavsky. *Stochastic dynamics and control*. Monograph series on nonlinear science and complexity. Elsevier Science, Amsterdam, 2006.

[208] Catherine Tallon-Baudry, Olivier Bertrand, Claude Delpuech, and Jacques Pernier. Stimulus specificity of phase-locked and non-phase-locked 40 hz visual responses in human. *Journal of Neuroscience*, 16(13):4240–4249, 1996.

[209] Peter J Thomas and Benjamin Lindner. Asymptotic phase for stochastic oscillators. *Physical review letters*, 113(25):254101, 2014.

[210] U.S. Thounaojam, J. Cui, S.E. Norman, R.J. Butera, and C.C. Canavier. Slow noise in the period of a biological oscillator underlies gradual trends and abrupt transitions in phasic relationships in hybrid neural networks. *PLoS. Comp. Biol.*, 10(5):e1003622, 2014.

[211] Gerd Tinkhauser, Alek Pogosyan, Simon Little, Martijn Beudel, Damian M Herz, Huiling Tan, and Peter Brown. The modulatory effect of adaptive deep brain stimulation on beta bursts in parkinson's disease. *Brain*, 140(4):1053–1067, 2017.

[212] Roger D Traub, Miles A Whittington, Ian M Stanford, and John GR Jefferys. A mechanism for generation of long-range synchronous fast oscillations in the cortex. *Nature*, 383(6601):621, 1996.

[213] Lloyd N Trefethen and Mark Embree. *Spectra and pseudospectra: the behavior of nonnormal matrices and operators*. Princeton University Press, 2005.

[214] Lev S Tsimring. Noise in biology. *Reports on Progress in Physics*, 77(2):026601, 2014.

[215] Henry C Tuckwell. *Stochastic processes in the neurosciences*. SIAM, 1989.

[216] Nicolaas G van Kampen. Remarks on non-markov processes. *Brazilian Journal of Physics*, 28(2):90–96, 1998.

[217] Nicolaas Godfried Van Kampen. *Stochastic processes in physics and chemistry*, volume 1. Elsevier, 1992.

[218] Marieke K van Vugt, Per B Sederberg, and Michael J Kahana. Comparison of spectral analysis methods for characterizing brain oscillations. *Journal of neuroscience methods*, 162(1-2):49–63, 2007.

[219] Francisco Varela, Jean-Philippe Lachaux, Eugenio Rodriguez, and Jacques Martinerie. The brainweb: phase synchronization and large-scale integration. *Nature reviews neuroscience*, 2(4):229, 2001.

[220] Edward Wallace, Marc Benayoun, Wim Van Drongelen, and Jack D Cowan. Emergent oscillations in networks of stochastic spiking neurons. *Plos one*, 6(5):e14804, 2011.

[221] Kyle CA Wedgwood, Kevin K Lin, Ruediger Thul, and Stephen Coombes. Phase-amplitude descriptions of neural oscillator models. *The Journal of Mathematical Neuroscience*, 3(1):2, 2013.

[222] David K Welsh, Takato Imaizumi, and Steve A Kay. Real-time reporting of circadian-regulated gene expression by luciferase imaging in plants and mammalian cells. *Methods in enzymology*, 393:269–288, 2005.

[223] JO Willoughby, SP Fitzgibbon, KJ Pope, L Mackenzie, AV Medvedev, CR Clark, MP Davey, and RA Wilcox. Persistent abnormality detected in the non-ictal electroencephalogram in primary generalised epilepsy. *Journal of Neurology, Neurosurgery & Psychiatry*, 74(1):51–55, 2003.

[224] Hugh R Wilson and Jack D Cowan. Excitatory and inhibitory interactions in localized populations of model neurons. *Biophysical journal*, 12(1):1–24, 1972.

[225] Arthur T Winfree. *The geometry of biological time*, volume 12. Springer Science & Business Media, 2001.

[226] Annette Witt, Agostina Palmigiano, Andreas Neef, Ahmed El Hady, Fred Wolf, and Demian Battaglia. Controlling the oscillation phase through precisely timed closed-loop optogenetic stimulation: a computational study. *Frontiers Neural Circ.*, 7:49, 2013.

[227] Kong-Fatt Wong and Xiao-Jing Wang. A recurrent network mechanism of time integration in perceptual decisions. *Journal of Neuroscience*, 26(4):1314–1328, 2006.

[228] Dajun Xing, Yutai Shen, Samuel Burns, Chun-I Yeh, Robert Shapley, and Wu Li. Stochastic generation of gamma-band activity in primary visual cortex of awake and anesthetized monkeys. *Journal of Neuroscience*, 32(40):13873–13880a, 2012.

[229] Dajun Xing, Yutai Shen, Samuel Burns, Chun-I Yeh, Robert Shapley, and Wu Li. Stochastic generation of gamma-band activity in primary visual cortex of awake and anesthetized monkeys. *Journal of Neuroscience*, 32(40):13873–13880a, 2012.

[230] Jun Yamamoto, Junghyup Suh, Daigo Takeuchi, and Susumu Tonegawa. Successful execution of working memory linked to synchronized high-frequency gamma oscillations. *Cell*, 157(4):845 – 857, 2014.

[231] Jun Yamamoto, Junghyup Suh, Daigo Takeuchi, and Susumu Tonegawa. Successful execution of working memory linked to synchronized high-frequency gamma oscillations. *Cell*, 157(4):845–857, 2014.

[232] Juliana Yordanova, Tobias Banaschewski, Vasil Kolev, Wolfgang Woerner, and Aribert Rothenberger. Abnormal early stages of task stimulus processing in children with attention-deficit hyperactivity disorder–evidence from event-related gamma oscillations. *Clinical Neurophysiology*, 112(6):1096–1108, 2001.

[233] Na Yu, R Kuske, and YX Li. Stochastic phase dynamics: Multiscale behavior and coherence measures. *Physical Review E*, 73(5):056205, 2006.